Dissertation

submitted to the

Combined Faculty of Natural Sciences and Mathematics

of Heidelberg University, Germany

for the degree of

Doctor of Natural Sciences

Put forward by

Janina Dorin Hakenmüller

born in: Tübingen

Oral examination: 14.10.2020

Looking for coherent elastic neutrino nucleus scattering with the CONUS experiment

Referees: **Prof. Dr. Dr. h.c. Manfred Lindner**

JProf. Dr. Loredana Gastaldo

Auf der Suche nach kohärenter elastischer Neutrino Kern Streuung mit dem CONUS Experiment

Das CONUS Experiment sucht nach kohärenter elastischer Neutrino Kern Streuung (CEνNS) an dem 3.9 GW_{th} Kernreaktor Brokdorf, Deutschland, in einem Abstand von 17 m zum Reaktorkern. Vier hoch-reine Geramnium Spektrometer (insgesamt 4 kg) mit niedriger Schwelle wurden in einer massiven Abschirmung platziert. Die Detektoreigenschaften und das elektronische Rauschverhalten wurden im Detail charakterisiert. Das beinhaltet das aktive Volumen, die Stabilität der Energieskala, die Verteilung der Zeitunterschiede zwischen den Ereignissen und ein vollständige Studie von Korrelationen zu Umgebungsparametern. Mögliche Reaktor korrelierte Untergründe wurden mit zielgerichteten Neutronen- und Gammastrahlungsmessungen außerhalb der Abschrimung untersucht. Mit Hilfe von Monte Carlo (MC) Simulationen wurde gezeigt, dass der Reaktor korrelierte neutroneninduzierte Untergrund innerhalb der Abschirmung vernachlässigbar ist. Für die CEνNS Analyse wurde die MC durch das Hinzunehmen der nicht Reaktor korrelierten Untergründe, insbesondere der myon-induzierten, die bei der niedrigen Überdeckung des Experiments dominieren, ausgeweitet. Aus einem Datensatz von 248 kg·d Reaktor AN und 59 kg·d Reaktor AUS Daten wurde die erste Obergrenze für CEνNS mit Reaktorantineutrinos in einer Likelihood Analyse abgeleitet. Quenching, die unvollständige Umwandlung von Rückstoßenergie in Ionisierungsenergie registriert von den Detektoren, ist die dominierende systematische Unsicherheit. Aus der ermittelten Obergrenze und der Vorhersage der erwarteten Anzahl an Ereignissen aus dem Standard Modell kann ein großer Bereich an Quenchingparametern aus der Literatur ausgeschlossen werden. Für den Zentralwert aus der Literatur von 0.16 ist die Obergrenze mit 90% C.L. nur einen Faktor zwei von der Standard Modell Erwartung entfernt.

Looking for coherent elastic neutrino nucleus scattering with the CONUS experiment

The CONUS experiment is looking for coherent elastic neutrino nucleus scattering (CEνNS) at the 3.9 GW_{th} nuclear power plant in Brokdorf, Germany, at a distance of 17 m to the reactor core. Four high-purity low threshold germanium spectrometers (in total 4 kg) are deployed within a massive shield. Detector properties and the electronics noise are characterized in detail. This includes the active volume, the stability of the energy scale, the time difference distribution of the events and a complete study of correlations to environmental parameters. Potential reactor-correlated backgrounds were examined by dedicated neutron and γ ray measurements outside of the shield. With the help of Monte Carlo (MC) simulations it was shown that the reactor neutron-induced background is neglible within the shield. For the CEνNS analysis, the MC was further expanded by including all non reactor-correlated background components, especially the muon-induced one, which is dominant at the shallow depth of the experiment. From an exposure of 248 kg·d reactor ON and 59 kg·d reactor OFF data the first upper limit for CEνNS with reactor antineutrinos is derived in a likelihood analysis. Quenching, the incomplete conversion of recoil energy to ionization energy registered by the detectors, is the dominant systematic uncertainty. From the evaluated upper limit and the Standard Model prediction of the expected number of counts, a wide range of the quenching parameters found in literature can be excluded. For the central value in literature of 0.16, the upper limit with 90% C.L. is only a factor of two away from the Standard Model expectation.

Contents

1 Introduction

Neutrinos are electrically neutral particles that only interact weakly within the Standard Model of particles physics. The precise measurement of fundamental neutrino interactions is an important tool to validate it and to look for physics beyond the Standard Model. One of the most explicit hints that the model is not complete is given by neutrinos. While the Standard Model predicts that they are massless, the discovery of neutrino oscillations [1] means that at least two of the three neutrino flavors have a mass. The Standard Model predicts six interactions [2] that were all seen in a detector since the first direction detection of neutrinos in 1956 [3]. They include inverse μ/τ decay, elastic neutrino electron scattering, (quasi-) elastic neutrino nucleon scattering, nucleon excitation and resonance production as well as deep inelastic scattering and jet production. The last one to be observed is coherent elastic neutrino nucleus scattering (CEνNS). Coherent scattering means that the neutrinos do not interact with the single constituents of the nucleus, but with the whole nucleus at once. The energy of the neutrinos is crucial to guarantee the coherency condition.

CEνNS was first detected in 2017 [4] for neutrinos in the energy range of 16-50 MeV at a pion-decay-at-rest source by the COHERENT experiment. Within the fully coherent regime at lower neutrino energies (e.g. below 20 MeV for Germanium (Ge) nuclei) the detection of the interaction is still pending. An ideal neutrino source to guarantee the energy conditions are nuclear reactors, where in the decay of fission products anti-neutrinos with less than 10 MeV are emitted. The CONUS (COherent elastic Neutrino nUcleus Scattering) experiment aims at detecting CEνNS with reactor anti-neutrinos and germanium spectrometers at the nuclear power plant Brokdorf (KBR) in Germany.

In the following, the characteristics of CEνNS are described and an overview on physics cases where CEνNS plays an important role are presented. The experimental challenges due to the nature of the interactions are highlighted. Within this thesis it is shown how the CONUS experiment faces these challenges and the first full CEνNS analysis of the experiment of Run1 and Run2 is depicted.

1.1 Coherent elastic neutrino nucleus scattering

In a CEνNS interaction, which is flavor blind, neutrinos exchange a neutral Z boson with all nucleon of a nucleus (N,Z):

$$\nu + (N, Z) \rightarrow \nu + (N, Z) \tag{1.1}$$

The interaction was predicted in 1974 by Freedman [5] and the differential cross section is given as:

$$\frac{d\sigma}{d\Omega} = \frac{G_f^2}{16\pi^2}(N - (1 - 4sin^2\theta_W)Z)^2 E_\nu^2 (1 + cos\theta) F^2(Q^2) \tag{1.2}$$

In the formula, G_f denotes the Fermi constant and θ refers to the scattering angle. The target nucleus is described by the number of neutrons N and protons Z. As the value of the Weinberg angle θ_W is $\approx$0.23 [2], the proton number nearly drops out making the cross section proportional to the number of neutrons squared. Moreover, the cross section is proportional to the neutrino energy E_ν squared. This is due to the coherency of the interaction. When the wavelength of the momentum transfer is larger than the size of a nucleus, the wavelength of the single nucleons add up quadratically leading to the enhancement of the cross section. Figure 1.1 shows how below 50 MeV the cross section dominates over the other interactions. Whether the coherency condition is fulfilled, depends highly on the energy of the neutrino. An upper limit in energy to ensure coherency can be derived from the diameter of the nucleus ($d_{nuc} = 0.0127\sqrt[3]{N+Z}$ [1/MeV]). For Ge nuclei below 20 MeV full coherency is ensured as the momentum transfer is smaller than one over the diameter of the nucleus. With increasing energy, the single constituents of the nucleus become visible. This is paraphrased by the nuclear form factor F depending on the momentum transfer Q. For a fully coherent interaction it is 1.

In the detector, the recoil of the nucleus hit by the neutrino is detected. The recoil is small as the (nearly) massless neutrino hits a massive nucleus. The maximum recoil energy T_{max} for a reflection of the neutrino amounts to:

$$T_{max} \approx \frac{2E_\nu^2}{m_{nuc}} \quad \text{with} \quad m_{nuc} \approx m_{neutron}(Z + N) \tag{1.3}$$

It is inversely proportional to the mass of the nucleus. This leads to a push-pull situation. While for a large cross section heavy nuclei are preferred ($\sigma \propto N^2$), the recoil energy decreases with higher mass. Therefore, a medium mass number is ideal for the detection of CEνNS such as e.g. Ge with Z=32 and N=38-42.

Assuming a Ge as target nucleus, the maximum recoil energy in the fully coherent regime for 10 MeV neutrinos and 1 MeV neutrinos amounts to 3 keV$_{nr}$ and respectively 0.03 keV$_{nr}$. This illustrates that an absolutely necessary prerequisite for a detection is a low enough energy threshold of the detector. Moreover, due to the so-called quenching effect the recoil energy is only partially converted into ionization energy E_{ee}, while the rest goes into phonons. Depending on the detector technology only the ionization energy can be registered which is for example the case for ionization Ge spectrometers (like the CONUS detectors). The ratio of ionization energy to phonons depends on the recoiling nucleus, but also the temperature of the material (see Figure 1.9 for Ge). Assuming a quenching factor of 0.2 (discussed in detail in section 1.4.5), this means that in end for 10 MeV neutrinos and 1 MeV neutrinos only 600 eV$_{ee}$ and respectively 6 eV$_{ee}$ are available for detection making a low energy threshold of the detectors even more necessary.

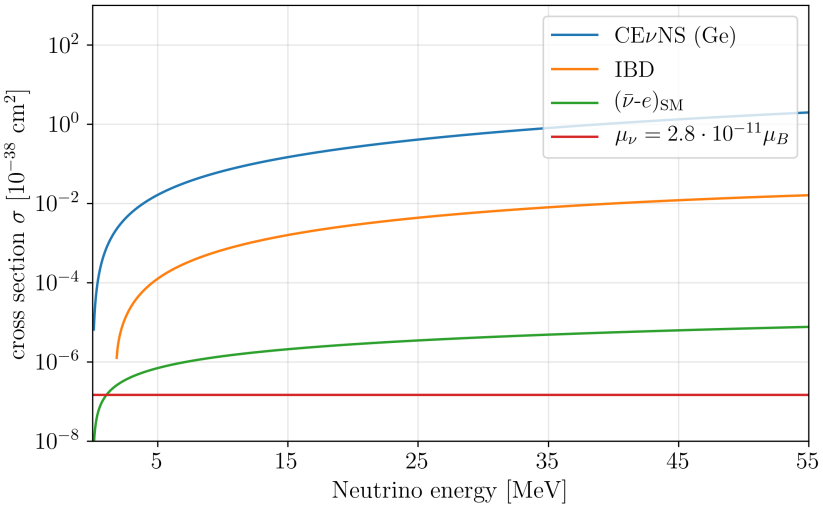

Figure 1.1: Neutrino interaction cross sections below 50 MeV: the cross section of CEνNS is about two orders of magnitude larger than the one for inverse β decay (IBD) with a threshold of 1.8 MeV. The cross section for electron neutrino scattering is much smaller. The current best experimental limit for the neutrino magnetic moment [15] is also marked. Figure courtesy to T. Rink.

1.2 Relevance of CEνNS

The detection of CEνNS is of interest to validate the Standard Model and to be able to precisely describe the interaction.

CEνNS occurs for example in stellar collapse. There, about 99% [8] of the binding energy is emitted in the form of neutrinos. They scatter coherently when moving outward and can for example accelerate iron layers in Super Nova explosions to above the escape velocity as described in [9]. This makes the interaction relevant for the respective astrophysical models.

On earth, CEνNS of ambient neutrinos is an inevitable background of Dark Matter experiments. Dark matter experiments are looking for the dark matter induced recoils, which is a signature indistinguishable from CEνNS. Figure 1.2 shows a recent exclusion plot of spin-independent dark matter searches. The current sensitivity is already close to the so-called neutrino floor [10] created by solar neutrinos, atmospheric neutrinos and diffuse Super Nova background. Especially ^{8}B solar neutrinos are in the near future within the reach of detection. While the neutrinos are an unshieldable background, the detection can also be beneficial because it offers the possibility to study the detector response to recoils.

Looking at the cross section equation (1.2), a precise detection of CEνNS with high statistics would also mean that the input parameters can be evaluated with high precision. This would be the nuclear form factor and the Weinberg angle. CEνNS opens up a new possibility to access nuclear form factors [12]. Contrary to

other methods, no strong or electro-magnetic effects have to be taken into account. Figure 1.3 shows exemplary the form factor of ^{74}Ge in dependence of the momentum transfer Q (black line). The dashed colored lines represent different orders of Q with higher orders becoming more important at a larger momentum transfer. Within the fully coherent regime it is almost one and the normalization can be fixed. For this purpose, neutrinos from a reactor with energies of less than 10 MeV marked as shaded red area in the figure are ideal. For a larger momentum transfer, the shape of the form factor can be determined, e.g. with neutrinos from pion-decay-at-rest sources. In this regard, measuring CEνNS with different neutrinos sources is complementary and highly desirably. The Weinberg angle (the weak mixing angle) found in the cross section as well, can be derived at low energies from a CEνNS measurement. It is usually determined at much higher energies at colliders (see Figure 1.4) e.g from the ratio of the W and Z boson masses by measureing the masses at $\sim$100 GeV [2]. CEνNS can help to examine the momentum dependence at lower energies as predicted by the Standard Model (the so-called "running"). Each deviation found can pinpoint to physics beyond the Standard Model.

Also in other ways, CEνNS experiments can look for physics beyond the Standard Model. The weak charge in the cross section $(N-(1-4sin^2\theta_W)Z)^2$ in equation (1.2) can be modified with additional couplings ϵ to describe non-standard neutrino-quark interactions (NSI). An overview on potential candidates is for example given in [14]. With CEνNS measurements these interactions can be constrained or even discovered.

Moreover, within the region of interest for CEνNS experiments and at higher energies one can also look for a neutrino magnetic moment, which scales with 1/E. While a minimal extension of the Standard Model to include neutrino masses predicts $\sim 10^{-19}\mu_B$ (with μ_B=Bohr magneton) which is far beyond the sensitivity of any experiment, there are many models especially introducing Majorana neutrinos that predict much higher values [15]. The current best limit of $< 2.8 \cdot 10^{-11}\mu_b$ [15] for solar neutrinos (marked also in Figure 1.1) is set by the Borexino experiment with a liquid scintillator deep underground. But it is also worth mentioning that the reactor-based GEMMA experiment with Ge spectrometers achieved $< 2.9 \cdot 10^{-11}\mu_b$ [16]. The reactor-based CEνNS experiment TEXONO determined a limit of $< 1.3 \cdot 10^{-10}\mu_b$ in 2003 [17].

At the other end of the spectrum, it is also possible to think of CEνNS as tool for reactor monitoring. Trying to employ neutrinos for reactor monitoring is attractive as a large number of neutrinos is emitted by the nuclear reactor and the detection can thus be placed far away from the reactor. However, due to the low interaction cross sections with the current status of detection technologies large detectors and elaborate shielding are required, which makes conventional monitoring tools preferably. Nevertheless, e.g. the WATCHMAN collaboration undertakes effort to develop a water-based Cherenkov detector of several kilotons to check the abidance of nuclear non-proliferation treaties in a distance of 10 km or more. Here, the neutrinos are supposed to be detected by inverse β decay, where higher statistics is feasible with the detector technology available. In principle, a CONUS-like detector

for CEνNS is much more compact, however the statistics with the energy thresholds and detector mass currently available is far too small for all practical purposes. This might change with future generation of CEνNS detectors.

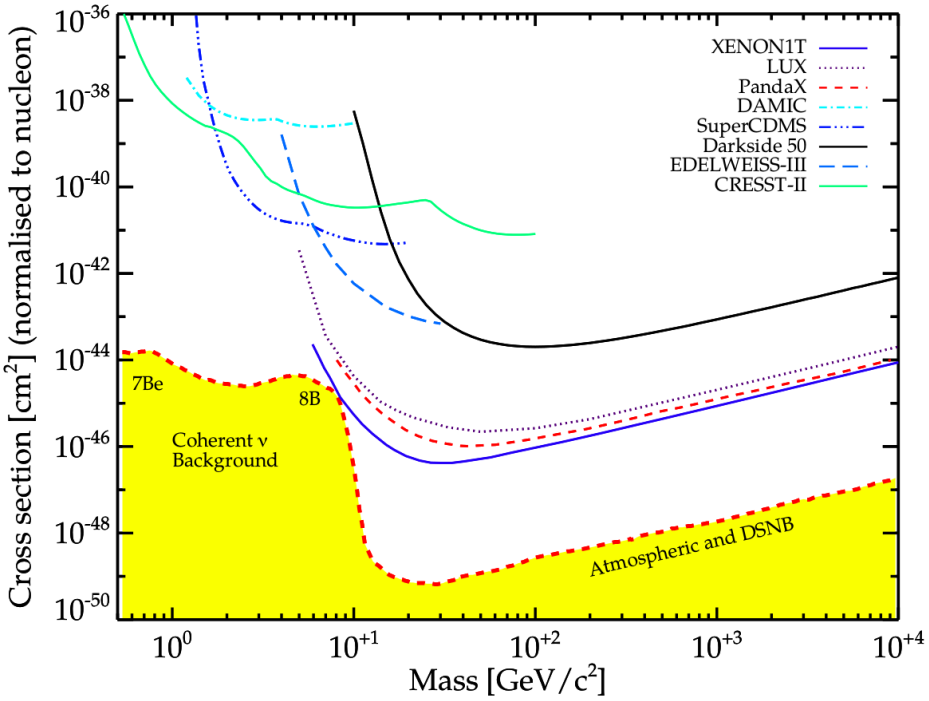

Figure 1.2: Spin-independent dark matter exclusion limits of various direct detection experiments. The sensitivity of current dark matter experiments starts to reach the neutrino floor. [11]

1.3 Experimental challenges

Three prerequisites have to be fulfilled for a successful detection of CEνNS: a strong neutrino source with neutrino energies within the coherent regime, a sufficiently low energy threshold and a successful background suppression adapted to the conditions due to the nature of the neutrino source. Figure 1.5 illustrates how the three components combine within an energy spectrum comparable to the one the CONUS experiment aims to detect.

Currently, three different kind of sources are used for the detection of CEνNS. At nuclear power plants, neutron-induced fission in a self-sustained chain reaction occur. Most of the fission fragments are radioactive and decay via β^- decays resulting in emission of antineutrinos with energies below 10 MeV. This guarantees a fully coherent interaction. On average 7.2 neutrinos per fission [20] are emitted depending on the isotope and there are $\sim 3 \cdot 10^{19}$ fissions per s and per GW created thermal power [20]. Thus, if it is possible to get close to the reactor core, a high neutrino flux

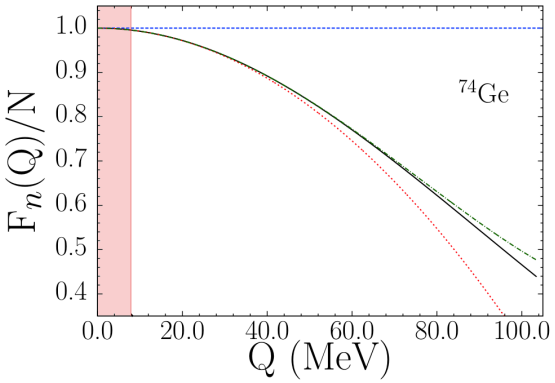

Figure 1.3: The black line corresponds to the theory prediction of the nuclear form factor of ^{74}Ge. The dashed colored lines represent different orders of Q (Q_0=blue (fully coherent), Q_2=red, Q_4=green). The red shaded area marks the range accessible by CEνNS with reactor neutrinos. [12]

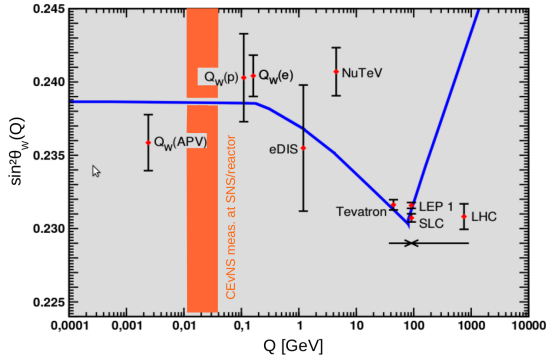

Figure 1.4: Running of the Weinberg angle, the detection of CEνNS offers the unique possibility to determine a value at a low momentum transfer [13].

can be achieved. The CONUS experiment is a reactor neutrino experiment set up at the commercial nuclear power plant of Brokdorf, Germany, with a maximum thermal power 3.9 GW_{th} at a distance of about 17 m to the reactor core. This results in a high anti neutrino flux of the order of 10^{13} $cm^{-2}s^{-1}$. More details on the location are given in Chapter 4. Next to the CONUS experiment, there are several other CEνNS experiments at nuclear power plants running or under construction e.g. TEXONO [21], νGen [22], and Nucleus [23].

Besides reactor neutrinos, neutrinos from pion-decay-at-rest-sources can be used for the detection of CEνNS as well. These neutrinos predominately have higher energies of several tens of MeVs, where the nuclear form factor already deviates from 1. Currently, only the COHERENT experiment [4] is set up at such kind of source, the Spallation Neutron Source in Oak Ridge, US. Protons hit a mercury target, where not only fast neutrons, but also pions are produced. In the decay of the pions neutrinos of different flavors are created. At a similar distance, the neutrino flux is several orders of magnitude smaller than at a nuclear power plant.

At even lower energies than the reactor neutrinos, there is a proposal to use a ^{51}Cr source [19], which emits mono energetic lines of neutrinos of several 100 keV. This has the advantage that the distance to the source can be short, if there are not too many contaminations of the source itself, which needs to be shielded. Additionally, the source can be brought to a location benificial to background suppression such as a deep underground laboratory. However, huge effort has to be undertaken to create such a source.

The type of source selected has an impact on the detector technology used. For the detection of the CEνNS interactions a low enough energy threshold is crucial

to be able to observe the induced recoil of the nucleus of the detector material. For neutrino energies above 10 MeV like at a pion-decay at rest source, a higher energy threshold is sufficient to be able to see a signal, while at a nuclear power plant a smaller threshold is required as, according to equation (1.3), recoils below $3\,\mathrm{keV}_{nr}$ are expected. CEνNS with neutrinos from a ^{51}Cr source require an even lower threshold. The CONUS collaboration decided on using 4 Ge spectrometers of 1 kg each as new developments enable an energy threshold below 300 eV, which is necessary taking the quenching effect into account, and the detector technology is compatible with the reactor environment. The principles of Ge spectroscopy are described in Section 1.4 and the CONUS detectors are characterized in detail in Chapter 2.

The last important ingredient for a detection of CEνNS is a successful background suppression. For reactor experiments the background can be determined when the reactor is off for maintenance (the so-called "outage") and compared to the reactor on time to extract a signal. However, at commercial power plants the outages are sparse. Pion-decay-at-rest sources work with short pulsed beams, making it possible to evaluate the background before and after each pulse. Both kind of experiments have to ensure that there is no source of correlated background, especially neutrons. Neutrons are a dangerous background because they induce nuclear recoils as well. At a nuclear power plant, the reaction chain creating the thermal power is sustained by neutron-induced fission resulting in the creation of more neutrons. There is a finite probability for them to escape the reactor core and potentially reach the experimental site. A detailed characterization of the reactor-correlated neutron-induced background for the CONUS experiment is described in Chapter 4.

For the steady state background muon-induced contributions dominate except for a ^{51}Cr source experiment as the two other neutrino sources are located at earth's surface. An adequate shield is required to suppress the background as much as possible and facilitate the detection of CEνNS. The relevant background sources and interactions are described in Section 1.5, the CONUS shield in Section 1.7.1 and the measured background of the CONUS experiment in Chapter 5.

1.4 High purity germanium spectroscopy

High purity Ge spectrometers (HPGe spectrometers) are ideal for the detection of CEνNS of reactor neutrinos because of their low energy threshold, the radio-purity of the detector material as well as the background suppression techniques available, and for practical purposes in the reactor environment. In the following, the principles of semi-conductor detectors are described with special focus on low energy threshold HPGe spectrometers. The information are extracted from [24] and from [25].

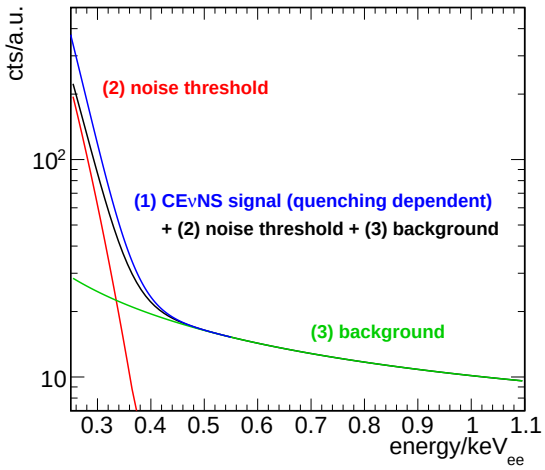

Figure 1.5: Illustration of the three prerequisites to be fulfilled for a successful detection of CEνNS with CONUS: (1) a neutrino source with a high flux within the coherent regime, (2) a sufficiently low energy threshold to see the signal and (3) a low enough background for the signal to become clearly visible.

1.4.1 Principles of Ge semi-conductor detectors

In semi-conductor detectors, charged particles create electron-hole pairs by ionization in a present electric field. By reading out the resulting current, the energy of the initial particles can be deduced. Neutral particles such as neutrinos can create electron-hole pairs indirectly by inducing recoils of the nuclei of the detector material that free the charges.

Metals, semi-conductors and insulators are characterized by the energy bands that the electrons can occupy and the energy gap in between. For metals, the higher energy bands are not fully filled and electrons can easily migrate causing electric conductivity. On the contrary, in an insulator there is a large energy gap greater than 5 eV [25] between the conductivity band (the first band not filled with electrons) at higher energies and the valence band (last band filled with electrons). For semi-conductors, the energy gap exists as well, but it is small (e.g. 0.67 eV at 77 K for Ge [24]) and thermal excitation of electrons can be enough to lift them into the conductivity band. This is the case for intrinsic semi-conductor such as germanium among other elements of Group IV of the periodic table. In the valence band, holes are left behind. By doping the semi-conductor material, the number of free charge carriers can be increased. In this process, donor atoms of either Group V (e.g. P) of the periodic table (more electrons) or acceptor atoms of Group III (e.g. B) of the periodic table (less electrons) are introduced in the crystal structure. When new covalent bounds are formed, either the left over electron is donated to the conductivity band creating a n-type material or an additional hole is produced in the valence band for a p-type material. Even without any donor or acceptor atoms, germanium crystals can be assigned n- or p-type due to natural impurities.

To convert the semi-conductor into a detector, an electrical field is required. This can be achieved by applying high voltage. However, for a pure semi-conductor due to the conductivity of the material, even without any radiation a high current is present (so-called leakage current). To get rid of the leakage current, a pn-junction has to be formed between p-type and n-type materials. The diffusion from each side of the

junction creates a region without any free charge carriers, the so-called depletion region (see figure 1.6). The charge distribution imbalance results in an electrical field. To increase this region, high voltage (HV) in reverse bias is attached forming a diode. The high voltage required scales with the size of the detector as well as the net impurity concentration of the initial semi-conductor material. The resulting diode can be viewed as a capacitor with the electrical field over the pn-junction. Figure 1.7 shows typical Ge detector configurations for p type bulk material.

1.4.2 Germanium diodes

The properties of the semi-conductor detectors are determined by the material, the net impurity concentration and the shape as well as the contacting of the detector. Ge is an ideal material for high resolution spectroscopy due to the small energy required to create an electron hole pair resulting in a large number of free charges. Moreover, nowadays, pure material without any donor atoms is available with little intrinsic impurities (HPGe spectroscopy). This is preferred as it results in a low high voltage of a few 1000 V required to conduct the detector. For the CONUS detectors the order of 1 impurity atom per 10^{12} Ge atoms is achieved. The small impurity concentration furthermore lowers the risk of charge trapping and guarantees a high charge collection efficiency. Regarding the detector shape, Figure 1.7 shows two typical configurations for p-type bulk material (different in size and shape). The pn junction is created each time by inward diffusion of Lithium (Li) donor atoms deposited on the outside of the bulk. The layer has a thickness of the order of 1 mm. The p+ contact can be a thin layer of acceptor atoms of the order of 100 nm thickness or it is limited to a small area (point-contact). The passivation layer (thickness of the order of 100 nm) is needed as isolation between the two contacts. Configuration (a) is a small flat detector with a point-contact. The capacity can be calculated comparable to the one of a parallel plate condenser. It scales with the diameter of the diode squared and the inverse of the thickness of the detector [24]. This leads for configuration (a) to a small capacity of the order of 10^{-12} F, making high resolution spectroscopy possible. As described below, the detector capacity is indeed directly correlated to the noise charge of the detector and therefore the energy resolution. For bigger diodes it is more difficult to achieve depletion with a point-contact. Thus such as for the larger semi-coaxial configuration (b) the p+ contact covers the complete area of the bore hole in the bulk. Consequently, the capacity is larger and the electric field is less uniform. However, the detection efficiency at high energies of a few MeV is bigger as well, because the higher energetic γ lines are more likely to be fully absorbed in such a diode. For the CONUS detectors the design (a) has been chosen due to the low energy threshold requirement. But for background examinations a higher detection efficiency at higher energies is beneficial and thus also studies with a semi-coaxial detector were carried out (called CONRAD (CONUS RADiation) detector).

While there are semi-conductor detectors that can be operated at room temperature, this is not possible for HPGe spectrometer. The small band gap leads to a

high leakage current already due to thermal excitation. Therefore, Ge spectrometers are conventionally cooled down with liquid nitrogen to 77 K. Alternatively, electrical cryocoolers can be used. For the CONUS detector this is a necessity as at the nuclear power plant no cryogenic liquids are allowed for safety reasons. Another benefit lies in the low maintenance as no regular refilling of liquid nitrogen is required.

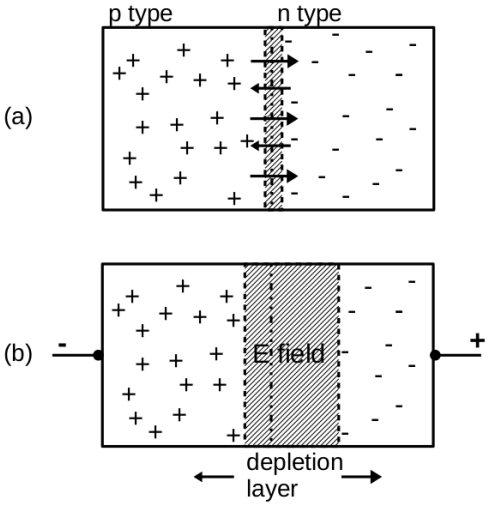

Figure 1.6: (a) p-type and n-type semi-conductor material brought in contact (b) HV connected in reverse bias to increase the depletion region (Figures based on [24]).

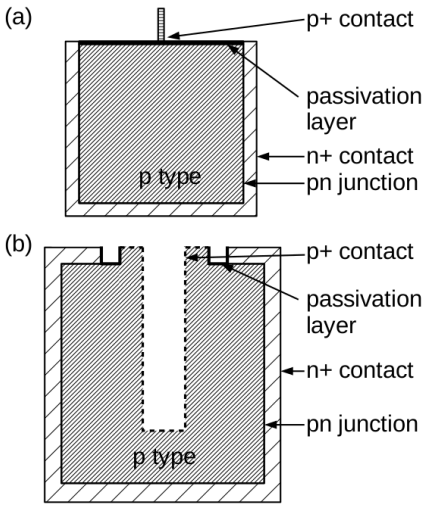

Figure 1.7: (a) point contact p-type Ge detector (b) semi-coaxial p type Ge detector.

1.4.3 Signal processing

The charges created inside the detector are collected at the preamplifier, the first component in the processing chain. For a charge sensitive preamplifier, the change in the charge (=current) is proportional to the deposited energy. As the current is also proportional to the output voltage, the deposited energy can be observed as increase in the voltage. The lowest voltage level without energy deposition is called baseline and events lead to an excess over the baseline. Figure 1.8 shows how events are collected as voltage steps with a rise time (duration of the increase) of less than 1 μs for each step until the end of the so-called dynamic range (property of preamplifier) is reached and a reset to the lowest level of the baseline has to occur. During the analogue to digital conversion in the DAQ, the dynamic range corresponds to a fixed number of channels and the energy of the event is given relative to the maximum number of channels. A calibration with signals of known energy is required to find the correspondence between channel number and energy. The reset is achieved with a transistor reset circuit. Thus, this type of preamplifier is called transistor reset preamplifier (TRP). Alternatively and more conventionally

used, an additional feedback resistor is included (RC preamplifier), which leads to an exponential decay back to the baseline after each voltage step. However, the intrinsic noise of this resistor (Johnson noise) adds to the overall electronics noise of the system. For low threshold applications such as CONUS it is beneficial to forgo the resistor and use a TRP system.

The time period immediately after the reset is cut away until a stable baseline is achieved. This takes about a few μs. But to ensure no undesired effects for CONUS logic pulses of the length of 60 to 180μs are used to inhibit the reset period during the data taking. The reset time periods add to the dead time of the electronics. The so-called dead time in general describes the fraction of the duration of the measurement, when no events are registered by the detector. This happens either due to vetos as for the TRP inhibit or because one event follows to quickly after another and the energy of the second event cannot be extracted correctly (pile-up). One additional advantage of a TRP system is that for a very high event rate the dead time will strongly increase, but the preamplifier will never lock-up. For a RC preamplifier above a certain event rate the pulses will pile up onto each other and no decay to the baseline is possible any more, leading to no output of the preamplifier at all. For CONUS being able to process high count rates of the order of MHz is of interest to study the noise events to the full extent.

For a good signal-to-noise ratio, the preamplifier has to be as close as possible to the diode. It is thus located within the cryostat and cooled down together with the diode for further noise reduction.

The output signal from the preamplifier is amplified and shaped to extract the energy information. For CONUS, this task is carried out by a commercial data acquisition system (DAQ), the Canberra Lynx Digital Signal Analyzer. Its main advantage is that it is a quick and easy to set up solution especially for pulse reset preamplifiers, but the drawback is that the pulse shape is not accessible. Only a list of events containing the time stamp of the event and the channel number is constantly printed out during data taking. The energy reconstruction, meaning extracting the channel number from the baseline, is carried out largely by the Lynx DAQ. Only the time constant of the shaping filter relevant for the energy resolution as described in the next section can be chosen by the user. The Lynx also provides the HV and the preamplifier voltage to the detectors.

1.4.4 Resolution and energy threshold of Ge spectrometers

An absolute necessity for the detection of CEνNS of reactor neutrinos is a low enough energy threshold. A prerequisite for the low energy threshold is a high peak resolution because the same noise that broadens the peaks also leads to an increase the detector threshold. This is because for an event of a certain energy different energy values can be detected depending on the noise fluctuations of the baseline.

In general, there are five contributions to the resolution σ: (1) intrinsic line width σ_{intr},(2) statistical uncertainty on the number of produced electron-hole pairs σ_{eh}, (3) uncertainty on the charge collection σ_{coll}, (4) electronic noise σ_{noise} and (5)

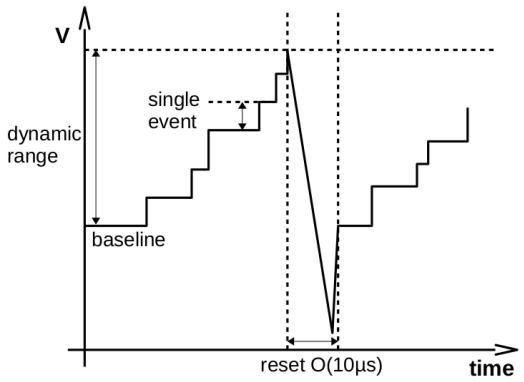

Figure 1.8: Baseline of a transistor reset preamplifier. The events are observed as voltage steps adding up over the baseline until the reset occurs. The rise time of the steps is less than 1 μs.

environmental vibrations σ_{env}. As independent sources they add up quadratically to the overall resolution:

$$\sigma^2 = \sigma^2_{intr} + \sigma^2_{eh} + \sigma^2_{coll} + \sigma^2_{noise} + \sigma^2_{env} \tag{1.4}$$

The intrinsic line width σ_{intr} (1) refers to the natural width in energy of the nuclear levels. Due the Heisenberg uncertainty relation this width is inverse proportional to the lifetime of the states. For example for the 10.37 keV line of ^{71}Ge with a half-life of 11.4 d this leads to an energy width of $\sim 10^{-21}$ eV. Even for much shorter half-lives, the width is in general orders of magnitude smaller than the other contributions to the resolution and thus negligible.

The uncertainty of the number of produced electron-hole pairs σ_{eh} (2) is related to the detector material. The energy required to create an electron-hole pair in Ge at 77 K is low with ϵ=2.96 eV [24], while e.g. for another popular semi-conductor material, Si, it is 3.63 eV at room temperature [24]. The large number of free charge carries make Ge highly suitable for high resolution spectroscopy. The deposition of the energy E_{dep} in a Ge diode leads to N_{eh} electron-hole pairs:

$$E_{dep} = N_{eh} \cdot \epsilon \tag{1.5}$$

For the 10.37 keV line this means $\sim$3500 electron-hole pairs are created. The current read out at the contacts of the diode is proportional to N_{eh} and thus the deposited energy. Therefore, the statistical fluctuation of N_{eh} fundamentally limits the best achievable resolution of the spectrometer. To describe this, it is not possible to directly apply Poisson statistics to N_{eh} as the individual electron-hole pairs are not independent due to being connected via the crystal lattice. Instead the Fano factor F as material constant is introduced as ratio between the observed variance and the one expected from Poisson statistics:

$$\sigma_{eh} = \epsilon \cdot \sqrt{F \cdot N_{eh}} = \sqrt{F \cdot E_{dep} \cdot \epsilon} \tag{1.6}$$

For Ge, F=0.11 was determined experimentally in 1991 [26]. An energy dependence of F is suspected [27]. The equation also shows that an overall square root energy dependence of the resolution can be expected.

While σ_{eh} (2) is only defined by the detector material, improvements on the resolution can be achieved by tuning the contributions (3)-(5).

The uncertainty on the charge collection σ_{coll} (3) summarizes effects that lead to a loss of charges on their way to the preamplifier and further in the electronics chain. Most notably this can occur if the charges are trapped in crystal defects or impurities. For HPGe detectors this probability is small to begin with. Crystal imperfections can potentially be created during the operation of the detector by radiation damage, but this is excluded for the CONUS detectors (see Section 4.4). Moreover, shallow traps can also be overcome by a high enough bias voltage at the crystal. For CONUS there is no indication that a significant contribution to the resolution comes from deficits in charge collection.

For all contributions to the resolution, the electronic noise (4) is the factor where the most technological development for the CONUS detectors went into. Assuming there is no problem with (3) or (5) and by comparing the measured resolution of γ-ray lines to equation (1.6), the overall contribution can be estimated which is conventionally referred to as the equivalent noise charge σ_{noise}:

$$\sigma_{noise} = \sqrt{\sigma^2 - F \cdot E_{dep} \cdot \epsilon} \tag{1.7}$$

Generally spoken, the electronic noise causes small variations of the baseline, where the signal pulses sit on (see Figure 1.8). It can be easily imagined that especially small pulses are strongly disturbed by these variations making a detection below a certain energy impossible. On the experimental site, σ_{noise} can be accessed by injecting signals from a pulse generator into the electronics chain and observing the output width. The method has been used to confirm the low electronics noise for the CONUS detectors as specified in the detector design (see Section 2.2.2). There is parallel noise and series electronics noise, named after the place of origin of the noise in the electronics chain relative to the detector. Parallel noise is created in the input circuit through the preamplifier parallel to the detector. Leakage current, the current that runs to the detector even if no signal is present, results in parallel noise. Foregoing the feedback circuit in the preamplifier resistor with a TRP system reduces this noise contribution. The series noise is created in the electronic components in series with the detector. It scales with the detector capacity. Thus, small flat detectors are preferable for a low noise. For both noise contributions keeping the electronics at a cold and stable temperature keeps the noise small. The selection of low noise electronics components by the manufacturers also plays an important role. Moreover, the noise level can be influenced by the selection of the shaping time constant of the filters when extracting the pulses from the baseline. An optimum value for the shaping time can be found minimizing both contributions. The last electronics noise addition, the flicker noise, is created by changes in the direct current in the electronics and increases with increasing current. It is potentially related to

charge carrier trapping in the electronics. The origin is less well understood than for the other two noise contributions.

Finally, the last term (5) having an impact on the resolution and the energy threshold σ_{env} are vibrations from the environment. Even small movements of the detector and its surrounding components can lead to changes to the overall capacity of the system impacting the noise characteristics. Similar to the electronics noise, the baseline is disturbed, which makes it more difficult to identify low energetic signals or can lead to the fake identification of noise events as signals. A source of this kind of noise is the cooling of the detector. Using liquid nitrogen, the boil-off and turbulences in the storage container can introduce microphonics into the system. But also electrical cryocooling such as for the CONUS detectors can lead to vibrating parts close to the detector with frequencies in the Hz range. The varying environmental conditions at the commercial nuclear power plant deviate far from laboratory conditions straining the cryocooling beyond the normal level, which makes a detailed study of this noise contribution for the experiment highly important. All kind of punctual events might lead to an increase of the energy threshold as well, which cannot be avoided if one is not working under laboratory conditions.

As all of the contributions except the negligible intrinsic line width are of statistical nature, the expected resulting peak shape is Gaussian. The induced noise events are observed as huge increase of events at the lower end of the spectrum. Ideally, a Gaussian-like shape is expected (see [27] and source therein), but this is distorted by the DAQ settings and filters. Also, vibrational noise from the environment (5) can have an influence on the shape of the noise peak.

1.4.5 Quenching

When detecting recoils with Ge spectrometers, the quenching effect has to be taken into account as only ionization energy can be registered, but not the energy transferred into phonons. Unfortunately, for the material the exact conversion of recoil energy E_{nr} into ionization energy E_{ee} is not well known. Within this thesis the semi-empirical Lindhard theory with the adiabatic correction introduced in [6] relevant below 1 keV_{nr} is used:

$$\begin{aligned} E_{ee} &= Q \cdot E_{nr} \quad \text{with} \\ Q &= \frac{k \cdot g(\epsilon)}{1 + k \cdot g(\epsilon)} \left(1 - exp(-\frac{E_{nr}}{\xi})\right) \quad \text{with} \\ g(\epsilon) &= 3\epsilon^{0.15} + 0.7\epsilon^{0.6} + \epsilon \quad \text{and} \quad \epsilon = 11.5 Z^{-7/3} E_{nr} \end{aligned} \tag{1.8}$$

The formula holds for the nuclear recoil energy in keV_{nr} and the adiabatic correction is described by $\xi = 0.16^{+0.10}_{-0.13}$. The k factor corresponding to Q at 1 keV_{nr} is referred to as quenching parameter within this thesis. Lindhard [7] originally determined k=0.157 for Ge, while Scholz et al. measured recently k=0.179±0.001 as best fit [6]. Figure 1.9 depicts the Lindhard theory with the adiabatic correction as black curve in

comparisons to further measurements from other authors showing large fluctuations. A detailed literature research by A. Bonhomme revealed that k=0.16±0.04 covers conservatively the available measurements to date. Thus, quenching is a dominant systematic uncertainty for the CEνNS analysis of CONUS. Therefore, it was decided to give all results in Chapter 6 in dependence of the quenching factor. Furthermore, in Figure 1.9 a dependence of the quenching parameter on the Ge temperature is observed. For the CDMS detectors at millikelvin a significantly lower quenching parameter above >1 keV$_{nr}$ was determined [28], while all the other data was collected at 77 K. The CONUS detectors are operated as well at 77 K-87 K

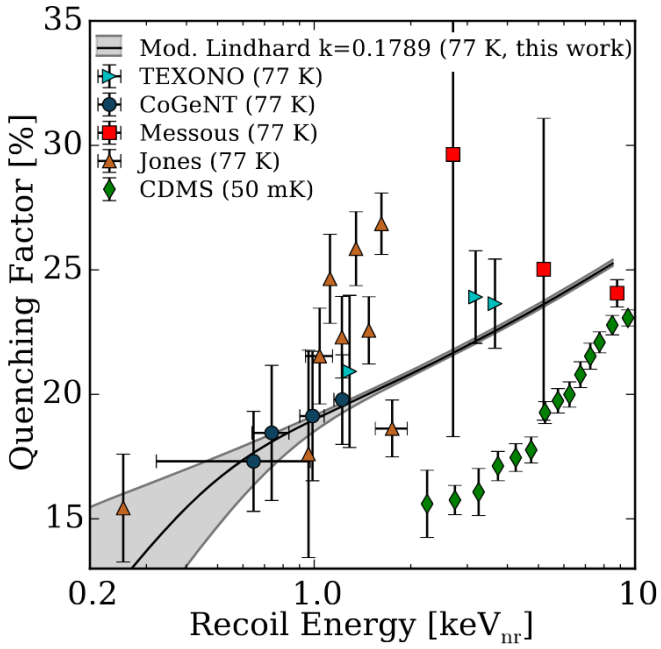

Figure 1.9: Quenching factor to convert the nuclear recoil energy into detectable ionization energy for Ge spectrometers. Various measurements are depicted with the modified Lindhard theory by Scholz et al. as black line. [6]

1.5 Background suppression techniques at reactor sites

To be able to see the small CEνNS signal, the lowest possible background is wanted. In the following, an overview on the dominant background contributions at shallow depth is given and it is described how they can be shielded. The type of shielding depends on the type of particles (γ-rays, electrons, neutrons and α particles) and the location respectively to the diode (in the diode, within the cryostat, within the shield and outside of the shield). Generally speaking, α particles and electrons can already be suppressed with little material, while a larger shield is required for high

energetic γ-rays. For neutrons, the required shielding strongly depends on their energy.

Next to the environmental radioactivity found everywhere, due to the nuclear power plant being located at the earth's surface especially the muon-induced background has to be taken into account. Moreover, potential additional contributions from the reactor have to be carefully examined.

The detailed background composition of the data collected with CONUS detectors experiment are given in Chapter 5.

1.5.1 Natural radioactivity

Primordial radioactivity comprises of the U and Th series (see Figure C.1 and Figure C.2 in the Appendix) and ^{40}K. It can be found everywhere in the earth's crust and consequently in many materials e.g. concrete. There can also be man-made contributions such as ^{137}Cs from nuclear weapon tests. The γ-rays emitted in these decays have energies up several MeV. They can be shielded by materials with a high density ρ and a large γ-ray attenuation coefficient μ_{att} [24]:

$$I(x) = I(0)exp(-x\rho\mu_{att}) \tag{1.9}$$

with $I(x)$ denoting the radiation intensity after a shield thickness of x and I(0) the intensity before the shield. Lead (Pb) with ρ=11.34 g cm^{-3} fulfills this criterion. It has conventionally been used, because it is rather easily available and not too expensive. A thickness of typically 15-20 cm is enough to successfully suppress the environmental radioactivity [29].

In general, the shield materials themselves should ideally not contain any radioactive contaminations especially for the inner shield layers. The same is true for the materials that the detectors are made of. If no prior knowledge is available, all of the materials have to be screened, meaning they are tested on radioactive contaminations. The examination can be carried out with Ge spectrometer setups such as GIOVE [30], but also mass spectroscopy is possible. If no contaminations are found, the materials are called radio-pure or clean.

This is often the case for Pb, only potentially ^{210}Pb activity has to be taken into account, which is described in more detail in Section 5.6.1. Regarding metals in general, Cu is often highly radio-pure due to the manufacturing process, where contaminations are removed in the electrolysis. The density is smaller than for Pb with ρ=8.92 g cm^{-3}. It is often used for the innermost shield layers and as cryostat material housing the Ge diode.

The closer a material sits to the Ge diode the more important is the cleanliness as contaminations cannot be shielded and next to the γ-rays also electrons might contribute to the background. Especially electronics components can be problematic and a search might be required for suitable parts. The Ge of the diode itself is found to be highly radio-pure in an examination carried out by the GERDA experiment [31].

1.5.2 Radon

Radon belongs to the natural radioactivity and can be found everywhere in the air as inert gas. It is listed here separately, because it has to be shielded differently. Radon is part of the Uranium (^{222}Rn) and Thorium decay chain (^{220}Rn) and exhaled by soil, stone and concrete. While the parent isotopes decay within the materials, radon is volatile and outgasses to the ambient air or can be dissolved in water. In the open air, the concentration varies depending on the ambient rocks with e.g. 8 Bq/m^3 in Regierungsbezirk Weser-Emsand, Schleswig-Holstein and up to 30 Bq/m^3 in the area around Stuttgart [34]. In closed spaces like cellars or underground laboratories the concentration can increase ten times or more above these values, especially if there is no ventilation.

To shield the Radon, it has to be kept away from the detector. This can either be achieved by sealing the shield Radon tight or by flushing the shield with Radon free gas. In practice, the first is often inconvenient if the shield is complex and has openings for source insertions, thus the latter is often carried out. Conventionally, boil-off nitrogen is used as it is often available when the detectors are cooled with liquid nitrogen. If this is not possible, Radon free air can be an alternative (see Section 5.5).

1.5.3 Cosmic ray background

Particles emitted by the sun, Super Nova remnants and extragalactic sources continuously hit the earth atmosphere. Most of them are protons [35]. They induce electromagnetic and hadronic cascades in the earth's atmosphere. At sea level a flux of about 300 m$^{-2}s^{-1}$ [36] arrives, consisting out of 15% electrons and γ-rays, 63% muons and 22% hadronic particles [37]. The flux is reduced by buildings and other kind of overburdens. To be able to compare the shielding quality of different overburdens, the unit meters of water equivalent (m w.e.) is introduced, which corresponds to the thickness of a water shield that would achieve the same suppression of the muon flux. Electrons and γ-rays are easily shielded by buildings and the hadronic component is fully suppressed by 10 m w.e [29] (see also Figure 1.10), which e.g. can already be achieved with a few meters of dirt on a concrete ceiling making this background irrelevant already at most shallow depth laboratories. Muons, however, with a mean energy of $\sim$4 GeV [38] at the earth surface are much harder to shield. They lose energy by ionization and radiation processes (bremsstrahlung, production of e^+e^- pairs, photo nuclear interactions) and the mean muon energy shifts towards higher energies as depth increases. At shallow depth up to 100 m w.e. the loss by ionization is more important, which makes it possible to calculate the muon spectrum underground [39], while for the radiation processes simulations are required as the radiation processes introduce random fluctuations. Figure 1.10 from [39] depicts the reduction of the muon flux with depth up to 100 m w.e. Thus, if possible, experiments searching for rare events are located deep underground for example at the Laboratori Nationali del Gran Sasso (LNGS) below 3500 m w.e.,

where a suppression of the muon flux of six orders of magnitude is achieved [40]. This is not feasible for the CONUS experiment due to the nuclear power plant being located at surface.

Muons induce electromagnetic cascades and neutrons inside the materials they pass through. This happens inside the concrete or steel enforced concrete of buildings, but the cross section is especially large for the high Z materials of the shield. The so-called bremsstrahlung continuum populating the energy range below 500 keV_{ee} is created, when the trajectory of passing electrons for the electromagnetic cascades is diverted within the electric field of heavy nuclei. Therefore, to achieve a low background at shallow depth, a muon anti-coincidence system (from hereon refereed to as "muon veto") is an absolute necessity. The muons are detected with e.g. plastic scintillator plates and after each muon signal the Ge data taking is closed for a certain time window until the muon-induced background has passed. The muon-induced background of the CONUS experiment is described in detail in Section 5.3. Additional neutron shielding is beneficial, as neutron capture in Ge can lead to long-lived states with a lifetime outside the veto window. Moreover, neutrons take a long time to scatter in Pb [41] and might not arrive at the diode within the veto window. Also muon-induced neutrons that are created in the concrete needs to be shielded as they are not suppressed by the active muon veto. Muon-induced neutrons at shallow depth have energies of around 1 MeV (see Figure 4.22). To shield these neutrons, they first need to be thermalized. This is done most effectively by hydrogenous materials, as the neutrons lose the most energy when scattering with target nuclei of small masses as the energy loss is inverse proportional to the mass number [42]. Materials with a high neutron absorption cross section are then used to remove the thermal neutrons, e.g. ^{10}B is a good candidate with a total thermal neutron cross section of $\sim$3.8 kb [42] (nearly all nuclear capture (n,α) with an emission of low energetic γ-rays). As many muon-induced neutrons are created inside the shield, an onion like design with layers of borated PE in between proofed to be successful [30].

1.5.4 Cosmogenic activation

The hadronic component of the cosmic rays at earth's surface can activate materials by spallation reactions [43]. This means that radioactive isotopes are produced, that can be short-lived, but also can have half-lives of several years. For the CONUS experiment, the activation of Ge and Cu is of interest, as these contaminations cannot be shielded. It is only possible to avoid their contribution by keeping the diodes and the detector parts underground below 10 m w.e. as much as possible. Section 5.4 shows how this has successfully been achieved for the CONUS detectors. As the activation stops with an overburden of more than 10 m w.e. only the decay is observed which means that the background decreases over time and it has to be investigated if this is relevant for a physics analysis of a certain data set of several months.

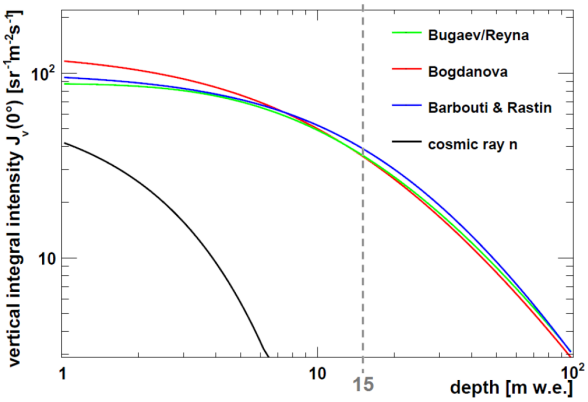

Figure 1.10: Muon flux reduction with depth of overburden. Several models from literature are compared in [39] and give similar results. The neutrons from the cosmic ray hadronic component are already fully suppressed by 10 m w.e. .

1.5.5 Reactor-correlated background

All background contributions presented up to now are shared among all experiments set up at shallow depth. At a nuclear power plant, potential additional background has to be considered due to the fission reactions inside the reactor core. This is especially relevant for experiments in close vicinity such as CONUS, where the neutrino flux is high, but there might also be reactor-correlated neutron and γ-ray background. At a nuclear power plant neutrons induce fission in the fuel assemblies in the reactor core and the energy released is used for the thermal power production. In each fission reactions, about 2-3 neutrons are created depending on the fissile isotope. One keeps up the fission process, but there is also the chance that some of the neutrons escape the reactor core. Fission also creates γ-rays. Additionally, neutrons can activate materials inside the reactor core by (n,p) reactions. Especially the activation of oxygen in the water might be relevant, as the water circuit connecting the reactor core to the steam generators can transport the activation products potentially closer to the experimental site compared to the actual location of the reactor core. For example, ^{16}N with a half-life of 7.13 s [44] is created that decays via the emission of high-energetic γ-ray lines. These additional background contributions make it necessary to carefully characterize the location of the experiment and Monte Carlo (MC) simulations can be used to check whether there are contributions remaining inside the shield. This is demonstrated for the CONUS experiment in Section 4.4.

1.6 Radiation interactions in Ge spectrometers

When ionizing radiation or neutrons reach the diode, electron hole pairs are created that can be read out as signals as described in Section 1.4. Full energy peaks (FEPs)

are observed if the energy of mono energetic γ-ray lines or electrons is fully deposited in the Ge. If only a partial energy deposition occurs, either because the particles lost energy on the way to the diode or they escape the diode without depositing all of their energy, a continuum below the peak arises. Recoils populates the low energy range of the spectrum. In the following, a short overview on the most important interactions for γ-rays, electrons and neutrons is given.

1.6.1 Interactions of electromagnetic radiation on Germanium

A summary of the interactions of electromagnetic radiation in Ge can be found in [24]. The type of interaction depends strongly on the energy of the γ-rays as can be seen in Figure 1.11. Below about 100 keV the photoelectric effect contributes the most, where the photons interact with a bound electron of the atomic shell. The so-called photo electron is emitted and leaves the atom in an excited state, while the photon is absorbed. When returning to the ground state, the vacancy of the photo electron is filled with electrons from higher shells. The excitation energy is emitted by the release of further electrons (Auger cascade) or the emission of γ-ray lines, so-called X-rays. Edges are observed in the absorption curve from photo electrons because the discrete binding energies of the shell, where the photo electrons are emitted from e.g. the K shell absorption edge in Ge at 11.1 keV. Overall, the photo effect leads to the complete deposition of the energy in the diode. There is only a small probability that the X-rays escape the diode.

For higher γ-ray energies of 100 keV to several MeV, Compton scattering becomes dominant. The γ-rays scatter on a (bound) electron and the energy transfer depends on the scattering angle. The γ-ray will never transfer the full energy to the recoiling electron, but it loses energy in this way. In the end, the γ-ray line will be either fully absorbed leading to a FEP or it will escape the detector, such that the energy depositions create a continuum below the peak.

Above 1022 MeV pair creation can occur and the interaction dominates for γ-rays with energies of several MeV. This means that the γ-ray creates an electron positron pair in the Coulomb field of an atom. The positron will annihilate immediately into two 511 keV γ-rays. If one or both of these γ rays escape the detector, but the remaining energy of the original γ-ray is observed the so-called Single Escape Peaks (SEP) or Double Escape Peaks (DEP) will be seen.

Next to all the interactions, the γ-rays also scatter coherently (nearly) without energy deposition. The γ-rays are absorbed and remitted potentially in another direction. At higher photon energies of at least 5 MeV (material-dependent), photo nuclear interactions might occur as well that can lead to the creation of neutrons.

The mean free path length until an interaction occurs in Ge is for γ-rays of the order of 1 MeV several 1 cm, while for γ-rays at 100 keV it is of the order of 0.1 cm. This means that there is a finite possibility for the γ-rays to escape the detector, which will lead to a partial energy deposition in the continuum. It is more likely for higher energetic γ-rays. Electrons, however, have a much shorter range. An electron with 1 MeV kinetic energy deposits it fully within a volume of a few mm^3

and for 100 keV electrons it is even several orders of magnitude smaller (calculated from [45]). In general, it can be assumed, that electrons fully deposit their energy within the Ge, making the single mechanism less relevant than for the γ-rays.

To sum it up, for the continuous background at very low energies below 10 keV_{ee}, partial energy depositions of Compton scattering and β decays are most important. Moreover, the thin layer on the surface of the diode where the charge collection is not complete, can also induce events below the FEPs (see Section 2.2.5).

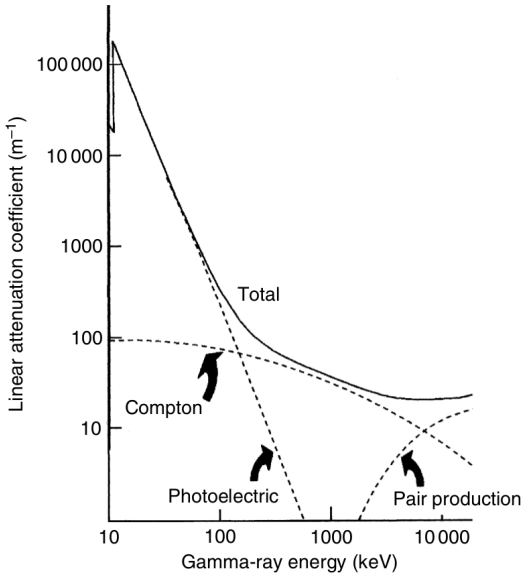

Figure 1.11: Linear attenuation coefficient of Ge [24].

1.6.2 Neutron interaction on Germanium

Neutrons hitting Ge nuclei can induce recoils comparable to CEνNS, which makes this background contribution highly important to investigate.

Within this thesis, thermal neutrons are defined as neutrons with energies within $[1{\cdot}10^{-9}, 4{\cdot}10^{-7}]$ MeV, there is a range of intermediate neutron energies of $[4 \cdot 10^{-7}, 0.1]$ MeV and fast neutrons refers to neutron energies in $[0.1, 19.6]$ MeV. The neutron fluence rate describes the number of neutrons per area and unit of time.

For the CONUS experiment, the neutrons arriving at the diode range from thermal energies up to several MeV (see Section 4.22). In Ge, for thermal neutrons, neutron capture dominates. At higher energies up to $\sim$1 MeV the largest contribution comes from elastic scattering, while above inelastic scattering is comparable [46]. Figure 1.12 shows exemplary the neutron capture cross section for ^{74}Ge, which depict this behavior. For the other Ge isotopes the cross section looks similar except for the exact location and width of the resonance lines. In the following, the signature of the three interactions is briefly described:

Elastic neutron scattering ^{A}Ge(n,n)^{A}Ge leads to recoiling Ge nuclei. It is comparable to CEνNS except that the mass of the neutrons is much larger than the mass

of the neutrino and has to be taken into account when calculating the recoil energy. The maximum recoil energy is given as:

$$Tmax \approx \frac{E_{neutron} m_{neutron}}{mnuc} \quad \text{with} \quad m_{nuc} = m_{neutron}(Z+N) \tag{1.10}$$

This means that for a 1 MeV neutron energy a maximum recoil of a Ge nucleus of 55 keV_{nr} is expected. While for neutrinos it is assumed that only one recoil is created, one neutron will most likely induce several recoils due to the much larger scattering cross section. The elastic scattering of neutrons leads to an increasing continuum towards lower energies, which is similar to the one expected from CEνNS in Figure 1.5.

For inelastic neutron scattering ^{A}Ge(n,n'γ)^{A}Ge, a recoil is induced as well, however, also additionally γ-ray lines are emitted. This means that the recoil only contributes to the low energy part of the spectrum if the γ rays escape the detector. Else, the energy depositions added up and the recoils are observed as as characteristic tail above the γ-ray lines.

In neutron capture processes ^{A}Ge(n,γ)$^{A+1}$Ge, the neutron is absorbed by the Ge nucleus leaving it in a highly excited state. In the deexcitaton process mono energetic γ-ray lines of up to several MeV are emitted. The ground state after the capture might not be stable. The absorption of the neutron also creates a recoil, however, as most neutron capture processes are induced by thermal neutrons the recoil will be tiny. Moreover, also the emission of γ-ray lines creates recoils:

$$T \approx \frac{E_{\gamma}^2}{2m_{nuc}} \quad \text{with} \quad m_{nuc} = m_{neutron}(Z+N) \tag{1.11}$$

Thus, the emission of a 10 MeV γ-ray creates a recoil of 0.7 keV_{nr}.

Like for the neutrino induced recoils, the quenching effect as described in Section 1.4.5 has to be taken into account. Assuming an energy threshold around 300 eV_{ee} means that due to the quenching the recoils from γ-ray emissions after neutron capture are not seen in the detector. In Chapter 7 about measurements with ^{252}Cf neutron sources the signature described here can be observed in the spectra.

1.7 Monte Carlo simulations for background suppressions examinations

As shown in the previous two sections, there are many potential background sources that can be shielded with a wide range of materials. However, particles passing through the shield materials can induce new background contributions as well. For the particles arriving at the diode, depending on their energy, different interactions will occur and energy is deposited. All energy depositions summed up correspond to the measured energy for the event. To be able to disentangle all these contributions and predict the effect of shielding, Monte Carlo (MC) simulations are essential tools.

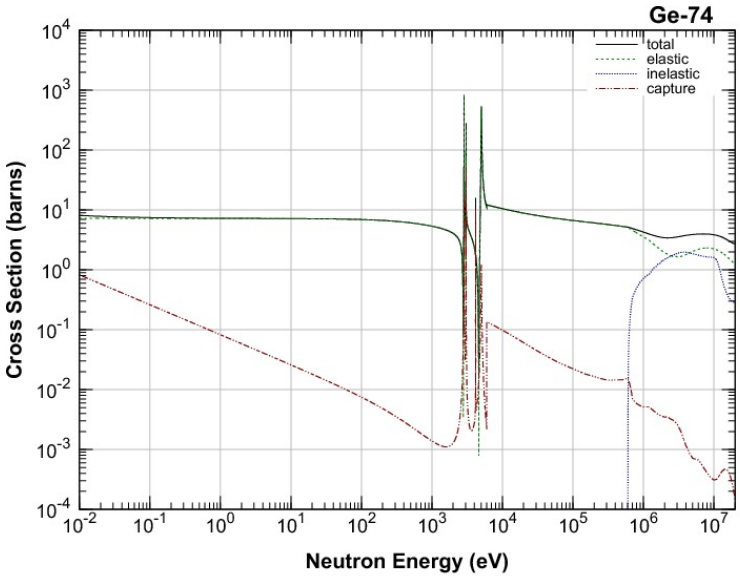

Figure 1.12: Cross section of neutron interactions with ^{74}Ge below 100 MeV (Figure from JENDL-4.0 database [117]).

The simulation framework MaGe [48], based on Geant4 [49, 50], is used to study the background of the CONUS experiment in detail. The two different versions Geant4.9.6p04 and Geant10.4.3 are utilized and differences are highlighted at the respective places. MaGe provides a physics list (a collection of the relevant physics models and cross section) specialized on low energies and low background experiments. The electromagnetic processes are modeled with the "Livermore" physics models with a low energy applicability limit of 250 eV. For the neutron propagation, the "Neutron High Precision Models (NeutronHP)" below 20 MeV is used. To save computation time, secondary production cuts are applied in the MC. Below a certain energy threshold, no secondary particles are created, but the energy deposition is carried out fully by the original particle. Due to the low energy threshold of CONUS, secondary production cuts of 1.2 keV$_{ee}$ for γ-rays and of 850 eV$_{ee}$ for electrons and positrons are applied corresponding to a similar range of the particles in Ge.

The input of a Geant4 simulation consists out of geometry models with the dimensions and materials of the detector, shield and surroundings, that needs to be implemented by the user. For the source, the type of particle (so-called "primary particle"), the energy, angular distribution and shape of the source have to be specified. For each event, one primary particle is started and propagated through the geometry. For each energy deposition at the diode, the energy, type of particle and the location of the energy deposition is registered. Statistics is collected by simulating a large number of events. After the simulation, within the so-called "post-processing", all the energy depositions during one event in one detector are added up. They

correspond to the energy detected in reality. During post-processing it is possible to take into account inefficiencies in charge collection. This is important to take into account energy depositions in the layers at the surface of the diode and also to include the quenching effect. The loss of ionization energy due to quenching is not implemented (see Figure 7.6a of a ^{252}Cf measurement for a comparison of a neutron source MC with and without quenching). The effect has to be added manually. To identify the recoils in the MC within the sensitive volume (the Ge diode) the identity of the particles depositing energy, according to the particle data group (pdg) code [51], is registered. It is assumed that all energy depositions by nuclei are quenched. Thus, using the Lindhard theory with adiabatic correction (see Section 1.4.5), the ionization energy is calculated. Moreover, below 10 keV$_{nr}$ energy depositions by neutrons directly are observed. Those are assumed to be events that were not propagated until the final state. Due to the small energy deposited, they are assumed to be recoils as well and consequently quenching is applied.

While the MC simulation helps to predict and understand background contributions, the data collected can has to be used to validate the simulation. Within this thesis independent measurements of the neutron flux within the shield were used to validate the muon-induced neutrons. Moreover, with the help of ^{252}Cf sources the propagation of neutrons through the shield was studied in detail.

1.7.1 CONUS shield

In the following, the shield of the CONUS experiment is described as basis for the following chapters. The CONUS shield is inspired by the shield design for shallow depth of the material screening detector GIOVE [30]. The detector is located at LLL with an overburden of 15 m w.e., but background rates comparable to detectors located several 100 m w.e. deeper underground were achieved. The background suppression techniques as described in Section 1.5 are applied. The shield is displayed in Figure 1.13. It consists of 25 cm of Pb to shield environmental γ background. There are 10 cm of borated PE (3% equivalent of natural B), produced from PE and boric acid enriched in ^{10}B, to capture and moderate neutrons. Additional plates of pure PE of 5 cm each were added at the bottom and the top of the shield. Organic plastic scintillator plates, equipped with plates of photo multiplier tubes (PMTs), are used as active muon veto and also contributing to the moderation of neutrons. The CONUS muon veto system is described in [52]. The four CONUS detectors are placed are placed within the detector chamber of 25 l. The shield is enclosed with a steel cage, which can be flushed to remove radon. Without the active muon veto, the shield is referred to as passive shield, which becomes an active shield by switching on the veto. In Chapter 4, the performance of the shield to suppress reactor-induced background is evaluated and in Chapter 5 all other steady-state background source and their suppression by the shield are examined. The implementation of the shield geometry into the MC is displayed in Figure 4.4.

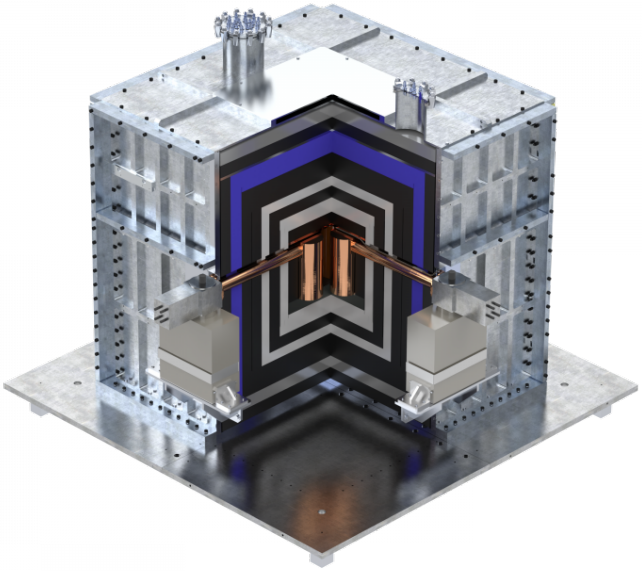

Figure 1.13: CONUS detectors inside the CONUS shield: layers of Pb in dark gray, layers of borated PE in white, layers of PE in light gray and plastic scintillator plates in blue. The shield is enclosed in a steel cage.

1.8 Location and time line of the CONUS experiment

The CONUS experiment is located at the commercial nuclear power plant of Brokdorf, Germany (KBR) inside room A408 at a distance of ∼17 m to the reactor core (top view shown in Figure 1.14). The concrete of the building and the storage pool for spent fuel assemblies as well as the pool for loading them into the transport cask provide an overburden of 10 to 45 m w.e. depending on the solid angle. More details on the location are given within this thesis and in [53]. In the following, an overview on the time line of the experiment is given, starting with commissioning measurements at KBR and MPIK.

In December 2016, the first measurement campaign started at KBR as preparation. The neutron background on site was determined in close cooperation with the Physikalisch-Technische Bundesanstalt (PTB), Braunschweig (at positions 1 and 2 marked in Figure 1.14). Meanwhile, the shield and the detectors were assembled and thoroughly tested during the approximately half-year long commissioning phase at the underground Low Level Laboratory (LLL) at the Max-Planck-Institut für Kernphysik, Heidelberg (MPIK), in 2017. The detectors were characterized with various radioactive sources as described in Chapter 2 and the background suppression of the shield was examined with several combinations of detectors. The background data collected during this time is used for comparison to the data collected at the nuclear power plant. Next, the shield was set up at the nuclear power plant of Brokdorf,

Germany (KBR) within three weeks at the beginning of 2018. The detector were brought underground on 24.01.2018 at room A408 KBR. This is followed by a two month long commissioning phase until the beginning of Run1. The physics data taking started with the outage of Run1 in April 2018 and is followed by the collection of six months reactor ON data. In this time period, the environmental γ-ray background was characterized with the HPGe spectrometer CONRAD (position 3 see Figure 1.14). Run1 ends with changes in the DAQ settings leading to an optimization phase until May 2019. During the optimization phase the first mini outage occurred. Mini outages refer to short periods of time of a few days were the reactor is turned OFF for special actions. The optimization phase ends with the beginning of Run2 in may 2019, this time the Run started with the collection of reactor ON data followed by the outage in June 2019. At the end of the outage, KBR conducted a leakage test of the containment building. This means that overpressure was applied to the containment building. For the CONUS experiment for safety reasons the vacuum in the cryostats was broken. They were filled with gaseous Argon during the test and the vacuum was restored after the leakage tests. This, however, caused changes in the noise characteristics and the background of the detector. Nevertheless, further reactor ON time was collected. To counteract against the impact of the leakage test, the diode temperatures were changes in September 2019, which marks the beginning of Run3. Further notable events in the following months are the movement of the air conditioning (AC) in October 219 and a second mini outage in November 2019. In the beginning of 2020, a ^{252}Cf calibration campaign was conducted, which was followed by an optimization phase in preparation for Run4. Table 1.1 summarizes this time line. During the data collection, regularly ^{228}Th calibrations and pulser measurements are carried out every 1 to 4 weeks.

Within this thesis the four CONUS detectors are refereed to as Conus-1 to Conus-4 and there is also Conus-5 used for research and development purposes. In Chapter 2 to Chapter 5 the region of interest (ROI) refers to the integral range of $[0.3,1]\,\mathrm{keV}_{ee}$, which approximately corresponds to the ROI for the CEνNS analysis. The exact analysis thresholds are given in Chapter 6. In Figure 1.14, the temperature control measures and sensors referred to in Chapter 2 and Chapter 3 are displayed. The room temperature inside room A408 is reduced by a cold air ventilator and an AC. The shield is enclosed by a plastic tent, that was half-open during Run1 and fully closed with the middle of the outage of Run2. The air from the AC is directed into the tent and the configuration is referred to as "cold house". Temperature data is collected with the tdf sensor close to the tent during Run1, while for Run2 HOBO sensors were placed at the cryocooler air outlet of each detector. The cryocoolers themselves also register various temperature values and the consumed electrical power (see Section 2.1.3). Radon is evaluated with monitoring device on top of the shield. A list of all relevant sensors and their uncertainties is provided in the appendix in Table A.1. The breathing air bottles to flush the shield to remove radon background (see Section 5.5) are also marked.

time period	occurrences
Dec. 2016 - Feb. 2017,	characterization of neutron background,
Aug. -Dec. 2017	in cooperation with PTB
June - Dec. 2017	assembly and testing of shield and detectors at MPIK
January - Feb. 2018	transport and assembly of shield and detectors at KBR
Feb. - Mar. 2018	commissioning at KBR
01.04.2018 - 07.05.2018	outage of Run1
08.05.2018 - 31.10.2018	reactor ON data collection of Run1
August 2018 - October 2018	measurement of external γ-ray background with CONRAD
Oct. - beginning May 2019	optimization phase 1
13.04.2019 - 24.04.2019	first mini outage during optimization phase
16.05.2019 - 08.06.2019	first phase of reactor ON data collection of Run2
08.06.2019 - 28.06.2019	outage of Run2, additional CONRAD measurements
beginning July 2019	leakage test of KBR
09.07.2019 - 25.09.2019	second phase of reactor ON data collection of Run2
25.09.2019 - 17.11.2019	begin reactor ON Run3 with change of diode temperature
10.10.2019 - 17.10.2019	movement of AC at experimental site during Run3
17.11.2019 - 23.11.2019	second mini outage, which is the outage of Run3
23.11.2019 - 14.01.2020	second phase of reactor ON data collection for Run3
14.01.2020 - 04.02.2020	^{252}Cf source calibration

Table 1.1: Overview of the time line of the CONUS experiment relevant to this thesis. Outages start with the beginning of the ramp down of the reactor and end with the reactor being fully ramped up again.

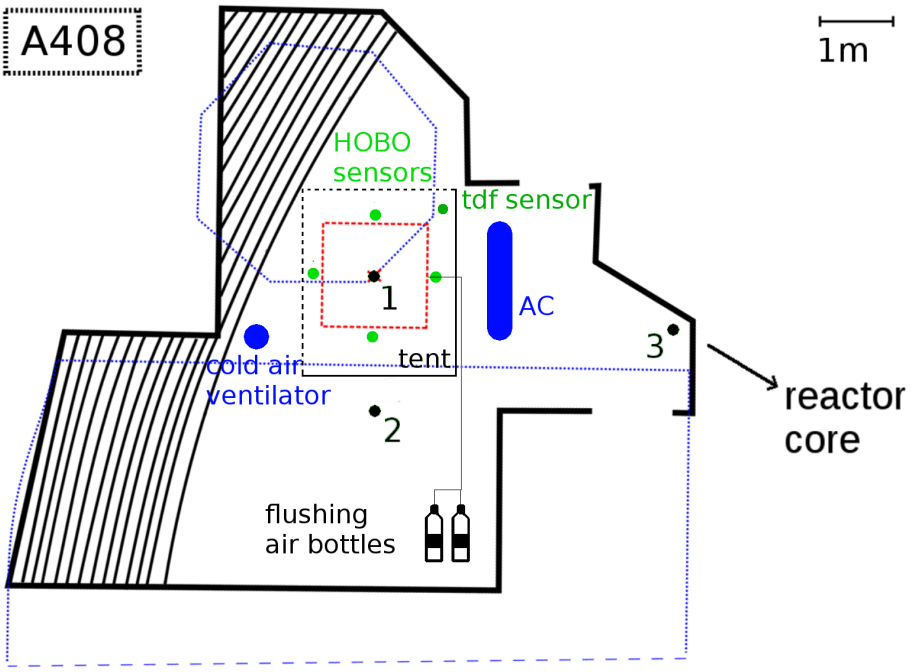

Figure 1.14: Top view of room A408 at KBR, where the CONUS experiment is located. The blue dashed lines represent the spent fuel storage pool and the smaller pool for loading the spent fuel assemblies into the transport cask. The shield is marked with the red dashed lines. It is enclosed by a plastic tent. For Run1 the tent was half-open (sides with dashed line open), while it was fully closed in the middle of the outage of Run2. The numbered locations corresponds to the reactor-correlated background measurement campaign described in Chapter 4. The air condition (AC) and the cold air ventilator have an impact on the temperature inside the room. The AC was moved in October 2019. The temperature sensors (green) registered this temperature. For Run1 the tdf sensor next to the shield was used, for Run2 a HOBO sensor was places at the air outlet of the cryocooler of each detector.

2 CONUS detectors

2.1 Detector design for CONUS

2.1.1 Demands on detector design

A successful detection of CEνNS requires both, a very low energy threshold and a very low background. HPGe spectrometers are ideal for this purpose as discussed in Section 1.4. The CONUS detectors were designed in close cooperation with Mirion Technologies, Canberra Lingolsheim [54] keeping both prerequisites in mind as well as the special demands by the location of the experiment at a commercial nuclear power plant. At the nuclear power plant, no remote access is allowed meaning real-time monitoring is not possible. Therefore, stable running detectors and especially a stable energy scale are an absolute necessity. In the following, the detector design is described and the outcome of the detailed detector characterization is elaborated. It is shown how the CONUS detectors meet the design goals especially regarding the energy resolution.

Moreover, due to safety reason at KBR the detectors have to be equipped with electrical cryocoolers instead of liquid nitrogen cooling. The consequences of the electrical cryocooling for the energy scale are discussed in this chapter, the impact on the noise of the HPGe spectrometer is examined in detail in Chapter 3.

The radiopurity of the detector components as well as the cosmic activation are included in Chapter 5 about the background achieved with the CONUS detectors and inside the CONUS shield.

2.1.2 Description of HPGe diodes and cryostat

For CONUS four Ge crystals in a cylindrical shape and a mass of 1 kg each are employed inside the shield at KBR. A fifth detector of similar design is used research and development purposes. The detectors are referred to as “Conus-1” to “Conus-5”. The p-type crystals are covered at the side and at one cover with a thin n-type layer $\mathcal{O}(1\,\mathrm{mm})$ to create the diode. The HV contacting is done via this layer as well. The signals are read out at the point contact on the opposite side of the diode. To isolate the contact as well as to protect the diode surface, this side is covered by the so-called passivation layer $\mathcal{O}(100\,\mathrm{nm})$. Figure 2.1 gives an overview on how the diode looks like. No charge collection for events occurring within the passivation layer is assumed. At the other sides of the diode directly at the surface the charge collection efficiency is zero as well within the so-called dead layer. This is followed by a region where the charge collection gradually increases (so-called transition layer)

until the full charge collection depth is reached as depicted in the same figure. If not all the charges are collected, this leads to the reconstruction of the event at a lower energy than the amount that was originally deposited. The active volume of the diode is defined as the part, where the full charge collection depth is achieved and all events are detected at the correct energy. It is assumed that only neutrino events within the active volume can be detected. Thus, it is an input parameters for the CEνNS analysis. They are determined via source measurements as described in Section 2.2.5. Furthermore, the information is required for a precise MC simulation of the detector setup.

The diode and the cold electronics are housed in a Cu cryostat (see Figure 2.2). A good and stable cold transfer from the cooling to the diode has to be achieved, which is simpler with a short cooling finger. Thus, a shorter cooling finger corresponds to a lower electronics noise. However, it still must be feasible to set up a massive shield of a certain thickness around the detector. In the end, it was possible to have a sufficiently long cooling finger for the elaborated shield described in Chapter 5, while achieving a sufficient cold transfer for a very low energy threshold.

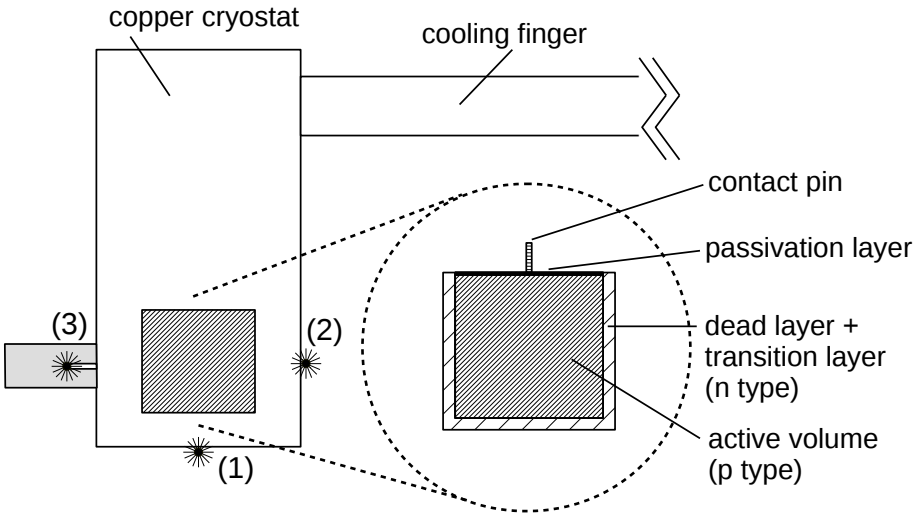

Figure 2.1: HPGe diode within Cu detector end cap. The inset displays a detailed view of the p-type point-contact diode with the dead layer/transition layer, the passivation layer and the contact pin at the point contact. The position of the source measurements for the detector characterization are marked with (1), (2) and (3).

2.1.3 Electrical cryocooling

The CONUS detectors are equipped with electrical pulse-tubed cryocoolers (Cryo-Pulse 5 Plus from Canberra Lingolsheim [55]). Pulse-tubed cryocooler work by converting heat to mechanical work. The basics of PT cryocoolers are described in [56]. The working gas is Helium. The mechanism is similar to Stirling coolers, but no moving parts close to the cold point are required, which is beneficial for low noise applications. The piston is driven by a compressor. A valve connects alternately the lower and the higher pressure side to the piston (see Figure 2.3). The typical frequency of the piston is 1-50 Hz. The advantages of electrical cryocooling are in general that the equipment is low maintenance, reliable and no regular refilling of liquid nitrogen is required.

Several parameters are available to monitor the performance of the cryocooler. This includes the electrical power and the temperature at various points within the cooler (see Figure 2.2 and numbers therein). There is no sensor directly at the diode (4) to fullfill radio purity requirements, but the expected temperature is extrapolated from the measured value at the cooling finger (3). Moreover, the temperature of the air at the compressor (2) is registered. For the CONUS experiment, this means that there is no data on the temperature within the detector chamber available.

The performance of the cryocooler depends on the room temperature as well as the vacuum within the cryostat. Figure 2.4a and Figure 2.4b show a long term comparison between the cryocooler electrical power of Conus-1 for Run1 and Run2 to the room temperature at KBR. During Run1 the room temperature was registered only with one sensor at the side of the shield next to Conus-1. Starting with Run2 more detailed information were collected with one sensor at the air outlet (1) of the cryocooler of each detector. At the beginning of run1 at KBR a clear correlation between the cryocooler power and the room temperature is observed. If the room temperature increases, more power is required to maintain the same performance. However, after several months the power of the cryocooler increases even though the room temperature stays constant. This observation can be explained by a small and slowing increasing decline in the vacuum within the cryostat. The correlation to the room temperature persists, but the power stays at a higher level. For Run2/3 the plot is renormalized such that the curves overlay again in the beginning. While for Run1 there are jumps in the temperature that are not seen in the cryocooler power, it turns out that the air temperature at the cryocooler outlet is fully linearly correlated to the cryocooler power.

The only counter measure against the decline of the vacuum is to pump the cryostat. This was carried out for all detectors after the outage of Run2 due to the leakage test of KBR (described in Section 3.2.3). After the pumping the cryocooler power has been successfully reduced to a level even below the start value at KBR. Later on the diode temperature had to be reduced, which leads to a higher power consumption (see also Figure 2.17 for the same effect).

The impact of the cryocooler performance on the energy scale of the Ge spectrometers is discussed in Section 2.2.3, while the consequences for the noise of the

Ge spectrometers are elaborated in Chapter 3.

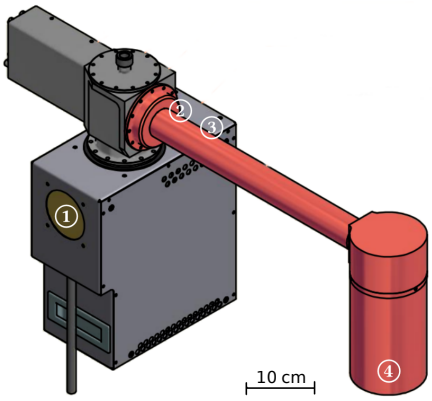

Figure 2.2: CONUS detector equipped with an electrical cryocooler. The diode and the cooling finger are fully enclosed by the shield. Monitored temperature: (1) compressor temperature, (2) cold head, (3) cold tip, and (4) diode temperature (extrapolated).

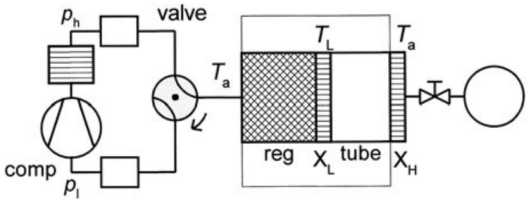

Figure 2.3: Schematic overview of a PT cryocooler with decoupled compressor (GM type). The application to be cooled down to temperature T_L is connected at X_L. T_a denotes the room temperature.[56]

2.2 Detector characterization

The detector properties were characterized with radioactive sources and pulse generator measurements during the commissioning phase at MPIK. For this purpose, a small Pb shield, so-called "Mini CONUS" was built (see Figure 2.5), which can host up to two detectors. The used sources must have strong lines within the available energy range of the detectors up to 450 keV_{ee}. Therefore, ^{241}Am, ^{57}Co, ^{133}Ba and ^{228}Th sources were chosen. They were placed either next to the detector or below the detector end cap as depicted in Figure 2.1. An overview on the measurements and the characterized features of the detectors is given in Table 2.1. This includes the depletion voltage, the active volume and the longterm stability as well as the impact of the cryocooler on the collected data. Furthermore, additional tests regarding the diode temperature were carried out in summer 2019 with Conus-5 at the surface laboratory 11A at MPIK. Here, the detector has been enclosed inside a Pb shield and a thermal isolation. The thermal isolation offered the possibility to keep the temperature around the diode stable as well as to be able to heat up the surrounding of the diode end cap without that of the cryocooler. To evaluate the longterm stability, the ^{228}Th calibration data collected at KBR during Run1 with the detectors fully enclosed in the CONUS shield every 1 to 4 weeks is included as well.

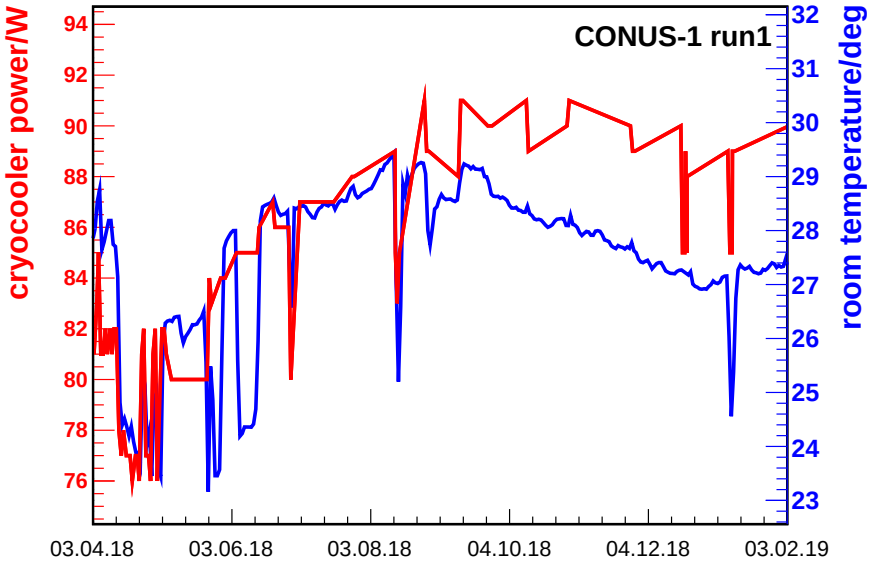

(a) Cryocooler power of Conus-1 registered by the shifter compared to A408 room temperature (collected with the tdf sensor) during Run1.

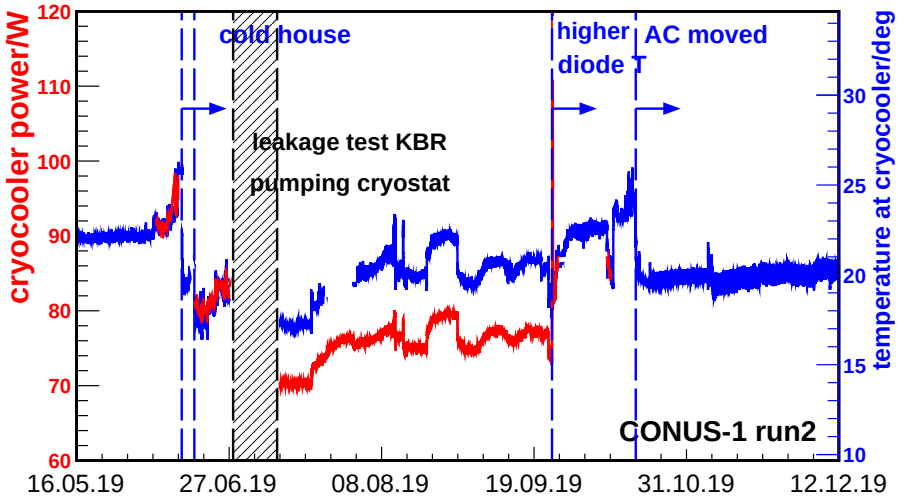

(b) Cryocooler power of Conus-1 registered by the cooler compared to the A408 room temperature (collected with the HOBO sensor) during Run2.

Figure 2.4: Observed correlation of the cryocooler power to the room temperature at A408 KBR for Run1 and Run2. The correlation is broken as the vacuum declines. A clear improvement in the power consumption was observed after the pumping of the cryostat. Also, the cold house (lower room temperature) reduces the power consumption (see Section 3.2.2)

location	shield	source	characterized features
LLL (MPIK)	5 cm Pb	^{241}Am	active volume, transition layer
		^{241}Am	diode pos.
		^{57}Co	peak pos. stability, temp. dep.
		^{57}Co	HV scan and depletion voltage
		pulser, ^{57}Co, ^{241}Am	peak resolution
11A (MPIK)	5 cm Pb + thermal isolation	^{57}Co	peak pos. temp. dependence
		^{57}Co, bkg	cryocooler noise, microphonics
A408 (KBR)	CONUS shield	^{228}Th	peak pos. stability, temp. dep.
		pulser, ^{228}Th, bkg	peak resolution
		^{228}Th	transition layer

Table 2.1: Overview on the measurements carried out for the detector characterization and understanding at different locations.

All peaks were fit with a Gaussian added to a background function. The latter can be a flat background or a step function depending on the surrounding spectral shape of the peak:

$$\text{fit function} = N \cdot exp\left(-\frac{1}{2}\left(\frac{E-\mu}{\sigma}\right)^2\right) + \text{bkg} \tag{2.1}$$

The mean μ of the Gaussian corresponds to the peak position. The peak resolution is described by the Full-Width-at-Half-Maximum (FWHM). It translates into the variance σ of the Gaussian by FWHM$\approx$2.3548 σ. The normalization of the peak content is represented by N. The peak count rate is derived via a counting method according to DIN Norm 25482-5 [57]. The complete peak area is supposed to be covered by 2.5 times the FWHM. Outside of this energy range the background on the right and left side is determined by the integral over 1.25 times FWHM on each side. It is subtracted from the peak area to derive the peak count rate.

2.2.1 Depletion voltage and working voltage

When ramping up the HV of a Germanium spectrometer, an electric field is created within the diode and free charges are collected. With increasing high voltage (HV) this depleted region grows (see Figure 1.6). The capacity decreases until at some point all free charges are collected. From this point on, all additionally deposited charges by external radiations are read out as signals at the correct energy. The peak position and resolution become independent of the HV at full depletion. To be on the safe side, the working voltage given by the manufacturer is usually several 100 V above this depletion voltage. The depletion voltage is a crystal property and depends on the impurity concentration as well as the detector geometry.

For the CONUS detectors, the depletion voltage has been measured via HV scans with a ^{57}Co source placed close to the detector end cap. Starting at the working voltage of the detector, the voltage was decreased in 50 V steps (or smaller for

Figure 2.5: Mini CONUS setup during commissioning at MPIK for maximum two detectors.

Figure 2.6: Side scan along detector end cap with a ^{241}Am source in a Cu collimator. The cryostat is covered with plastic wrap to maintain radio purity.

Conus-2) and data were collected for at least 1 h at each voltage point to collect up to 10000 counts in the 122.06 keV line. Especially at lower voltages also much longer measurements were carried out. After adjusting the HV and before starting the next measurement, 10 min were waited to ensure that the detector has stabilized again. The 122.06 keV line of ^{57}Co was analyzed. The peak position, resolution and peak count rate were evaluated in dependence on the HV. The results can be found in Figures 2.7 to 2.9. Before depletion due to the decreasing capacity and reduced charge collection efficiency, the peak position moves with increasing HV to higher channels, while the resolution gradually improves. The ratio of the count rates to the count rate at working voltage confirms that before depletion not all charges are collected and there are huge losses to the peak count rate. The point of depletion is clearly marked by a sharp jump in all curves. The values are summarized in table 2.2 with the uncertainty dominated by the grain of the scan.

There is a second method to collect information on the depletion voltage for low noise pulse reset preamplifiers. During the ramp up of the HV, the noise on the baseline can be observed with an analogue oscilloscope. At depletion, due to the drop in capacity the noise suddenly drops creating a flat baseline. The depletion voltage is equal to or above this HV value, as can be seen in Table 2.2.

For Conus-2, an additional phenomenon can be observed in the HV scan, the

detector	depletion voltage HV scan [V]	voltage noise drop [V]	working voltage [V]
1	2710±25	2730±1	3000
2	2560±25	2070±1	2700
3	2810±25	2785±1	3000
4	3200±25	3190±5	3400

Table 2.2: Depletion voltage evaluated from HV scans and working voltage of the CONUS detectors given by the manufacturer.

so-called "bubble depletion" [32] or "pinch-off" effect [6]. This is a discontinuity observed in the peak position, resolution and count rate curves in Figures 2.7 to 2.9. It originates from a combination of the detector geometry, impurity concentration and applied voltage, that leads to a zero electrical field within the center of the diode. Thus, close-by holes are slowed down or trapped, which drastically reduces the capacity. The effect has been observed before e.g. for the GERDA-II diodes [60]. However, contrary to what has been reported there the count rate within the bubble strongly increased. The underlying reason for this behaviour is not undertstood for the CONUS detectors. The exact shape of the bubble was not reproducible after repeating the scan, which hints that it is a rather delicate interplay between several effects like the duration between the changes of the HV and the difference between the single voltage steps.

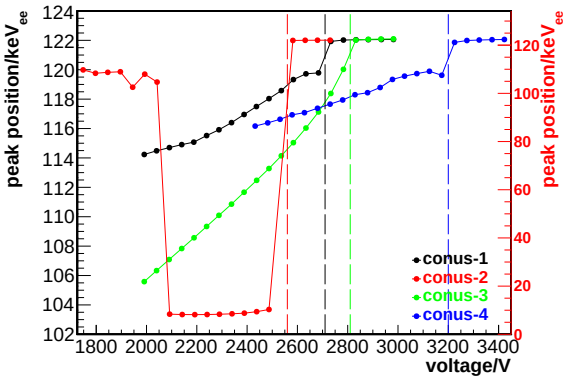

Figure 2.7: Dependence of the peak position on the applied voltage for Conus-1 to -4. The depletion voltages are marked as dashed line. Above this HV the peak position is stable.

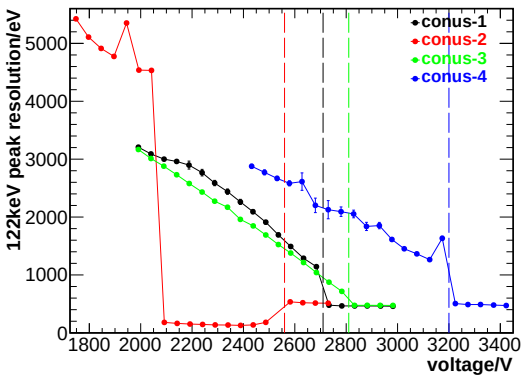

Figure 2.8: Dependence of the peak resolution on the applied voltage for Conus-1 to -4. The depletion voltages are marked as dashed line.

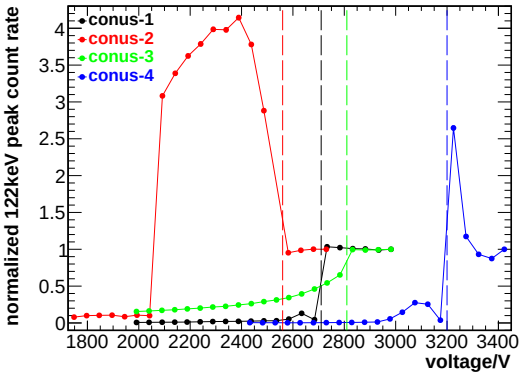

Figure 2.9: Dependence of the peak count rate on the applied voltage for Conus-1 to -4. The depletion voltages are marked as dashed line.

2.2.2 Energy resolution

An excellent resolution is crucial for the CONUS experiment to achieve a very low noise threshold. The detectors were optimized in this respect and the resolution was checked with pulser measurements and measurements with radioactive sources. The resolution of the pulser peaks is only determined by the electronics chain, while for the physics peaks the width is further blurred by additional contributions (see Section 1.4.4). The achieved FWHM is summarized in Table 2.3 and Figure 2.10 shows an exemplarily fit of the 60 keV line of ^{241}Am. Next to the excellent resolution, a highly Gaussian shape of the peak is observed. A comparable performance for the pulser measurements was reached at MPIK and KBR showing that at the nuclear power plant a similar quality of the grounding as under laboratory conditions can be achieved. The energy resolution of the CONUS detectors makes it possible to resolve peaks very close in energy such as e.g. the 99.0 keV and 103.0 keV line of ^{241}Am or the 238.6 keV and 241.0 keV line of a Th source. The former peak combination is depicted in Figure 2.11 for Conus-1 in comparison to a conventional semi-coaxial detector to show the improvement achieved in the development of the CONUS detectors. Another advantage of the high resolution is that all counts from a line are spread over less bins, which improves the visibility of lines with small count rates. The high resolution achieved is a prerequisite for a low energy threshold, but it is not sufficient. The noise of the CONUS detectors is discussed in more detail in the next Chapter.

resolution detector	pulser MPIK [eV_{ee}]	pulser KBR [eV_{ee}]	^{241}Am 59.54 keV [eV_{ee}]	^{57}Co 122.06 keV [eV_{ee}]
1	74±1	69±1	327.5±0.3	463.2±0.4
2	75±1	77±1	336.0±0.4	491.8±0.3
3	59±1	64±1	335.5±0.3	476.6±0.5
4	74±1	68±1	332.6±0.7	481.2±0.4

Table 2.3: Peak resolution of the CONUS detectors (FWHM) measured with a pulse generator at MPIK and KBR and with several sources at MPIK.

The energy resolution of the physical peaks is energy-dependent due to the number of electron hole pairs varying with the energy of the initial particles. An overall square root dependence is expected (see equation (1.6) in Section 1.4.4). To include the detector response in the signal expectation and the MC spectra, it is necessary to be able to describe the energy-dependence of the resolution with a function. In order to do this, the FWHM of in total eight lines from the lowE background data and the Th calibration data collected at KBR were plotted against the energy of the lines by W. Maneschg. A three parameter model was found to fit best to the data: FWHM$=A_{res} + 2.355\sqrt{B_{res} 0.00296(E - C_{res})}$. Individual coefficients were determined for all four detectors and used for the CEνNS analysis. For the energy approaching zero, the resolution gets close to the FWHM of the pulser.

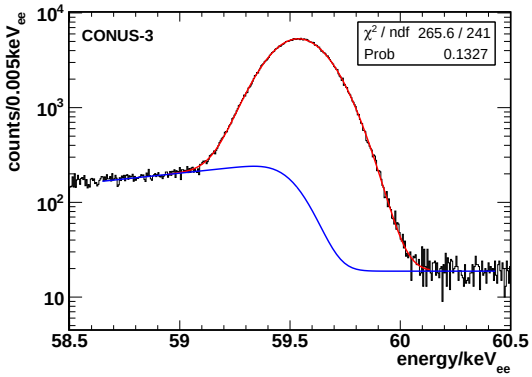

Figure 2.10: Fit of 59.5 keV line of ^{241}Am for Conus-3. The red function describes the Gaussian peak plus background and the blue functions fits the background.

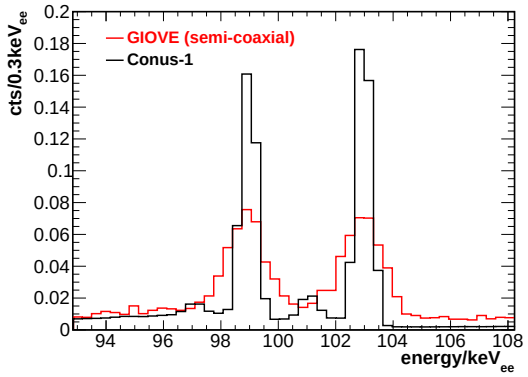

Figure 2.11: Comparison of 99.0 keV and 103.0 keV lines of ^{241}Am for a conventional coaxial detector and a high resolution CONUS spectrometer (both normalized to the integral range of [95,105] keV$_{ee}$). With the CONUS detector even the X-ray in between the lines can be resolved.

2.2.3 Stability of peak position

Longterm measurements

A stable operation of the detectors is crucial to the success of the experiment, especially as no remote surveillance and control of the detectors is possible. It is an important prerequisite for a reliable calibration. For the low energy range, the CONUS experiment relies on the intrinsic X-ray lines (see Section 6.2). For a precise calibration several weeks of statistics accumulated in these lines are required. It is therefore impossible to correct for small shifts in energy scale.

Within the commissioning at MPIK the stability was tested during a long-term measurement with Conus-2 with a ^{57}Co source. Data were collected continuously

detector	source/location	position [keV$_{ee}$]	resolution [eV]
2	^{57}Co/MPIK	122.09±0.02 (0.02%)	496±5 (1%)
1	^{228}Th/KBR	238.629±0.016 (0.01%)	671±9 (1%)
2	^{228}Th/KBR	238.611±0.018 (0.01%)	774±16 (2%)
3	^{228}Th/KBR	238.637±0.022 (0.01%)	716±13 (2%)
4	^{228}Th/KBR	238.627±0.014 (0.01%)	688±11 (2%)
1	bkg/KBR	10.368±0.002 (0.02%)	345±11 (3%)
2	bkg/KBR	10.371±0.004 (0.04%)	371±15 (4%)
3	bkg/KBR	10.365±0.004 (0.04%)	326±16 (5%)
4	bkg/KBR	10.372±0.003 (0.03%)	351±11 (3%)

Table 2.4: Longterm stability of peak position and resolution. The measurements at MPIK extended over three months. For KBR, measurements over nine months were analyzed. The uncertainty corresponds to the standard deviation of the mean value.

over about 3 months with several breaks in between. Figure 2.12a and Figure 2.12b show the 122.06 keV peak position and peak resolution plotted against time. The shaded boxes mark the measurement periods that have been analyzed separately. The peak position turned out to be highly stable with a weighted average and standard deviation of (122.09±0.02) keV (0.02%). The weighted average and standard deviation of the peak resolution is (496±5) eV$_{ee}$ (1%).

The result was confirmed by the ^{228}Th calibration data taken at KBR in a period over nine months. For Conus-1, data were collected for 1 h per calibration, for the other detectors for 1800 s. There was a maximum time distance of four weeks between two calibrations. The peak position and resolution of the 238.63 keV line were analyzed and are given in Table 2.4. The 10.37 keV peak position in the background data, analyzed in weekly binning, also gives comparable results.

Temperature dependence of peak position at LLL and at KBR

While the peak position and resolution of the CONUS detectors are highly stable, the excellent resolution of the detectors makes it possible to study the behavior of the peak position over time in even more detail. Partially during the commissioning at LLL the surrounding temperature had been monitored. For these time periods the ^{57}Co data were split into time bins of 6 hours. Figure 2.13 shows the temperature measured with the tdf temperature sensor and the peak position over time. A clear correlation is found. The same analysis was carried out for the ^{228}Th data collected at KBR every one to four weeks over a course of nine months for Run1. Once again, a dependence on the room temperature is visible for all detectors in Figure 2.13.

This can be explained by the temperature dependence of the energy ϵ required to create an electron-hole pair in Ge (see Section 1.4.1). The underlying reason is that the band gap E_g of semi-conductor detectors is temperature-dependent:

$$E_g = E_g(0) - b\frac{T^2}{T + T_0} \tag{2.2}$$

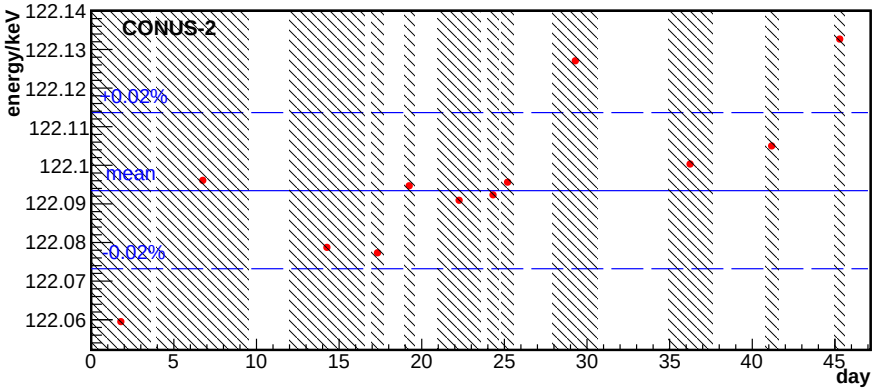

(a) Peak position of the 122.06 keV line of ^{57}Co.

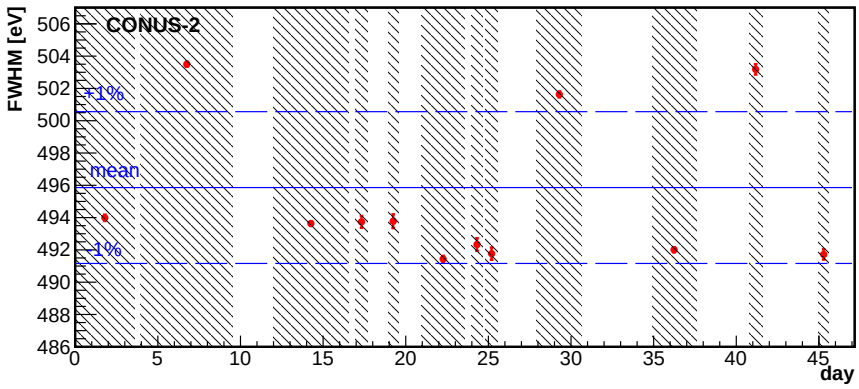

(b) Peak resolution of the 122.06 keV line of ^{57}Co.

Figure 2.12: Long term stability measurement at LLL with a ^{57}Co over the period of about three months. The peak position (a) and resolution (b) is evaluated. The shaded areas correspond to the data taking periods. The weighted mean and 1 sigma standard deviation are given.

For Ge, the band gab close to absolute zero approaches $E_g(0)$=0.743 eV and the band gap decreases with higher diode temperature T. The parameters b and T_0 (Debye temperature) are material dependent, for Ge b=$4.8{\cdot}10^{-4}$ eV/K and T_0=235 K [58]. The resulting temperature dependence of ϵ is less straight forward and several models are proposed in literature based on Shockley theory. Figure 2.15 from [58] shows a comparison of the models and existing data. The CONUS detectors are cooled down to 77-87 K. In this temperature range $\epsilon \approx$2.96 eV and depending on the model $\frac{\Delta\epsilon}{\Delta T} \approx$ -(0.0007-0.0016)$\frac{eV}{K}$ is expected.

To extract the coefficient from the LLL CONUS data, a linear fit of the peak position versus room temperature data is made. It gives the energy-dependent temperature-induced shift of the peak position in Table 2.5. This can approximately be converted to the temperature-induced change in the energy to create an electron-

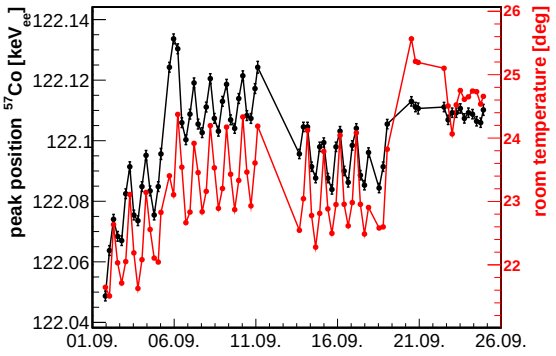

Figure 2.13: Peak position of the 122.06 keV line of the ^{57}Co source measurement in comparison to the room temperature at LLL. The data shows a zoom-in into a short time frame of Figure 2.12a.

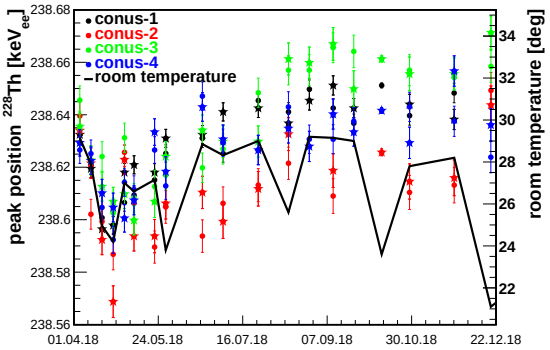

Figure 2.14: Peak position of the 238.63 keV line of the ^{228}Th calibration measurements in comparison to the room temperature at KBR.

hole pair ϵ in Ge by:

$$\frac{\Delta\epsilon}{\Delta T} \approx \frac{\epsilon_{ref}}{E_{ref}} \frac{\Delta E_{meas}}{\Delta T} \text{ with } E_{ref} = 122.06\,\text{keV} \text{ and } \epsilon_{ref} = 2.96\,\text{eV} \tag{2.3}$$

The outcome is comparable to the value expected from literature.

The same analysis was carried out for the ^{228}Th data collected at KBR. The derived $\frac{\Delta\epsilon}{\Delta T}$ here is smaller than expected. This can most likely be explained with the room temperature changes not being representative for the temperature differences close to the diode. The detectors were fully enclosed by a Pb shield of at least 40 cm thickness and the detector chamber was flushed with air from air bottles deposited at the corner of A408. Meanwhile, the temperature was detected close to the shield enclosed by a half open tent (displayed in Figure 1.14). Due to this instable situation large fluctuations where observed on the temperature (see also Section for a description of the situation 3.2.1). All in all, the smaller $\frac{\Delta\epsilon}{\Delta T}$ pinpoints to the change in the diode temperature being smaller than the temperature change observed in the environment. A better agreement in the behavior over time has been achieved when comparing to the cryocooler power/cold tip temperature monitored by the shifter during Run1.

To sum it up, strong indications were found that even though an increased room temperature leads to an increased cryocooler power, the cryocooler is not able to fully stabilize the situation. The diode temperature changes nevertheless leading to a tiny shift in the peak position. Potentially, the temperature registered by the cryocooler sensor half way inside the shield is not directly representative for the diode temperature. Therefore, two dedicated tests at MPIK were carried out to collect more information and to examine the consequences for the CONUS analysis.

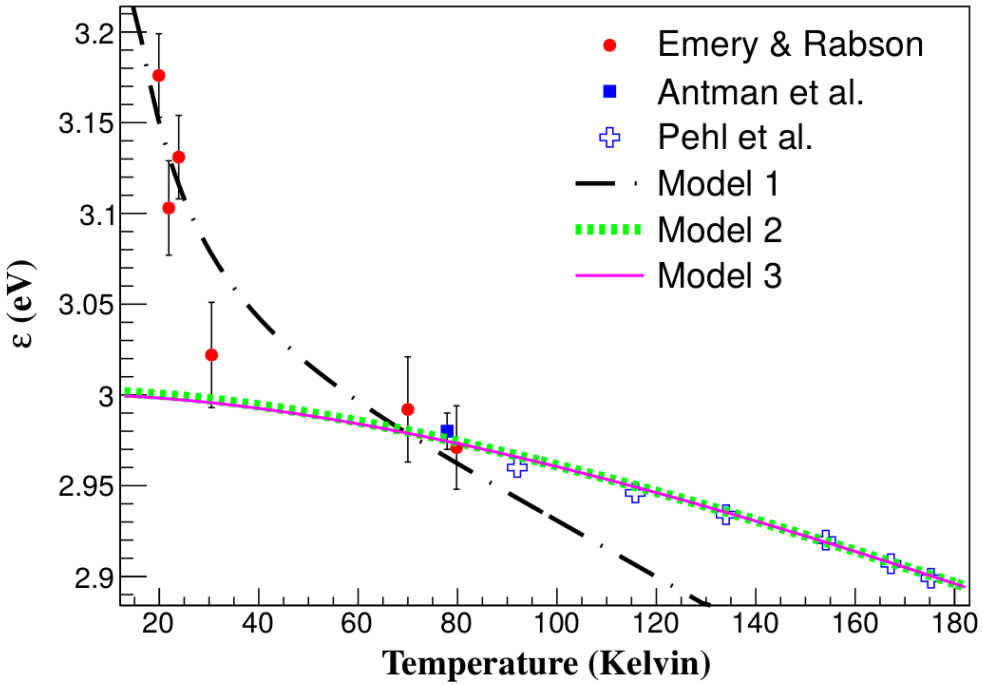

Figure 2.15: Temperature dependence of the energy required to create an electron hole pair in Ge. The data and models in the figure are described in [58]. For the CONUS detectors, the temperature regime of 77-87 K is of interest.

Dedicated tests on temperature dependence of peak position at MPIK

To study the temperature-dependence in even more detail, dedicated measurements with the Conus-5 detector at Heidelberg in the 11A laboratory were carried out. Two tests were undertaken:

1. increase of room temperature around the diode, but not around the cryocooler
2. deliberate change of the diode temperature via the controller of the cryocooler

For both tests, the detector end cap was enclosed in a thermal isolation made of Styrofoam (see Figure 2.16 with open isolation). The isolation has a hole, used to insert a blow dryer to heat the vicinity of the diode without increasing the temperature around the cryocooler outside the isolation.

Test (1) was carried out to quantize the effect on the peak position from a strong increase in temperature around the diode without giving the cryocooler the possibility to compensate for it. A blow dryer was used to heat the area around the diode, but not the cryocooler itself due to the thermal isolation. A ^{133}Ba source has been placed on the detector end cap. The shaded areas in Figure 2.18 correspond to the time periods when the blow dryer was running. An increase of the temperature of at least 10 deg was induced in the air around the detector end cap. Meanwhile, a second temperature sensor at the cryocooler confirmed that the isolation was working and

Figure 2.16: Conus-5 at the 11A laboratory at MPIK enclosed by a Styrofoam housing. The front side is opened to see the interior, otherwise closed. The hairdryer is used to heat the air close to the diode while the Styrofoam housing avoids the increase of the environment temperature.

the temperature stayed constant within the uncertainties of the sensor. Nevertheless, an higher cryocooler power was observed, but only by approximately 5 W (nominal cryocooler power approximately 100 W). Looking at the data taken at KBR, this increase is small compared to the strong temperature change. It is assumed that the Cu transfered the heat towards the sensor of the cryocooler somewhere along the cooling finger of 42 cm length. With delay a shift in the peak position of the 356 keV line of ^{133}Ba of 0.055 keV is observed. The test proves that even for the strong temperature increase around the detector end cap over several hours, only a tiny, but nevertheless significant, shift of the diode position is created. The vacuum inside the cryostat effectively isolates the diode. According to equation (2.3) the shift scales with the energy of the peak, meaning that at lower energies an even smaller effect is expected ($\sim$2 eV roughly extrapolated from the single data point). In consistency with this observation, the peak position of the 10.37 keV line over time at KBR overall does not show a clear correlation with the room temperature. This makes the systematic uncertainties sub dominant next to the other ones of the energy scale calibration, most notably driven by the statistics of the line count rates (see Section 6.2). Therefore, for the CEνNS analysis it is foregone to correct for the effect. However, periods of strongly enhanced temperature were removed from the data set nevertheless for other reasons described in Section 3.2.3).

For (2), the diode temperature was changed from 73 to 83 K in 1-2 K steps via the crycooler controller. In this way, the impact of a well known and large change of the diode temperature itself could be studied. After each change there was a waiting time of several hours for the change to take full effect over the whole diode.

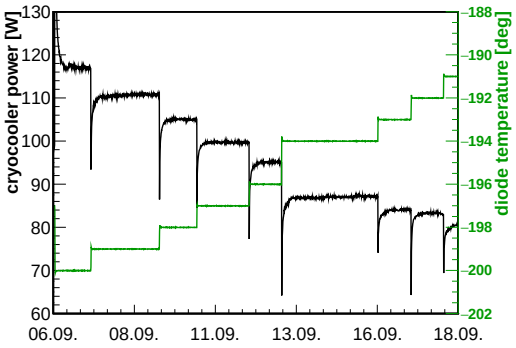

Figure 2.17: Manual increase of the diode temperature in several steps over time, resulting consistently in a decrease of the cryocooler power.

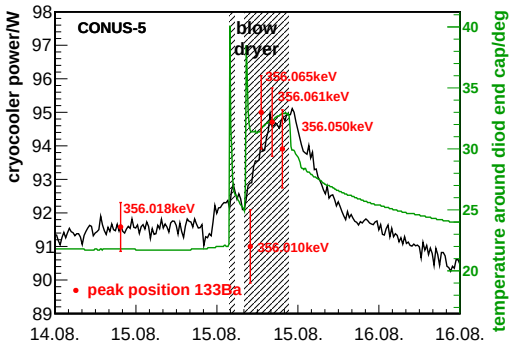

Figure 2.18: Shift of the peak position of the 356.0 keV line of ^{133}Ba by increasing the air temperature around the detector end cap.

Figure 2.17 shows how the cryocooler power adapts as well with each change. The stable environmental temperature was confirmed by a temperature sensor close to the detector end cap. Data were collected with a ^{57}Co source for at least five hours or longer.

From the peak position of the 122.06 keV line a value for ϵ is calculated via (see appendix for derivation of formula):

$$\epsilon_{meas} = \frac{E_{ref}}{E_{meas}}\epsilon_{ref} \text{ with } E_{ref} = 122.06\,\text{keV} \text{ and } \epsilon_{ref} = 2.96\,\text{eV} \tag{2.4}$$

In Figure 2.19 the determined ϵ is plotted against the set point diode temperature and in a first approximation a linear fit was made. The resulting $\frac{\Delta\epsilon}{\Delta T}$ is added to Table 2.5. The outcome is close to the expected range of literature values, but slightly smaller. In the figure, it is clearly visible that the data points deviate from a fully linear behavior. They match the observations from previous measurements collected in Figure 2.15 taken from [58], while they disfavor all three theory models mentioned in the publication. The resolution of the peak was evaluated as well. In agreement with less electron hole pairs (larger ϵ) at lower diode temperature, the resolution decreases with increasing diode temperature.

Translating the shift from test (1) to a change in the diode temperature, reveals that it corresponds to an approximate increase of only 1 deg even though the air around the detector end cap increased by about 10 deg. It confirms the previous conclusion that changes in the air temperature are sub dominant for the energy scale stability.

2.2.4 Diode position

To be able to set up a precise MC simulation, the geometry needs to be well known including the position of the diode. To confirm the position from the construction

source/location/shield	detector	Δ T temp. change	energy keV	$\frac{\Delta E}{\Delta T}$ keV/K	$\frac{\Delta \epsilon}{\Delta T}$ keV/K
^{57}Co/LLL/Mini CONUS	2	environment	122.06	0.028±0.004	0.0007±0.0001
^{57}Co/11A/small shield	5	diode	74.97	0.013±0.002	0.0005±0.0001
			136.47	0.026±0.002	0.00055±0.00003
			122.06	0.023±0.001	0.00057±0.00003
^{288}Th/KBR/CONUS	1-4	environment	238.63	∼0.008	∼0.0001
literature					0.0007-0.0016

Table 2.5: Observed shift of the peak position induced by temperature changes in the environment or of the diode at around 80 K. The required change in the energy per electron hole pair ϵ was derived from the data.

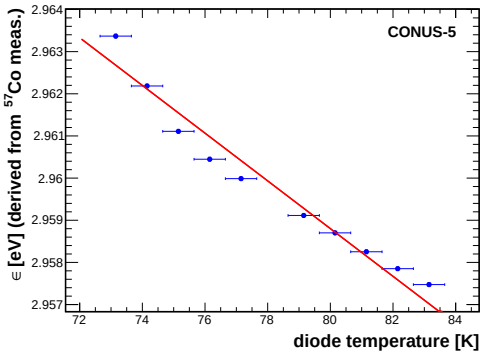

Figure 2.19: Measured change of ϵ in dependence of the diode temperature.

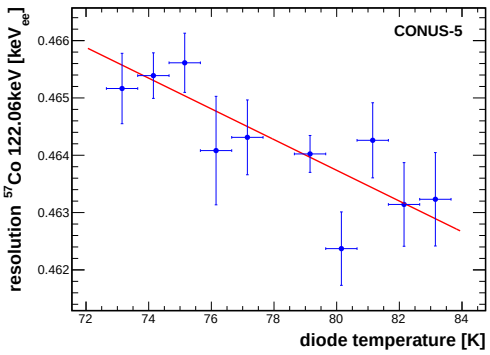

Figure 2.20: Measured change of the resolution in dependence of the diode temperature.

drawing, a scan along the side of the diode was carried out with the ^{241}Am source. The source was enclosed into a collimator with an hole diameter of 1.727 mm that was moved along the side of the detector end cap (see Figure 2.1 position (3) and Figure 2.6). Data were collected in short distances at the ends of the diode and in greater steps in the middle. The scan was carried out only for Conus-3 expecting the geometry to be identical for all the detectors. At each point the count rate of the 59.54 keV line was evaluated and plotted against the position of the collimator with the reference point being the top of the end cap. The scan result in Figure 2.21 confirms the nominal diode position marked with dashed blue lines. Within the shaded areas the Cu diode holder is thicker which is reflected in the lower count rate.

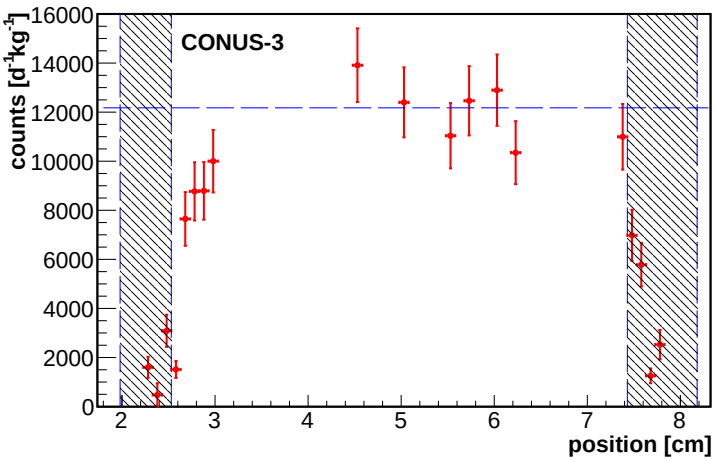

Figure 2.21: Count rate of the 59.54 keV line along the diode end cap. The outer dashed lines mark the nominal diode position, the shaded areas belong to the regions, where the Cu of the diode holder is thicker according to the construction drawings by the manufacturer. The total diode height corresponds to 62 mm.

2.2.5 Full charge collection depth, active volume and slow pulses

Evaluation of active volume

For the active volume determination the energy-dependent attenuation of γ-ray lines within the n+ layer surrounding the crystal from the side and below is utilized. A ^{241}Am radioactive source emitting several γ-rays of different energy was employed. The source was placed uncollimated either below or at the side of the detector as can seen in Figure 2.1. The count rate of three different peaks was evaluated and the following ratio r_{att}^{meas} was calculated:

$$r_{att}^{meas} = \frac{N_{60\,\mathrm{keV}}}{N_{99\mathrm{keV}} + N_{103\mathrm{keV}}} \tag{2.5}$$

As the attenuation is different for the different energies, the ratio is sensitive to the thickness of the attenuating layer. The measurements were reproduced in the MC simulation and the same ratio r_{att}^{MC} is evaluated. In the MC, the location of all the energy depositions within the diode is registered. During post-processing different charge collection efficiencies can be given to the energy depositions depending on their location in the diode. To determine the active volume, zero charge collection efficiency outside the active volume was assumed and the thickness of the non-sensitive layer was varied in 0.025 mm steps. Figure 2.23 shows the dependence of r_{att}^{MC} on the layer thickness, which was fit with an exponential function. By comparing the measured ratio to the curve, the thickness of the insensitive layer was found. Table 2.6 lists the outcome. The values are larger than the nominal

values of 0.5 mm given by the manufacturer. The determined value is an effective quantity adopted to fit best to the implementation of the MC based geometry model at hand.

The uncertainties taken into account in the analysis are listed in Table 2.7. With 10^{10} γ-rays per line it was made sure to minimize the statistics uncertainty of r_{att}^{MC} to below 1%. This is also necessary to avoid correlation due to using the same MC for all data points of the curve. An overall Geant4 uncertainty and an uncertainty on the branching ratio of ^{241}Am as quoted in [60] were assumed. In general, the geometry of the detector around the diode is well known and it has been assured by the MPIK mechanical workshop that the determined thickness of the Cu parts is accurate. Thus, no contribution to the budget of systematics is assumed. The dominating uncertainty comes from the source position. Due to the source being located directly at the cryostat, already small shifts of 0.3-0.5 mm have a large impact of 2-6% depending on the source position as estimated by the MC. The influence of the slow pulse implementation as described below was not quantified, but is negligible in comparison to the other systematics according to [60]. All the uncertainties add up to the two curves that enfold the best fit to r_{att}^{MC} in Figure 2.23. For the measured data, only statistics uncertainties are taken into account. The blue lines in Figure 2.23 show how the uncertainty is read off by looking for the intersection between the 1 σ band around the measured value and the uncertainty curves from the MC.

For the CONUS detectors, it is assumed that the active volume corresponds to the diode volume minus the dead layer and the transition layer. Due to the size of the diode no inactive regions within the diode volume are expected. Consequently, the active volume amounts to (0.91-0.94) kg as listed in Table 2.6, with a relative uncertainty of $\pm$1%.

Evaluation of transition layer

The area outside the active volume is not fully insensitive to the charges deposited there. Instead, the efficiency decreases gradually within the so-called transition layer as described in Section 2.1.2. This is not considered in the active volume evaluation presented above, but it is relevant to correctly describe the spectral shape of the measured integral background in the MC. With the help of the source measurements, the thickness of this layer can be evaluated as well. For the charge collection efficiency ϵ_{cc} the following shape is assumed as described in [6] for Ge spectrometers:

$$\epsilon_{cc} = 1 - \frac{1}{e^{(x-(\mathrm{DL}+0.5\mathrm{TR}))/0.17\mathrm{TR}} + 1} \tag{2.6}$$

In the equation, DL represents the dead layer thickness in mm and TR the transition layer thickness in mm. The interaction depth below the diode surface is denoted by x. It is illustrated for Conus-1 in Figure 2.22. The charge collection efficiency is implemented in the post-processing of the MC. This requires the MC to be folded

with the energy resolution of the detector. The energy dependence of the energy resolution can be described by $A_{res} + B_{res} \cdot \sqrt{E_{ee}}$ (see Section 1.4.4). The three lines from the ^{241}Am measurements are used to evaluate the parameters A_{res} and B_{res} for each detector. The thickness of the transition layer in the MC is adapted until the shape of the 60 keV line of the ^{241}Am source measurements and the continuum below can be reproduced.

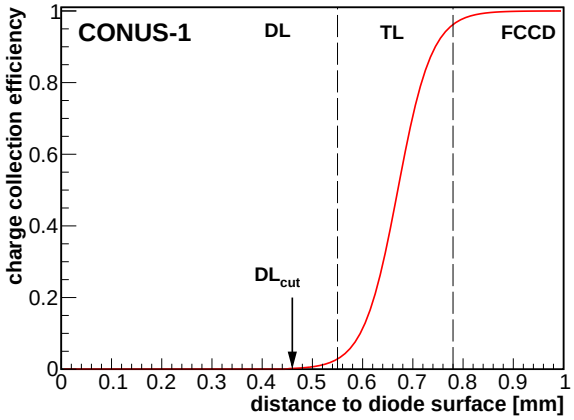

Figure 2.22: Model for the charge collection efficiency. DL represents the dead layer, TR stands for the transition layer and FCCD denotes the full charge collection depth. Below DL_{cut} the charge collection efficiency is set to exactly 0.

The outcome of the optimization of the slow pulse implementation is shown exemplarily for Conus-1 in Figure 2.24 compared to the MC assuming no transition layer and the ^{241}Am measurement. All spectra are normalized to the count rate in the peak after the subtraction of the background. It can clearly be seen how events from the full-energy peak are reconstructed at lower energies, which leads to the observed continuum. However, this procedure is not enough to fully determine the charge collection efficiency at low energies. As can be seen in Figure 2.22, the charge collection efficiency decreases smoothly towards zero, which means that there is a finite possibility for very high energetic energy depositions to be reduced to energies below 1 keV_{ee} close to the energy threshold. To check how well the model reproduces the events in this energy region the ^{228}Th calibration measurements with active muon veto at KBR are used. This is preferred over the ^{241}Am data as the exact same DAQ settings are applied for the physics data taking and the surrounding materials close to the source are precisely known. The source is located in the middle of the copper plate covering the detector chamber. The following isotopes are simulated and added up according to the branching ratios: ^{212}Bi, ^{212}Pb, ^{222}Ra, ^{224}Rn and ^{208}Tl. The MC outcome is compared to the measured data normalized to the energy range [6,14] keV_{ee}. The MC is adapted to the data by introducing an additional parameter DL_{cut}. Between the diode surface and the DL_{cut} (also marked in Figure 2.22 for Conus-1) the charge collection efficiency is set to exactly 0. This has no influence on the comparison of the MC with the ^{214}Am peak.

Figure 2.25 also shows the spectral shape of the ^{228}Th calibration, if no slow pulses were present according to the MC model. The spectrum is much flatter. With the help of pulse shape analysis it would be possible to cut away events from the

transition layer, however, this information is not available for the CONUS detectors and thus these events have to be taken into account when describing the shape of the background at low energies.

detector	dead layer DL [mm]	transition layer TR [mm]	DL + TR [mm]	active mass [kg]
1	0.57	0.20	0.77±0.03	0.94±0.01
2	0.52	0.17	0.69±0.03	0.95±0.01
3	0.48	0.16	0.64±0.03	0.94±0.01
4	1.08	0.22	1.32±0.04	0.91±0.01
nominal			0.5	0.96

Table 2.6: Dead layer and active volume of the CONUS detectors, determined with ^{241}Am source measurements at LL and by the manufacturer.

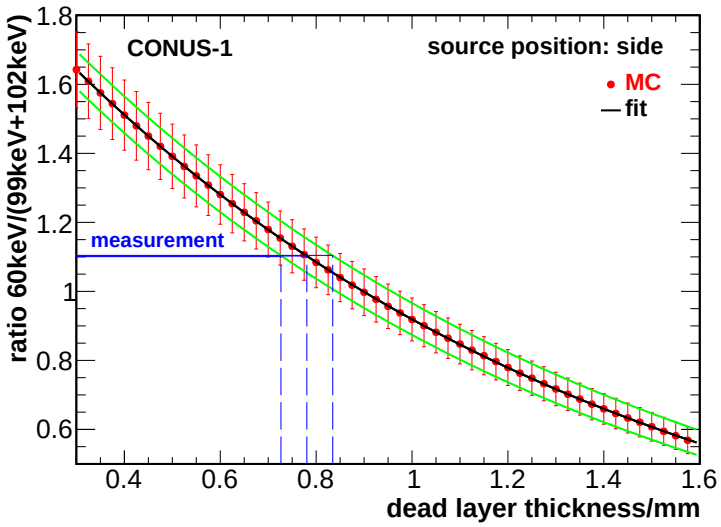

Figure 2.23: Line ratio r_{att}^{MC} in dependence of the dead layer thickness. The measured ratio is marked as blue line.

2.2.6 Geometric detection efficiency

The geometric detection efficiency expresses the probability to detect a γ-ray or electron of a given energy it had when entering the detector. To illustrate how this looks like, an isotropic mono-energetic point source below the cryostat in position (1) in Figure 2.1 was simulated with energies from 10 keV to 3000 keV. The fraction of counts arriving in the full energy peak was determined and plotted against the energy in Figure 2.26. For comparison, one curve was determined without the transition layer and the dead layer and one including all the layers.

systematic	uncertainty on active volume
Geant4 physics	±2%
branching ratio	±1.8%
MC statistics	<1%
MC geometry Cu	negligible
source position	±2-6% (source pos. dep.)
data statistics	±0.3-1.4% (det. dep.)

Table 2.7: Uncertainty contributions of the active volume determination with ^{241}Am source measurements.

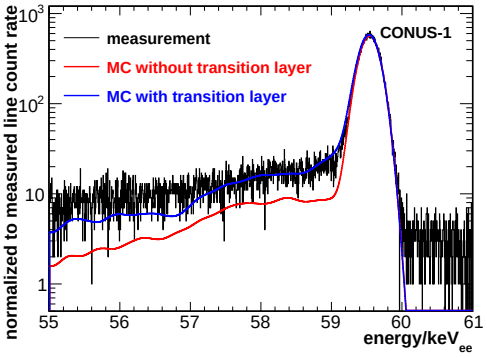

Figure 2.24: 60 keV line of ^{241}Am: measured data, MC simulation with and without slow pulse implementation; all normalized to peak count rate.

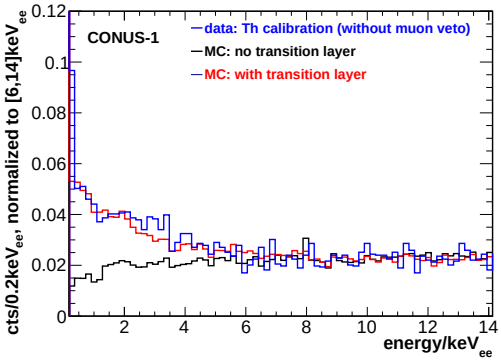

Figure 2.25: Th calibration measurement at KBR: measured data, MC simulation with and without slow pulse implementation; all normalized to the integral count rate in [6,14] keV$_{ee}$.

The efficiency peaks at around 200 keV and decreases towards higher energies. This occurs because the attenuation coefficient in Ge for γ-rays decreases towards higher energies meaning that it is less likely that all of the energy is deposited in the material. The shape of the decrease is also determined by the size of the diode. For larger diodes such as CONRAD the detection efficiency decreases less strongly making such detectors preferable to detect γ-rays from outside the cryostat as it is required e.g. for material screening. Above 1022 keV pair production can occur as Figure 1.11 shows. This means that e+e- pairs are created. If this happens close to the edges of the diode, it is possible that the γ-rays produced in the absorption of the particles leave the diode. This leads to single escape peaks (SEP) and double escape peaks (DEP) at energies of 511 keV or respectively 1022 keV below the full energy peak. The occurence of single and double escape peaks is more likely to occur within large diodes. Figure 2.26 depicts the probability for the CONUS diodes, showing that it can be assumed that these peaks are irrelevant for the CONUS background.

Towards lower energies, the attenuation by the Cu parts of the cryostat and the dead layer limit the capability to register γ-ray and electron signals from outside the

cryostat. For the CONUS detectors including the dead layer determined in the last section, the efficiency drops to zero at about 60 keV for γ-rays. As a charged particles, electrons are even more likely to being absorbed. All counts in the spectrum below this energy are either created within the cryostat or come from only partial energy depositions of higher energetic particles. The former contribution can be either created by decays within the Ge, radioactive contaminations of cryostat parts or recoils of Ge nuclei induced by neutrinos or neutrons. All of these background contributions are discussed in detail in Chapter 5. For the latter contribution, either the Compton continua of higher energetic γ-rays are observed or slow pulses lead to a reconstruction of signals at lower energies as they originally had. They can be a sizable contribution at lower energies as Figure 2.25 shows.

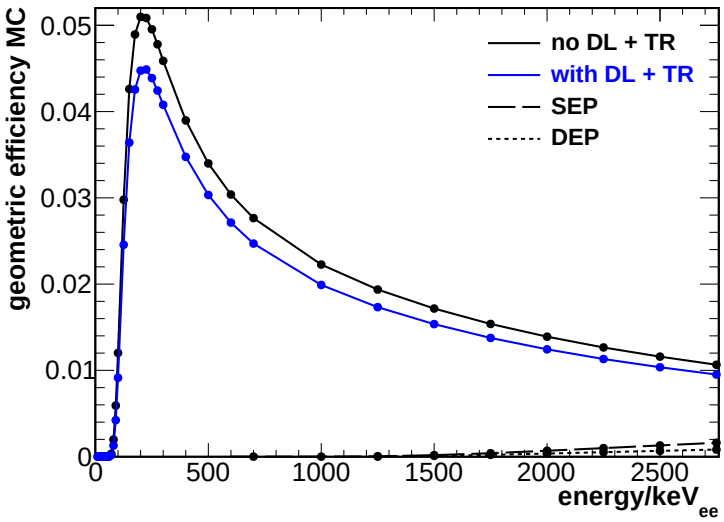

Figure 2.26: Geometric efficiency curve of Conus-1 for isotropic mono-energetic γ point source located directly below the cryostat end cap.

2.3 Summary on the CONUS detectors

The four Conus HPGe spectrometers were characterized in detail using radioactive sources. The excellent energy resolution was confirmed, which is a prerequisite for a low energy threshold. The active mass of the detectors was evaluated as well. Moreover, the thickness of the transition layer at the surface of the diode, where the charge collection is incomplete, was determined. The results are required as input for the background model. Moreover, it could be shown that the energy scale of the detectors is highly stable with less than 0.04% relative standard deviation over several months. Due to the high resolution of the detectors it was even possible to observe a correlation to the diode temperature within this extremely small variations.

3 Noise studies and cuts

For the noise and the energy threshold of HPGe spectrometers not only the detector design is important, but also the data acquisition system has a large impact. The environmental conditions can contribute as well. For Run1 and Run2/3 of the CONUS experiment the commercial Lynx DAQ by CANBERRA is used and introduced in the following. Moreover, two important tools for the examination of noise and spurious events are presented: the noise integral and the time difference distribution analysis. It will also be shown how the far from laboratory conditions at the nuclear power plant have an influence on the experiment.

3.1 Data acquisition system

The DAQ extracts the measured events from the signal of the preamplifier. The amount of information available as well as the impact the user can have on the process depends on the system used. The Lynx allows for a limited range of possibilities for adjustments by the user. The most important settings for the CONUS experiment are described in the following.

3.1.1 Lynx settings

Each detector requires its own Lynx DAQ while it is possible to split the signal of detector on more Lynx. During data taking the so-called TLIST is constantly printed out. This is a list of all registered events containing the time stamp of the event and the channel number, related to the energy of the event via the calibration.

The gain (coarse/fine) defines the registered energy range. Including the internal attenuator, a maximum energy range of up to about 500 keV_{ee} can be achieved with the electronics of the CONUS detectors in combination with the Lynx DAQ. This dynamic range is covered by at maximum 32768 channels. For the CONUS experiment an excellent energy resolution is crucial and more bins are preferred in the small ROI below 1 keV_{ee}. Thus, at KBR for all four detectors the maximum energy range was limited to $\sim$15 keV_{ee} (in the following referred to as "lowE" range), resulting in about 0.5 eV per channel. This choice means that the 10.37 keV line and the lines at lower energies are still available for calibration. Moreover, a fifth Lynx was employed in parallel to additionally monitor the background at higher energies, especially radon-induced one, up to 450 keV_{ee} for one detector (in the following referred to as "highE" range).

The Lynx DAQ extracts the channel number from the baseline itself and the user has no access to the detected pulses. By shaping filters (differentiation and

integration) the pulses are extracted from the baseline (see Figure 1.8) and the channel number is determined from the pulse height.

Only the time constant and discriminator level of the filters can be set by the user. Table 3.2 depicts the shaping time constants recommended by the manufacturer for the ideal resolution and the lowest noise level. The slow discriminator level basically determines when a step in the baseline within the shaping time is recognized as a signal. The filter has a time constant of several ten μs comparable to the shaping time in Table 3.2. For a lower level, more events at the noise threshold are registered, but the dead time of the system increases as well. A trade-off has to be found. The fast discriminator filter with a time constant of 200 ns comparable to the rise time of a pulse is used to reject pile-up. Pile-up means that two signals are measured so close to each other in time that the energy of at least one of the events cannot be evaluated correctly. One or both of them have to be discarded. Both filter settings depend on each other. During the commissioning and optimization phase of CONUS special attention was paid to optimize the settings to look for signals close to the noise threshold.

Moreover, the DAQ enables anti-coincidence to logic pulses. This feature is used for the muon veto system (see Section 1.7.1) and to remove the TRP resets (see figure 1.8). The vetos are applied online and for the duration of the veto logic pulses no data is acquired. An additional dead time is therefore introduced to the system in both cases, which has to be included for the determination of the live time.

3.1.2 Live time evaluation

The real time of the measurement is the duration between the start and the end of the measurement. However, events are not collected during the full time period, because the veto signals inhibit the read out and the DAQ filters remove pile-up events. This introduces the so-called dead time to the system. The live time of the measurement relevant for the data analysis is evaluated from the product of (1-dead time) and real time.

It holds in general that the higher the count rate, the more often the end of the dynamic range is reached and a reset is induced. Thus, more TRP vetos are triggered resulting in a correlation between count rate and dead time. The Lynx evaluates the dead time due to TRP resets as well as due to pile-up itself (referred to as Lynx dead time) but not for the muon veto system. The Lynx dead time is evaluated constantly during data taking and for the analysis a mean value is calculated. The statistical fluctuations of the dead time are considered negligible.

The dead time from the muon veto has to be evaluated separately and is included offline into the analysis via the muon veto dead time correction factor. The dead time depends on the length of the veto window and the reactor status. During reactor ON times there is an reactor-induced γ-ray background (see Section 4.3) with energies up to several MeV. The plastic scintillator plates of the veto are only shielded b y 5 cm of Pb. Due to the high energies and the large flux, a small portion of the γ-rays exceed the trigger threshold of the muon veto. The additional veto

triggers increase the dead time by nearly a factor of 2. To determine it, the muon veto rate over time is registered during reactor ON time for two weeks with an additional DAQ system not permanently present at KBR. A clear correlation to the thermal power is found. The rate can be extrapolated to zero thermal power, which corresponds to the actual muon-induced signals. From the rate, a muon veto dead time correction factor of 0.965±0.002 during reactor OFF time and 0.942±0.002 during reactor ON time is derived by W. Maneschg and used in the data analysis.

3.1.3 Electronics detection efficiency

The capability of the electronics chain and the DAQ to extract small signals from the baseline gives the minimum lower limit in energy for the detection threshold. This is described by the electronics efficiency that degrades towards lower energies close to the ROI for CEνNS. Thus, the decrease has to be carefully quantified and taken into account for the signal analysis. As this is an electronics effect, it can be evaluated with artificial signals created with a pulse generator and injected directly into the preamplifier. The frequency of the signals is well known. Comparing it to the detected count rate gives the value of the efficiency. Scans over the relevant energy range have been carried out to quantify the decrease in efficiency. Figure 3.1 depicts the outcome of the analysis by T. Hugle for Run2. Due to the changed DAQ settings an improvement was observed between the runs. In the ROI for CEνNS down to about 250 eV_{ee} for Run1 the detection efficiency lies at (94±5)% to (98±5)% depending on the detector. With the improved DAQ settings in Run2, (100±1)% were achieved for all four detectors. The electronics efficiency curves approach 0 way lower at about the pulser resolution (see Table 2.3). It gives the lower most limit of the energy threshold, while for phyciss events the additional contribution to the noise apply as described in Section 1.4.4.

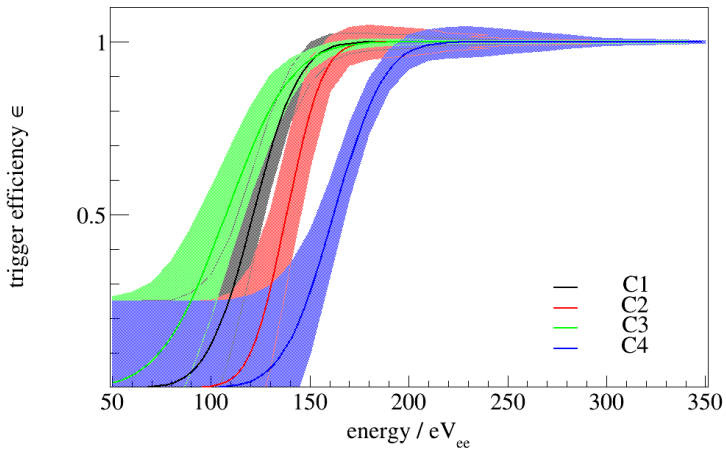

Figure 3.1: Electronics efficiency curves of the four CONUS detectors for Run2. Plot prepared by W. Maneschg.

3.2 Noise integral and investigation of noise peak

Close to the energy region where the electronics detection efficiency starts to decrease, an approximately exponential increase in the spectrum due to noise events is observed. An overview of the origin of these noise events for HPGe spectrometers in general is given in Section 1.4.4 and the separation between noise events and background signals is discussed in Section 3.3.2. As the CONUS experiment is looking for signals close to and within this energy range, it is of great interest to study the stability of the noise and impact of external factors on its count rate.

For this purpose, the "noise integral" is introduced: it is defined as the integral from channel zero to a channel at higher energies such that most of the noise peak is covered (approximately 200-250 eV_{ee}). The upper end of the integral range corresponds to the cut threshold channel for the time difference distribution. There, the distribution of the time difference between the registered events is analysed above a certain channel, where physical-like events can be separated well from noise events. The cut and the selection of the cut channel are described in Section 3.3.2). The cut channel is clearly below the ROI for CEνNS. The advantage of looking at the energy range of the noise integral is the high statistics as well as prevention of bias as this interval is not used for the CEνNS analysis. The integral starting at the cut threshold channel to the end of spectral range is referred to as "above noise integral". Time binnings of 1 h or 1 d were dissected to study correlations to the environment. The noise integral also changes with the DAQ filter settings that are defining the trigger threshold of the electronics. For example, for a lower slow discrimination value an increase in the noise integral is observed given all other settings stay constant (see Section 3.1.1). Thus, only periods with the same DAQ settings are analyzed together.

The noise integral is compared to the environmental data (see sensors in Figure 1.14) and the cryocooler monitor data constantly collected at KBR. Observed spikes and jumps are also cross-checked with the occurrences at the nuclear power plant. The temperature related correlations are discussed here in detail. The occurrence of spikes due to a lot of events following in a very short time period is examined closer in connection with the time difference distribution analysis in Section 3.3.1 and in Section 3.3.5. In Section 3.3.5 also another correlation to data from the nuclear power plant is discussed.

3.2.1 Correlation of noise integral to room temperature

An overall correlation of the noise integral to the cryocooler power is found, shown exemplary for Conus-1. Special effects are examined by looking at the outages of Run1 and Run2 for all the detectors. As the cryocooler power is mostly correlated to the room temperature (see Section 2.1.3), the same is automatically true for the noise integral as long as there is no decline of the vacuum inside the cryostat.

For Run1, Figure 3.2a displays the behavior of the noise integral and the cryocooler power over time. In Figure 3.2b and Figure 3.4 for Run2 the correlation comes out

even more explicitly. This can be understood by looking in detail at the temperature profile around the shield as well as the way the environment monitoring was carried out.

For Run1, the plastic tent around the shield was half-open leading to an inhomogeneous temperature distribution around the shield. It had also been opened at the closed sides from time to time by the shifters for maintainance reasons. The room temperature was measured with a sensor at the edge of the shield close to Conus-1 and the cryocooler power was mostly documented by the shifter, meaning that there are up to 3 weeks without data points. Overall, this means that collected environmental data is not fully representative for the cryocooler performance.

The situation was improved starting with Run2 by constantly and automatically monitoring the cryocooler power over time for all detectors, so there are (nearly) no long periods without data points. Moreover, the temperature of the air outlet of the cryocooler was monitored as well, which is directly correlated to the cryocooler power (see Section 2.1.3). To achieve a more homogeneous temperature around the shield at the beginning of Run2 the tent was fully opened before it was fully closed in the middle of the outage (cold house) (see Figure 1.14). All in all, this explains why the correlation to the cryocooler power is more prominently visible during Run2.

The inhomogeneous and partially unknown temperature around the shield during Run1 is also a potential explanation for some of the anomalous behavior of the noise integral. Looking at the longterm development of the noise integral, an approximate correlation to the cryocooler power/room temperature holds most for time periods and detectors. But during short-term large changes in the room temperature ($\sim$3 deg from a blackout of the cold air ventilation for a few hours), also anti-correlations or no reaction of the noise integral to the room temperature at all were observed for some detectors in Run1 (see Figure 3.3). It is suspected that this occurs from a discrepancy between the temperature directly at the cryocooler, the temperature registered halfway inside the shield by the cryocooler and the actual temperature at the diode. The temperature inside the shield is not known and the situation is further complicated by the air brought in to flush the shield against Rn background. The air bottles for the flushing are located outside the tent where no temperature data is collected (location of breathing air bottles marked in Figure 1.14). Possibly, if the cryocooler registered a stronger increase of the temperature than it is actual occurring inside the shield, its action does not stabilize the situation, but lead to an actual cooling of the diode below the previous level. The decrease in noise by the lower diode temperature might compensate or even exceed the stronger vibrations due to the higher cryocooler power, resulting in an overall drop of the noise level. The hypothesis is supported by the temperature dependence of the peak position, which shows that the cryocooler does not fully compensate changes of the ambient temperature (see Section 2.2.3).

During Run1 at some point the decline of the vacuum in the cryostat becomes more important for the cryocooler power than the room temperature. Thus, the cryocooler power stays at a high level even though the room temperature decreases. The noise integral follows the behavior of the cryocooler power with the exception of

Conus-2. This detector is most strongly affected by the vacuum leak, but after a few months of data taking at KBR the noise integral constantly drops over time for the next few months. It is speculated that the strong increase of the cryocooler power leads to a huge deviation from the usual range of parameters that the cryocooler operates in resulting in undefined behavior. In general, a too strong cooling of the diode could lead to a decrease of the noise if this overcompensates the higher noise due to the higher cryocooler performance. Due to the unstable situation, all of these data were omitted from the CEνNS analysis.

To sum it up, the observations strongly indicate that the cryocooler induces noise. This is examined in more detail in connection with the reaction of the HPGe spectrometers to mechanical vibrations and the analysis of distinct frequencies found in the noise in Section 3.3.4 after the introduction of the time difference distribution as analysis tool.

The consequences for the data taking at KBR and for the CEνNS analysis are discussed in the following.

3.2.2 Room temperature management at KBR

Next to the non-stable temperature profile due to the status of the tent also the room temperature at KBR deviates far from laboratory conditions. Within the containment of the nuclear power plant, there is no direct exchange with ambient air. Instead the location of the experiment is equipped with an AC and a cold air ventilator (see Figure 1.14). While the AC provides a stable temperature, the air of the cold air ventilation depends on the seasons as well as the overall air flow in the pipe system of the containment. There are also intentional and unintentional blackouts of the ventilator, which leads to an immediate increase of the temperature by up to 8 deg. This is especially problematic as these occurrences are more frequent during the outages (see Figure 3.3 and Figure 3.4 for the temperature over time during the outages in April 2018 and in June 2019). During the outage, the cold air ventilation is switched off for maintenance from time to time. Moreover, when the reactor pressure vessel is opened and the fuel assemblies are removed, the ventilation in the whole containment is stopped to avoid the potential distribution of radioactive traces within the reactor containment. The increase of the noise during the reactor OFF periods must be avoided for the CONUS experiment. Thus, following directly from the outcome of the analysis of the noise integral, at the middle of the outage of June 2019 the tent was completely closed and the air flow from the AC was directed into the tent. The arrangement is referred to as "cold house". In Figure 3.4 it can be seen how this lead to a decrease in the noise integral starting on 14.06.2019. Closing remaining leaks on the 17.06.2019 further improved the situation. For future data taking even more measures to lower and stabilize the temperature are planned, to achieve a lower and even more stable noise threshold.

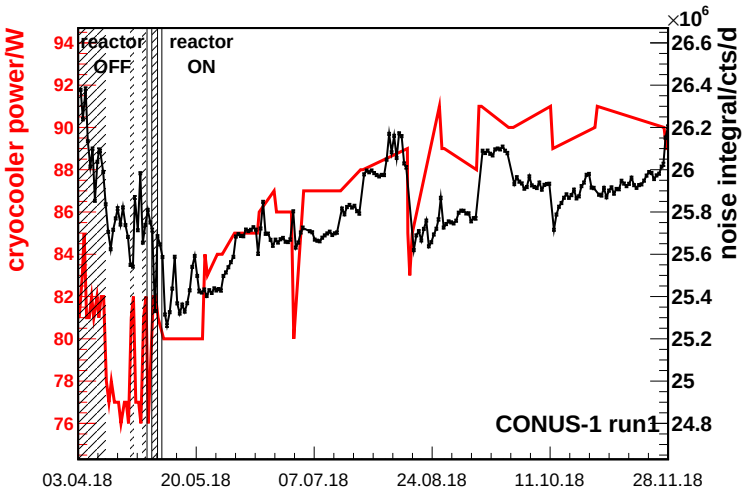

(a) Conus-1, Run1.

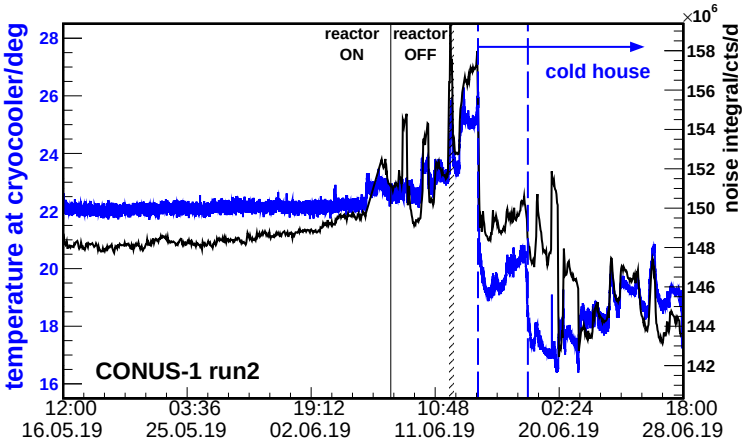

(b) Conus-1, Run2.

Figure 3.2: Correlation of the noise integral of Conus-1 to the cryocooler power. Shaded areas mark the time periods when the ventilator was OFF. Also changes in the air flow of the ventilation system have an impact.

3.2.3 Noise-Temperature-Correlation Cut

The CEνNS signal is expected close to and within the energy range where the noise increases exponentially over the background. Therefore, if the noise is stable over time, the analysis threshold can be moved to lower energies increasing the chance to observe a signal. However, as described before due to the varying room temperature the noise is not fully stable over time especially before the introduction of the cold house. Datasets collected during periods with almost exaclty the same temperature settings are too short for an analysis or not available at all as discrepancies between reactor ON and OFF times are observed. Moreover, for Run1 no detailed

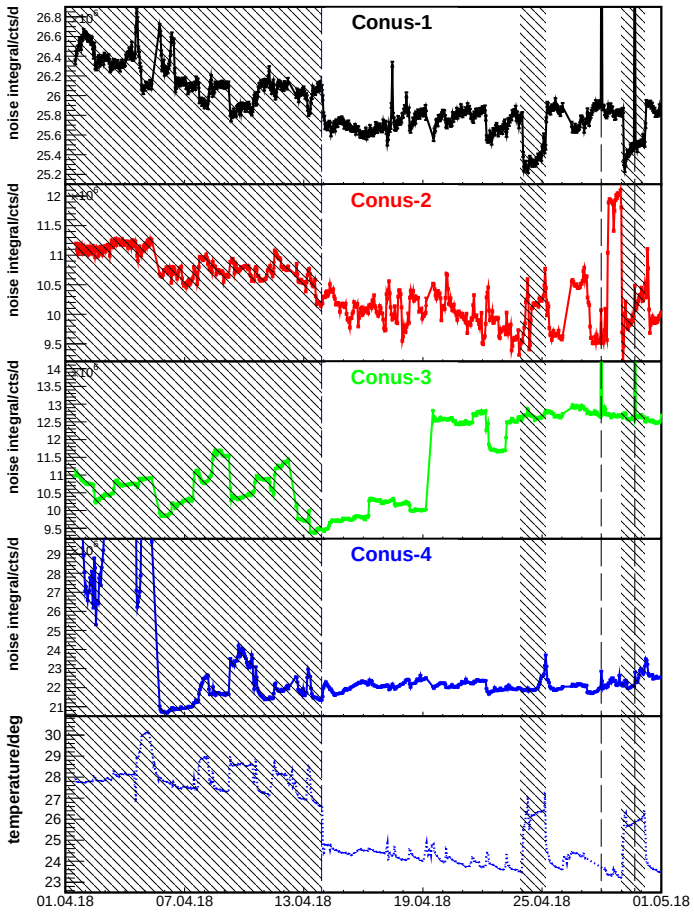

Figure 3.3: Noise integral of outage of Run1 for all detectors. The room temperature is displayed for comparison and the shaded areas mark the times when cold air ventilator was off. A partial correlation between the noise integral and the temperature was found for some of the detectors. The black dashed lines mark the spikes induced by the main cooling pumps (see Section 3.3.5).

information on the temperature are available. Instead a data selection was carried out:

1. periods of increased temperature for known reasons are removed
2. maximal allowed variation of the noise is defined, time periods where the noise deviates from these upper and lower limit are cut (see red lines in Figure 3.5a and Figure 3.5b)
3. above noise integral was checked for stability

In this way, also conspicuous behavior of the noise not related to temperature can be cut away. In the following the cut is referred to as Noise-Temperature-Correlation Cut (NTC cut). Figure 3.5a and Figure 3.5b displays the noise integral where the shaded areas mark the cut time periods. In this way, the noise variations can be

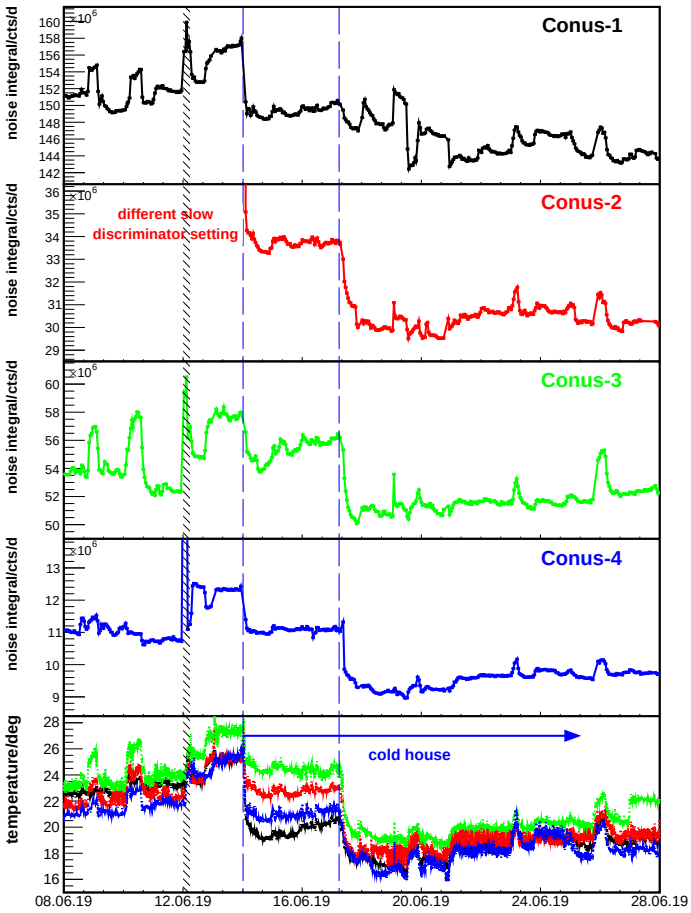

Figure 3.4: Noise integral of outage of Run2 for all detectors. The temperature at the cryocooler outlets is displayed for comparison and the shaded areas mark the times when cold air ventilator was off. A clear correlation between the noise integral and the temperature was found. The noise integral with different slow discriminator settings is not comparable.

restricted to a few percent. However, the consequence of the cut is also an explicit reduction of statistics for all runs. Especially the reactor OFF time is diminished by about 50%. The final live times of the CEνNS analysis are detailed in Section 6.1. Even though of the cut, it is not possible to fully remove the temperature dependence from the data set, thus the CEνNS analysis threshold in Section 6.4 is chosen in such a way to be above the energy range where the remainders of the correlation are observed.

The outage of Run2 in June 2019 was concluded with a leakage test of the containment of the reactor building. This means that overpressure was applied to the containment building. For the CONUS detectors for safety reasons this required for the vacuum in the cryostats to be broken. They were filled with gaseous Argon during the test and the vacuum was restored afterwards by pumping the cryostats. However, the measures resulted in a change of the noise characteristics of two of

the detectors. The noise integral increased drastically, making a comparison to the dataset aquired before impossible. Further undesired effects were observed for all detectors as well.

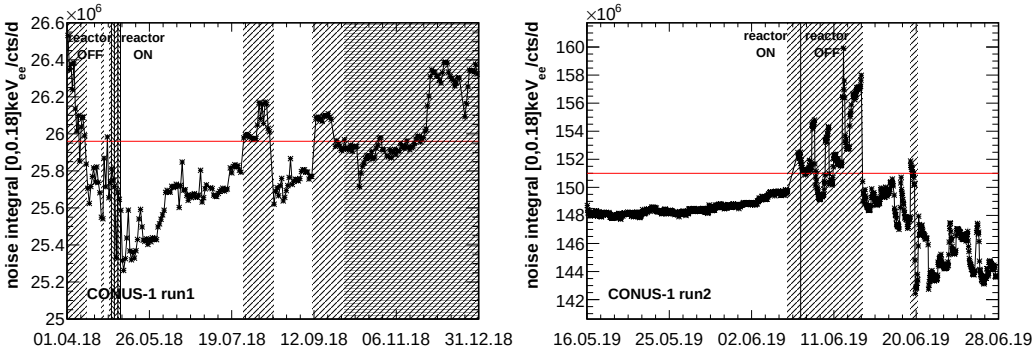

(a) Application of NTC cut on Conus-1 Run1.

(b) Application of NTC cut on Conus-1 Run2.

Figure 3.5: Noise integral of Conus-1, where the time periods removed by the temperature-dependent noise integral are marked as shaded areas. The double-shaded area is cut due to the above noise integral. The red lines show the maximum allowed noise integral.

3.3 Creation of time series

The TLIST data collected by the Lynx are used to study the time difference between the events as described below. Noise events can be identified in this way and their classification is described in the following section. During the processing of the data, these noise events are discarded according to the time difference distribution (TDD) and a histogram with the number of events in each channels (corresponding to a certain energy via the energy scale calibration) is created. The TDD is also useful to look for frequencies in the noise events.

3.3.1 Classification of events

The time difference between one event to the next one is calculated. The most information can be extracted by plotting the logarithm of the time differences as it stretches from several microseconds to several hours. Figure 3.6b shows the TDD of CONUS-1 for an exemplary measurement of Run1. The different TDDs include all events starting from energy 49 eV, 95 eV, 141 eV, 187 eV and 233 eV up to the full spectral range. The energies are also marked in the energy spectrum of the noise peak in Figure 3.6a. The noise peak is the exponential increase of events at the lower end of the spectrum.

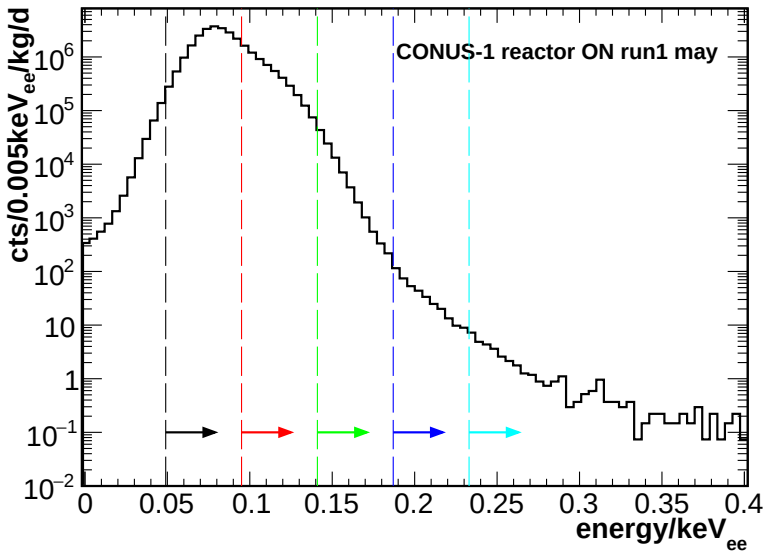

(a) Noise peak of Conus-1 for selected measurement of Run1.

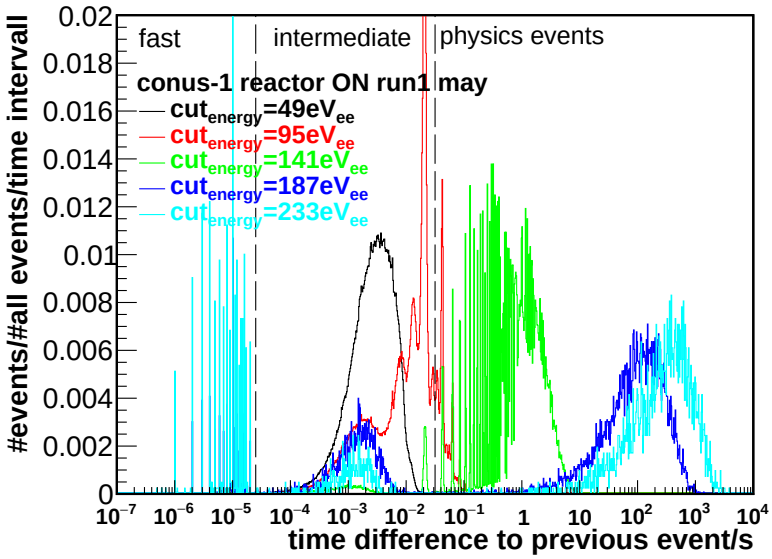

(b) TDDs for various energy thresholds.

Figure 3.6: The TDD in (b) include all events above the energy thresholds marked in (a). With more events from the noise peak included, the three classes of events cannot be separated properly.

The total number of events in the spectrum is dominated by the events therein. Therefore, the TDD starting from 49 eV only shows the overall frequency range of the noise. To be able to examine the distribution of the physical events and the events at the beginning of the noise threshold, the noise events below a certain energy threshold are cut from the TDD. With increasing cut energy the TDD separates into

three regions (see also Table 3.1): (1) Physical distributed events above $\Delta t = 10^{-1.5}$ s (2) intermediate events from $10^{-1.5}$ s to $10^{-4.6}$ s and (3) fast events with $\Delta t < 10^{-4.6}$ s. They are discussed in detail in the following. The full Conus-1 Run1 reactor ON data set is used as an example. The respective time differences are plotted in Figure 3.8.

The exact shape of the TDD depends on the DAQ settings as well as external disruptions and microphonics. The TDD for the different detectors are not identical, but they share the same features. Above a certain energy (e.g. 187 eV for Conus-1 in Figure 3.6b) the distribution of physical-like events is clearly separated from noise events making it possible to cut them away as described in Section 3.3.2.

type	time range	type
(1) physical	0.03 s to ∼1 h	physical-like events
(2) intermediate	25.1 μs to 0.03 s	microphonics
(3) fast	<25.1 μs	failure pile-up rejection, last event physical-like

Table 3.1: Overview of event types observed in the TDD analysis.

Physical-like events

The shape of the physical distribution above $10^{-1.5}$ s can be understood starting from a Poisson distribution. For $N(t)$ the number of events in the time range [0,t] the probability for the nth event to occur within the time range is:

$$P(N(t) = n) = \frac{(\lambda t)^n e^{-\lambda t}}{n!} \tag{3.1}$$

Here, λ represents the expected value. Setting n to zero gives the probability for observing no event within t, while the complement corresponds to the probability distribution of the time differences within the time range:

$$P(\delta t \leq t) = 1 - P(\delta t > t) = 1 - e^{-\lambda t} \tag{3.2}$$

The derivative leads to the probability density function (pdf) which describes the data displayed in the plots:

$$\mathrm{pdf}(\delta t) = \lambda e^{-\lambda t} \tag{3.3}$$

This proofs that the time difference between the events of a Poisson distribution is distributed exponentially itself. In Figure 3.7 the normalized TDD of the physical-like distribution is shown with a linear axis. It corresponds to the distribution of physics events in Figure 3.8 with the logarithmic axis. A fit confirms that equation (3.3) matches the data very well.

The scatter plot of the TDD against the energy of the events in Figure 3.9 shows that the corresponding events are indeed distributed over the whole spectral energy range. The expected γ-ray lines are visible as clusters of events.

For more events within the same measurement time, the time differences between the physical-like events become shorter. This moves the plotted distribution to the left. For lowE background measurements the maximum time difference between two registered physical-like events can be up to 500 s. When applying the muon veto it increases up to $\sim$1 h. For all four detectors it was found that a clear separation from the noise distribution can be achieved down to time differences of $10^{-1.5}$ s=32 ms between events. However, it is not guaranteed that all events within this time regime are of physical origin, just that all events follow a Poisson distribution. Figure 3.6b reveals that by lowering the energy cut threshold, lines start to appear within the physical-like distribution that originate from noise and are discussed in Section 3.3.4.

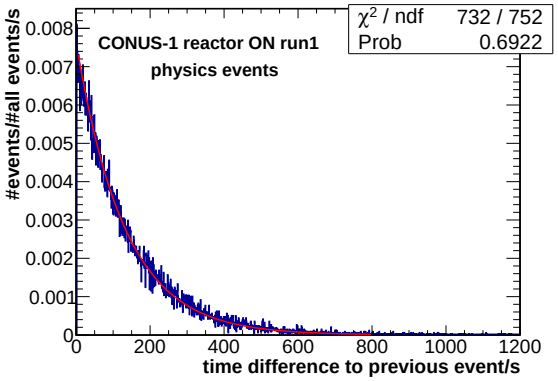

Figure 3.7: Linear TDD of Conus-1 Run1 reactor ON data with exponential fit. The exponential shape of the distribution is expected of events from a Poisson distribution.

Fast events

In the TDD in Figure 3.8 events are observed following faster than 25.1 μs up to 0.4 μs after each other. In over 80% of the cases, there is only one event following in such a fast succession. Higher multiplicities are rare. The time difference is shorter than the shaping time of the detectors (see Table 3.2), indicating problems of the DAQ with the energy reconstruction. Figure 3.10 shows the energy spectrum of the last event in succession in green and all other ones in red. The energy spectrum of the last events correspond to the expected energy spectral shape, while all other events have a non-physical distribution. Plotting the energy of these first events against the energy of the following events in Figure 3.11 reveals that the last event always has higher energies than the events previous in the succession. All in all, it was concluded that the last events are physical and all other events in the succession have to be cut away.

The appearance of this feature of the TDD is highly dependent on the DAQ filter settings. The feature is more pronounced for a low fast discrimination threshold and can be made to disappear completely by increasing the threshold (as it has been done for Run2). This hints that the events are created by a failure in the pile-up

rejection system. Moreover, in calibration data with a higher total number of events, the feature is more pronounced, which supports the connection to pile-up.

detector	shaping time [μs]	flat top
1	16.4	1.0
2	15.0	0.8
3	16.8	1.0
4	16.8	1.0

Table 3.2: Trapezoidal filter settings for energy reconstruction of the CONUS detectors.

Intermediate region

Between the fast events and the physical events an intermediate region can be identified in the TDD in Figure 3.8 from 25.1 μs up to 0.03 s. All of these events are close to the energy threshold as can be seen in Figure 3.9 and 3.12. In about two thirds of the cases the sequences consist only of two events, but up to about ten events following each other within this time regime can be found in regular cases. If the slow discrimination threshold is lowered towards the noise level, more of the events are observed. It could be shown that events within this regime can be created deliberately by knocking on the cryostat (details on the reaction of the CONUS detectors to mechanical vibrations in Section 3.3.3). The events are due to microphonics and cut away completely.

Within the intermediate region, so-called catastrophic events are observed as well (see the spikes in Figure 3.14). Catastrophic events are defined as a burst of events within the intermediate time regime with multiplicities of several tens or higher and energies above the TDD cut energy threshold. The duration of this phenomenon is at maximum a few seconds or even shorter. Next to the TDD they also appear in the above noise integral as distinct spikes. Figure 3.16 shows that despite the short duration they lead to a significant increase of the number of counts at the energy threshold. No direct connections to occurrences around the building were found. Nevertheless, regarding the reaction of the CONUS detectors to mechanical vibrations, a similar reason is suspected. Especially as this kind of events mostly occurred during the outages, where more work within the containment of the reactor building is going on. With one exception they are cut away successfully by the TDD cut as e.g. seen in Figure 3.16. If this is not possible the time period has to be removed.

3.3.2 Time difference distribution cut

The observed features of the TTD are used to cut away noise events. In order to do this, the lowest energy threshold to still be able to separate the physical-like events from the faster noise sequences has to be found. This approach minimizes

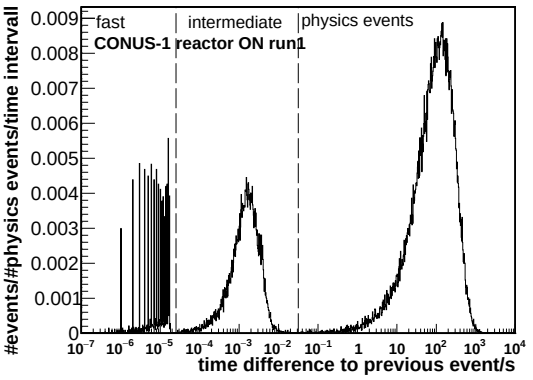

Figure 3.8: TDD of Conus-1 Run1 reactor ON with cut_{energy}=187 eV_{ee}.

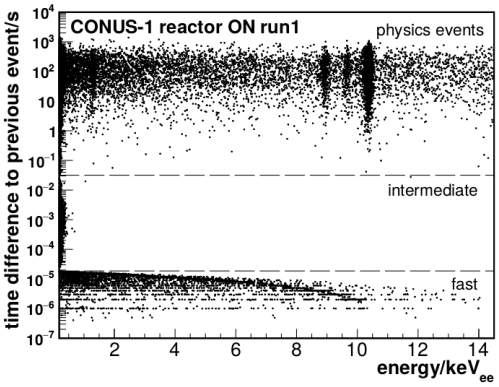

Figure 3.9: Scatter plot of the TDD and the energy of the events.

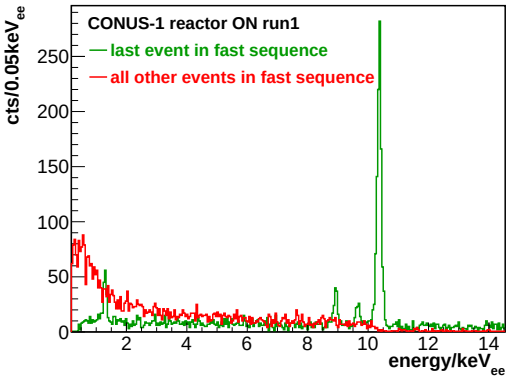

Figure 3.10: Energy spectrum of fast events from TTD.

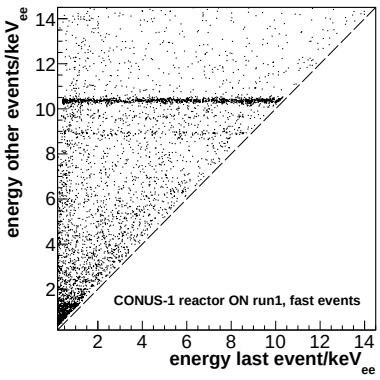

Figure 3.11: Scatter plot of fast events.

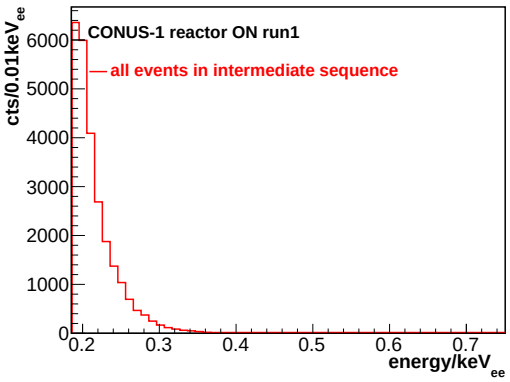

Figure 3.12: Energy spectrum of intermediate events from TDD.

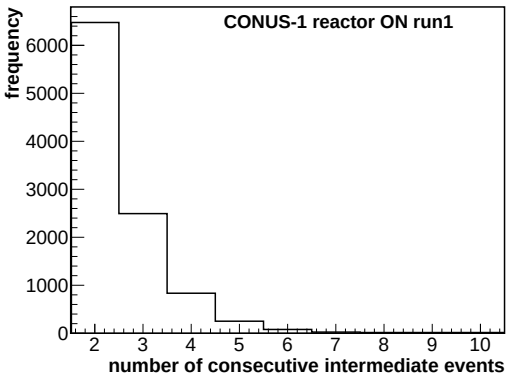

Figure 3.13: Multiplicity of intermediate events.

the loss of physical events. The energy threshold depends on the detector and the DAQ settings and lies between 0.18 keV_{ee} and 0.23 keV_{ee} for Run1 and Run2. This

is well below the analysis threshold. Figure 3.14 and 3.15 show the TTD for Run1 for the reactor OFF And ON periods including the data sets used for the CEνNS analysis. Comparing reactor ON and OFF periods the cut can be applied in the same fashion. The only difference observed are the catastrophic events during the reactor OFF period that become visible as spikes and structures in the intermediate time regime.

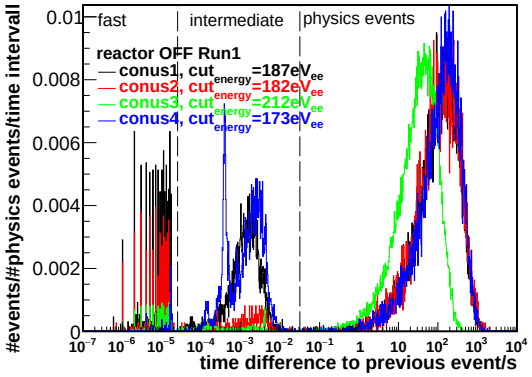

Figure 3.14: Comparison of TDDs of all detectors during the reactor OFF Run1.

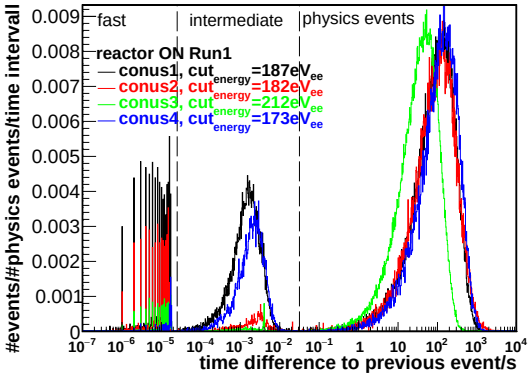

Figure 3.15: Comparison of TDDs of all detectors during the reactor ON Run1.

The cut is applied as described in the categorization of the event types. It is applied on the TLIST level during the conversion of the event list to the channel histogram. The loss on the live time is negligible in comparison to the DAQ dead time. Figure 3.10 and Figure 3.16 give examples on the effectiveness of the cut. Depending on the detector and the Lynx settigns, 5% to 50% of all events above the cut threshold are removed by the cut.

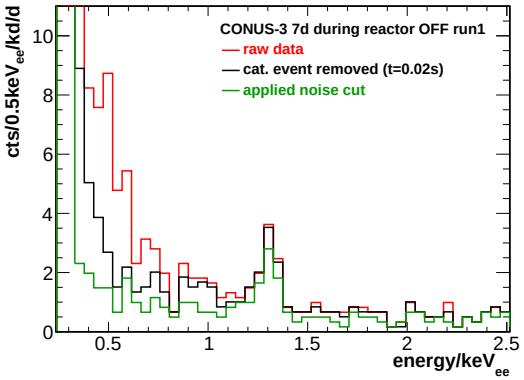

Figure 3.16: Impact of a catastrophic event of 0.02 s on the energy spectrum of Conus-3 for a measurement of 7 d.

3.3.3 Mechanical vibrations

To better understand the events in the intermediate region of the TDD, the response of the CONUS detectors to mechanical vibrations was studied. Moreover, the temperature dependence of the noise integral suggests that the operation of the cryocooler creates noise events in a similar fashion. The TDD was used as a tool to confirm this hypothesis by looking for frequencies within the noise specific to the cryocooler. Lastly, it is also shown how the TDD analysis can be employed to collect more information on features observed in the noise such as spikes induced by the main cooling pumps of the nuclear power plant.

Manually-induced vibrations

Two dedicated test were carried out to examine the reaction of the CONUS detectors to mechanical vibrations.

With Conus-5 at the 11A laboratory a detailed test was made to check the sensitivity to the environment. During this test, the cryocooler had been placed on a Cu plate. Catastrophic events in the TDD were observed for knocking on:

- the cryostat arm
- the opening for the vacuum pumping of the cryostat
- the cryocooler box
- the Cu plate below the cryocooler

For a visualization of the cryocooler see Figure 2.1. All respective logarithmic TDDs in Figure 3.17 have in common, that there is a large excess of intermediate events. In each case the same frequencies in the range of a few kHz are observed, which seem to be the resonance frequency of the system.

No reaction of the detectors in the TDD was found from acoustic vibrations:

- clapping
- jumping up and down next to the detector
- loud music

At KBR, a vibration test were carried out as well. It was carefully knocked on the end of the cryostat sticking out of the shield close to the cryocooling for about 30 s, while data in the lowE settings was collected. The TDD analysis revealed catastrophic events here as well (see Figure 3.19). Frequencies in the range of up to 10 kHz were observed. The energy spectra in Figure 3.20 show the large number of events induced within the short time period that indeed populate the region at the energy threshold of the detector.

All in all, it could be confirmed that catastrophic events can indeed be created by mechanical vibrations and that such kind of events populate the intermediates

region of the TDD. It is suspected that the catastrophic events observed during physics data taking are created in a similar fashion.

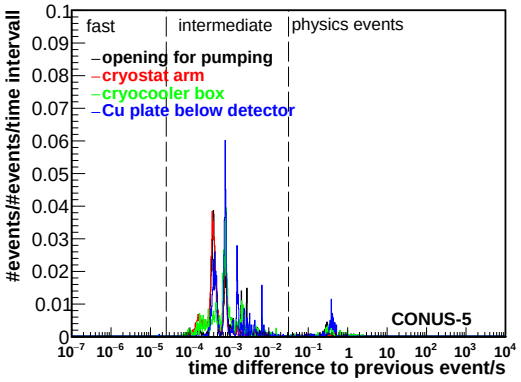

Figure 3.17: Microphonics tests at 11A with Conus-5. Catastrophic events were created by mechanical vibrations.

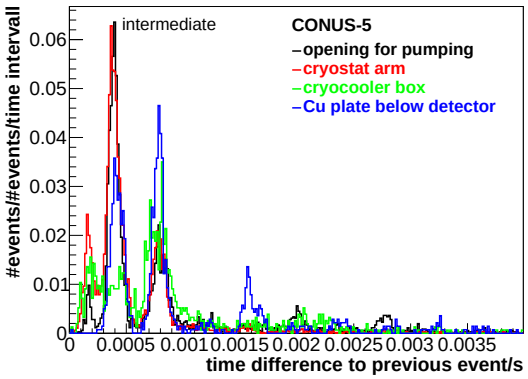

Figure 3.18: Corresponding linear plot of the intermediate region of Figure 3.17.

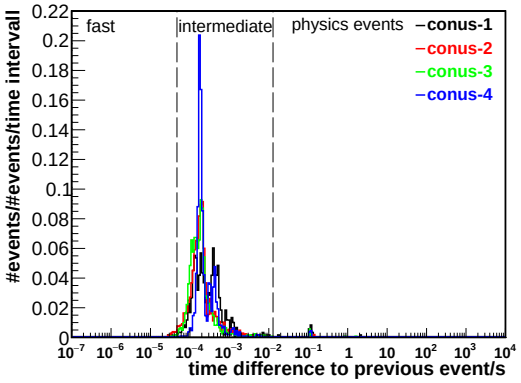

Figure 3.19: TDD created by knocking on the end of the cryostat arm of the detectors at KBR for 30 s.

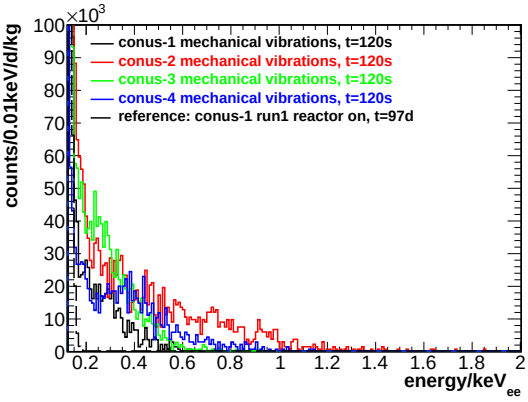

Figure 3.20: Events induced by knocking on the end of the end of the cryostat arm of the detectors at KBR for 30 s.

3.3.4 Cryocooler-induced noise

An in-depth investigation of the correlation of the noise to the cryocooler power was conducted. As dataset Conus-3 before and during the outage of Run2 in June 2019 was chosen as notable temperature changes have been observed during this time with respective changes in the cryocooler power (see Figure 3.22). It is assumed that the results are representative for the other detectors and runs. Additionally, at the 11A laboratory for Conus-5 deliberate changes in the diode temperature were induced to test the impact on noise peak.

Cryocooler-induced vibrations in Conus-3

The observed correlation between the noise integral and the environment temperature via the cryocooler power was discussed in Section 3.2.1. For Conus-3 Run2 the noise integral covers the energy range up to 0.23 keV_{ee}. By adapting this range, it is even possible to find an almost linear correlation for the energy range of [0.13,0.28] keV_{ee} to the cryocooler power as it is shown in Figure 3.22. Within this energy range, marked in Figure 3.21 for an exemplary measurement, the noise induced by the cryocooler dominates. At lower energies the other noise contributions of a HPGe spectrometer (see Section 1.4.4) start to contribute more and more and the linearity gets lost.

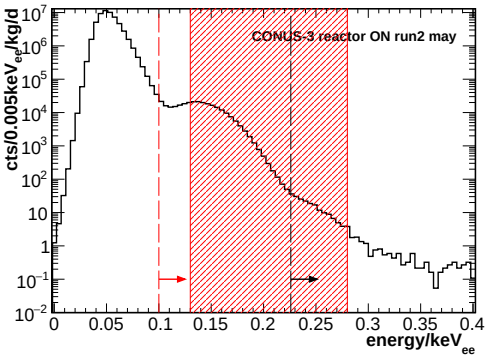

Figure 3.21: Noise peak of an exemplary Conus-3 measurement. The shaded red area marks the integral range compared to the cryocooler power in Figure 3.22. The black line corresponds to the energy cut threshold of the noise cut and the red line corresponds to the energy cut threshold used for Figure 3.23 to look for frequency lines induced by the cryocooler.

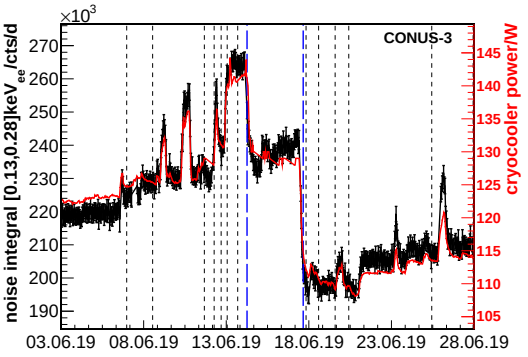

Figure 3.22: Almost linear correlation of noise within the integral range of [0.13,0.28] keV_{ee} during Run2 to cryocooler power. The dashed blue lines mark the introduction of the cold house and improved cold house. The black dashed lines correspond to the exemplary measurements analyzed for Figure 3.24.

The events within the energy range of the linear correlation to the cryocooler power were studied with the help of the TDD with an energy cut threshold of 0.1 keV. This cut energy is clearly below the threshold for the TDD cut (see Figure 3.21) and the separation between physical-like and noise events is not given any more. Figure 3.23 shows the linear TDDs of selected measurements, which contain lines of different frequencies. The frequency of the observed lines is the inverse of the time difference of the highest peak closest to zero. The smaller peaks at a multiple of the time difference are created if events in-between are not registered by the DAQ e.g. due to the muon veto. By further lowering the energy cut threshold of the TDD, the line features get lost in the continuum confirming that other noise contributions become more important at this point.

Two different kinds of frequency lines are observed: sharp lines with a constant frequency over time at 44 Hz and broad peaks at 2.2-3.2 Hz that shift with the changes in cryocooler power. The constant frequency over time is assigned to the compressor of the cryocooler. The temperature-dependent frequency was associated with the piston of the cryocooler. The piston is directly in touch with the volume of the working gas of the cooler, where the application to be cooled down is connected. The frequency range is typical for this kind of cryocoolers [56]. For the marked measurements in Figure 3.22 the piston frequency was determined. Figure 3.24 shows the correlation plotted with the cryocooler power including a linear fit.

All in all, it could be shown that the cryocooler creates noise. The part of events that contribute to the intermediate region in the TDD can be cut by the noise cut. However, when lowering the energy threshold, there are more and more cryocooler noise contributions within the time regime of the physical-like distribution, which cannot be removed without an undesired loss of physical events. Thus, the strategy to get rid of these events is to achieve a stable and low environmental temperature for the CONUS detectors. This provides the chance of a lower energy threshold for the future.

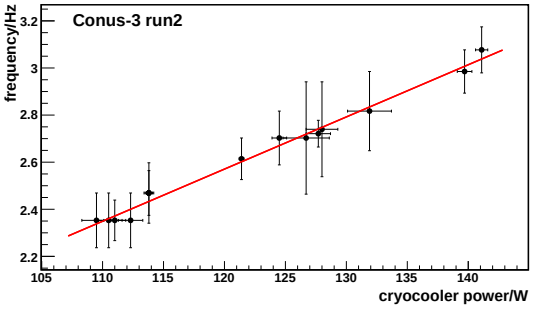

Figure 3.23: Linear TDD starting at 100 eV_{ee} of Conus-3 for different cryocooler power values. The frequencies induced by the cryocooler become visible.

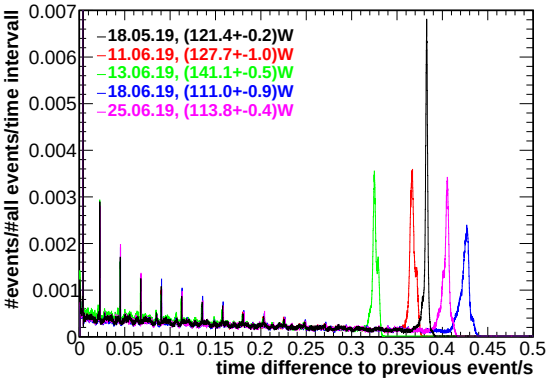

Figure 3.24: Correlation of the frequency of the lines observed in the TDD of the Ge noise and the cryocooler power for Conus-3 at KBR Run2.

Impact of diode temperature on noise in Conus-5

The measurement campaign at the 11A laboratory is introduced in Section 2.2.3. Among others the diode temperature was changed via the controller of the cryocooler, while the environment temperature was stabilized as good as possible. A lower diode temperature requires a higher cryocooler power and vice versa as depicted in Figure 2.17. For background measurements the impact on the noise peak was studied for a temperature variation between 73 K and 85 K (nominal diode tem-

perature 75 K). Figure 3.25 shows how part of the noise peak clearly increases for a lower diode temperature, which requires more power from the cooler. The measurements confirm that the noise induced by the cryocooler can be found in the energy range of the upper end of the noise peak as observed for Conus-3 at KBR. This can lead to a double structure of the noise peak. Any reduction of the diode temperature and the temperature of the cold electronics close by could potentially lower the other electronics noise contributions, but in the data collected this is overall subdued by the increased noise from the cryocooler. Just for the step from 76 K to 73 K a decrease in the noise for the colder temperature is observed.

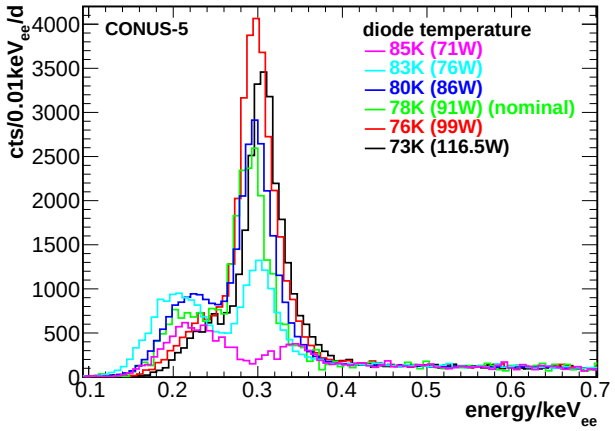

Figure 3.25: Impact of the increase of the cryocooler power on the noise peak. The cryocooler power increased due to the reduction of the diode temperature.

3.3.5 Special events and observations

Large spikes in the noise integral have been observed in the data at end of the outages (e.g. see Figure 3.26a and Figure 3.3). The TDD in Figure 3.26b (linear, starting from channel 0) shows that a range of frequencies at about 10 kHz can be assigned to the spikes in the noise integral. The distinct frequencies indicate mechanical vibrations as cause. Indeed, due to the point in time of their occurrence they can be assigned to the water pumps of the nuclear power plant. The KBR has four main cooling pumps. They transport the cooling water through the loop pipes from the reactor core to the steam generator and back. The pumps run with a frequency of 1500 turns/min. During their ramp up before the reactor is turned on, they pass through their resonance regime accompanied by strong vibrations and acoustic noise. The ramp up of the pumps also leads to a short break down of the power grid, which should be evened out by the UPS of the CONUS DAQ. The observed spikes in the Ge data can mostly be connected to the point in time when the pump closest to the CONUS experiment is started. The spikes last for about 3 min and afterwards the integral returns to the previous value, meaning that only

the traversing through the resonance regime is seen in the TDD and not the general running of the pumps. In one case, also the feedwater pump was seen in the noise data.

The pump-induced events are observed dominantly within the noise integral energy regime way below the analysis threshold. However, to be on the safe side the hours of data taking including the ramping up of the pumps are removed from the data sets.

Next to the spikes for two detectors during Run1 and the optimization phase afterwards a correlation between the noise integral and the thermal power of the reactor was observed. Figure 3.27 shows the data collected during the ramp on of the reactor after the mini outage in April 2019. The already discussed spikes from the main cooling pumps can be seen, but additionally, the noise integral follows closely the thermal power of the reactor. In this clearness, the correlation is only visible for a stable room temperature during a few short time periods of Run1. Furthermore, it was only observed for Conus-2 and Conus-3. For Run2 due to the changed DAQ settings it is not visible at all, but covered by other noise contributions. The observation is found to be related to a grounding loop in connection with the active muon veto. The muon veto rate is correlated to the thermal power due to the registered ^{16}N γ-rays created by fission neutrons in the cooling cycle of the reactor (see Section 3.1.2). Improvements on the grounding scheme are planned for the future.

The correlation is restrained to the energy range below 200 eV_{ee}, which is clearly below the analysis threshold (see Section 6.4) and has thus no impact on the CEνNS analysis.

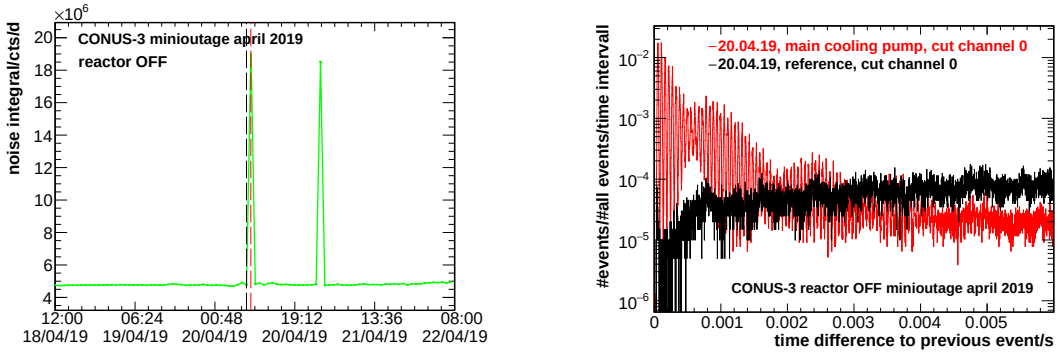

(a) Noise integral of Conus-3 during the mini outage in April 2019.

(b) TDD for time periods marked with red and black lines in (a).

Figure 3.26: Signature observed in the Ge data due to the ramp up of the main cooling pumps of loop 1 of KBR.

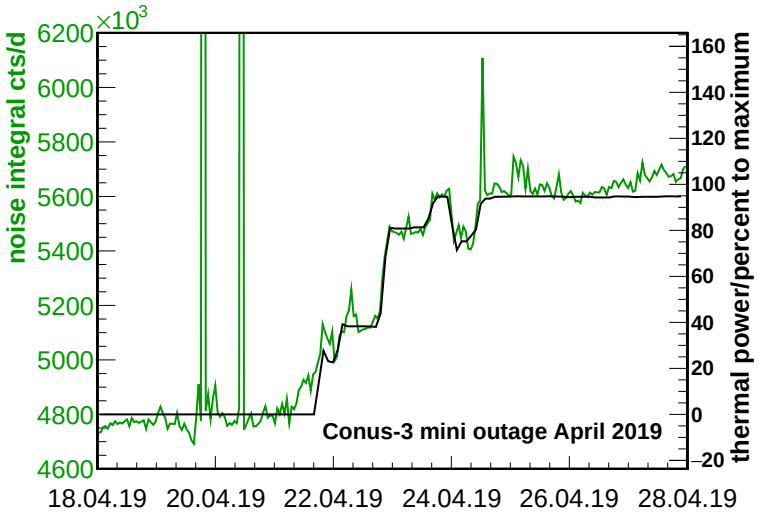

Figure 3.27: Correlation between the noise count rate observed in Conus-2 and Conus-3 to the thermal power of the reactor due to a grounding loop. The spikes are created during the ramp up of the main cooling pumps of KBR.

3.4 Summary on noise studies and cuts

A low and stable noise threshold is crucial for a detection of CEνNS. The DAQ and the noise of the CONUS detectors, especially the correlations to the environment, were studied in detail. It was found that the electrical cryocooling creates noise in the HPGe spectrometers. The performance of the cryocooler is correlated to the room temperature, which indirectly impacts the Ge noise in this way as well. At the nuclear power plant, the room temperature is not stable and varies by several degrees over time, especially during the reactor OFF time, where additional operations are going on at the reactor. Thus, for Run1 and Run2 the NTC cut had to be introduced and the data sets for the CEνNS analysis were restricted to time periods with approximately constant noise. Moreover, the TDD analysis was developed as tool to examine the time difference between the events. In this way, noise events from failures in the pile-up cut of the DAQ and from microphonics can be cut away with nearly no loss in live time. With the TDD analysis, it was also possible to extract frequencies from the noise, that could be connected to the cryocooler or the ramp up of the main cooling pump of KBR.

4 Reactor-correlated background

The short distance of the location of the CONUS experiment of ∼17 m to the reactor core guarantees an high neutrino flux. However, there might also be potential reactor-correlated background. Neutrons are especially problematic, as they can induce recoils comparable to CEνNS (see Section 1.6.2). But also reactor-correlated γ-ray background can lead to an instable count rate in the CONUS detectors. Therefore, dedicated measurement campaigns were carried out: in cooperation with the PTB the neutron background was evaluated in a Bonner Sphere Spectrometer (BSS) measurement before the setup of the CONUS experiment and the γ-ray background outside the shield was determined during Run1 with the CONRAD HPGe detector. By detecting γ-rays from neutron capture also information on the neutron background can be determined indirectly.

The content of this chapter is mostly published in [53].

In the following, first of all, the measurement devices (BSS NEMUS and HPGe spectrometer CONRAD) and the MC simulation required as support are described. Next, it is reported on the measurement campaigns at KBR, the data analysis and the outcome. Finally, the measured reactor-correlated neutron fluence rate inside A408 is propagated through the shield to show that inside the shield the background is negligible.

4.1 Description of measurement devices and MC for reactor-correlated background

4.1.1 Bonner Sphere Spectrometer NEMUS

The BSS for the neutron measurement campaign at KBR is described in [53]: "A Bonner sphere Spectrometer [62, 63] consists of a set of moderating spheres with different diameters and a thermal neutron sensor that is placed at the centre of each sphere. Each sphere plus thermal sensor combination has a different energy-dependent response to neutrons. The peak of the neutron response function shifts to higher neutron energies as the size of the moderator increases (the responses of the Bonner spheres used for the measurements at KBR are shown in Figure 4.1). It is usual practice to measure also with the thermal neutron sensor without a moderating sphere (i.e. the bare detector).

The measurements of the neutron background at KBR were carried out with the BSS NEMUS [64] of PTB. It consists of ten PE spheres with diameters[1] 3, 3.5,

[1] In this paper we use the convention of labeling each Bonner sphere by its diameter in inches,

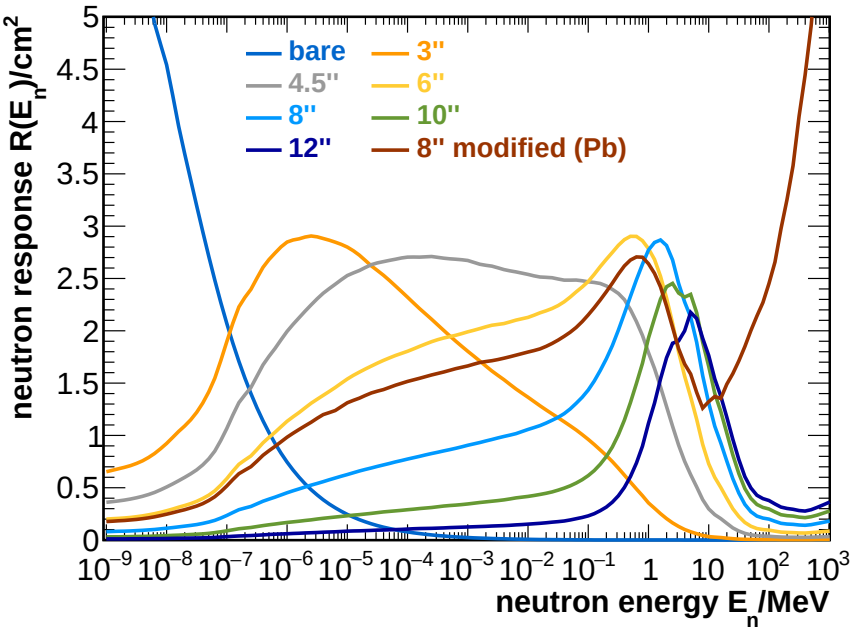

Figure 4.1: "Neutron response functions of the Bonner spheres used for the measurement. At thermal neutron energies $E_\mathrm{n} \sim 10^{-9}\,\mathrm{MeV}$ the response of the bare detector rises to $R(E_\mathrm{th}) = 6.2\,\mathrm{cm}^2$." Figure published in [53].

4, 4.5, 5, 6, 7, 8, 10 and 12". The set also contains a bare detector (diameter 3.2 cm = 1.26"), a Cd-covered detector, and four modified spheres with lead (Pb) and copper (Cu) shells. Thanks to the metal, embedded in the PE spheres, the response functions dramatically increase for neutron energies above $E_\mathrm{n} \sim 50\,\mathrm{MeV}$. The central thermal neutron sensors are spherical ^{3}He-filled proportional counters (type SP9, company Centronic Ltd. [65]), detecting the thermalized neutrons via the reaction:

$$\mathrm{n} + {}^3\mathrm{He} \rightarrow {}^3\mathrm{H} + \mathrm{p} + \mathrm{Q}, \text{ with } \mathrm{Q}{=}764\,\mathrm{keV}. \tag{4.1}$$

For the measurements carried out at KBR, we used SP9 counters with ^{3}He pressure of $\sim 200\,\mathrm{kPa}$. In order to cover the complete energy range of the expected neutron field and yet minimize the required measurement time, we chose a minimal subset of spheres, namely a bare counter, 3, 4.5, 6, 8, 10 and 12", plus the modified sphere of 8" diameter containing a Pb shell of 1" thickness. The inclusion of the modified sphere improves the spectrometric properties of the system at higher energies and allows to check for the presence of high-energy cosmic-ray induced neutrons ($E_\mathrm{n} \sim 100\,\mathrm{MeV}$ [66]), even though due to the massive concrete shield above the CONUS site their contribution is expected to be very small."

In general, the neutron count rates measured at KBR were very low, of the order of ~ 10 counts per hour and detector, or less. To determine the number of neutron-induced events in the pulse height spectra (PHS) recorded with the SP9 counter, the

1 in = 2.54 cm.

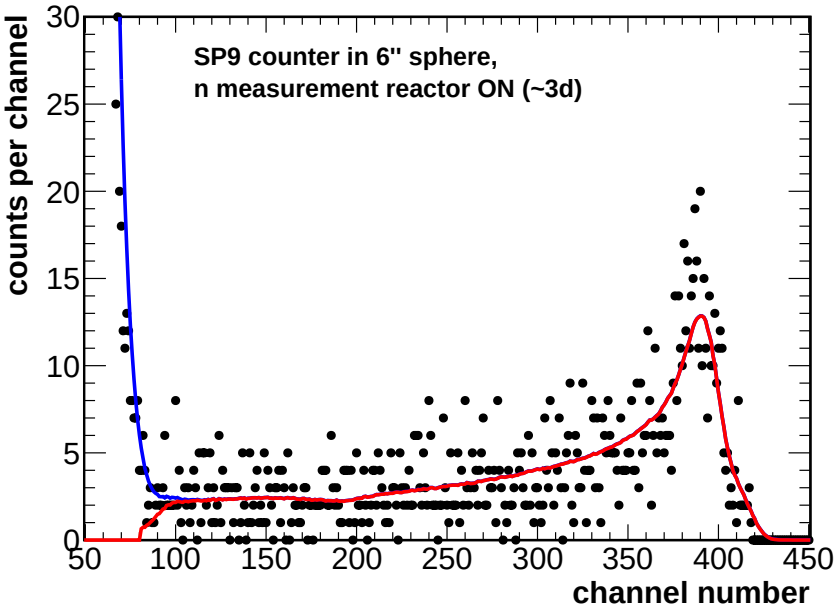

Figure 4.2: "Pulse height spectrum of a ^{3}He-filled proportional counter acquired after 3 days of measurement during the reactor ON period. The solid blue line depicts the total fit function including the background. The solid red line shows the fit function describing the neutron-induced component of the PHS." The peak at around channel 390 corresponds to the deposition of the full energy of 764 keV, freed in the reaction of thermal neutrons on ^{3}He (see equation (4.1)). Figure published in [53].

procedure, previously developed for measurements in underground laboratories [68, 69, 70], was applied. Figure 4.2 shows a typical PHS, together with the fit function to describe the PHS shape and to extract the neutron signal from background.

Specifications of the HPGe spectrometer CONRAD

With the help of HPGe spectrometers the γ ray background from the environment can be detected. This includes the natural radioactivy (see Section 1.5.1). In the energy range above 2.7 MeV$_{ee}$, also lines from neutron capture can be visible. If the cross section is known well enough, neutron fluence rates can be derived from (see Section 5.3.3 for neutron capture on Ge inside the shield).

The specifications of the HPGe spectrometer CONRAD used for the measurement campaign at KBR are described in [53]: "For background studies without shield at the reactor site the ultra-low background p-type coaxial HPGe detector CONRAD (m =2.2 kg), with the diode refurbished by Mirion Technologies, Canberra Olen [67], is employed within the CONUS experiment. It has been used furthermore for background studies inside the CONUS shield during the commissioning phase of the experiment at the MPIK underground laboratory. The large detector mass is

beneficial to especially detect high energetic γ-lines up to $\sim$11 MeV_{ee} as the detector also has a high geometric detection efficiency at these energies. To be allowed to set it up at KBR, the detector was upgraded with an electrical cryocooling system.

The detector has an active mass of (1.90±0.15) kg, which was determined as described in [30], [71], [52]. The thickness of the inactive layer at the diode surface has been evaluated from the ratio of the absorption of ^{241}Am γ-lines at different energies compared to a MC simulation and amounts to (2.5±0.1) mm. Moreover, to adjust to the measured line count rates from ^{60}Co measurements in different positions, the bore hole dimensions were adapted. All in all, 85% of the Ge crystal are active.

With the help of pulser scans over the whole energy range up to 11 MeV_{ee} it could be confirmed that the detection efficiency due to electronics is constant over the whole spectral range. Furthermore, the peak position has been found stable within 1 keV_{ee} over a period of 2 months. A small non-linearity within the energy scale has been discovered making it necessary to calibrate separately the two energy regions, where γ-lines have been observed (below 2700 keV_{ee} and above 4500 keV_{ee}), with two linear functions.“

inter-action	model	energy range	cross section
elastic	hElasticCHIPS	E1	GheishaElastic, ChipsNeutronElasticXS
	NeutronHPElastic	E2	”, ChipsNeutronElasticXS
			NeutronHPElasticXS
inelastic	BertiniCascade	E1	GheishaInelastic, Barashenkov-Glauber
	NeutronHPInelastic	E2	“, Barashenkov-Glauber,
			NeutronHPInelasticXS
capture	G4LCapture	E1	GheishaCaptureXS
	NeutronHPCapture	E2	”, NeutronHPCaptureXS
fission	G4LFission	E1	GheishaFissionXS
	NeutronHPFission	E2	“, NeutronHPFissionXS

Table 4.1: ”Geant4 MC models for neutron propagation and absorption.” The energy range E1 refers to 19.5MeV<E<10 TeV and E2 corresponds to <20MeV. Table published in [53].

4.1.2 Setup of MC simulation for reactor-correlated background

The setup of the MC simulation for the reactor-correlated background is described in [53]: ”The MC simulation framework MaGe [48], based on Geant4 (version Geant4.9.6p04) [49, 50] is applied to support the understanding and to complement the neutron measurements via an ab initio calculation. In a first step, the neutron propagation from the reactor core to room A408 is simulated as well as

the propagation of neutrons from the spent fuel assemblies inside the storage pool above room A408. In the second step, the neutrons arriving in A408 are propagated through the CONUS shield towards the HPGe diodes employing the measured neutron spectrum inside A408 as input. The relevant neutron interactions, models in Geant4 and the applied cross section data sets are listed in Table 4.1."

Nuclear power plant and room A408

The geometry of the nuclear power plant and the implementation in the MC is described in [53]: "From construction plans, the overall structure and main concrete parts of the reactor building were implemented using the information on the concrete. The reactor as starting point of the neutrons was modeled in detail, including all the 193 fuel assemblies. In the MC, these are approximated by four fuel rods instead of the 236 as in reality, each made up of Zirconium alloy cladding tubes filled with UO_2 pellets. The size of these fictive fuel rods was chosen so that the overall mass of a fuel assembly is reproduced correctly. The reactor core is filled with borated water with a B concentration of 500 ppm of enriched ^{10}B (1% boric acid, 99% water) as expected in the middle of a reactor cycle. A mean water temperature of 320°C and a pressure of 15.7 MPa have been assumed, leading to a water density of 0.687 g cm^{-3} [77]. The reactor core is contained inside the reactor pressure vessel (RPV) made from ferritic steel with a thickness of at least 25 cm. Eight openings can be found at the top of the reactor core for the loop pipes leading the water from the core to the steam generators, where they heat up the water in the secondary cycle, and afterwards return it to the core. For simplicity, only the two loop pipes on the side of room A408 have been implemented into the MC geometry. The reactor core is enclosed by the biological shield and heat insulation amounting to more than 2 m of concrete thickness in total. This is followed by an empty room around the biological shield with a width of several meters. In the geometry, not all details of this space were implemented, but special attention was paid to ensure this area to be closed to all sides to allow for backscattering of neutrons. Adjacent to this space behind a concrete wall of 1.3-1.45 m thickness, the room A408 can be found. The interior was modeled as in Figure 1.14. Also steel doors are included as well as the concrete walls of the neighboring room. Room A408 has a height of 2.8 m and the concrete ceiling, which is also the floor of the spent fuel storage pool, has a thickness of 1.85 m. The spent fuel storage pool and the cask loading pond are lined with several centimeters of steel and filled with 13.3 m of borated water. Between the active part of the spent fuel assemblies and the floor of the pool, there is a distance of about 80 cm. The amount of spent fuel assemblies within the storage pool is variable in the MC. The ^{10}B content is constantly 2300 ppm (5% boric acid, 95% water). The most important features of the implemented geometry including the location of the middle of the CONUS shield can be found in Figure 4.3."

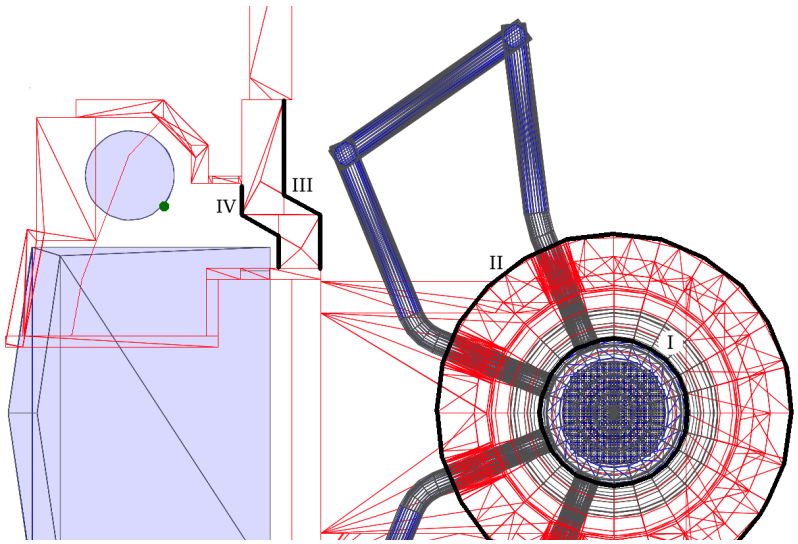

Figure 4.3: "Top view of implemented MC geometry including room A408, the overburden and the reactor core with surrounding. Concrete structures are displayed in red, the blue areas correspond to the spent fuel storage pool and the cask for shipment of spent fuel assemblies. For simplification only two of the four loop pipes are implemented (only selected volumes are displayed for a better overview)." The wired structures represent filled curved volumes. Figure published in [53].

Geometry of CONUS shield and HPGe detectors

The CONUS shield is described in Section 1.7.1. The detailed implementation in the MC is despicted in Figure 4.4. It is placed inside the geometry of room A408 (see Figure 4.3). The semi coaxial HPGe CONRAD without any shielding is also included in the MC. The Cu cryostat with cooling finger and the interior is modelled in the MC. The detector is placed inside the MC geometry close to the wall next to the space around the reactor core, where the data were collected during the measurement campaign (see Figure 1.14).

Input spectra and output for reactor neutron MC

The input spectra and output for the reactor neutron MC are described in [53]: "At a nuclear power plant, neutrons are created predominately inside the reactor core via fission and immediate evaporation from fission products. Over the whole cycle, more than 50% of the fissile material is made up of ^{235}U, while ^{238}U, ^{239}Pu and ^{241}Pu contribute as well [78]. The ^{235}U neutron fission spectrum according to a Watt distribution function is displayed as black line in Figure 4.14, with a mean neutron energy of 1.95 MeV [79]. As the neutron spectra of the main other isotopes undergoing fission such as ^{239}Pu are very similar, in MC simulation the ^{235}U fission spectrum is employed as initial spectrum for the neutrons. Most of these neutrons are moderated within the reactor core and induce fission again, fueling the chain reaction employed to create the power output of the reactor. However, about 10^{-4}

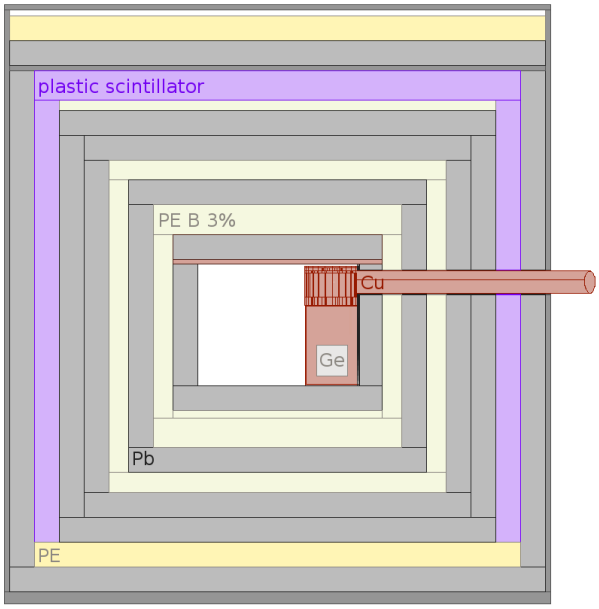

Figure 4.4: "Side view of the implementation of the CONUS shield geometry and exemplary one detector within. The HPGe diode is marked in gray inside the Cu cryostat. The shield is surrounded by a stainless steel cage assuring safety requirements (dark gray)." Figure published in [53].

of the neutrons will leave the reactor core before they either hit fissile material, are absorbed in the fuel assemblies' structures or are moderated enough to induce another fission (see Table 4.7). This is most likely to happen at the border of the reactor core, thus justifying to start neutrons only within the volumes of the UO_2 pellets of the first and second outer-most ring of fuel assemblies in the MC simulation (in total 104 of 193 fuel assemblies, see Fig. 5 in [53]). For the purpose of the propagation outwards from the reactor core, the ongoing fission reactions are not required and consume computation time, thus all fission products are killed immediately by the MC. Due to the huge decrease of the neutron flux along the way towards room A408, the MC simulation has been split into four steps where the spectrum of neutrons passing a certain geometric boundary was registered and used as a new input spectrum for the next part of the MC simulation (see Figure 4.3 for the single steps denoted with I-IV). In the end, the spectrum of the neutrons leaving the walls adjoined to the space around the reactor core is recorded. Moreover, the neutrons hitting a 6" diameter air sphere at about the location of the middle of the shield of the CONUS experiment are tracked to be compared to and to be used in the analysis of the BSS data. The device itself is not simulated, since the conversion to the measured PHS is carried out by the response functions as described in Section 4.1.1. Alternatively, to represent several spheres set up at the same time, the neutrons passing through a fictional horizontal air plate (size: 2 m×3.5 m) are accounted for. Furthermore, for the CONRAD detector measurements, the last step is repeated with this detector present inside room A408. All hits inside the HPGe detector are registered. The decreased charge collection efficiency outside the active volume is added in the post-processing.

Besides the reactor core, neutrons are also emitted by the spent fuel assemblies in the storage pool above the CONUS experiment. The majority of the neutrons

are emitted by actinides, especially by ^{244}Cm, while other isotopes only contribute to a few percent [80]. Thus the Watt distribution function for ^{244}Cm is used as initial spectrum. Assuming the storage pool is filled with the maximum number of fuel assemblies, neutrons were started from the volume of those 192 fuel assemblies located above room A408 and registered in the horizontal air plate described above."

Initial spectrum and output for the particle propagation through the CONUS shield

The initial spectrum and output for the particle propagation through the CONUS shield are described in [53]: "Assuming a homogeneous neutron flux inside A408, neutrons are started isotropically from a hemisphere (radius=1.4 m) spanning around the CONUS shield towards the floor. To take into account backscattering effects, the walls, ceiling and floor of room A408 are included in the simulated geometry (see Figure 4.3). The measured neutron spectrum in the exact location of the CONUS experiment is used as input for the neutron energy (see Figure 4.13). The neutrons are propagated through the CONUS shield. All neutrons arriving at the HPGe diodes are registered. Moreover, all energy depositions inside the HPGe volume are saved as well as the identity of the particles responsible for the energy deposition. No dead layer is assumed and the charge collection efficiency in the different sub-volumes of the HPGe diode is added in the post-processing. For the CONUS experiment the region of interest lies in the very low energy range of the spectrum (below 1 keV$_{ee}$) and thus in this simulation the secondary production cuts are lowered to 1.2 keV$_{ee}$ for γ-rays and 850 eV$_{ee}$ for electrons and positrons, increasing the computation time. This means that below these thresholds, the particles will not produce further secondary particles, but the whole remaining energy will be deposited directly in one location. For hadronic processes there is no such threshold, as also low energetic thermal neutrons can travel large distances by scattering.

Additionally to the neutron propagation simulation, also the measured γ-ray background inside A408 (see section 4.3) has been used as MC input. Mono-energetic γ-rays were started from the wall closest to the reactor core and the resulting spectrum inside the CONUS diodes was evaluated. All in all, more than 10^4 d in CPU time have been spent on the propagation of the neutrons through the reactor building geometry and the CONUS shield."

Validation of MC

The validation of the MC is described in [53]: "For a reliable MC result, it is important to validate the physics processes involved. In MaGe, for electromagnetic interactions this has been done among others for source measurements in [30] and [71] as well as [81], [82] and [83], for muon-induced interactions in [39]." More details on the muon-induced neutrons in the MC can be found in Section 5.3.

"For neutrons, however, there are in general much less validation campaigns available. The propagation of neutrons through shield materials have been examined

at the MPIK by carrying out ^{252}Cf source measurements within and in front of the CONUS shield and a similar shield of another HPGe spectrometer, GIOVE [30]. The correct propagation of the neutrons through the shield was confirmed" (see Chapter 7).

"An overall good agreement for the isotopes relevant here for the probability of the number of emitted γ-rays in neutron capture has been found (see table 4.2). Especially the relative branching ratio between the different γ-lines is in excellent agreement with the literature values. However, additional γ-lines occur in the de-excitation spectrum in the MC, that are not supposed to be created. This has to be corrected for by removing all MC events containing such γ-lines. "

neutron capture	energy [keV] [84]	br MC	br lit
^{54}Fe(n,γ)^{55}Fe	9297.80±1.00	abs. 49.9(*)	abs. 56.8±4.9 [85]
^{56}Fe(n,γ)^{57}Fe	7645.58±0.10	abs. 23.6	abs. 29.00±4.94 [84]
	7631.18±0.10	rel. 86.22(*)	rel. 86.21±19.94 [84]
	7278.82±0.90	rel. 20.70	rel. 20.69±4.58 [84]
^{63}Cu(n,γ)^{64}Cu	7916.26±0.08	abs. 28.74(*)	abs. 33.10±0.60 [84]
	7638.00±0.09	rel. 48.94	rel. 48.99±1.50 [84]
	7307.31±0.06	rel. 27.07	rel. 27.18±0.61 [84]
	7253.05±0.06	rel. 12.54	rel. 12.48±0.27 [84]

Table 4.2: "The branching ratio (br) in Geant4 of the main γ-lines from neutron capture on the isotopes relevant at KBR are compared with literature values. For the lines marked with (*) the MC generates two neighbouring γ-lines close in energy. Out of those one was recognized to be not physical and was neglected. The absolute branching ratio refers to the ratio of emitted γ-rays per neutron capture (given for strongest line), while the relative branching ratio is given in respect to the strongest emitted line." Table published in [53].

4.2 Bonner sphere measurements at KBR

4.2.1 Measurement campaigns with Bonner spheres

The measurement campaigns with the Bonner spheres are described in [53]: "Three data sets were collected during the measurement campaigns at KBR, summarized in Table 4.3. The data set DS-3 (reactor ON) was acquired with the arrangement shown in Figure 4.5, where the Bonner spheres were placed one after another in the central position of the CONUS site (position 1 in Figure 1.14). A bare detector, placed 1.8 m away (position 2 in Figure 1.14) from the measurement position, was used as a monitor of the thermal neutron fluence rate during the entire campaign. The thermal neutron counters within the Bonner spheres were at a height of 51 cm above ground, identical to the vertical centre of the future CONUS setup.

data set	reactor state	time period	Bonner spheres arrangement
DS-1	ON	08.12.16–04.01.17	all spheres used simultaneously
DS-2	OFF	09.02.–26.02.17	all spheres used simultaneously
DS-3	ON	31.08.–04.10.17	spheres swapped at central position

Table 4.3: "Overview of data sets collected during the measurement campaigns with the NEMUS spectrometer in room A408 at KBR." Table published in [53].

Due to the low neutron count rates, the measurement times amounted to 3–4 d per Bonner sphere, with the exception of the 12" sphere. The measurement time with this sphere was set to 9 d, because an extremely low count rate was expected.

The data sets DS-2 (reactor OFF) and DS-1 (reactor ON) were acquired with the Bonner spheres distributed around the central position of the future CONUS setup, as shown in Figure 4.6. The distance between the individual spheres was chosen to be 1 m or more, in order to reduce the effect of neutron scattering from one sphere to another. With the reactor OFF, the neutron count rates were of the order of ~ 1 count per hour. Therefore, given the time slot available during the KBR reactor outage, it was necessary to measure with all the spheres simultaneously. DS-1 was the first test run inside the room A408 before the actual measurement campaign and will only be used as a reference to illustrate the spatial inhomogeneity of the neutron field inside A408 and the correlation to the thermal power.

As the reactor power varies with time due to load follow operation, it was necessary to normalize the neutron counts from the individual BSS measurements of DS-3 to a quantity related to the reactor power. For this, the thermal power P_{KBR} in units of [GW], with the time resolution of 1 h is used. The evaluation of the thermal power with its uncertainty is described in [53]. Based on the start and stop times of the BSS measurements, we were able to calculate the thermal energy output E_{KBR} in units of [GW h] corresponding to a given neutron measurement."

4.2.2 Measurement results with BSS

The measurement results with the BSS at KBR are described in [53]:

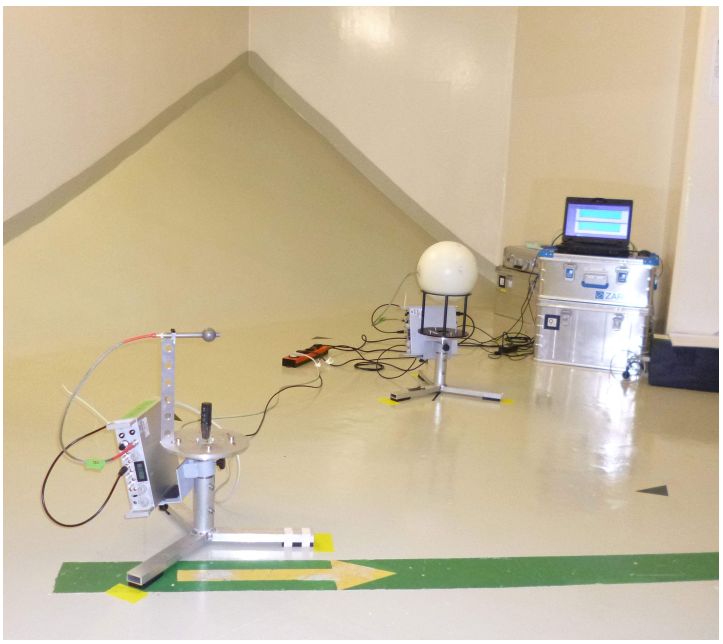

Figure 4.5: "Experimental arrangement used for the DS-3 measurement (reactor ON). The bare detector in the foreground was used as a monitor of the thermal neutron fluence rate. The Bonner sphere in the back was placed in the central CONUS position. Other Bonner spheres were placed on this position one after another." Figure published in [53].

Neutron energy distribution inside A408 during reactor ON time

"Figure 4.7 shows the data from the reactor ON measurement (DS-3). The neutron counts in the individual Bonner spheres were normalised as follows:

$$N_{p,i}^{(1)} = \frac{C_i^{(1)}}{E_{\mathrm{KBR},\,i}}\,, \quad E_{\mathrm{KBR},\,i} = \sum_j P_{\mathrm{KBR},\,j} \cdot t_j\,, \tag{4.2}$$

where i denotes a given Bonner sphere from the subset used at KBR, $C_i^{(1)}$ is the number of neutron-induced counts determined via fits of the PHS and $N_{p,i}^{(1)}$ is the number of counts normalized to the thermal energy output $E_{\mathrm{KBR},\,i}$ of the KBR reactor during the measurement with the Bonner sphere i.

Averaging the neutron counts $C_i^{(1)}$ per measurement times t_i, the neutron count rate in the bare counter amounted to ∼66 counts per hour. In the 12" sphere, the average neutron count rate was as low as ∼2 counts per hour. Correspondingly, the relative uncertainty of the normalized neutron counts $N_i^{(1)}$ ranged from 2.6% for the bare counters (3-4 d measurement time) up to 5.8% for the 12" sphere (∼9 d measurement time). The values include the systematic uncertainty of the corresponding thermal energy output $E_{\mathrm{KBR},\,i}$ of 2.3%.

The additional bare SP9 detector used as a neutron monitor for DS-3 allowed us to check the consistency of the data. The monitor readings were also analyzed

Figure 4.6: "Experimental arrangement used for the DS-1 (reactor ON) and DS-2 measurement (reactor OFF). The Bonner spheres were distributed around the central position of the future CONUS setup. The bare detector is located at the central position." Figure published in [53].

using the fitting procedure of low-level neutron data mentioned in Section 4.1.1. The number of neutron-induced counts in the monitor per GW h of thermal energy output was determined (weighted mean) as $f_{\mathrm{mon}/E_{\mathrm{KBR}}} = (16.00 \pm 0.15)\,\mathrm{GW\,h^{-1}}$, averaged over the whole DS-3 data set. During all DS-3 measurements, this ratio was constant within ±3%. The same holds for the readings of the Bonner spheres: the two normalizations, either using the thermal energy output according to Eq. 4.2, or the monitor readings as a scaling factor, agreed to within ±3%.

To analyze the data, we used Bayesian parameter estimation [86]. The shape of the result of the propagation of neutrons from the reactor core (see plot of $\Phi_{MC}(E_n)$ in Figure 4.13) indicates that the neutron energy spectrum extends up to a few hundred keV. This is consistent with previous Bonner sphere measurements at reactors behind shielding [87, 88]. For the reactor ON and OFF measurements, there is an additional component in the form of a peak at around 1 MeV, caused by neutrons induced by muons in the reactor building. Therefore, we introduced a parameterized model (similar to the one in [89]), which consists of a thermal peak, an intermediate region, which is flat in the lethargy representation ($d\Phi/d\log(E_n)$) up to a few hundred keV followed by a smooth drop, and a peak above. The fluence and mean energy of this peak corresponds to the peak at around 1 MeV in the neutron energy spectrum measured under reactor OFF conditions (see Figure 4.9). We considered two models, one allowing for a slope in the intermediate region and one setting this slope to zero (corresponding to a $1/E_{\mathrm{n}}$ behavior). The complete model contained three free parameters: the magnitude of the thermal peak and the magnitude and

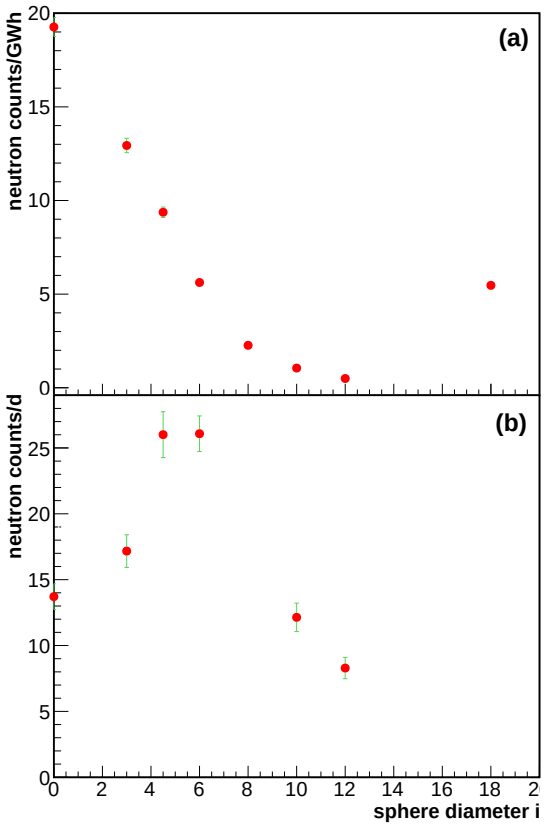

Figure 4.7: "Neutron counts in the individual Bonner spheres, as a function of the sphere diameter i in inch. The data point at $i = 0$ corresponds to the bare detector. The data point at $i = 18$ corresponds to the 8" modified sphere. The error bars are in some cases smaller than the size of the symbols. **(a)** Data from DS-3 (reactor ON), normalized to 1 GW h of the reactor energy output E_{KBR} according to Eq. 4.2. **(b)** Data from DS-2 (reactor OFF), normalized as counts per 24 h." Figure published in [53].

slope of the intermediate region. The analysis was done using the software package WinBUGS [90].

It was checked, whether the BSS data indicate the presence of high-energy cosmic-ray induced neutrons ($E_{\mathrm{n}} \sim 100\,\mathrm{MeV}$). This was done by considering, in addition to the model described above, a second, preliminary model, which included a high-energy peak at this energy. The analysis showed that the BSS data favors the models not including such neutrons. This is expected due to the massive concrete shielding of the reactor building, surrounding the CONUS experimental site. From the BSS data alone it could not be determined whether there is a slope of the intermediate region significantly different from zero. The detailed MC calculations clearly indicate a non-zero slope (cf. Section 4.2.3). Therefore we decided to use here the results of the non-zero slope model only. The resulting neutron energy distribution $\Phi^{(1)}(E_{\mathrm{n}})$ is plotted in Figure 4.8 in terms of the lethargy representation. The integral quantity of the neutron fluence normalized to the KBR thermal energy output $\Phi^{(1)}$, derived from the analysis, is stated in Table 4.4 for the individual E_{n} regions of the neutron energy distribution. The overall shape of the solution $\Phi^{(1)}(E_{\mathrm{n}})$ agrees reasonably well with the MC predictions, as discussed in Section 4.2.3.

The solution indicates a highly thermalized neutron field, as about 80% of the total fluence $\Phi^{(1)}$ is due to thermal neutrons of energies $E_{\mathrm{n}} \leq 0.4\,\mathrm{eV}$. Therefore, the count rate observed in a given Bonner sphere has a non-negligible contribution

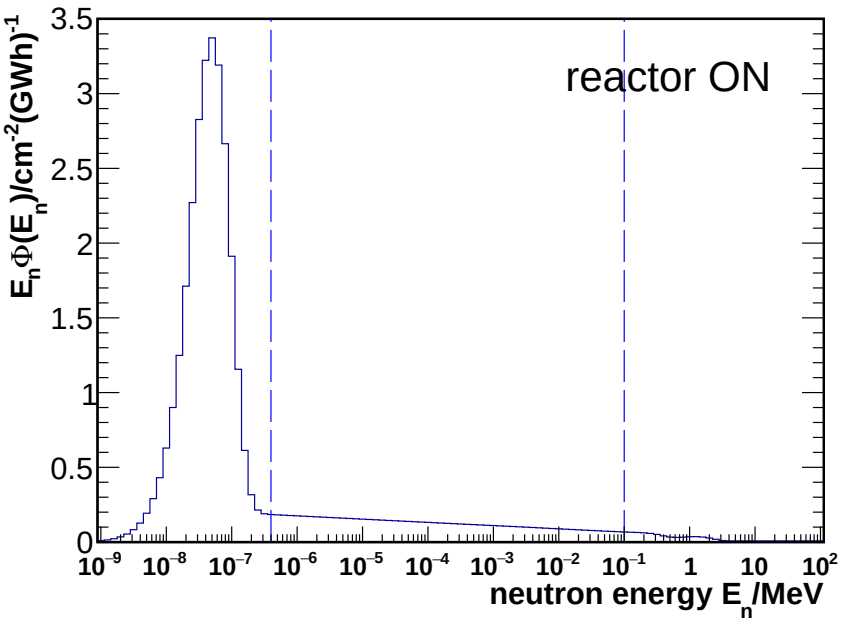

Figure 4.8: "Solution of the neutron energy distribution $\Phi^{(1)}(E_\mathrm{n})$ resulting from the analysis of the DS-3 data normalized to the energy emitted by the reactor." Figure published in [53].

from thermal neutrons, even for large Bonner spheres (for example, 30–50% of the measured counts in the 8–12" spheres are due to thermal neutrons[2]). This is one reason why the fast component has a relatively large uncertainty of the order of 30%.

The bare counter used for monitoring was running permanently during the data collection of DS-3. For a few days, at the central position of the CONUS experiment also a bare counter was placed. Comparing the neutron count rates measured by both counters and correcting them for slightly different sensitivities, a relative difference of (18.8±2.3)% was found. This demonstrates inhomogeneities in the thermal field inside room A408 and underlines the importance to characterize the neutron spectrum at the exact location, where an experiment is planned."

Neutron energy distribution inside A408 during reactor OFF time

"The data from the reactor OFF measurement (DS-2) are depicted in Figure 4.7. In this case the normalization was done simply as

$$N_i^{(2)} = \frac{C_i^{(2)}}{t_i}\,, \tag{4.3}$$

[2]These portions were determined via folding the solution of $\Phi^{(1)}(E_\mathrm{n})$ with the response functions of the individual spheres, and then comparing the expected counts in the region of thermal neutron energies to the total expected counts.

E_n region	$\Phi^{(1)}$ $[\mathrm{cm}^{-2}\,(\mathrm{GW\,h})^{-1}]$
thermal	6.42 ± 0.41
intermediate	1.56 ± 0.21
fast	0.15 ± 0.05
total	8.13 ± 0.32

Table 4.4: "Neutron fluence $\Phi^{(1)}$ derived from the analysis of the DS-3 measurement, and normalized to the KBR thermal energy output of 1 GW h. The uncertainties are stated as standard uncertainties (1 standard deviation). The E_n regions are defined as follows: thermal $[1.0 \times 10^{-9}, 4.0 \times 10^{-7}]$ MeV; intermediate $[4.0 \times 10^{-7}, 0.1]$ MeV; fast [0.1, 19.6] MeV." Table published in [53].

E_n region	$\Phi^{(2)}$ $[\mathrm{cm}^{-2}\,\mathrm{d}^{-1}]$
thermal	4.47 ± 0.67
intermediate	4.19 ± 1.15
fast	6.35 ± 0.96
total	15.03 ± 0.99

Table 4.5: "Neutron fluence rate $\Phi^{(2)}$ derived from the analysis of the DS-2 measurement (reactor OFF), normalized per 24 h. The uncertainties are stated as standard uncertainties (1 standard deviation). The definition of the E_n regions is identical to Table 4.4." Table published in [53].

where $C_i^{(2)}$ is the number of neutron-induced counts determined via fits of the PHS and $t_i \equiv t$ is the measurement time which was common for all Bonner spheres and amounted to 18 d. The measurement uncertainties of the neutron count rates $N_i^{(2)}$ were in the range of 5–10%. The highest count rates compared among the spheres were not observed in the bare detector, but instead in the 4.5 and 6" spheres, indicating that the neutron field was no longer dominated by thermal neutrons during reactor OFF time.

For the analysis, we used a parameterized model consisting of a thermal peak, a peak at $E_\mathrm{n} \sim 1$ MeV, and an intermediate region, which is flat in the lethargy representation. Thus, the complete model contained five free parameters: the magnitude of the thermal peak, the magnitude and the slope of the intermediate region, and the magnitude and mean energy of the $E_\mathrm{n} \sim 1$ MeV peak. The solution $\Phi^{(2)}(E_\mathrm{n})$ is plotted in Figure 4.9. The integral quantity of the neutron fluence rate $\Phi^{(2)}$ derived from the analysis is listed in Table 7. The largest contribution ($\sim$40%) to the total neutron fluence is now in the fast neutron region $E_\mathrm{n} = [0.1, 19.6]$ MeV."

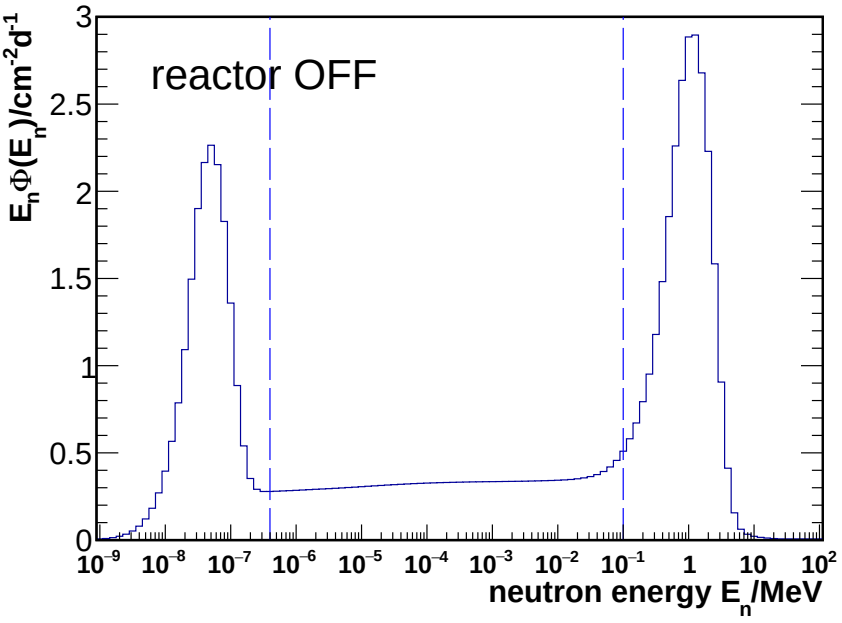

Figure 4.9: "Solution of the neutron energy distribution $\Phi^{(2)}(E_\mathrm{n})$ resulting from the analysis of the DS-2 data normalized to the measurement time." Figure published in [53].

Correlation to thermal reactor power

"The mean value of the neutron count rate per day is compared to the mean thermal power per day as well as the neutron flux measured with the ex-core instrumentation in Figure 4.10 and Figure 4.11 for both measurement campaigns. Both curves are normalized to their mean value during the campaign. Overall, for both cases a correlation between the neutron fluence rate in A408 and the data from the reactor was observed. DS-3 took place immediately after the refueling of the reactor in 2017 and the reactor power was nearly constant except for the increase in the middle of the month. The thermal power data as estimated from the energy balance in the secondary circuit and the ex-core instrumentation are in very good agreement. Both match the course of the thermal neutron fluence in room A408 as well. During DS-1 at the end of the previous reactor cycle were more variations in the thermal power. This is due to less demand for electricity during holiday seasons and competing renewable energy production.

Small discrepancies are observed between the total thermal power determination as compared to the ex-core instrumentation measuring neutrons at the top and bottom of the core. They occur because the maximum of the thermal power has moved up or down along the z-axis of the reactor. The effect is displayed in Figure 4.12 where exemplary for a few days the relative contribution of the 32 parcels to the overall reactor power is displayed using the data from the reactor core simulation described in [53]. The dashed lines correspond to the days in Figure 4.10 when the

bottom instrumentation gives values above the total thermal power from heat. For those days the maximum of the power density is at the bottom of the reactor core. The shift of the maximum is initiated, because at the beginning of a reactor cycle the thermal power is distributed nearly symmetrically with a maximum slightly below the middle of the core where the leakage of neutrons is small. At the end of the cycle the fuel in the middle of the reactor-core is mostly burned up leading to the maximum moving outwards. Additionally, when reducing the thermal power due to external constraints, the control rods are inserted into the core from the top causing a shift of the maximum to the bottom. Strong maxima on top of the core can also be produced at the end of a cycle because - if there is a negative temperature gradient within the core - more reactivity is freed in the upper half.

From the comparison to the thermal neutron fluence in A408, it was found that the best agreement could be achieved for the counters on top of the reactor core independent of the location of the maximum of the thermal power along the z axis. The neutrons seem to be more likely to escape the reactor core at the top, where the openings for the loop pipes of the cooling cycle are located.

All in all, the thermal fluence in A408 was observed to be fully correlated to the reactor power and reactor core instrumentation meaning the reactor is by far the dominant source of thermal neutrons inside the room. Consequently, the reactor monitoring data can be used to predict the thermal neutron fluence inside room A408 at any given time.“

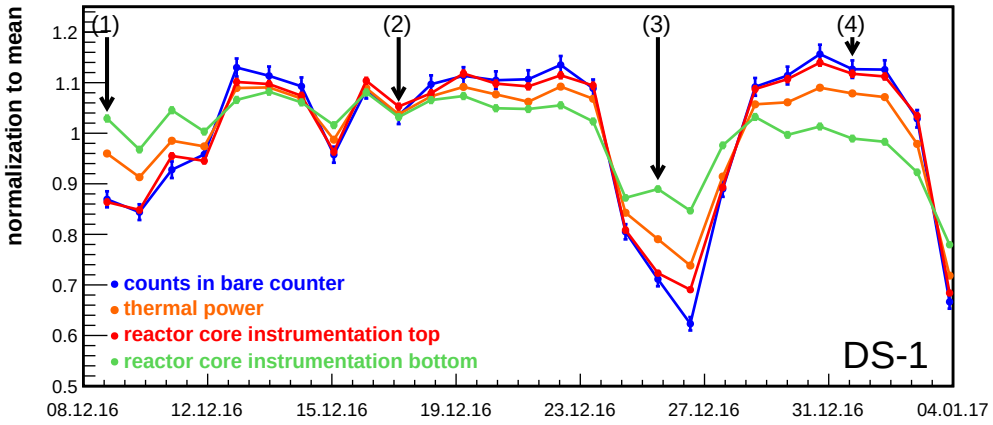

Figure 4.10: “DS-1 at the end of a reactor cycle; counts in bare BSS compared to the thermal power and the core instrumentation. The arrows indicate the days, where the thermal power distribution along the z axis is shown in Figure 4.12.“ Figure published in [53].

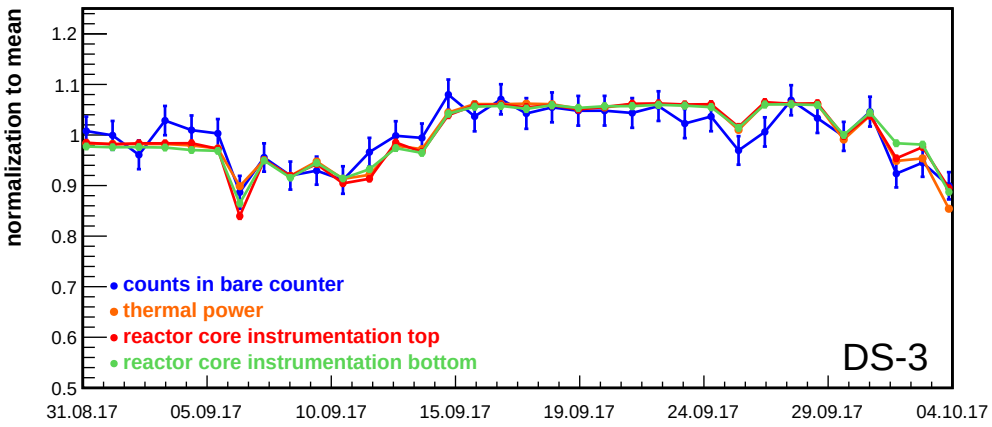

Figure 4.11: "DS-3 at the beginning of a reactor cycle; counts in bare BSS compared to the thermal power and the core instrumentation." Figure published in [53].

Comparison of neutron fluences ON-OFF

"The comparison of the neutron fluences during reactor ON and OFF time is important to disentangle the thermal power correlated neutron contribution from other steady-state neutron sources.

Due to the different normalisations, it is necessary to make some simplifying assumptions. In a rough approximation we consider the KBR reactor as a source of neutrons, and the neutron fluence $\Phi^{(1)}$ as being normalised to a unit of "activity" of this source. In Section 4.2.2 a linear correlation between the reactor power and the thermal neutron fluence within A408 was observed, justifying this approach.

For the estimate we used the time-resolved thermal power data P_{KBR} already applied in the DS-3 measurement. The mean duty cycle of the KBR reactor during the overall DS-3 measurement (total measurement time of 34 d) amounted to 88.9%, i.e. the mean thermal power of the reactor was

$$P_{\mathrm{KBR}}^{\text{DS-3 mean}} = (0.89 \pm 0.02) \cdot P_{\mathrm{KBR}}^{\max} = (3.47 \pm 0.08)\,\mathrm{GW}\,. \tag{4.4}$$

Multiplying the values of $\Phi^{(1)}$ by the following factor of a mean thermal energy output

$$E_{\mathrm{KBR}}^{\text{DS-3 mean}} = 3.47\,\mathrm{GW} \cdot 24\,\mathrm{h} = 83.3\,\mathrm{GW\,h}\,, \tag{4.5}$$

we obtain the mean neutron fluence $\Phi_{\mathrm{mean}}^{(1)}$ which would hypothetically be present in A408 if the reactor would be running at the constant level of $P_{\mathrm{KBR}}^{\text{DS-3 mean}}$ over the period of one day. Both quantities $\Phi_{\mathrm{mean}}^{(1)}$ and $\Phi^{(2)}$ have units of $[\mathrm{cm}^{-2}\ \mathrm{d}^{-1}]$ and we define the "ON − OFF" difference,

$$\Phi_{\mathrm{mean}}^{(\mathrm{res})}(E_{\mathrm{n}}) = \Phi_{\mathrm{mean}}^{(1)}(E_{\mathrm{n}}) - \Phi^{(2)}(E_{\mathrm{n}})\,, \tag{4.6}$$

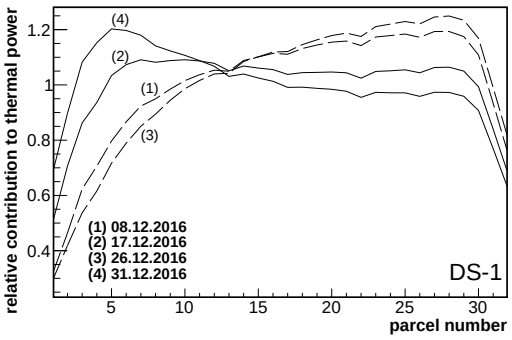

Figure 4.12: "Relative distribution of thermal power along the z-axis during DS-1 from core simulation data for selected days over the one month period. The dashed lines (1) and (3) correspond to the days, where the bottom core instrumentation in Figure 4.10 gives the highest contribution different to (2) and (4)." Figure published in [53].

E_n region	$\Phi^{(1)}_\mathrm{mean}$	$\Phi^{(2)}$	$\Phi^{(\mathrm{res})}_\mathrm{mean}$
thermal	534.8 ± 34.4	4.47 ± 0.67	530.3 ± 34.4
intermediate	130.0 ± 17.2	4.19 ± 1.15	125.8 ± 17.3
fast	12.3 ± 4.1	6.35 ± 0.96	6.0 ± 4.2
total	677.2 ± 27.0	15.03 ± 0.99	662.2 ± 27.1

Table 4.6: "Comparison of neutron fluence rates $\Phi^{(1)}_\mathrm{mean}$ (reactor ON at constant mean level for time duration of 24 h) and $\Phi^{(2)}$ (reactor OFF), and their difference $\Phi^{(\mathrm{res})}_\mathrm{mean}$. All quantities are stated in units of [$\mathrm{cm}^{-2}\ \mathrm{d}^{-1}$]. The uncertainties are stated as standard uncertainties (1 standard deviation). The definition of the E_n regions is identical to the one used in Table 4.4." Table published in [53].

as the residual neutron fluence $\Phi^{(\mathrm{res})}_\mathrm{mean}$, caused solely by the fission neutrons from the reactor core.

The comparison of $\Phi^{(1)}_\mathrm{mean}$ and $\Phi^{(2)}$ is summarized in Table 4.6. The uncertainties of $\Phi^{(\mathrm{res})}_\mathrm{mean}$ in the individual energy regions were obtained by propagating the statistical uncertainties of $\Phi^{(1)}_\mathrm{mean}$ and $\Phi^{(2)}$. In the thermal and intermediate regions, the absolute values of $\Phi^{(2)}$ amount to a tiny fraction of $\Phi^{(1)}_\mathrm{mean}$ values, therefore $\Phi^{(\mathrm{res})}_\mathrm{mean}$ retains the characteristics of a highly thermalized neutron field. For the fast neutron component, the residual neutron fluence rate is $(6.0 \pm 4.2)\,\mathrm{cm}^{-2}\mathrm{d}^{-1}$, which is compatible with zero within the uncertainties.

To estimate the residual neutron fluence for any given reactor power, the results in Table 4.6 have to be divided by the mean thermal power from Eq. 4.4 and scaled with the respective thermal power. This was done for the maximum thermal power in Table 4.10.

The neutron energy distribution $\Phi^{(\mathrm{res})}_\mathrm{mean}(E_\mathrm{n})$ is shown in the lethargy representation in Figure 4.13. It is plotted together with the neutron energy distribution from the

MC outcome $\Phi_{\mathrm{MC}}(E_{\mathrm{n}})$ which describes the neutrons arriving on the outside of room A408 from the KBR reactor core. The MC output is discussed in detail in the next section. The distribution $\Phi_{\mathrm{MC}}(E_{\mathrm{n}})$ was scaled in such a way that the integral of the fluences in the thermal region $E_{\mathrm{n}} = [1.0 \times 10^{-9}, 4.0 \times 10^{-7}]$ MeV match.“

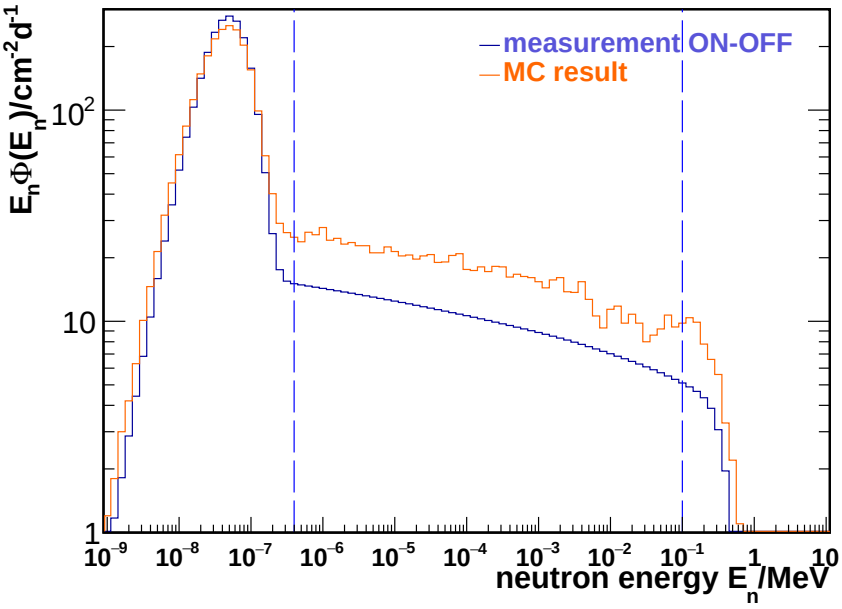

Figure 4.13: “Neutron energy distributions of the residual fluence $\Phi^{(\mathrm{res})}_{\mathrm{mean}}(E_{\mathrm{n}})$, calculated via Eq. 4.6 from the experimental BSS data analysis, and the calculated fluence $\Phi_{\mathrm{MC}}(E_{\mathrm{n}})$ based on MC simulations. The distribution $\Phi_{\mathrm{MC}}(E_{\mathrm{n}})$ was scaled to match the integral fluence of $\Phi^{(\mathrm{res})}_{\mathrm{mean}}$ in the thermal neutron region. The vertical dotted lines indicate the limits of the individual E_{n} regions, as defined in Table 4.4.“ Figure published in [53].

4.2.3 Results from MC at KBR

The results from the MC at KBR are described in [53]:

Propagation from reactor core to A408

“In the MC simulation, the propagation of neutrons from the reactor core is split into four steps as indicated in Figure 4.3. Before leaving the reactor core, most of the fission neutrons are moderated and absorbed inside the reactor fuel, fuel rod claddings and borated water (see Figure 4.14, blue spectrum). In the MC, absorption by fission fragments is not taken into account. Only remnants of fast neutrons can reach the inside of the RPV wall (marked as (I) in Figure 4.3). The shape of the spectrum is dominated by the neutron absorption cross sections of light nuclei like oxygen (O) or B, which can be observed in Figure 4.14(b) with a linear

y-axis. There are no longer neutrons above 17 MeV and about 10% of the neutrons are in the thermal energy regime. The thermal distribution is shifted towards higher energy with respect to the thermal distribution at room temperature as the mean temperature inside the RPV is at about 320 °C. The overall fluence of neutrons from the outer fuel assembly ring hitting the RPV wall is reduced by a factor of $1.4{\cdot}10^{-4}$, while for the second outer ring it is $1{\cdot}10^{-5}$, as these neutrons have to pass the additional layer of fuel assemblies where they can be absorbed or induce fission. The order of magnitude difference justifies the approach to only start neutrons from the outer volumes of the reactor core. Most neutrons arrive at the RPV wall on the level of the reactor core. Nearly no neutrons reach the area about 1 m above or below the extension of the core (see Fig. 4 in [53]).

Next, the neutrons go through the steel of the RPV and several layers of concrete to the outside of the biological shield (marked as (II) in Figure 4.3). This leads to a partly thermalization of the spectrum with about 70% of the fluence inside the thermal peak. Also, the maximum neutron energy is lowered to ∼2.5 MeV and the overall fluence is suppressed by an additional factor of $6.5{\cdot}10^{-6}$ (see Figure 4.14, red spectrum). Many neutrons scatter back and forth between the different concrete layers of the biological shield, where they are thermalized and absorbed before they can leave the shield.

Starting from the outside of the biological shield, only the neutrons arriving at the outside walls of A408 (walls split into 3 plates) are of interest (location marked as (III) in Figure 4.3). A reduction of $9{\cdot}10^{-3}$ is expected from simple solid angle considerations, which is the suppression factor observed in the MC. The shape of the spectrum is slightly different due to the reflection of neutrons on the ceiling (see Figure 4.14, orange). About 72% of the total fluence can be found inside the thermal peak already similar to the spectrum expected inside room A408.

In the last step, the neutrons are propagated through the wall of A408 interfacing the area around the biological shield. The neutrons leaving the wall on the other side (the wall is split into 3 plates) are registered as well as those arriving inside an air plate and a sphere inside the room (marked as (IV) in Figure 4.3). The last concrete wall leads to a complete thermalization of the spectrum (see Figure 4.14, green spectrum). The MC predicts a complete thermalized spectrum, while from the BSS measurement a thermal neutron fluence contribution of at least 80% is expected, but also the neutron spectrum goes up to a few hundred keV even though with large uncertainties. Potentially, this discrepancy originates in the limited knowledge on the geometry and exact concrete composition of the wall. Thus, instead of the MC spectrum inside the room, the spectrum of neutrons hitting the outer wall was used to support the BSS analysis (see Section 4.2.2) and compared to the measured spectrum in Figure 4.13 achieving a good agreement.

The neutron fluence is reduced by a factor of 10^{-8} traveling through the outside wall of A408. Due to the already highly thermalized spectrum outside the room, a large fraction of neutrons is captured inside the wall, which is exploited in the measurement with the HPGe spectrometer CONRAD without shield (cf. Section 4.3). Reducing the hydrogen content in the MC inside the concrete by a factor of

location	area [m^2]	suppress. factor to previous	max. neutron energy
reactor core	42.2 (cylinder)	1	>20 MeV
inner wall of RPV (I)	62 (cylinder)	$1.6{\cdot}10^{-4}$	16.2 MeV
outside wall bio. shield (II)	355.2 (cylinder)	$6.5{\cdot}10^{-6}$	2.5 MeV
outside wall A408 (III)	18.4 (3 plates)	$9{\cdot}10^{-3}$	1 MeV
inside wall A408 (IV)	10.2 (3 plates)	$4{\cdot}10^{-8}$	0.17 eV
total	1	$3.6{\cdot}10^{-20}$	

Table 4.7: "Supression of neutron fluence rate during propagation from reactor core to A408 in the MC corresponding to the respective surfaces." Table published in [53].

two increases the number of observed neutrons leaving the wall by a factor of 4 with the spectrum still completely thermalized. This shows the relevance of knowing this number precisely.

All suppression factors are summarized in Table 4.7. In the MC an overall reduction of $3.6{\cdot}10^{-20}$ for neutrons entering through the wall of A408 with an area of $10\,m^2$ is obtained, making it possible to access room A408 at any time even when the reactor is operational at full thermal power.

A significant amount of neutrons hitting the wall several times, scattering back inside the room, are observed. Comparing the total number of neutrons entering through the adjoined wall to the space around the biological shield, about 10% more neutrons leave the inclined middle piece of the wall than the straight wall pieces."

Normalization of MC

"To normalize the MC simulation, the number of neutrons per fission is required. The usable energy released per fission by the four main fission isotopes (^{235}U, ^{239}Pu, ^{238}U and ^{241}Pu) weighted with the respective fission fractions (see Table 4.8) can be used to determine the number of fissions required to achieve a certain thermal power output. The fission fractions have been evaluated as mean value from a wide range of similar reactors in various states of the reactor cycle. The given uncertainty corresponds to the standard deviation of the mean value. Depending on the isotope, about 2.5 neutrons are released per fission (see Table 4.8). This leads to a total number of free neutrons for the maximum thermal reactor power of $(3.1 \pm 0.1) \cdot 10^{20}\,s^{-1}(3.9\,GW)^{-1}$ which will be applied as normalization for the MC. For a reactor at the point of criticality, one neutron per fission will induce the next step in the fission chain, while the others are thermalized and absorbed in the materials of the reactor core with a small fraction leaving the reactor core. The MC follows the propagation of these neutrons going outwards from the core. The approximation in the MC that only neutrons from the outer ring of fuel assemblies and the second outer ring have a chance to escape the reactor core as described in

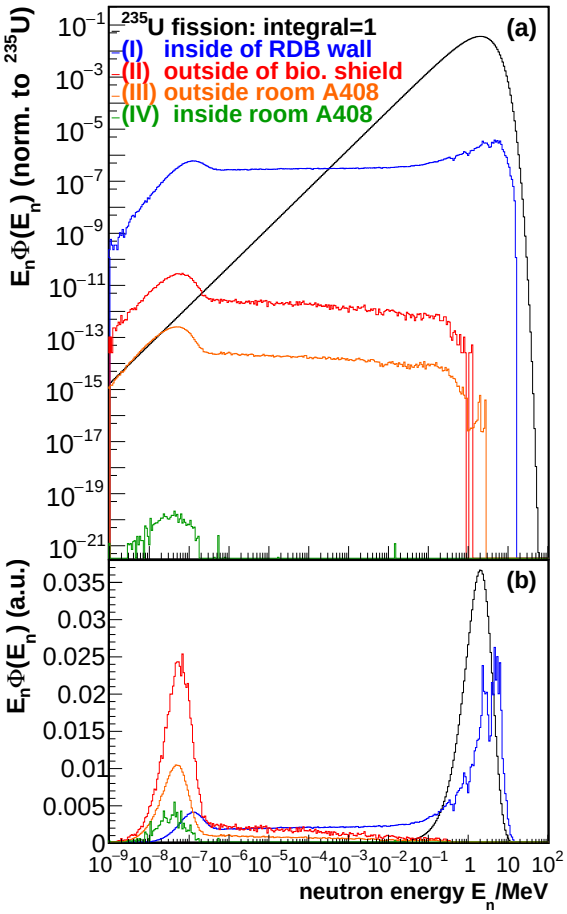

Figure 4.14: "(a) MC neutron spectra of the propagation from the reactor core to room A408, the fission spectrum is normalized to 1 (b) same spectra as in (a) with a linear y-axis scaled arbitrarily to make spectral features visible." Figure published in [53].

Section 4.1.2 has to be accounted for in the normalization. From the core simulation data with a high spatial resolution, as described in [53], it was found that consistently during the collection of DS-1 and DS-3 (16.3±0.1)% of the thermal power is created by the outer ring of fuel assemblies and (30.4±0.1)% by the second outer ring. The higher neutron flux for the second outer ring is partially compensated by their higher absorption probability, such that the contribution is a factor of 7 below the one of the outer ring.

By scaling the MC in this way, for 40 years of operation with maximum thermal power $(3.7\pm0.1)\cdot10^{18}\,\mathrm{cm}^{-2}$ neutrons are expected to hit the wall of the RPV. This number is consistent with the maximum level of $10^{19}\,\mathrm{cm}^{-2}$ for this range of time found in the safety guidelines for German PWRs [91].

For the total thermal fluence rate inside room A408, $(16\pm1)\,\mathrm{cm}^{-2}\mathrm{d}^{-1}(3.9\,\mathrm{GW})^{-1}$ are expected in the MC. Comparing directly with the result for the thermal fluence rate for the reactor ON minus reactor OFF subtraction obtained from the BSS measurements (see Table 4.10), the MC lies below the measurement by a factor of 38. This has to be contrasted with the suppression of the initial neutron flux from the reactor core by more than 20 orders of magnitude and the overall complexity of the simulation. Unknown factors in the geometry of the extended void space around

the biological shield as well as of the exact composition of the steel enforced concrete further handicap a more exact reproduction of the measurement result.

As in the MC only thermal neutrons arrive inside A408, for the comparison to the measured spectrum instead the spectrum in front of A408 at the outside wall has been used (see Figure 4.13). In the MC, only 72% of the neutrons are found inside the thermal peak as the last step of the thermalization is still missing. The agreement of the overall shape of the distributions is very good, keeping in mind again the complexity of the MC simulations. This confirms that the remaining neutrons at energies above 1 MeV seen in the reactor ON spectrum in Figure 4.8 are indeed not thermal power correlated and correctly removed by subtracting the reactor OFF spectrum. These neutrons are presumably created by muons passing through the concrete of the building. By generating neutrons in the MC inside the spent fuel assemblies in the cooling pond, it was confirmed that this is not the origin of the fast neutrons. In fact, from the neutrons of the spent fuel assemblies, no contribution to the fluence inside room A408 is expected.“ In total, more than 10^{12} neutrons were started from the spent fuel assemblies located in the area above the room. The neutrons were started from two different single fuel assemblies: one closest at the row at the side closest to the CONUS experimental site and one in the middle of the area of the spend fuel storage pond above A408. MC simulations were carried out with only the single fuel element inside the pool, where the neutrons were started from, and with all places inside the pool filled. In the MC, the steel holder of the fuel assemblies were not included in the MC. The number of neutrons emitted from the spent fuel elements depends on the time spend in the reactor core during reactor ON time, the time after discharge from the reactor core and the enrichment. According to [92] and [93] for the typical maximum time spent in the reactor core and an enrichment of 4% directly after discharge conservatively estimated 10^9 n per s and per assembly are expected. In none of the simulations any neutrons were registered inside A408. For the neutrons hitting the bottom of the pool already a suppression of $\sim 10^7$ was observed for all simulated configurations. Combining all combinations and assuming in total 133 spent fuel elements directly above the room, for the target plate of 7 m^2 (see Section 4.1.2), were the neutrons were tagged inside A408, an upper limit on the neutron fluence rate can be set:

$$n^{total}_{\text{spent fuel}} < 1\,\text{cm}^{-2}\text{d}^{-1} \tag{4.7}$$

The upper limit is clearly below the neutron fluence rate measured with the BSS during reactor OFF time in Table 4.6.

4.3 CONRAD detector at KBR

4.3.1 Measurement campaign with CONRAD detector

The measurement campaign with the CONRAD detector is described in [53]: ”The CONRAD HPGe spectrometer was deployed inside room A408 from 16.08.2018 to

fission isotope	energy release per fission [MeV] [94]	fission fraction [95],[96]	number of neutrons per fission [78]
^{235}U	202.36±0.26	56.8±3.2	2.432±0.004
^{239}Pu	211.12±0.34	30.2±0.4	2.875±0.006
^{238}U	205.99±0.52	7.6±2.4	2.937±0.007
^{241}Pu	214.26±0.33	5.4±0.7	2.829±0.011

Table 4.8: "Reactor physics input for the calculation of the neutrons produced in the reactor core that is used for the normalization of the MC simulation." Table published in [53].

12.10.2018 during reactor ON time. The detector was mounted onto an Aluminum (Al) plate and was placed next to the wall closest to the reactor core as can be seen in Figure 4.15 and Figure 1.14, position 3. This results into a mean distance of 13.5 m to the reactor core for this detector.

Within ∼51 d of live time, the energy spectrum in the range from 0.4 to 11.6 MeV_{ee} were recorded continuously except during a few hours of ^{228}Th calibrations and pulser measurements carried out about every 10 d. In this way, the stability of the energy scale and detection efficiency was checked. Small fluctuations within a standard deviation of about 1 keV_{ee} in the large energy range were observed. Thus, for each time interval between ^{228}Th calibrations the measurement itself with the clearly present background lines was used for the energy calibration. The calibrated spectra were combined afterwards.

The acquired data set was split into daily and hourly time bins to compare to the thermal power available as described in [53]."

4.3.2 Measurement results with the CONRAD detector

The measurement results with the CONRAD detector are described in [53]:

HPGe energy spectrum acquired with reactor ON

"In the measurement with the non-shielded HPGe spectrometer CONRAD inside A408, the contributions from natural radioactivity dominate the spectrum below 2.7 MeV_{ee}. The spectrum is displayed in Figure 4.16. Contributions from the Th and U decay chains are visible as expected from the activity measurements of the concrete samples from the floor [53]; ^{137}Cs, ^{40}K and ^{60}Co were found as well. By doing a HPGe screening measurement of the Al board and the plastic holder below the detector, it could be confirmed that except for ^{40}K, all measured contaminations originate from the interior of A408 and have not been brought inside with the detector setup.

Above 2.7 MeV_{ee}, thermal power correlated contributions dominate. The strongest γ-lines in Figure 4.17 are created from the decay of the short-lived ^{16}N with a half-life of 7.13 s [98]. The isotope is produced predominantly in (n,p) reactions on

Figure 4.15: "CONRAD detector at room A408 of KBR. The Cu cryostat with the HPGe diode has been placed near the closest wall to the reactor core." Figure published in [53].

^{16}O in the water of the primary cooling cycle. For this activation process neutron energies higher than 10 MeV are required [97]. The neutrons within the RPV have the highest contribution within this range (described in Section 4.2.3). Thus, most of the longer living ^{16}N ions will be produced there and transported to the outside with the flowing cooling water. The closest distance of the CONRAD detector to the loop pipes amounts to 3.8 m. Not only the decay lines, but also single and double escape peaks (SEP and DEP) from this isotope were observed, where one or both of the γ-rays from e^+e^- pair production within the HPGe diode leave the detector.

While below the main lines of ^{16}N, there is no chance to see other isotopes, at higher energies several γ-lines from neutron capture were identified [84]. Predominately, γ-lines from neutron capture on Fe are seen created in the reinforced concrete wall. Moreover, lines from neutron capture on Cu can be found, which are created by the capture of thermal neutrons inside A408 in the Cu of the detector cryostat.

All identified thermal power correlated γ-lines are listed in Table 4.9 together with the literature values from [84] and [98]. The count rates were determined by a counting method except for the double peak structure of ^{57}Fe at 7631 keV and 7646 keV, which were fitted with two gaussian functions. In the same energy range at 7638 keV, a line from ^{64}Cu is expected, but overlaid by the Fe lines. To disentangle the two contributions, the count rate from the Cu γ-line has been calculated from the count rate of a clearly visible line from the same isotope at higher energies, which was corrected for by the relative branching ratio of the line and the detection efficiency due to the detector geometry derived from the MC. The result was subtracted from

the count rate evaluated for the double peak structure.

For the CONUS experiment, 25 cm of Pb are used to shield against natural radioactivity. The total absorption cross section of Pb is approximately constant from 2 to 10 MeV [99], meaning all γ-rays inside the room are expected to be successfully suppressed by the shield. This is examined in detail in Section 4.4.4."

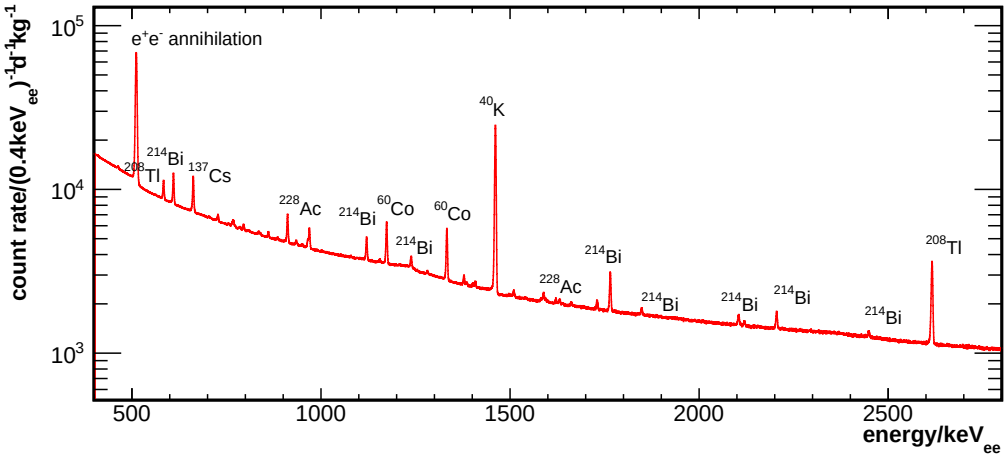

Figure 4.16: "Spectrum of CONRAD detector inside A408 without any shield below 2700 keV. It is dominated by natural radioactivity in the surrounding. For the strongest lines except the 511 keV line the decaying isotope is given." Figure published in [53].

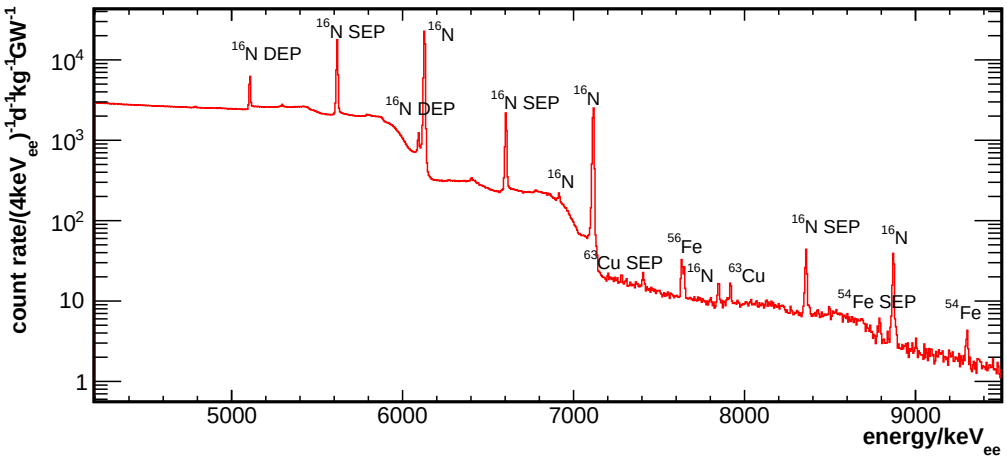

Figure 4.17: "Spectrum of CONRAD detector inside A408 without any shield above 2700 keV dominated by thermal power correlated contributions. The spectrum is normalized to the mean reactor power. For the strongest lines the decaying isotope is given." Figure published in [53].

energy [keV$_{ee}$]	energy lit [keV]	count rate [cts/d/GW]	count rate MC [cts/d/GW]
^{53}Fe(n,γ)^{54}Fe			
8790.9±0.6	8786.8±1.0 SEP	9.6±0.6	(2)9±1
9301.0±0.6	9297.8±1.0 (br 100%)	11.3±0.5	(2)11±1
^{56}Fe(n,γ)^{57}Fe			
7280.0±0.7	7278.82±0.09 (br 20.69%)	11.5±1.1	(2)13±1
7632.8±0.1	7631.2±0.1 (br 100%)	137±4*	(2)111±1
7646.6±0.1	7645.6±0.1 (br 86.21%)	double peak	
^{63}Cu(n,γ)^{64}Cu			
7406.2±0.3	7405.26±0.08 SEP	27.2±1.3	(1)37±3
n. d.	7638.00±0.09 (br 48.94%)	15.7±1.6*	(1)19±2
7916.9±0.2	7916.26±0.08 (br 100%)	29.7±1.0	(1)37±3
^{16}O(n,p)^{16}N			
5106.96±0.01	5106.63±0.04 DEP	12612±146	
5617.51±0.01	5617.63±0.04 SEP	49972±575	
6093.28±0.04	6093.15±0.14 DEP	1605±21	
6128.14±0.01	6128.63±0.04 (br 67.0%)	85086±979	
6604.36±0.01	6604.15±0.14 SEP	7163±83	
6915.0±0.4	6915.5±0.6 (br 0.038%)	155±4	
7115.37±0.02	7115.15±0.14 (br 4.9%)	10097±116	
7848.4±0.3	7847.3±0.5 DEP	31±1	
8359.7±0.1	8358.3±0.5 SEP	135±2	
8870.8±0.1	8869.3±0.5 (br 0.076%)	152±2	

Table 4.9: "Identified thermal power correlated γ-lines in the spectrum of the non-shielded CONRAD detector inside A408 during reactor ON time. The energy and branching ratios (br) from literature are given as well. The count rates marked with * were measured as one-peak structure and the single count rates were extracted as described in the text. (1) and (2) mark the different ways the MC is scaled. For (1), the measured thermal neutron fluence inside A408 has been used ((597±39) cm^{-2}d^{-1} for 3.9 GW) and thus the uncertainties of the BSS measurement result dominate the uncertainties. For (2), the MC has been scaled with the number of neutrons expected to arrive at the outside wall from the ab initio calculation starting at the reactor core ((477±20)·10^6 d^{-1} for 3.9 GW). Here, only statistic uncertainties and uncertainties on the literature values are included." Table published in [53].

Correlation to thermal power for the CONRAD detector measurements

"Due to the high statistics in the 6.1 MeV line of ^{16}N the thermal power reactor data was compared to the peak count rate for an hourly binning. The result in Figure 4.18 shows a strong correlation, meaning that with the help of a HPGe spectrometer in the distance of 13.5 m to the reactor core, the current thermal power can be precisely predicted for the specific case of A408, comparable to the thermal neutron fluence (cf. Section 4.2.2). Similar correlations limited by statistics are observed for the γ-lines from neutron capture."

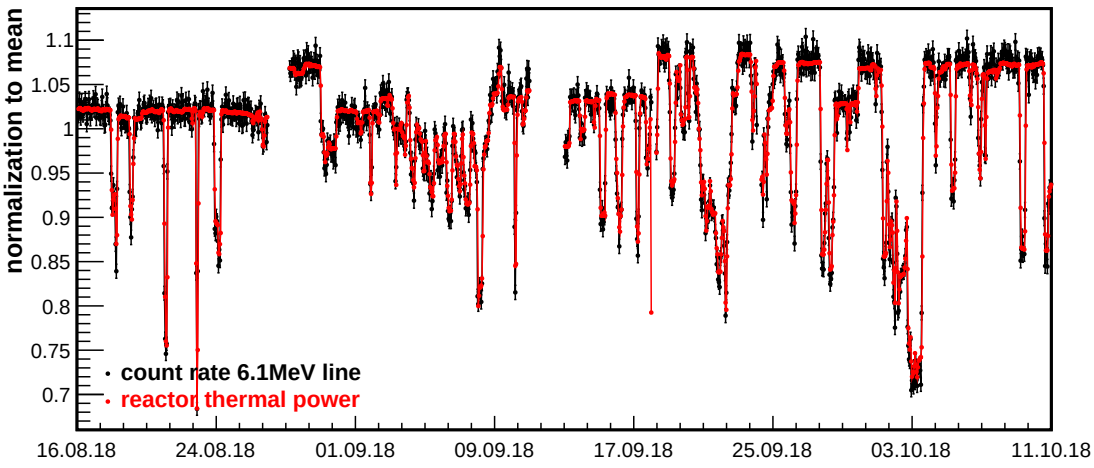

Figure 4.18: "Correlation of thermal power to the count rate in the 6.1 MeV γ-line of ^{16}N. The curve is interrupted if no thermal power data is available and during the calibration of the detector." Figure published in [53].

4.3.3 Comparison of the CONRAD detector measurements with MC

"The neutron capture inside the walls of A408 and the Cu cryostat can be reproduced in the MC. In the last step of the propagation of neutrons from the reactor core to A408, the detector is placed at the wall closest to the reactor core as in reality. For the direct approach simulating the neutrons passing the outside wall of A408, available statistics for the signals inside the HPGe diode are too low to get a reliable result.

Instead, two different sets of simulations were run. (1) First of all, thermal neutrons were started from the inside wall of A408 and normalized to the thermal power correlated thermal neutron fluence determined with the BSS (see Table 4.10). For the Cu lines, an excellent agreement has been found, while for the Fe lines this MC configuration predicts a count rate of at least a factor of 5 lower. This means that

most of the neutron capture reactions responsible for this signal already occur, while the neutrons travel through the walls before they enter room A408.

(2) Simulating neutrons passing through the outside wall of A408, the spectrum of the γ-rays leaving the respective wall to the inside of the room were registered. In a second step, mono-energetic γ-rays were started from this wall to determine the geometric detection efficiency of CONRAD. It lies at the order of 10^{-5} to 10^{-4} at the range of 7 to 10 MeV_{ee}. The outcome of the simulation was scaled with the normalization from Section 4.2.3 and the reduction of the neutron fluence in step 1 to 3 from the propagation from the reactor core in Table 4.7. Next, it has been added up with the results of (1) to take into account neutrons being captured within room A408 and not before entering it. All in all, for the neutron capture on ^{54}Fe and ^{56}Fe the same order of magnitude for the count rates have been found as in the measurement (see Table 4.9). Especially, the agreement between MC and measured data is better than observed for the neutron fluence as stated in Section 4.2.3. This seems to indicate that especially the last step of the propagation through the wall predominately contributes to the lack of neutrons inside A408 expected in the MC."

4.4 Expected impact of neutron-induced background signals on CONUS data

The expected impact of the neutron-induced background signals on the CONUS data is described in [53]:

4.4.1 Reactor-induced neutrons at CONUS diodes

"Using the measured thermal power correlated neutron spectrum from Section 4.2.2, neutrons are propagated through the CONUS shield. The neutrons arriving at the diodes as well as the induced energy depositions in the HPGe diode are registered. All results are normalized to the maximum reactor power of 3.9 GW. The main uncertainties originate from the uncertainty on the initial spectrum. The results in this Section are given exemplary for C1.

In Figure 4.19 the neutron fluence rate through the diode surface is displayed and Table 4.10 summarizes the rates in various energy ranges. Registering only neutrons entering the diode for the first time reduces the fluence by 16% showing that the backscattering of neutrons around the diode cannot be neglected, especially in the intermediate and thermal energy region. The energy spectrum of these backscattered neutrons is plotted in Figure 4.19 as well.

Less than 10% of the neutrons at the diode have energies larger than 100 keV, while the maximum neutron energy lies clearly below 1 MeV. Those fast neutrons are the remnants of the fast neutrons started outside the shield, which is illustrated in Figure 4.20. In this Figure, the projection on the y-axis is the spectrum of the neutrons arriving at the diode, while the projection on the x-axis corresponds to the part of input spectrum of the MC, where the neutrons did indeed reach the diode.

Further, it shows that most of the intermediate or thermal neutrons at the diode are created in the thermalisation of these fast neutrons within the shield, while the contribution of neutrons with thermal or intermediate energies outside the shield is nearly negligible. The amount of inelastic neutron scattering processes inside the shield creating more than one neutron is also insignificant. There is a small fraction of neutrons at the diode at intermediate or fast energies that have been induced by thermal neutrons outside the shield. These are the entries in Figure 4.20 above the 45° diagonal. In the capture of thermal neutrons, highly energetic γ-rays with energies up to 10 MeV can be released from the absorbing nuclei. Those can create fast neutrons by photonuclear reactions with heavy elements such as Pb. This has been confirmed by starting 8 MeV γ-rays in the MC simulation at the innermost Pb layer and observing the neutrons arriving at the diode.

All in all, the CONUS shield proves to be highly effective to shield against the reactor neutron induced fluence inside A408 by reducing the overall fluence by a factor of $3{\cdot}10^{-6}$. The thermal neutrons from outside the shield are completely absorbed."

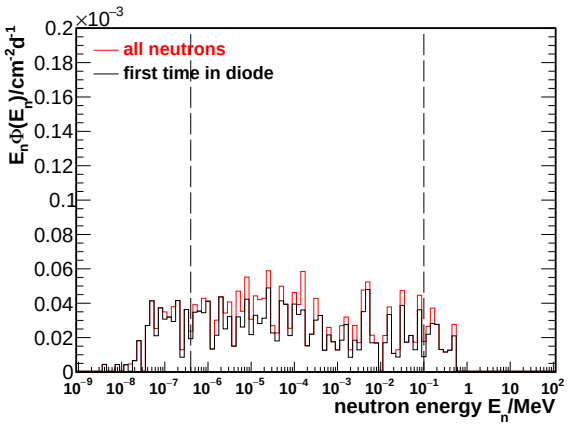

Figure 4.19: "Spectrum of reactor-neutron induced neutrons at one CONUS HPGe diode predicted by MC." Figure published in [53].

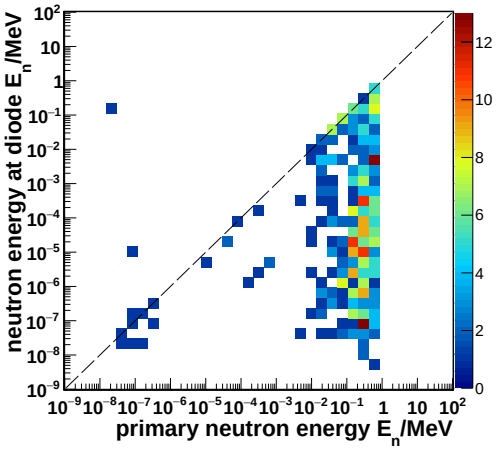

Figure 4.20: "Neutrons arriving at one CONUS HPGe diode plotted against the energy of the primary neutrons. Dashed line at 45° for orientation." Figure published in [53].

4.4.2 Expected signal in p-type HPGe detectors

"The neutrons at the diode with energies from the spectrum of Figure 4.19 interact with Ge by neutron capture (mostly thermal neutrons), elastic scattering and inelastic scattering (mostly high energetic neutrons). In elastic and inelastic scattering processes recoils of Ge atoms can occur." (see also Section 1.6.2)

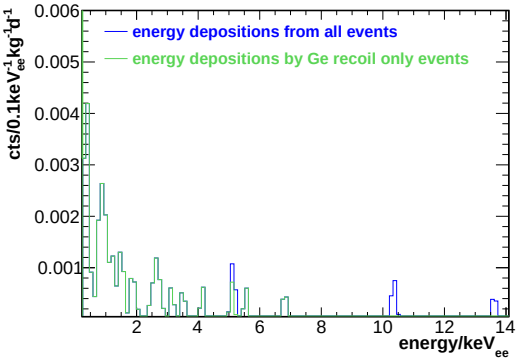

Figure 4.21: "Expected MC spectrum within an HPGe diode from reactor neutrons at low energies. The outcome of the MC has been adapted to the detector response. Moreover, the spectrum of events consisting of only Ge recoils is displayed." Figure published in [53].

E_n region	n outside shield [cm^{-2}d^{-1}]	n arriving at diode [cm^{-2}d^{-1}]	first n [cm^{-2}d^{-1}]
thermal	597±39	$(0.39\pm0.04)\cdot10^{-3}$	$(0.36\pm0.04)\cdot10^{-3}$
intermediate	142±19	$(1.67\pm0.01)\cdot10^{-3}$	$(1.38\pm0.01)\cdot10^{-3}$
fast	7±5	$(0.17\pm0.03)\cdot10^{-3}$	$(0.14\pm0.03)\cdot10^{-3}$
total	745±30	$(2.24\pm0.10)\cdot10^{-3}$	$(1.89\pm0.10)\cdot10^{-3}$

Table 4.10: "Measured reactor neutron induced fluence rate outside the shield compared to the neutron fluence rate at the surface of one CONUS HPGe diode inside the shield from MC for maximum thermal power of the reactor. The measured neutron spectrum inside A408 has been used as input for the simulation. The definition of the E_n regions is identical to Table 4.4." Table published in [53].

Detector response

"To determine the expected energy spectrum in the detector, the MC output has to be adapted to the true detector response.

The MC does not take into account that the energy deposition by a recoiling nucleus is not fully converted into ionization energy. This material-dependent loss is described by the quenching effect. It is included in the post-processing of the MC by correcting the energy deposition of recoils using the Lindhard theory with the fit parameters including the adiabatic correction from the measurement in [6]. The energy loss parameter k [6] is set to 0.2 for a conservative approach in the estimation of a background contribution.

Moreover, using the parameters described in Section 2.2.5, in the post-processing of the MC the transition layer and dead layer are included as well as the efficiency loss towards the detection threshold. Finally, as there is no electronic response in the

energy keV_{ee}	MC $[kg^{-1}d^{-1}]$	measurement $[kg^{-1}d^{-1}]$
$[0.3, 0.6]$	0.006 ± 0.002	12 ± 1
$[0.6, 11]$	0.025 ± 0.005	148 ± 2
$[11, 400]$	0.15 ± 0.03	716 ± 16

Table 4.11: "Expected count rate by reactor neutrons inside the CONUS shield for the maximum reactor thermal power of 3.9 GW compared to the measured background during reactor OFF time." Table published in [53].

MC, the spectrum is folded with the energy resolution observed in the background measurements." (for the characterization of the CONUS detectors see also Chapter 2)

Reactor neutron-induced contribution in HPGe detector spectrum

"For CEνNS, the recoil of Ge atoms is observed. Thus, neutron-induced recoils are the most relevant background source. In total, $(0.58 \pm 0.03)\,d^{-1}kg^{-1}$ Ge recoils for the full reactor power occur by elastic and inelastic neutron scattering over the whole energy range down to $0\,keV_{ee}$. For $(37 \pm 3)\%$ of the recoils, no additional energy is deposited inside the diode and the signature in the detector corresponds to the one expected from CEνNS. This can happen if the neutron only interacts via elastic scattering and no additional particles were created by the neutron traveling through the shield. Alternatively, this is also possible if the γ-rays created in an inelastic scattering process leave the diode without further interaction.

In Table 4.11, for the neutron-induced contribution the expected count rates are listed in the region of interest of CEνNS and at higher energies compared to the count rates observed at the experimental site during reactor OFF time. The expected spectrum in the low energy regime is displayed in Figure 4.21 as well as the spectrum induced by recoil events without further energy depositions. The recoil events create an increasing background towards the detection threshold. Above the energy range displayed only a few events are scattered over the whole spectrum. Furthermore, in Figure 4.22 the expected CEνNS signal is shown. The signal [5] has been adapted to the CONUS experiment in internal sensitivity studies and has been folded with the detector response as described for the neutron contribution with the same energy loss parameter for quenching.

The figures and the plot clearly show that th neutron-induced thermal power correlated background is negligible for maximum reactor power over the whole spectral range. The expected CEνNS signal exceeds the neutron background by at least one order of magnitude.

Comparing the integral ranges outside of the region of interest between reactor ON and OFF data for one month of reactor OFF data and six months of reactor ON data, the results are consistent with the findings here. "

4.4.3 Comparison to muon-induced neutron background

"The dominant source of neutrons within the CONUS shield are muon-induced neutrons. Contributions from the hadronic component of cosmic rays as well as neutrons from the (α,n) reactions are considered negligible. Muon-induced neutrons are created in the concrete and steel of the reactor building as well as in the CONUS shield. The first contribution has been determined by the Bonner sphere measurement during reactor OFF time as described in Section 4.2.2 and is propagated through the shield in the same way as the reactor-induced neutrons. The latter one has been approximated by using the outcome from simulations in the underground laboratory at MPIK. The method has been described in [39] and has been applied to the CONUS shield in [61]. To correct for the thicker overburden, the results have been scaled with a factor of 1.62^{-1} as described in Section 4.2.2. Comparing the different neutron fluence rates at the diode, with $(10.8\pm0.2)\,\mathrm{cm^{-2}d^{-1}}$ [3] most of the neutrons at the diode have been created by muons inside the high-density materials of the shield, followed by $(0.126\pm0.005)\,\mathrm{cm^{-2}d^{-1}}$ muon-induced neutrons inside the overburden and the tiny contribution of $(0.0022\pm0.0001)\,\mathrm{cm^{-2}d^{-1}}$ from the reactor-induced neutron component, which again illustrates the successful suppression of neutrons from outside the shield. The spectral shape of the neutrons is depicted in Figure 4.23. Both, the neutron spectrum induced by muons inside the shield and in the concrete propagated through the shield, peak at fast neutron energies slightly below 1 MeV. The higher neutron energy leads to a recoil spectrum that extends to higher energies.

To reduce the muon-induced background at shallow depth, the CONUS shield contains an active muon veto with an efficiency of around 99%, effectively reducing all prompt background components correlated to muons passing through the shield by about two orders of magnitude. This means that the prompt contribution of muon-induced neutrons inside the shield will be of the same order of magnitude as the one of the muon-induced neutrons in the concrete overburden.

Figure 4.22 summarizes all the neutron-induced contributions and the CEνNS signal. The muon-induced neutron contributions created inside the concrete and inside the shield (displayed without and with applied muon veto) clearly dominate above the reactor-correlated contribution, but this is a steady-state background constant during reactor ON and OFF periods and thus can be distinguished from the CEνNS signal in this way. It will be included as input in the global fit for the background modeling of the CONUS experiment."

4.4.4 Reactor-induced γ-radiation inside CONUS shield

"Mono-energetic γ-lines with the energies of two dominant γ-lines from ^{16}N observed with the CONRAD detector above 2700 keV were propagated through the CONUS

[3] The results was obtained with Geant4.9.6, where an underproduction of muon-induced neutrons occurs. In Section 5.3, a higher neutron fluence rate of $(18.1\pm0.6)\,\mathrm{cm^{-2}d^{-1}}$ is determined and validated with a BS measurement inside the shield.

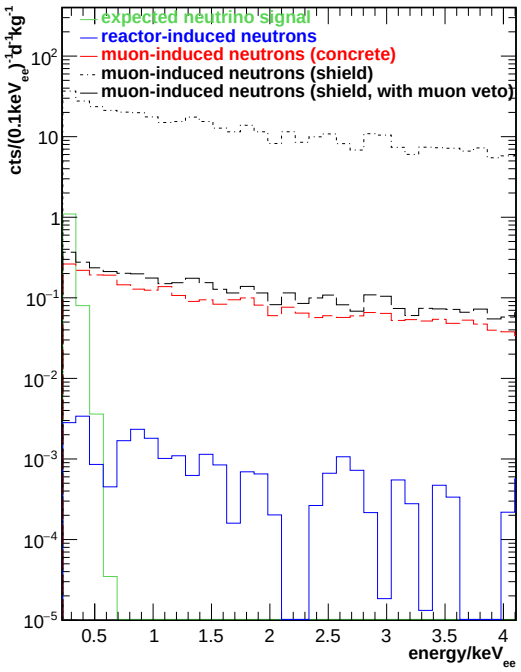

Figure 4.22: "Comparison of the reactor-correlated neutron spectrum at the HPGe (from MC) and the expected CEνNS signal. The dashed line represents the steady-state muon-induced neutron contributions (from MC) from neutrons created in the concrete and inside the shield (reduced by the muon veto). The short dashed line corresponds to the muon-induced neutrons inside the shield without applied muon veto." Figure published in [53].

shield. The wall adjoined to the space around the reactor core had been chosen as starting point. The simulation outcome was normalized by the number of γ-rays per day and 3.9 GW. This amounts to $(50.0\pm0.7)\cdot10^3$ for the 6129 keV γ-line and to $(6.1\pm0.1)\cdot10^3$ for the 7115 keV γ-line, such that the measured count rates inside the CONRAD detector can be reproduced (see Section 4.9). Adding up the contributions from the MC and including the detector response, a negligible integral count rate from 0 to 450 keV of $(11\pm2)\cdot10^{-5}\,\mathrm{kg^{-1}d^{-1}}$ is determined. This is seven orders of magnitude smaller than the measured background rate in Table 4.11. Thus, the 25 cm of Pb inside CONUS completely shield this reactor-correlated contribution."

4.5 Summary on reactor-correlated background

The reactor-correlated neutron background at KBR has been determined with BSS measurements before the setup of the CONUS experiment. A strongly thermalized field with a fluence rate by a factor of two lower than the on earth's surface was found. Differences of 20% in the thermal neutron fluence rate in a distance of a few meters away were evaluated meaning it is important to characterize the background at the exact location of the experiment. With the help of MC simulations it could be shown that the reactor-correlated neutron background is negligible inside the CONUS shield. A small contribution of the non-reactor correlated muon-induced neutron background created in the concrete in the building is predicted inside the CONUS shield.

Moreover, with the unshielded HPGe spectrometer CONRAD the reactor correlated ^{16}N γ rays from the cooling cycle of the reactor were detected above 2.7 MeV$_{ee}$.

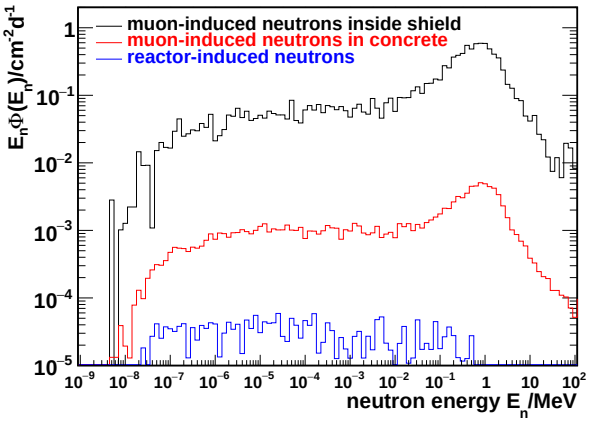

Figure 4.23: "Comparison of MC neutron spectra at the HPGe diode from various sources." Figure published in [53].

Due to the high statistics in the single lines, a precise correlation to the thermal power is observed. Additionally, the γ-ray lines from neutron capture on the steel enforced concrete are registered by the detector. Indirectly,the neutron fluence rate determined with the BSS measurements are confirmed. The γ-ray background is suppressed by the 25 cm Pb of the CONUS shield.

5 CONUS shield and background

5.1 Experimental data for background studies

The CONUS shield (see Figure 1.7.1)and detectors were first set up at the LLL at MPIK in various configurations. During this commissioning phase at MPIK the functionality of all components was tested. It was exercised to setup the shield accurately and precise in preparation for the more demanding environment at the nuclear power plant. Additionally, this procedure enabled the unique possibility to study the impact of the different overburdens at both locations on the same shield. Moreover, the background could be examined without any potential additional contributions from the reactor.

In total, the shield was rebuilt five times before it was shipped to KBR (referred to as LLL-Phase 1 to 5 in the following). In LLL-Phase 1 the background of the shield was evaluated with the known radio-pure CONRAD detector. For LLL-Phase 2 and 3 one CONUS detector was included as well and in Phase 4 three CONUS detectors were placed inside the shield. In this way, the background of the newly developed detectors could be checked. During LLL-Phase 3 data with a ^{252}Cf source were collected referenced in Section 7 to observe the reaction of the detectors to nuclear recoils and test the activation of Ge states. Moreover, the measurement periods were exploited to test different DAQ settings and to optimize all parameters with respect to the resolution and the low energy range. In the last Phase the chance was taken to measure the neutron rate within the shield with a 5" BS detector to validate the MC results.

In the next step at the beginning of 2018 the detectors and the shield were shipped to KBR. Data are collected continuously, split into commissioning and optimization phases and physics runs. The commissioning and optimization at KBR focused on the DAQ settings especially regarding the resolution and the low energy range. The only improvement regarding the background concerns the radon mitigation strategy discussed in Section 5.5.2. Thus, for the background analysis discussed in this chapter the data are mostly not separated according to the different runs.

During the data taking at KBR, highE background data up to 450 keV$_{ee}$ was collected for one detector at a time, while the lowE range <15 keV$_{ee}$ is available for all detectors (due to constraints by the DAQ described in Section 3.1.1). During Run1, highE data were mostly collected for Conus-1, while during Run3 Conus-3 was chosen. For the other two detectors, a few weeks of data could be taken within the optimization phases. By default, the active muon veto is switched on during data taking, but a few measurement were carried out without over night to examine the muon-induced contribution in detail. The highE energy range is calibrated with

regular ^{228}Th measurements, while for the lowE range a self calibration is carried out (see Section 6.2).

5.2 Overview on background suppression within the CONUS shield

Figure 5.1 displays the overall background suppression capability of the shield at KBR. Without a shield, the background is dominated by natural radioactivity and γ-rays from the decay of ^{16}N. The background rate is only about a factor of four larger than at LLL and the radio purity of the concrete is for uranium and thorium comparable to the LLL laboratory [53]. The passive shield reduces the measured background by three orders of magnitude. The remaining background is now dominated by the prompt muon-induced radiation. The shape is defined by the innermost shield layer. The bremsstrahlung's continuum from the muon-induced electromagnetic cascades scales with Z^2, while the self-shielding goes with Z^5 (Z=atomic number) [24]. Thus, by choosing Pb as innermost shield layer a lower continuum compared to e.g. Cu can be achieved, which is typically used due to the radiopurity of the material. The impact of the innermost Pb layer can be directly shown in a comparison of the spectra without muon veto of the CONRAD detector within the CONUS shield and the GIOVE detector within a comparable shield with Cu as innermost layer [30]. Figure 5.2 displays the predicted lower continuum below 500 keV$_{ee}$. Both detectors are large semi-coaxial diodes of similar mass and thus a direct comparison is possible, while for the smaller CONUS detectors the spectrum looks different due to geometric effects. The muon-induced background of the CONUS detectors is discussed in detail in Section 5.3.

Switching on the active muon veto, further reduces the background by one order of magnitude. Line background from the metastable Ge states (see Section 5.3.4) and cosmic activation (see section 5.4) becomes visible. The remaining integral background still contains muon-induced contributions (see Section 5.8.1 about the muon-veto efficiency), but also the radon and ^{210}Pb decay chains (see Section 5.6 and Section 5.5) are relevant. The measurements with the known radio-pure CONRAD detector inside the shield showed no other contaminations from shield except of ^{210}Pb.

MC simulations were used to examine all of these components in detail (description of simulation frame work in Section 1.7). The geometry implementation as introduced in Section 4.1.2 is used. To compare the MC simulations to the data, the detector response is taken into account: slow pulses due to the transition layer (see Section 2.2.5), folding with the energy resolution (see Section 2.2.2), the electronics trigger efficiency (see Section 3.1.3) and the muon veto dead time correction for measurements with applied muon veto (see Section 3.1.2).

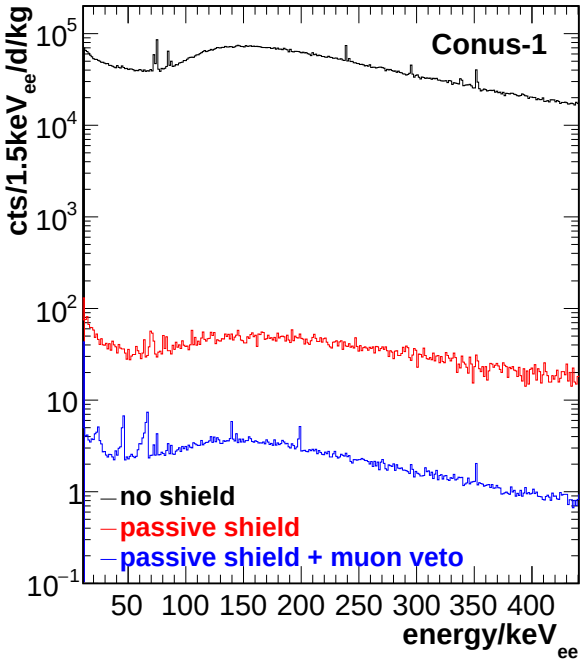

Figure 5.1: Background suppression achieved with the CONUS shield at shallow depth at KBR: Without shield the background is dominated by the natural radioactivity of the surroundings. The passive shield suppresses the background by three orders of magnitude and the remaining spectrum is dominated by muon-induced contributions. Switching on the active muon veto, further suppresses the background by about one order of magnitude.

5.3 Muon-induced background

Without applied active muon veto, the background is dominated by prompt muon-induced contributions. They are comparable for all the four detectors within the shield. The only visible line are X-rays of Pb. The 511 keV peak from pair creation is outside of the energy range of the CONUS detectors. MC simulations are used to examine the component in detail. The method is described and validated for MaGe based on Geant4.9.6 in [39] for the GIOVE detector at the LLL with an overburden of 15 m w.e. Using a model of the muon spectrum at the surface, the muon spectrum underground is calculated. This spectrum is the input for the MC simulation, where the muons are propagated through the shield. An excellent agreement between the measured data and the muon-induced background above $\sim$70 keV$_{ee}$ was found, while an underproduction of secondary muon-induced neutrons by 40% to 60% was reported in [39] and in [100]. The same simulation method is applied to the CONUS shield.

First of all, the prompt muon-induced continuum is compared to the measured spectrum without active muon veto. This also includes a comparison between the data collected at LLL and KBR. The performance of the simulation is discussed. The production of neutrons by muons is studied in more detail by a direct measurement of the neutron fluence rate with a BS inside the CONUS shield and the indirect evaluation by neutron capture on Ge. In this context, the performance of Geant4.9.6 and Geant4.10 is compared. Finally, the preparation of the spectrum for the background model is discussed.

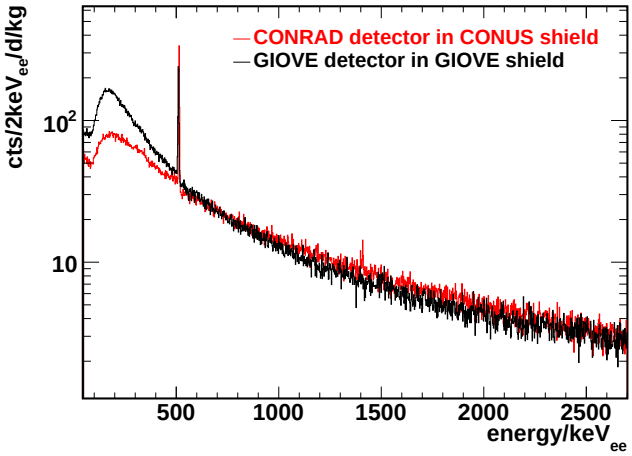

Figure 5.2: Background measured without active muon veto: The spectrum measured by CONRAD in the CONUS shield, where the innermost layer is made out of Pb, is compared to data collected with GIOVE with Cu as innermost shield layer. A lower continuum is observed for Pb because of the better self-shielding of the muon-induced bremsstrahlung. The figure is published in [61].

5.3.1 Prompt muon-induced background

In the first step, the measurements without active muon veto within the CONUS shield at LLL and KBR are compared in Figure 5.3. By applying a scaling factor of 1/1.62 to the LLL spectrum, the data collected at KBR can be well reproduced. The spectral shapes agree, which indicates that the same physical processes are responsible for the creation of the background radiation. The overburden of the LLL is well known with 15 m w.e. and from the scaling factor of 1.62 an effective overburden of about 24 m w.e. can be derived for the CONUS experimental site at KBR. This means that well validated simulation framework for the LLL laboratory can be modified for KBR by the use of the scaling factor.

Comparison to MC

Second, the outcome of the simulation is compared to the data in Table 5.1, Figure 5.4 and Figure 5.5. The comparison is carried out for Conus-1 as here the most statistics for the measurements is available. The data are corrected for the background with active muon veto assuming a veto efficiency of 97% (see Section 5.8.1). For the MC simulation a 10% uncertainty on the angular distribution is assumed.

Overall, a good agreement was achieved. Above 100 keV$_{ee}$ the MC reproduces the measured data very well within 2%. Below down to 10 keV$_{ee}$ the Pb X-rays are not observed in the MC simulation and the count rate is too small by 20%. In the lowE range, too many counts are found in the MC down to 0.4 keV$_{ee}$. Below this energy the measurement strongly increases above the MC. The discrepancies are examined in more details in the next sections.

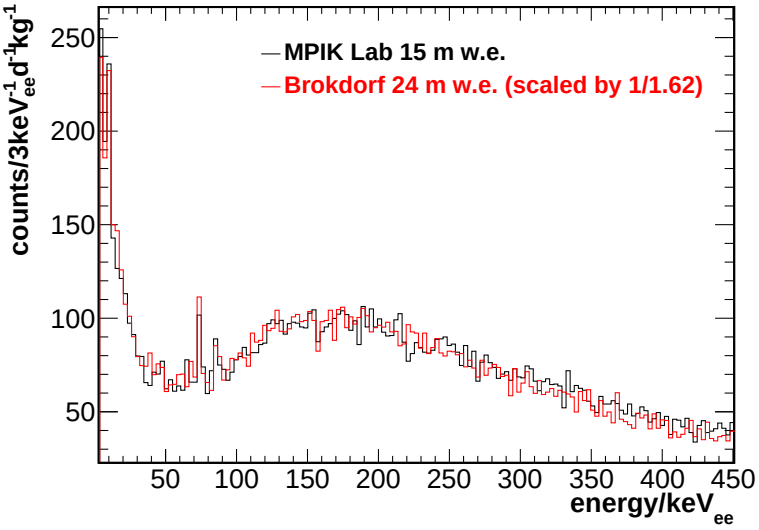

Figure 5.3: The measurement without active muon veto at KBR and LLL are compared. They only differ by a factor of 1.62 and the spectral shapes agree. The figure is published in [53].

integral range	meas. data cts/d	MC cts/d	MC (rescaled) cts/d	rel. contribution el-mag./neutron -induced in MC
[0.4, 1]keV$_{ee}$	145±10	155±20	130	8%/92%
[2,7]keV$_{ee}$	400±15	440±40	390	18%/82%
[10,100]keV$_{ee}$	2300±30	1900±200	–	71%/29%
[100,440]keV$_{ee}$	7700±60	7800±800	–	82%/18%

Table 5.1: Comparison of the measured prompt-muon induced continuum as measured at KBR to the MC simulation. An excellent agreement above 100 keV$_{ee}$ is found. At lower energies, discrepancies are observed, especially in the shape as depicted in Figure 5.5.

In the MC, it is possible to disentangle the electromagnetic contribution from the neutron-induced spectrum. This is done by flagging all events, where a neutron is created at some point. The separation is displayed in Figure 5.4 and Figure 5.5 as well and Table 5.1 gives the relative share of both contributions for each energy range. Above 50 keV$_{ee}$ the electromagnetic bremsstrahlung's continuum dominates. The neutron-induced spectrum is assumed to be created by γ-rays from neutron capture or inelastic scattering. At energies below and also within the ROI for CEνNS, neutron recoils from elastic and inelastic scattering dominate the spectrum.

Muon-induced X-rays in Pb

To learn more about the discrepancy between the MC simulation and the data, the Pb X-rays were examined more closely. First of all, it is confirmed that the X-rays

location	74.97 keV Pb X-ray [cts/d]	
A408 KBR without muon veto	29±6	
LLL without muon veto	53±8	ratio LLL/KBR: 1.8±0.3
A408 KBR with muon veto	1.8±0.2	veto efficiency: 0.94±0.21

Table 5.2: Line count rate of the 74.97 keV Pb X-ray at KBR and LLL in measurements without active muon veto. From the measurement with muon veto a veto efficiency can be derived.

are indeed muon-induced. In the measured spectrum, the K shell X-ray lines of Pb at 74.97 keV (100% rel. intensity), 72.80 keV (60% rel. intensity) and 84.94 keV (23% rel. intensity) [109] are visible due to the very good energy resolution. The count rate of the strongest line at 74.97 keV is compared to the line count rate at LLL and the line count rate with active muon veto. The results are shown in Table 5.2. Within statistics the ratio of the line count rate between LLL and A408 KBR is comparable with the scaling factor of 1.62 derived from the integral count rates. Moreover, the line count rate is strongly suppressed by the active muon veto. Both observation are in agreement with the lines being muon-induced.

To check whether the X-rays are created at all in the MC, all Cu parts are replaced by air volumes in the simulation (Cu plate on top of detector chamber, Cu cryostat and diode holder). In the outcome, the lines are visible and the count rate is only about a factor of five higher than in the measurement. Already 6 mm of Cu would suppress this count rate by more than a factor of 100 (according to formula (1.9) with γ-ray attenuation coefficient from [110]). Moreover, the spectral shape below 70 keV_{ee} is (almost) identical without the Cu part, while above the continuum is almost flat. This is the same effect of the stronger self-shielding of the bremsstrahlung by Pb than Cu as already seen in Figure 5.2. As the spectral shape in the MC matches well with the measured data without active muon veto in Figure 5.4, there are more hints for an underproduction of X-rays than for an over attenuation in the materials surrounding the diode.

5.3.2 BS measurement

At the end of the commissioning at LLL measurements with the 5"BS (part of the BSS NEMUS spectrometer by PTB) inside the CONUS shield were carried out. The measurements were reproduced in a MC simulation to validate the muon-induced neutron production in the simulation framework.

Description of BS measurement inside the CONUS shield

A ^{3}He-filled proportional counter enclosed in a 5" PE sphere was placed within the detector chamber, where usually the HPGe spectrometers are located. Details on BSS are given in Section 4.1.1 in connection with the neutron measurements

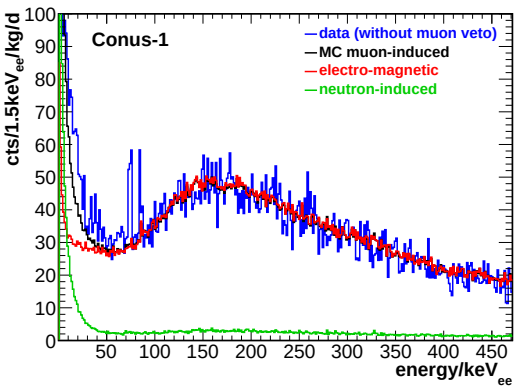

Figure 5.4: HighE muon-induced background: A measurement without active muon veto is depicted in comparison to the MC simulation. The electro-magnetic and neutron-induced background contributions are shown separately.

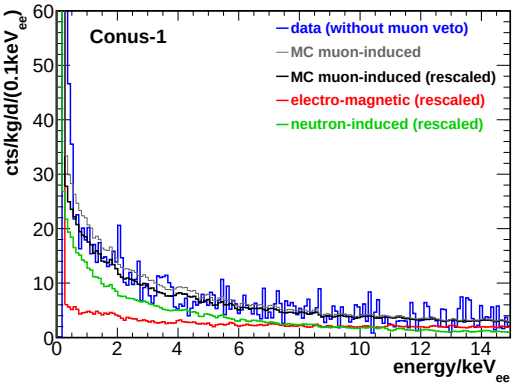

Figure 5.5: LowE muon-induced background: A measurement without active muon veto is depicted in comparison to the MC simulation. The electro-magnetic and neutron-induced background contributions are shown separately. The MC is rescaled to match the data.

at KBR. Spheres of different diameter are characterized by broad neutron response functions (cf. Figure 4.1) peaking at different neutron energies. In general, to acquire a spectrum, it would be preferable to carry out measurements with several spheres. However, due to the large effort to open up and close the CONUS shield, data were only taken with a single BS. The sphere diameter was selected such that a high response is guaranteed at the energy where the MC simulation predicts the highest neutron fluence rate (see Figure 4.1 for the response functions of for different sphere diameters). This is around 1 MeV. To avoid bias from backscattering, the sphere has been placed approximately in the middle of the detector chamber (see Figure 5.6 and Figure 5.7 of the open shield). One opening to the inside of the shield designated for the cryostat arm of the Ge spectrometer has been used as cable shaft for the DAQ of the BS. A pocket Multi Channel Analyzer (MCA) was employed (see Figure 5.8).

In total, without muon veto a live time of 94.5 h was collected and for measurements with active muon veto the collected data amount to 82 h live time.

BSS data analysis

The measurements during the day turned out to contain a lot of noise from people working in the laboratory and noise on the power grid. Thus, only the data collected over night are considered. The count rate detected by the BS is derived from the pulse height spectra by M. Zboril (PTB) as described in Section 4.2 for the BS measurements at KBR. The outcome of the analysis is displayed in Table 5.4 in comparison to the MC result.

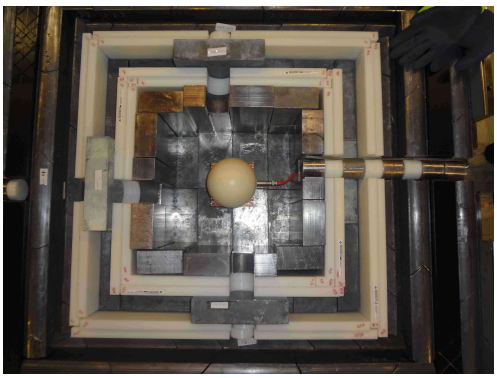

Figure 5.6: Half-open CONUS shield with BS inside seen from above.

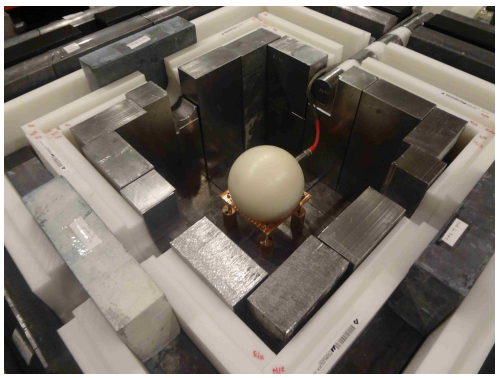

Figure 5.7: Half-open CONUS shield with BS inside seen from side.

MC simulation of BS measurement inside the CONUS shield

All MC simulations have been carried out with Geant4.9.6 (release 2015) and Geant4.10.3 (release 2017) to compare the neutron physics implemented in both versions. If not stated specifically the results correspond to Geant4.10. For the geometry a sphere with an outer diameter of 3.3 cm and a wall thickness of 0.1 cm was implemented to represent the bare counter. It is enclosed with another sphere of diameter 12.64 cm (5"), which corresponds to the PE sphere to thermalize the neutrons. MC simulations with all volumes filled with air as well as simulations with the bare counter made out of steel and the outer sphere filled with PE with a density of 0.954 g/cm^2 were carried out. Both options are described below. Muons were started from the walls of the laboratory with an energy spectrum and angular distribution corresponding to an overburden of 15 m w.e. as previously described for the Ge data. The outcome of the MC is scaled with the respective muon rates. A 10% uncertainty on the normalization is assumed directly on the spectrum and by variations in the angular distribution.

The thermalization of the neutrons within the PE sphere is not simulated in Geant4. Instead the neutron spectrum from the MC is folded with the 5" sphere response function in Figure 4.1. The response function is well validated within the BSS framework, while the thermalization in Geant4 might be less accurate. In this way, no additional systematic uncertainty is introduced. Therefore, the PE sphere is replaced with an air sphere with the radius of the PE sphere in the MC geometry. The neutrons coming from all directions that are hitting the air sphere are registered (see blue line in Figure 5.9 on the right). As soon as the neutrons enter the volume, the propagation of the neutrons is stopped. Only to examine the backscattering of neutrons on the PE sphere within the narrow detector chamber, simulations have been run with the full setup. In this case, in the MC the propagation of the neutrons entering the volume of the bare counter is discontinued (see red line in Figure 5.9 on the right). The difference between stopping all neutrons and only the thermal is examined as well, as only the thermal ones are absorbed in the counter in reality. It

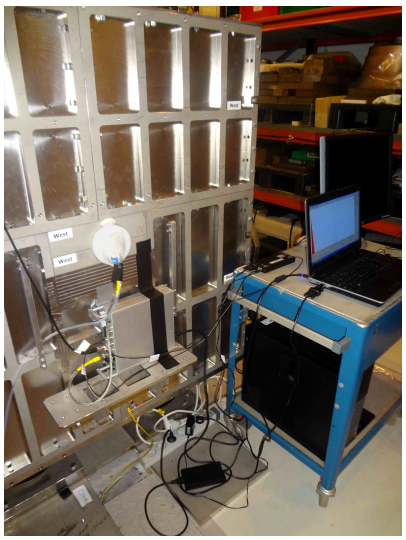

Figure 5.8: Closed CONUS shield. The BS cables leaving the shield are visible as well as the DAQ for the BS.

turns out that the difference is small (less than 1%).

The fluence rates given in Table 5.3 are normalized by the sphere area where they are scored on, respectively 502 cm^2 for the 5" sphere. About 70% of the neutrons have energies around 1 MeV with a continuum down to thermal energies (see Figure 5.10). It is clearly visible that the PE sphere modifies the spectral shape in the thermal regime. There is an increase of about 10% from backscattered neutrons that have been thermalized. In total, a neutron fluence rate through the surface of 25.9 $n/d/cm^2$ is determined with Geant4.10. For Geant4.9.6, however, the fluence rate is diminished by 60%. The spectral shape in Figure 5.11 reveals that the loss occurs over the whole spectral range. It is comparable for all energy ranges. Comparing the outcome to the measurement results will make it possible to judge which prediction is closer to reality.

The angular distribution of the neutrons arriving at the surface of the 5" sphere were analyzed as well. The angle between the direction of the neutrons hitting the sphere and the surface normal was evaluated. For both versions of the MC, with air volumes and the full setup, an $\cos(\theta)\sin(\theta)$ distribution was observed in Figure 5.13. This corresponds very well to an isotropic flux on a sphere confirming that the neutrons scatter in the detector chamber from all directions.

Moreover, the MC makes it possible to study the energy and the origin of the muon-induced neutrons that hit the BS. Figure 5.12 shows that most neutrons are created by μ^- by negative muon capture $\mu^- + p \rightarrow \nu_\mu + n\ (+\gamma)$, which is not possible for μ^+. Figure 5.14 reveals the shield layers, where the neutrons are created. This also includes secondary neutrons induced by neutrons. As expected, they are dominantly produced inside the heavy Pb shield. The neutrons from the innermost layer have the highest chance to reach the BS. The neutrons produced in the outer layers are thermalized and captured in the borated PE layers sandwiched with the

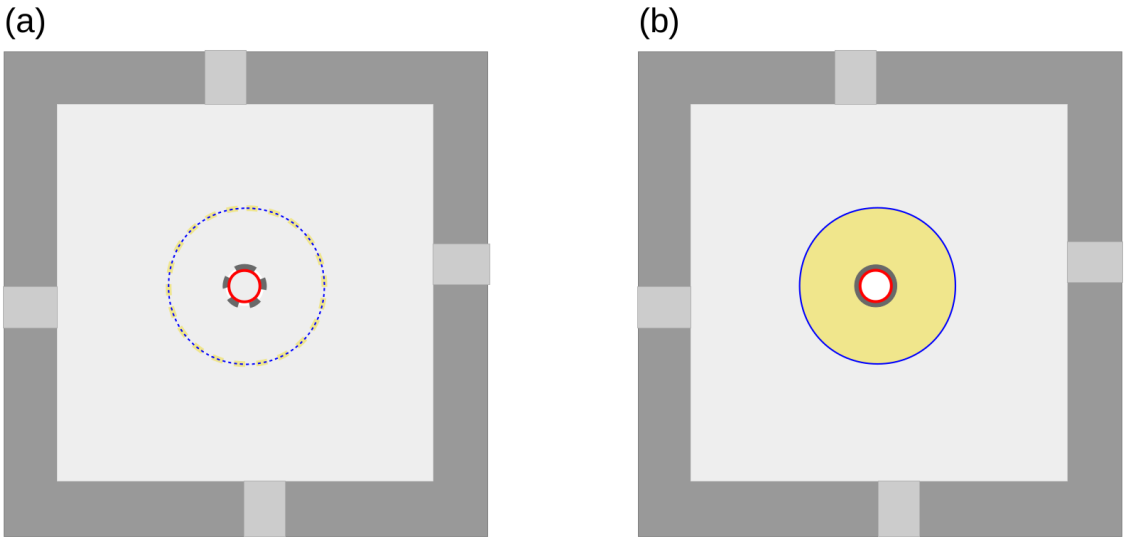

Figure 5.9: Simulated configurations of the BS within the CONUS shield: (a) air sphere, (b): full setup. The blue line marks the surface of the 5" sphere, where the neutrons are scored, the red line represents the surface of the bare counter.

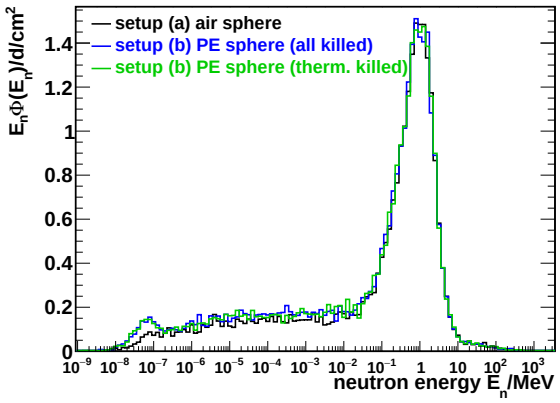

Figure 5.10: Spectra of muon-induced neutrons within the CONUS shield hitting the 5" sphere for the different simulated configurations: setup (a) air sphere with all neutrons stopped that hit the sphere, setup (b) PE sphere with all neutrons stopped that hit the bare counter and setup (b) PE sphere with thermal neutrons stopped that hit the bare counter.

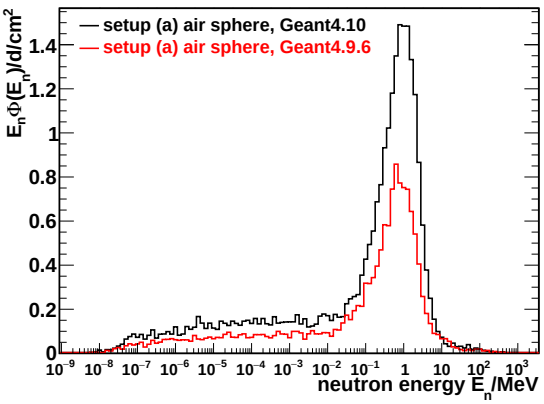

Figure 5.11: Comparison of energy spectrum of muon-induced neutrons produced in Geant4.10 and Geant4.9.6. For the ladder not enough neutrons are produced.

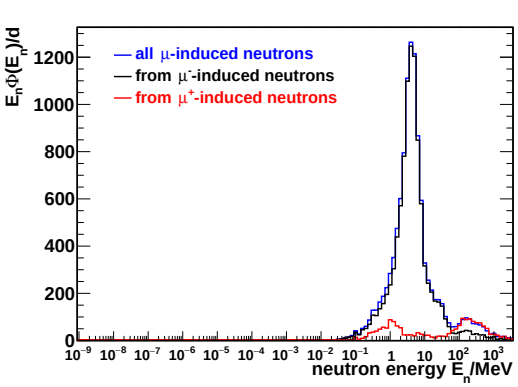

Figure 5.12: Energy spectrum of muon-induced and neutron-induced neutrons at creation that reach the BS. The distributions for μ^+ and μ^- are given.

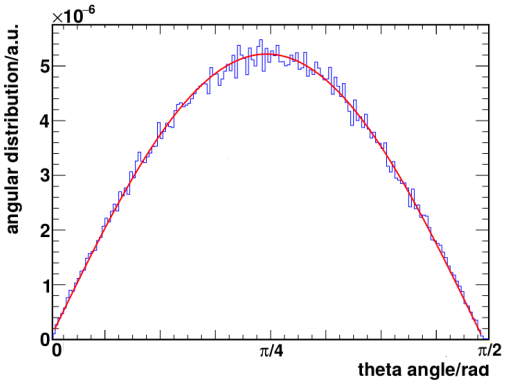

Figure 5.13: Angular distribution of neutrons hitting the surface of the 5" air sphere with fit of a $\cos(\theta)\sin(\theta)$ function corresponding to an isotropic distribution of the neutrons.

type	Geant4.10		Geant4.9.6
	air volume $cm^{-2}d^{-1}$	full setup $cm^{-2}d^{-1}$	air volume $cm^{-2}d^{-1}$
Thermal	1.0 ± 0.1	1.6 ± 0.2	0.5 ± 0.1
Intermediate	8.3 ± 0.8	9.6 ± 0.9	5.1 ± 0.5
Fast	16.7 ± 0.2	16.8 ± 1.7	9.2 ± 1.0
Total (through surface)	25.9 ± 0.3	28.0 ± 2.8	14.9 ± 1.5

Table 5.3: MC result of the neutron fluence rate at the diode for different configurations and Geant4 versions.

Pb layers. Thus, mostly fast neutrons are observed at the BS as can be seen in Figure 5.10.

Result of BS measurement inside shield

The outcome of the MC simulation is folded with the response function of the 5" BS by M. Zboril to derive the predicted count rate. The result is shown in Table 5.4 and compared to the measured count rate. An excellent agreement is found for the MC based on Geant4.10. For Geant4.9.6, the previously observed underproduction of muon-induced neutrons is confirmed with |data-MC|/data≈40%. The results agree well with the neutron fluence rates derived indirectly from the metastable Ge states from neutron capture (see Section 5.3.4).

Moreover, the count rate N with and without active muon veto is compared. The veto efficiency, defined as follows, amounts to:

$$\epsilon_{veto} = 1 - \frac{N_{\text{with veto}}}{N_{\text{without veto}}} = 0.81 \pm 0.02 \tag{5.1}$$

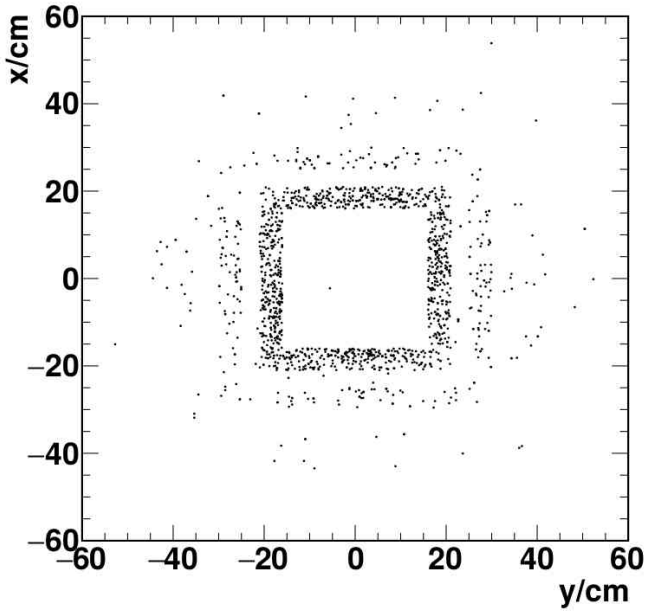

Figure 5.14: Location where the muon-induced and neutron-induced neutrons are created inside the shield that reach the BS. Most of them stem from the inner most Pb layer.

The efficiency is clearly below the one derived in the background model of approximately 97% (see Section 5.8.1). The deviation strongly indicates a delay in the registration of the neutrons in the counter. The delay is at least partially created during the thermalization within the BS, which has a time constant of the order of 100 μs [41]. The veto window for the measurements at LLL was 160 μs. Preliminary time-resolved MNCP6.1 simulations of the neutron interactions within the BS confirm the thermalization time constant for 1 MeV neutrons. In a next step, it will be disentangled whether the thermalization within the BS fully explains the difference in the veto efficiency or if neutron scattering within the shield is also relevant. For the data taking at KBR, to be on the safe side, the veto window was extended to 400 μs. In this way, also potentially delayed neutrons from the shield are vetoed, while only a life time loss of 1-2% occurs.

Muon-induced neutron component for background model

To be able to use the MC spectra in the background model, adaptations have to be made.

Within [10,100] keV$_{ee}$ there are not enough counts in the MC. Regarding potential reasons for this discrepancy, it was shown that overall the production of muon-induced neutrons in the MC is correct. However, data was only collected with one BS focusing on neutron energies of the order of 1 MeV. It cannot be excluded that a small higher energetic neutron contribution exists that is not found in the MC. This

	count rate/s	ratio
without veto	$(2.7\pm0.1)\cdot10^{-3}$	1.06
Geant4.10 air	$(2.6\pm0.3)\cdot10^{-3}$	1.0
Geant4.10 full setup	$(2.7\pm0.3)\cdot10^{-3}$	1.0
Geant4.9.6	$(1.5\pm0.2)\cdot10^{-3}$	1.8
with veto	$(5.1\pm0.6)\cdot10^{-4}$	

Table 5.4: Comparison of measured count rate in the 5"BS to the prediction from MC in various configurations. For Geant4.10 an excellent agreement is achieved, while for Geant4.9.6 not enough neutrons are registered by nearly a factor of two. By comparing the BS count rate with and without active muon veto, a veto efficiency of 0.81 ± 0.02 can be derived.

would result in an increasing continuum of neutron recoils at higher energies. However, test simulations of higher energetic neutrons at the diode indicate that such a contribution should also increase the lowE range, where a better agreement between MC and data is found. With the help of ^{252}Cf source measurements, quenching can be excluded as origin of the discrepancy, because no discrepancy in this energy range is found between MC and data. Thus, it seems more likely that the discrepancies originate from the electro-magnetic contribution, but no reason could be identified. Therefore, for the highE model instead of the MC the measured spectrum without muon veto is used to represent the background. This is unproblematic as the energy range is not used for a physics analysis. The spectrum is corrected for the contribution of not muon-induced components to the measurement.

Within the lowE range below 4 keV$_{ee}$ there are too many counts in the MC. To correct for this, the electro-magnetic and neutron-induced components are rescaled by 1.1 and 0.78 respectively. A quenching parameter 0.2 was used. Table 5.2 and Figure 5.5 show the agreement achieved in this way. For the highE range, the same rescaling leads to a bigger discrepancy to the measurement. Most likely, the rescaling is only functional and does not correspond to reality. Below 0.4 keV$_{ee}$ the measured spectrum increases strongly above the MC. With the information available, it was not possible to decide whether this is the noise threshold or a physical background. While the electronics noise threshold is lower for the measurements with active muon veto, it cannot be excluded that there is a difference in the noise level due to the muon veto. Therefore, it was foregone from adding this component to the MC spectrum. For the background, if the background would be physical, it would be counter balanced by the fit to the noise threshold (see Section 5.8.2).

5.3.3 Muon-induced neutron capture on Ge

As described in Section 1.6.2 prompt γ-ray lines are emitted in neutron capture. They contribute to the continuum, but now no distinctive lines were found in the spectrum without active muon veto as other background contributes dominate.

isotope	production	$T_{1/2}$	experimental signature	cross section	
				thermal [b]	fast ∼1 MeV [b]
^{71m}Ge	^{70}Ge(n,γ)^{71m}Ge, ^{72}Ge(n,2n)^{71m}Ge	20.4 ms	198.3 keV (sum), 23.4 keV	0.34±0.07 [115]	dnf
^{73m}Ge	^{72}Ge(n,γ)^{73m}Ge, ^{74}Ge(n,2n)^{73m}Ge	0.499 s	53.5-66.6 keV (sum), 13.3 keV	0.46±0.04 [115]	dnf
^{75m}Ge	^{74}Ge(n,γ)^{75m}Ge	47.7 s	139.5 keV	0.131±0.006 [112]	0.0069±0.0004 [114]
^{71}Ge	^{70}Ge(n,γ)^{71}Ge	11.4 d	10.37 keV, 1.3 keV	3.57±0.16(*)[115]	
^{73}Ge	^{72}Ge(n,γ)^{73}Ge	stable		0.86±0.11[115]	
^{75}Ge	^{74}Ge(n,γ)^{75}Ge	82.2 min	264.6 keV (11.4%) β (98.6%)	0.497±0.052 [112]	0.012±0.002 [114]

Table 5.5: In neutron capture on Ge, metastable states and long-lived isotopes are activated. The half-lifes are given in the Table together with the decay radiation and the cross section for thermal and fast neutrons if available. For [115] a mean value for the data evaluated in the work and the data citied there is given. (dnf=data not found).

Lines are only observed in the neutron source measurement (see Section 7.3). The active muon suppresses this prompt γ -ray background as well as the other muon-induced contributions, however, some of the states created in neutron capture have a life-time longer than the muon veto window of 400 μs and thus become visible in the background spectrum with applied muon veto. There are two categories: metastable states (also called isomeric) and radioactive isotopes (in situ activation). The γ-ray lines from metastable Ge states belong to the few visible lines in the background spectrum with applied muon veto. They were studied in detail in the following, because they can be used to indirectly derive the neutron fluence rate at the diode and the in situ activation of ^{71}Ge. This is the most notably activation, since it creates visible line background, but there are further isotopes that can contribute to the continuum. The impact of the ROI for all contributions is derived with the help of MC simulations. Due to the long live times, the decay is not observed in the MC of the muon propagation through the shield.

5.3.4 Metastable Ge states

Metastable states have a half-live longer than ordinary excited states. The metastable states occurring in excitation after neutron capture on Ge and their respective half-lives are listed in Table 5.5. Two of the states can also by created by higher energetic neutrons in (n,2n) interactions. Neutrons of at least 7 MeV are required [117], meaning the process is sub-dominant within the CONUS shield.

Signature in the detector

Neutron capture on four of the five stable isotopes of Ge lead to metastable states. However, the abundance of ^{76}Ge in natural Ge in Table 5.6 is at least three times smaller than for the other three stable Ge isotopes, while the thermal neutron capture cross section is comparable. Thus, ^{77m}Ge, created in the neutron capture of ^{76}Ge, is neglected in all following considerations. Figure 5.15 displays simplified schemes of the three metastable states creating line background visible in the background spectra. They all decay predominately via isomeric transition (IT) resulting in the emission of γ-rays and orbital electrons via internal conversion (IC). The emission probabilities in the figure are taken from MC. The type of radiation is relevant because electrons have a much shorter free mean path within Ge and are thus much more likely to deposit all of their energy within the detector. This also shows in the detection efficiencies given in Table 5.7. The dominant signatures observed in the detectors are also depicted in Figure 5.16 for the measured background of Conus-1:

- ^{71m}Ge: summation line at 198.3 keV (23.4+174.9 keV); 23.4 keV line alone from electrons as there is a finite possibility for the 174.9 keV line γ-rays to escape the detector
- ^{73m}Ge: summation line at 66.5 keV (13.3+53.3 keV) with a tail towards lower energies as the intermediate states has a half-live of 2.9 μs close to the shaping time of the DAQ, which leads to a partial summation of the 13.3 keV energy deposition; the 53.3 keV line can also be observed alone if the 13.3 keV energy deposition is not detected at all
- ^{75m}Ge: single line at 139.5 keV

Two of the final states of the decays are not stable: ^{75}Ge has a half-live of 82 min and ^{71}Ge has a half-live of 11.4 d. Thus, it can be said that the ongoing muon-induced neutron fluence leads to an in situ activation of the Ge. The activation rate can be derived from the count rate of the metastable states if sufficient knowledge on the cross sections is available.

isotope	abundance
^{70}Ge	20.5%
^{72}Ge	27.4%
^{73}Ge	7.8%
^{74}Ge	36.5%
^{76}Ge	7.44%

Table 5.6: Abundance of isotopes in natural Ge [111].

Neutron fluence rate at the detector

The count rate of the dominate lines from the metastable states at LLL and at KBR are given in Table 5.7. The MC simulation shows that the neutron fluence

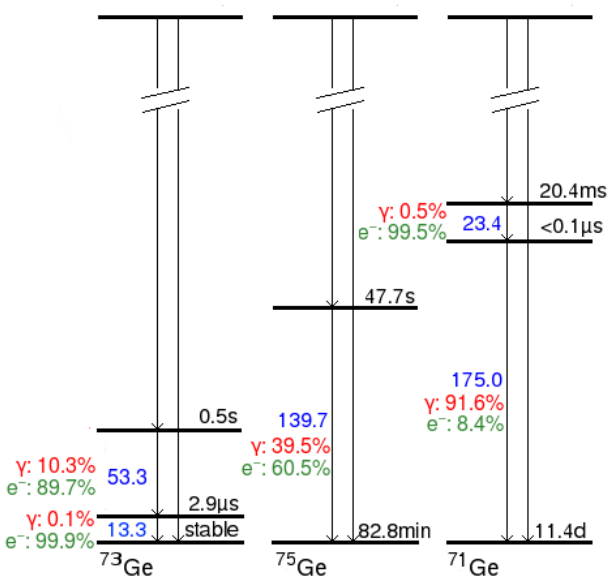

Figure 5.15: Meta stable Ge states created in muon-induced neutron capture on Ge.

rate within the detector chamber is isotropic (see Figure 5.13). Consequently, the same count rate for the four CONUS detectors can be expected. The collected statistics in the highE range differ strongly for the detectors, especially at KBR. Therefore, the count rates of the single detectors are combined by a weighted mean given in in the table. For the structure below 66.5 keV no fit was carried out, but the integral from 52.5 keV_{ee} to 67.2 keV_{ee} was calculated, subtracting the background left and right to it.

energy	detection efficiency (MC)	count rate LLL cts/d	count rate KBR cts/d	ratio
139.5 keV	0.83-0.86	4.4±0.5	2.8±0.2	1.7±0.2
198.3 keV	0.63-0.66	3.9±0.5	3.1±0.2	1.3±0.2
[52.5, 67.2] keV	0.89-0.93	38.1±1.5	19.0±0.6	2.3±0.1

Table 5.7: Count rate of dominant lines of the metastable Ge states at LLL and KBR.

The count rate of the lines give a good indication of the neutron fluence rate at the detector. First of all, the ratio between the data collected at the two locations is determined. The outcome confirms the ratio derived before from the spectra without active muon veto (see Section 5.3.1). Only for the structure below 66.5 keV the ratio is larger. Two potential reasons were identified: additional production of ^{73m}Ge by the decay of the cosmogenic induced ^{73}As with a half-life short enough to be decayed away for the data collection at KBR (see Section 5.4.1) and the described difficulties to extract the count rate from the structure.

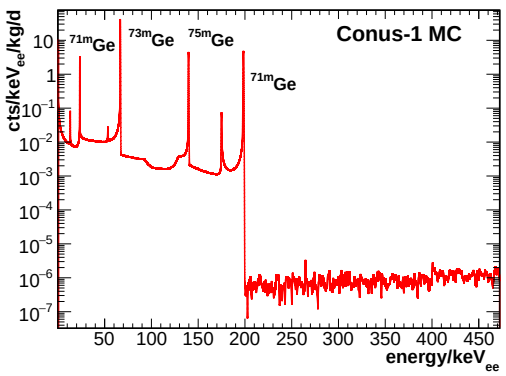

Figure 5.16: HighE background of CONUS-1: the visible lines created by the metastable Ge states are marked.

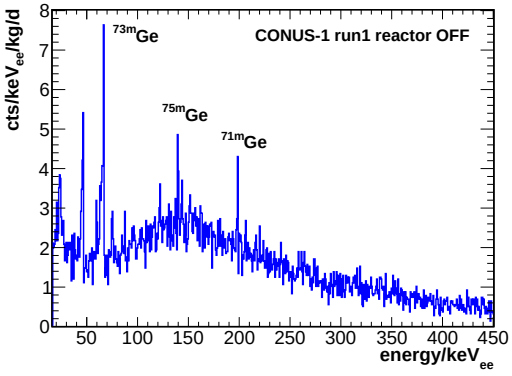

Figure 5.17: MC background contribution of metastable Ge states.

The line count rates can also be used to derive the neutron fluence rate at the diode. For this purpose, ^{75m}Ge is ideal, as ^{74}Ge, the isotope where the neutron capture occurs has a high abundance in natural Ge (see Table 5.6). Moreover, the efficiency can be determined easily as there are no summation lines for the dominant line of the decay at 139.5 keV. To extract the neutron fluence rate, the detection efficiency from MC ϵ_{det}, the amount of ^{74}Ge atoms in the crystal $N_{^{74}Ge}$ and the energy-dependent cross section is required. While the cross section in Figure 5.18 is highest for thermal neutrons, most of the neutrons arriving at the diodes have higher energies. To take this into account, the cross section is weighted by spectrum of neutrons arriving at the diode in the MC (comparable to Figure 5.10). From the line count rate N_{140keV} in the 139.5 keV line, the neutron fluence rate at the diode is derived in the following way:

$$\text{n fluence rate} = \frac{N_{140keV}}{\sigma_{weighted} \cdot \epsilon_{det} \cdot N_{^{74}\text{Ge}}}, \quad N_{^{74}Ge} = \frac{\text{abundance}(^{74}\text{Ge}) \cdot \text{m}_{\text{crystal}} \cdot \text{N}_\text{A}}{mol_{\text{Ge}}} \tag{5.2}$$

The results can be found in Table 5.8. The numbers differ from the fluence rates evaluated in the BS measurements (see Table 5.4) due to the normalization to different surfaces. The uncertainty on the indirect neutron fluence rate derived in this way is driven by the uncertainty of the measured line count rate. In agreement with the BS measurements (see Section 5.4) an underproduction of neutrons in Geant4.9.6 is observed [100]. Meanwhile, for Geant4.10 an excellent agreement is found. This shows that also this indirect method is valid to determine the neutron fluence rate at the diode, however it is less precise. Especially at higher energies, the cross section for the creation of the metastable states has large uncertainties. Additionally, a MC simulation is required to know about the shape of the neutron spectrum at the diode. Nevertheless, if an in situ BS measurement is not possible,

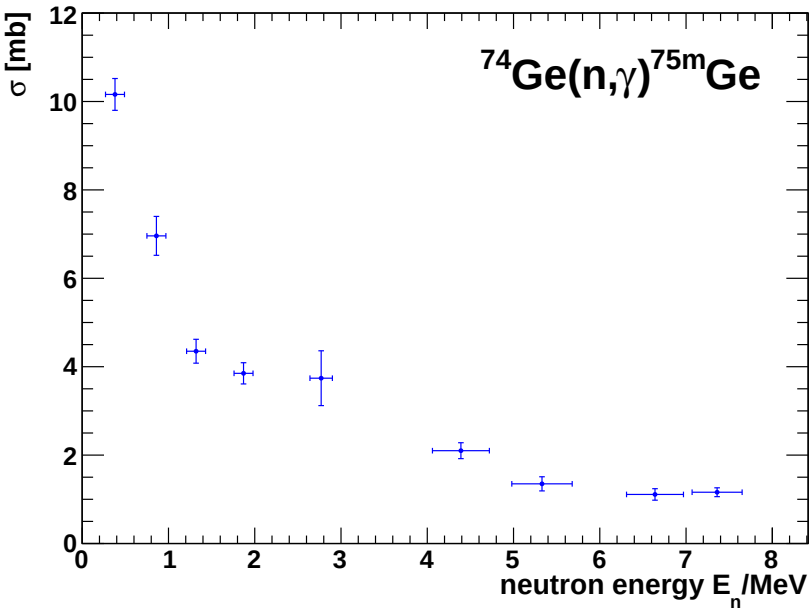

Figure 5.18: Neutron capture cross section of ^{74}Ge to ^{75m}Ge for fast neutron energies (data from [114]). For thermal neutrons the cross section is one order of magnitude larger with (130.5±5.6 mb [112], figure published in [53].

this method makes it possible to give an estimation on the neutron fluence rate at the detector nevertheless.

MC version	neutron fluence rate $cm^{-2}d^{-1}$
MC Geant4.10	29.4±2.9
MC Geant4.9.6	16.4±1.6
n capture on ^{74}Ge	32.0±5.2

Table 5.8: Comparison of MC results for both Geant4 version to indirect estimation of the neutron fluence rate at the diode from a neutron capture induced line.

Comparison of neutron fluence rate to other experiments

With information from literature this examination of the metastable states and neutron fluence rate can be extended to other experiments with Ge spectrometers with different shield and overburdens.

Table 5.9 lists all the experiments and locations considered. The overburden in m w.e. is given and the composition of the shield is described. High Z materials required to shield natural radioactivity are targets for muon to create neutrons. All experiments except GERDA [107] have a shield of 15 cm to 25 cm of Pb or

steel. Some of the shields include low Z materials to moderate these neutrons and neutrons from other sources. Also plastic scintillator plates of muon vetos act as moderators. Some of the shields include borated materials or Cd to capture the neutrons, but with a lower probability neutron capture can also occur inside the other shield materials like e.g. Cu. The active mass of the Ge detectors was also added to the table. The count rates are not compared directly as the detectors differ in size, instead the activity per Ge mass m_{act} is derived:

$$A_{^{7im}\mathrm{Ge}} = \frac{N_{^{7im}\mathrm{Ge}}}{\epsilon_{^{7im}\mathrm{Ge}} m_{act}}, \quad i = 1, 3, 5 \tag{5.3}$$

The activity determination requires knowledge of the detection efficiency of the line count rates ϵ. The detection efficiency is usually determined from MC. A high efficiency is expected, as the decay occurs within the Ge. For the CONUS detectors it is given in Table 5.7. If the information is not available in literature, the efficiency of a similar detector is used instead. There is a small possibility for decays within the dead layer to be registered, this was not taken into account as from literature often only the active mass of the detectors is available.

The 139.5 keV line of ^{75m}Ge is suited best for the comparison. No DAQ effects have to be taken into account and the statistics is higher than for the 198 keV line. Figure 5.19 shows the activity plot against the overburden. Shields containing low Z materials for the moderation of neutrons are marked in blue, the others in black. For the CONUS experiment the same shield has been set up at two locations. The red line marks the linear extrapolation between the two data points. In this way, the impact of a change in overburden can be gauged. From the activity the neutron fluence rate can be derived as described in Section 5.3.4 if knowledge on the spectral shape is available as e.g. for the MC of the CONUS experiment. As this is mostly not the case for the data extracted from literature, the calculation was forgone, but qualitative statements can be made nevertheless.

In the high Z materials of the shield muons induce neutrons, which the interaction processes depending on the muon energy. With a larger overburden, the muon flux decreases and the mean energy shifts to higher energies. Negative muon capture becomes less relevant and more neutrons are created in spallation processes which results in higher neutron energies up to 100 MeV [101]. There are less muons that can create neutrons, however due to the higher muon energy, the neutron yield in processes such as muon spallation and photo nuclear interactions increases [101]. All neutrons might lose energy until they reach the diode.

experiment/ location	depth [m w.e]	shield			mass (total)
		high Z materials	n moderation (+ capture)	muon veto	
CONUS/LLL (**)	15	25 cm Pb, 1 cm steel, 1 cm Cu	10 cm bor. PE, 5 cm PE	plastic scin. 5 cm	3.74±0.2
CONUS/KBR (**)	24	25 cm Pb, 1 cm steel, 1 cm Cu	10 cm bor. PE, 5 cm PE	plastic scin. 5 cm	3.74±0.2
CONRAD/LLL [52]	15	25 cm Pb, 1cm steel, 1 cm Cu	10 cm bor. PE, 5cm PE	plastic scin. 5 cm	1.94±0.15
GIOVE/LLL [102]	15	17 cm Pb, 5 cm Cu	15 cm bor. PE	plastic scin. 5 cm	1.81±0.12
CORRADO/LLL [102]	15	15-20 cm Pb, 5 cm Cu	none	prop. chamber	0.845
Texono/Kuosheng NPP [123]	30	15 cm Pb, 5 cm steel, 5 cm Cu one side	25 cm bor. PE	plastic scin. 9-12 cm	1.06
GEMMA/ILLN [20]	5	15 cm Pb, 5 cm Cu	16 cm bor. PE, 14 cm NaI	plastic scin. 8 cm	2
GEMMA/Kalinin NPP [20]	20	15 cm Pb, 5 cm Cu	14 cm NaI	plastic scin. 8 cm	1.5
Dortmund Low Bkg Facility [103]	10	15 cm Pb, 8 mm Cu	9.5 cm bor. PE	plastic scin. 5 cm	1.274±0.002
Belgrade [104]	0	15 cm Pb, 1 mm, Sn, 1.5 mm Cu	none	none	2.02
	0	15 cm Pb, 1 mm, Sn, 1.5 mm Cu	NaCl	none	2.02
	0	25 cm steel	none	none	0.63
	0	25 cm steel	NaI	none	0.63
Bratislava [105]	≈2 (*)	15 cm Pb, 1 mm Cd, 2 mm Cu	none	prop. chamber	0.96
Rossendorf [106]	2.5	15 cm Pb, 2 mm Cu	none	none	1
Felsenkeller [106]	125	20 cm Pb, 20 cm Fe	none	none	0.8
GERDA/LNGS [107]	3500	liquid Ar, steel cryostat	none	water tank	

Table 5.9: Comparison of shields for HPGe spectrometers at surface, shallow depth and deep underground. All shields contain high Z materials to suppress background from natural radio activity. Materials to moderate (and capture) neutrons are included in some configurations. The resulting count rates of the 139.5 keV line of the neutron-induced ^{75m}Ge isotope are displayed in Figure 5.19. (* cellar 7 store building, **analyzed by the author of the thesis)

Overall, Figure 5.19 shows that the neutron fluence rate below approximately 10 MeV at the diode decreases with higher overburden, thus the decreasing muon flux overcomes other effects. As the cross section for the production of the metastable states decreases with higher neutron energy (see Figure 5.18), no reliable statement can be made on the neutron fluence rate at higher energies than this.

The figure also shows that the additional shield layers to moderate and capture neutrons contribute to a reduction of the neutron fluence rate at the diode in any case at shallow depth, where most of the data points in the plot were collected. Comparing the CONUS shield (25 cm Pb) to the GIOVE shield with less Pb (15 cm) in total but the innermost Cu layer, no increase in the line activity is observed within the statistics. There is no significant contribution of the additional Pb layers. This is in consistency with Figure 5.14 showing that most of the neutrons arriving at the diode are created within the Pb layers closest to the diode, while the others are removed by the layers of borated PE.

For smaller overburdens than ∼10 m w.e. and especially at the earth's surface the hadronic component of the cosmic rays has to be considered as well [29]. This is reflected in the higher count rates compared to the red CONUS line in e.g. the shield test experiments at the Belgrade laboratory [104] at earth's surface, even if a moderator is included within the shield. Up to ∼100 m w.e. the muon-induced neutrons dominate the neutron background. Deeper underground with a better suppression of the muon-induced background, other neutron sources such as (α,n) reactions need to be taken into account as well and excel the muon-induced contribution at some point [40].

Nevertheless, muon-induced neutrons are always a concern, as they are created potentially close to the detectors in high Z materials of cryostats or holders. This is the case for the GERDA experiment deep underground at 3500 m w.e. only an upper limit for the line activity of ^{75m}Ge could be determined in [107]. MC simulations of the muon-induced neutron fluence rate predict a count rate of about one order of magnitude smaller than the determined limit [108]. The water tank of the muon veto effectively shields neutrons from (α,n) reactions inside the ambient walls, while muons can create neutrons in the steel cryostat close to the HPGe detectors.

Contribution to background model

To include the contribution into the background model the decay of the metastable states is simulated separately in the diode volume. This is in any case necessary because of the long half-live, meaning that the energy deposition should not be added to the prompt muon-induced energy depositions and the propagation is stopped in the MC. For Geant4.9.4 and Geant4.9.6 the creation of the states in neutron capture is any way not implemented in the MC. Only with the most recent version Geant4.10 the interaction occurs, but the implementation has not been validated within the framework of this thesis. Instead the observed line count rates are used to scale the MC in Figure 5.17. The DAQ effects in the decay of ^{73}mGe inducing the structure from 53 keV to 66 keV is not included in the MC. Comparing data and MC, the count

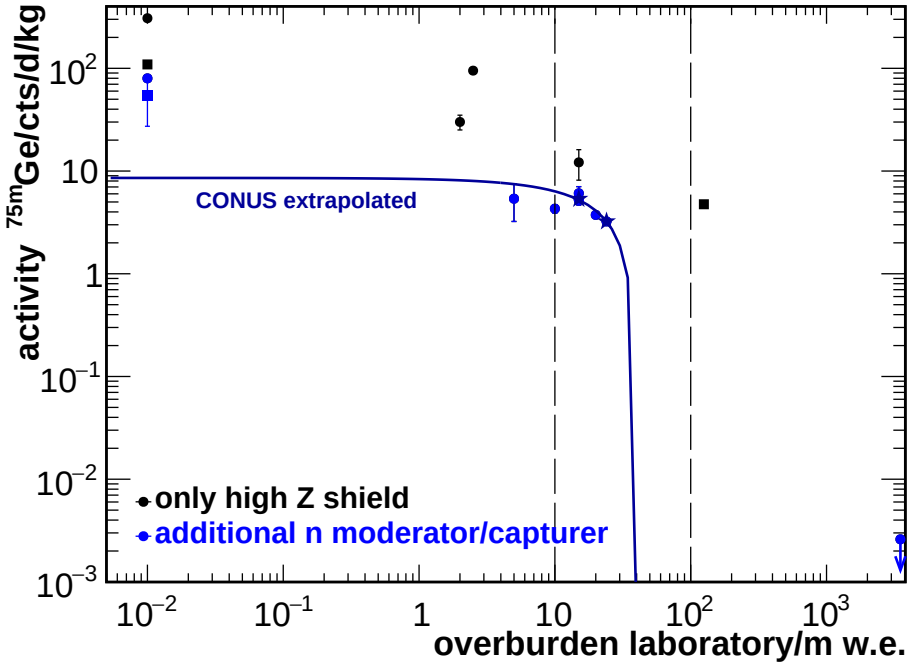

Figure 5.19: ^{75m}Ge line activity in dependence of the overburden and shield for various experiments with Ge spectrometers. The dots mark shields where the main high Z component is Pb, for the squares it is steel. Shields including materials to moderate and capture neutrons are denoted in blue. The stars represent the data of the CONUS experiment at LLL and KBR, extrapolated by the dark blue line.

rate in the structure around 23 keV line in the data clearly excels the contribution from the decay of ^{71m}Ge in the MC. An additional background contribution or DAQ effect is assumed. The hypothesis is supported by the observation, that at 23 keV not a single line, but rather a structure of several lines is observed for the full statistics of Conus-1.

The resulting contribution to the integral background in the MC is summarized in Table 5.10. On the one hand, in between the peaks only a few counts are deposited as most of the energy of the decays are deposited by electrons, which have a much shorter interaction range in Ge than γ-rays and are thus less likely to escape the detector. Moreover, at these energies Compton scattering as energy loss process for γ-rays in Ge is a lot less likely than the photoelectric effect (see Figure 1.11) further reducing the probability of a partial energy deposition. On the other hand, there can be a contribution to the continuum by slow pulses, which are especially important in the ROI at low energies (see Figure 2.25). All in all, comparing to the measured background the metastable states only have a minor contribution to the ROI.

integral range	MC metastable Ge cts/kg/d	$\mathcal{O}$(meas. bkg) cts/kg/d
[0.3,1]keV$_{ee}$	0.05±0.01	∼15
[2,7]keV$_{ee}$	0.09±0.01	20-30
[11,440]keV$_{ee}$	24.3±2.4	400-800

Table 5.10: Contribution of decays of metastable states to the ROI, exemplary for Conus-1. The order of magnitude of the measured background rates of the Conus detectors is given as reference, showing that the background is sub-dominant for the ROI.

5.3.5 In situ activation

The constant muon-induced neutron fluence rate at the diode leads to activation of Ge, Cu and Pb. Long-lived states with life-times from several hours to several days are created, which means they cannot be suppressed with help of the muon veto. The only lines observed from the in situ activation belong to the decay of ^{71}Ge. The ratio of the line count rate to the line count rate of the ^{71m}Ge decay makes it possible to draw conclusions on the cross section at the neutron energy responsible for the activation. For the other activated isotopes a rough estimation of the contribution to the continuum was carried out.

In situ activation of ^{71}Ge

The activation of ^{71}Ge occurs via neutron capture and (n,2n) reactions on ^{70}Ge. For the (n,2n) reaction neutrons of at least 10 MeV are required [117]. Thus, the interaction is considered negligible for the CONUS experiment even for measurements with the ^{252}Cf neutron source. Part of the deexcitation to the ground state goes via the decay of ^{71m}Ge. Thus, the ratio of the neutron energy-dependent cross sections is related to the count rates in the 198 keV and the 10.37 keV line. The detection efficiencies ϵ and branching ratios br of the lines have to be taken into account. The following relationship holds if the 10.37 keV line is only created by the decay of ^{71m}Ge:

$$r^{71} = \frac{\sigma_{^{71}Ge}}{\sigma_{^{71m}Ge}} = \frac{N_{^{71}Ge}}{N_{^{71m}Ge}} \frac{\epsilon_{^{71m}Ge}}{\epsilon_{^{71}Ge}} \frac{br_{^{71m}Ge}}{br_{^{71}Ge}} \tag{5.4}$$

Table 5.11 summarizes the respective data and parameters for Conus-1. In equilibrium, the production rate of ^{71}Ge via neutron capture corresponds to the observed decay rate of the isotope. The determination of the count rate in the 10.37 keV line from in situ activation is described in Section 5.4.4, details on the decay of ^{71}Ge can be found in Section 5.4.1. The calculation gives $r^{71}_{meas,insitu} = \frac{\sigma_{^{71}\mathrm{Ge}}}{\sigma_{^{71m}\mathrm{Ge}}} = 4.1 \pm 0.4$.

The ratio of the cross sections for thermal neutron energies amounts to $r^{71,therm}_{lit} = \frac{\sigma_{^{71}Ge}}{\sigma_{^{71m}Ge}} = 10.5 \pm 2.2$ (mean value of data provided in Table 5.5, the uncertainty covers both values). The value is more than a factor of two larger than $r_{meas,insitu}$ and only

Conus-1	^{71m}Ge	^{71}Ge
line	198.3 keV	10.37 keV
count rate/cts/d/kg	3.14±0.12	16.0±1.2
MC efficiency	0.66	0.93
branching ratio	1	0.876
activity/cts/d/kg	4.8±0.3	19.7±1.5

Table 5.11: Neutron capture on ^{70}Ge results in ^{71m}Ge and ^{71}Ge. The respective count rate of the decays of both isotopes were evaluated and can be used to examine the relation of the cross sections. This requires knowledge of the branching ratios and detection efficiencies also depicted in the table.

due to the large uncertainty of the cross sections just compatible within $3\,\sigma$. From the MC simulations, it is known that the neutron fluence rate at the diode are mostly of fast neutrons. The discrepancies potentially indicate that the cross section ratio differs to the one for thermal neutrons. To the knowledge of the author of this thesis, there is no direct measurement of the production cross section of ^{71m}Ge for fast neutrons. To confirm the hypothesis, the activation from fast neutrons with a ^{252}Cf source was analyzed in the same way. This is discussed in detail in Section 7.4.

In situ activation without observed line background

The branching ratio of the γ-ray line emitted in the decay of ^{75}Ge is only 11.4% and the line is not observed in the background data within the statistics available. However, the dominant decay branch is a β decay with an endpoint of 1177 keV. The contribution to the background is estimated similar to equation (5.4) with the help of the count rate in the ^{75}Ge line and the cross section ratio, which is in this case also available at higher neutron energies (see Table 5.5 and Figure 5.18). For thermal neutrons $\frac{\sigma_{^{75}Ge}}{\sigma_{^{75m}Ge}} = 3.8 \pm 0.4$, while at approximately 1 MeV $\frac{\sigma_{^{75}Ge}}{\sigma_{^{75m}Ge}} = 1.7 \pm 0.3$. At higher energies above 4 MeV it drops to 1 [114]. According to Table 5.3, the cross section for thermal neutrons is about 20 times larger than for fast neutrons, while at the diode about 30 times more fast neutrons than thermal ones arrive. Thus, a mean value of $\frac{\sigma_{^{75}Ge}}{\sigma_{^{75m}Ge}} = 2.4 \pm 0.4$ was adopted for the calculation. From the measured count rate in the 139.5 keV line and the detection efficiency of 0.86 for the line in Conus-1 derived from MC, a count rate of of (7±1) cts/d from the decay of ^{75}Ge is expected for the detector over the full spectral range and included into the background model.

In situ activation also occurs in Cu and Pb. In the copper parts of the cryostat and crystal holder ^{64}Cu and ^{66}Cu are created. The capture cross section is comparable to ^{71}Ge [117]. Both undergo a β decay and also γ-ray lines are emitted. However, due to the smaller Cu mass in close vicinity to the diode and the decays occurring outside of the active volume, the probability to detect these γ lines is at least one order of magnitude smaller. Thus, the background contribution is considered negligible. For

Pb, which persists in large quantities inside the shield, only one isotope, ^{209}Pb, can be activated in neutron capture. It decays via β decay with an end point of 644 keV. But the cross section for thermal neutron capture is several orders of magnitude smaller than for neutron capture on Ge [117]. This and the self-shielding of the high Z material means that the decay can be neglected for the description of the background.

5.4 Cosmogenic activation

Cosmic activation in Ge and Cu by the hadronic component of cosmic rays occurs during manufacturing and if the detectors are stored overground. The background contribution is examined in detail, because this background within or close to the crystal cannot be shielded. It can only be kept low by keeping the detector underground during manufacturing as much as possible to avoid the activation on the first hand. Moreover, some of the isotopes have half-lives of several hundreds of days, which means that the decay could be relevant for the data sets of the experiment. It has to be evaluated whether a time-dependent background contribution has to be taken into account for the CEνNS analysis.

To limit the number of potential isotopes examined, the half-life and the production rate in Ge and Cu were take into account. Before the start of Run1 the detectors were underground continuously at KBR for about 67 d. The transportation to KBR took less than 2 d and before this the detectors were mostly underground at the LLL at MPIK for the last four months of commissioning. Thus, for the physics data taking at KBR a lower limit on the half-life of 100 d has been selected. For the commissioning phase at LLL and KBR also ^{73}As is taken into account as its line is observed. An overview on the isotopes considered is given in Table 5.12. The signatures of the decays are also depicted in the table. For the signature of the decays several categories can be identified: only γ-rays or only X-rays or only β decay electrons are emitted or a combination there of. The emission of X-rays are of special interest because they are the only lines potentially visible in the spectral range below 15 keV. The X-rays are merely observed for decays within the Ge. All other contributions from outside are shielded by the Cu parts of the cryostat as can be seen in the efficiency curve in Figure 2.26. Additional γ or electron emission such as for ^{65}Zn can add up with the X-rays leading to a decrease in the observed X-ray line count rates. For some isotopes or decay volumes no line signature will be observed. This happens either if the isotope in question is a pure β emitter (e.g. ^{3}H) or if all γ-ray lines with a significant branching ratio are emitted at energies above the energy range of the CONUS detectors at about 450 keV (e.g. ^{60}Co). In general, for γ-rays with high enough energies, SEP and DEP are created and they can potentially be observed within the energy range available. However, Figure 2.26 shows that the detection efficiency of these peaks is very small for the CONUS detectors.

In the next section, the activation and decay of the isotopes is described in detail. For the most important ones, where the lines are observed in the experiment (^{68}Ge,

isotope	half life [d]	production rate Ge [cts/kg/d]	production rate Cu [cts/kg/d]	X-rays	γ-rays	β decay
^{68}Ge	270.95	59.1±43.9	no	x		
^{68}Ga	0.047	from ^{68}Ge	no	x	(x)	x
^{75}Zn	244.01	50.1±21.9	no	x	(x)	x
^{57}Co	271.8	7.59±3.9	54.8±19.2	x	x	
^{60}Co	1923.6	3.86±1.5	45.5±26.4	x	(x)	x
^{54}Mn	312.19	2.6±1.7	16.3±7.3	x	(x)	x
^{3}H	4493.88	78.05±57.4	no			x
^{55}Fe	1002.66	5.78±2.6	no	x		
^{73}As	80.3			x		

Table 5.12: Half-lives and production rates (mean value and variance of data found in [136] for Cu and found in [124] - [135] for Ge) of the cosmogenically activation isotopes at the earth surface relevant for the CONUS experiment. The decay of ^{73}As was only observed at LLL and during the commissioning at KBR. Column 5-7 classify the signature of the decays. (x) marks emission out of the energy ranges of the CONUS detector data acquisition.

^{68}Ga and ^{65}Zn), the implementation of the decays in Geant4 is checked against literature as well. This is followed by the derivation of the activation rates from visible lines in the CONUS data, that can be compared to the activation rates from literature. From the activation rates and the MC, the impact on the background can be quantified. If no lines are visible, the production rates from literature are used. It can be shown that the decay is negligible for the CEνNS analysis.

5.4.1 Relevant cosmogenic-induced isotopes for CONUS

All data on the nuclides is taken from the nuclear data table of the Laboratoire National Henri Becquerel [120] if not stated explicitly otherwise.

Each Ge diode has a mass of 0.975 kg that is activated. For Cu, the copper parts in close vicinity to the diode are taken into account, in total 2 kg. Radio activity from decays within the volume of the crystal holder are most likely to be observed in the detectors. Not all isotopes activated in Ge can be activated in Cu, but in Cu the activation rate is about 5-15 times higher than in Ge (see Table 5.12).

LowE line background: ^{68}Ge/^{71}Ge, ^{68}Ga, ^{65}Zn and ^{73}As

The cosmogenic induced lines visible in the lowE range of the CONUS experiment are all created in EC transitions. They all share similar features: the K shell emissions with energies around 10 keV are emitted with a probability of approximately 0.9, while the L shell lines lie at about 1 keV with an order of magnitude smaller emission probability (see Table 5.13). With the current energy threshold of the CONUS experiment the M shell contributions cannot be observed. Some isotopes additionally emit γ-ray lines and electrons that sum up with the X-rays and Auger electrons.

The dominant line within the lowE range of CONUS is the 10.37 keV line emitted by the K shell of ^{68}Ge and ^{71}Ge (both 100% EC). The ^{68}Ge isotope is produced by spallation reactions, which require neutrons of at least ∼20 MeV [137], e.g:

$$^{70}\mathrm{Ge} + \mathrm{n(fast)} \rightarrow^{68} \mathrm{Ge} + 3\mathrm{n} \tag{5.5}$$

Thus, the reaction only occurs at the earth surface. On the contrary, ^{71}Ge is created in neutron capture by thermal neutrons up to a few MeV. This makes in-situ activation within the shield possible (see Section 5.3.5) or via a ^{252}Cf neutron source (see Section 7.4). Both decays result in the same line energies, but the half-lives differ with 278 d for ^{68}Ge and 11.4 for ^{71}Ge. This feature can be used to disentangle the contributions as done in Section 5.4.4. The branching ratios (see Table 5.13) differ slightly as well.

The decay of ^{68}Ge results in ^{68}Ga, which decays instantly itself by EC (10.86%) and positron emission (89.14%). The K shell X-ray line at 9.69 keV from the EC transition is observed in the CONUS background. Due to the smaller EC branching ratios the line count rate is expected to be about one tenth of the count rate in the 10.37 keV line of ^{68}Ge. There are also γ-rays (highest branching ratio 1.778 for 511 keV line) and electrons emitted (end point energy for dominant decay: 1899.1keV).

Moreover, ^{65}Zn is created in spallation reactions with fast neutrons at the earth's surface:

$$^{70}\mathrm{Ge} + \mathrm{n(fast)} \rightarrow^{65} \mathrm{Zn} + 2\mathrm{n} + \mathrm{He} \tag{5.6}$$

In the ^{65}Zn decay (100% EC) with a half-life of 244 d next to the X-rays and Auger electrons at 8.96 keV also γ-rays at 1115.54 keV (branching ratio 50.2%[116]) and 511 keV (2%[116]) are emitted and there is a β decay with an endpoint of 329.9 keV. Summations of the K shell emission with the 1115.54 keV γ-ray line diminish the effective efficiency of the line from close to 0.9 to 0.4.

The L shell emissions of all the isotopes discussed are emitted at an energy around 1 keV. They are so close in energy that they are observed as a single broad peak, even with the excellent resolution of the CONUS detectors.

The accuracy of the MC simulation in the decay of the isotopes was examined. The ratio between K shell and L shell emissions is calculated and compared to literature in Table 5.13. An excellent agreement is found. For older Geant4 versions (4.9.4 and 4.9.6), within the L shell sub shells the emission is found to be incorrectly, as the energy is distributed equally over the three shells instead according to the branching ratios. This is fixed in Geant4.10. with improvements in the atomic deexcitation module [138]. With the more recent Geant4 version also the non-natural line width of several 100 eV observed by the author of this thesis disappears.

Regarding the energy of the emitted lines, small discrepancies of up to a few 10 eV are found to the energy values from literature that are used for the calibration of the CONUS data. Geant4 relies on the calculations of the "Evaluated Atomic Data Library" (EADL) [121]. This means most notably, that the 10.37 keV line is

placed at 10.33 keV. The discrepancies still persist throughout all Geant4 versions examined. The L shell X-ray lines around 1.3 keV are spread slightly broader in the MC. For the CEνNS analysis it is not necessary to correct for the shifts in energy as the ROI is sufficiently away from the peaks.

A detailed examination of the ^{71}Ge decay in the MC can be found in [122]. It was confirmed that the emission of X-ray cascades and Auger electrons is done correctly relative to each other.

As a side remark, it is also mentioned that in the LLL data and during commissioning at KBR, one additional line is observed created in the decay of ^{73}As, which is also produced in spallation reactions at earth' surface. Contrary to the other isotopes, ^{73}As (100% EC) has a much shorter half-life with 80.3 d. The K shell line is emitted at 11.10 keV with no emission of additional particles. Thus, it is irrelevant for the KBR data. Most notably about the decay is that it results exclusively in the metastable state ^{73m}Ge, thus increasing the line count rate from this decay compared to what is expected from neutron capture (see Section 5.3.4).

HighE line background: ^{57}Co

The only isotope with visible line background in the CONUS data from the activation of Ge and Cu is ^{57}Co. It is possible to separate the two volumes according to the signature of the decay.

The isotope decays with a half-life of 271.8 d to the excited states of ^{57}Fe. The largest contribution to the γ emission comes from the deexcitation of the 5/2- state, where γ-rays with energies of 122.06 keV are emitted with a branching ratio of 85.49%. The full deexcitation of the ground state occurs via emission of 14.42 keV γ-rays with a branching ratio of 9.18%. Furthermore, with a probability of 10.71% the $5/2^-$ state decays directly to the ground state by emitting 136.47 keV. X-rays are emitted as well with energies of 6 to 7 keV (K shell). If the decay occurs within the Ge, the single peaks are only visible if a X-ray or γ-ray does not deposit any energy at all within the Ge. At such low energies this only seldom occurs making the summation peak at 143.5 keV (=122.06keV+14.42keV+6-7 keV or 136.47+6-7 keV) the largest contribution with a detection efficiency of 0.69. This is followed by a line at 21.5 keV(=14.42keV+6-7 keV) with a detection efficiency of 0.09. The probability to observe the X-rays alone is small. For the decay to occur within the Cu the X-rays and the 14.42 keV γ-ray have too little energy to reach the Ge diode. Thus no summation will happen. The 122.06 keV is most likely to be seen in the detector followed by the 136.47 keV γ line with 1/9 of the branching ratio. The detection efficiency strongly dependence on the location of the Cu parts with respect to the Ge diode. The largest detection efficiency of the 122.06 keV line is observed for the crystal holder with a mass of 0.5 kg. Summing up all contributions from Cu parts close to the diode (m_{ges}=2.0 kg) and weighted by the mass of the single parts a total efficiency of 0.03 is found. The described signatures for the decay in Ge and Cu are illustrated in Figure 5.20, where the spectra are scaled with the respective masses and production rates assuming equal exposure.

isotope	energy MC	energy literature	branching ratio MC (Geant4.10)	ratio K/L MC (Geant4.10)	ratio K/L lit
^{68}Ge	10.33	10.3664±0.0005	0.865	0.132	0.133±0.003
	1.291	1.2977±0.0011	0.113		
^{71}Ge	same as ^{68}Ge	same as ^{68}Ge	0.876	0.119	0.119±0.003
	same as ^{68}Ge	same as ^{68}Ge	0.105		
^{68}Ga	9.69	9.6586±0.0006	0.0789	0.110	0.111±0.001
	1.252	1.1936±0.0009	0.0087		
^{65}Zn	8.96	8.9789±0.0004	0.430	0.110	0.114±0.001
	1.101	1.0966±0.0004	0.047		

Table 5.13: Comparison of K and L shell energies of the cosmogenic background implemented in the MC (EADL database [121]) and literature [118] with estimated uncertainties from [119]. The branching ratios were also extracted from MC. The K to L shell ratio is taken from [120].

No line background

For the complete description of the cosmogenic background contributions four more isotopes created in spallation reactions at the earth's surface without visible line background are included: ^{55}Fe, ^{60}Co, ^{54}Mn, ^{60}Co, and ^{3}H.

^{55}Fe dominantly decays by the emission of X-rays (100% EC) with a K shell line at 6.54 keV. There is a γ line at 126 keV with a branching ratio of 10^{-7}. The isotope has a half-life of 2.74 yr. Due to the much smaller production rate (see Table 5.13) and the short sea level exposure of the CONUS detectors (see Section 5.4.2), the count rate is below the sensitivity of the CONUS detectors. Also, almost no iron has be used as material within the cryostat.

This is similar for the decay of ^{54}Mn (100% EC) with a half-life of 312.1 d. X-rays are induced as well with the K shell line at 5.99 keV, but the count rate is too small to be observed due to the low production rate in Ge. In Cu, the production rate is higher, but the X-rays do not reach the active volume of the diode. Additionally, a γ-ray at 834.848 d (99.98%) is emitted outside of the highE energy range of the CONUS detectors.

Furthermore, ^{60}Co is created in both, Ge and Cu, if stored overground. It has a half-life of 5.27 yr and decays via β^- decay. The Q value of the dominant decay lies at 318.13 keV. With a branching ratio of nearly 100% γ-rays with 1173.2 keV and 1332.5 keV are emitted. There is only a minor contribution by X-rays. The energies of the dominant γ lines are out of the energy range observed with the CONUS detectors, but the Compton continuum contributes to the integral background. The β decay is more important within the Ge diode than the Cu parts.

Lastly, ^{3}H originates from nuclear reactions by the hadronic component of the cosmic rays. It decays exclusively by β decay with a half-life of 17.79 d. The end point is with 18.6 keV close to the lowE range of the CONUS detectors. Even though the production rate has large uncertainties, the contributions were observed for Ge spectrometers by the EDELWEISS experiment deep underground [43].

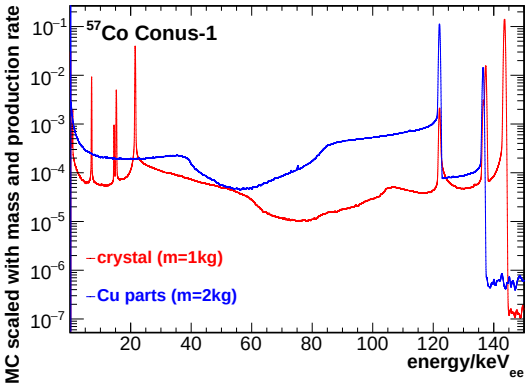

Figure 5.20: MC simulation of ^{57}Co decays within the diode and the Cu cryostat parts.

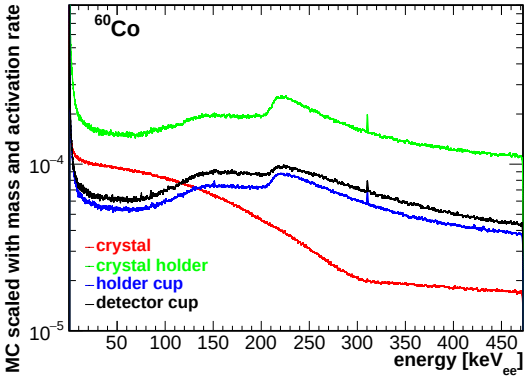

Figure 5.21: MC simulation of ^{60}Co decays within the diode and the Cu cryostat parts.

5.4.2 Activation history

For all the isotopes listed in Table 5.12 the energy threshold for the production reactions by protons and neutrons lies well above the mean energies of the particles remaining underground if an overburden of approximately 10 m w.e. or more is guaranteed (see chapter). During the commissioning at LLL and since the detectors are deployed at KBR no further activation is expected. Only in situ activation from neutron capture described in Section 5.3.5 occurs.

Table 5.14 summarizes the total effective sea level exposure of the Ge crystals and Cu parts of the detectors. For the Ge crystals it is assumed that the activation except for ^{68}Ge starts with the end of the crystal pulling as all previous activation is removed during the crystallization process [43, 139]. The activation history for the germanium before the crystal pulling is not known and thus for ^{68}Ge only a minimum and maximum production rate can be derived. The copper parts had been stored underground at LLL and the in situ activation there is assumed to be negligible. The beginning of the work on the copper parts is supposed to be the start of the activation. During the detector production whenever no work was ongoing the crystals and Cu parts were brought to the LLL to keep them underground as much as possible. This results in the overall low exposure. Conus-1 was the first detectors produced and extensive testing was carried out, which results in high sea level exposure and thus the largest background contribution. But even for this detector line background such as from the decay of ^{55}Fe and ^{54}Mn is not seen in the data taking at KBR (see Section 5.4.1), while it is visible inn other Ge based shallow depth experiments e.g. TEXONO [123].

5.4.3 Count rate in experiment

For the observed line background the count rate over time was fitted with a model of the decay to be able to determine the count rate for each point in time. With

detector	total effective sea-level exposure [d]	
	Ge	Cu
Conus-1	135	∼116
Conus-2	99	∼73
Conus-3	66	∼101
Conus-4	91	∼116

Table 5.14: Total effective sea level exposure of the Ge crystals and Cu cryostat parts of the CONUS detectors before deployment at KBR evaluated by W. Maneschg.

the help of the MC simulation the respective contribution of the ROI and the time development can be studied. Furthermore, from the count rate and the activation history of the detectors production rates can be derived and compared to literature. For all cosmogenic contributions without lines it was relied on the production rates from literature to scale the MC simulation and determine the decaying contribution to the ROI.

5.4.4 Cosmogenic background of CONUS with visible lines

Table 5.15 summarizes the line background of all the cosmogenic induced lines observed at LLL and KBR within the lowE range and highE range. Due to the short half-live the 11.10 keV line of ^{73}As was only seen at the beginning of data collection at KBR. To determine the activation activity at deployment at KBR, the decay over time was observed for various lines. To do this all available data were split in approximately monthly time bins. The data sets start in February/March 2018 at KBR except for ^{57}Co and ^{73}As were also the data at LLL were taken into account. The line count rates were determined according to the method described in Section 2.2. This means that each peak was fitted to find the width and the net peak area was extracted via the counting method. Due to statistics for all except the 10.37 keV line the spectra in monthly binning were not fitted individually, but the combined spectrum was used to determine the peak width. Only the statistics uncertainties are taken into account and the data collected during reactor OFF time are corrected for the difference in the muon veto dead time (see Section 3.1.2).

Figure 5.22 to Figure 5.27 shows the count rates plot against the time exemplary for Conus-1. The 10.37 keV line is the only line analyzed with more than one isotope contributing. The fit model consists of the decay of ^{68}Ge activated at the earth surface, the decay of ^{71}Ge from the in-situ activation at LLL and during transport

energy [keV]	isotope	energy range
1.3	^{68}Ge/^{71}Ge, ^{68}Ga, ^{65}Zn	lowE
8.96	^{65}Zn	lowE
9.69	^{68}Ga	lowE
10.37	^{71}Ge	lowE
11.10	^{73}As	lowE
122.06, 143.5	^{57}Co	highE (C1)

Table 5.15: All cosmogenic induced lines observed in the background data of the CONUS experiment. The energies, isotopes and energy ranges, where the lines are visible, are given.

and finally the balance of the in situ activation and decay of ^{71}Ge at KBR:

$$\begin{aligned} N^{^{68}\mathrm{Ge}}(t) = & \underbrace{N^{^{68}\mathrm{Ge}}_{ref0} \cdot exp\left(\frac{ln(2)}{T^{^{68}\mathrm{Ge}}_{1/2}}(t - t_{ref})\right)}_{\text{decay } ^{68}\text{Ge surface}} \\ & + \underbrace{N^{^{71}\mathrm{Ge}}_{ref1} \cdot exp\left(\frac{ln(2)}{T^{^{71}\mathrm{Ge}}_{1/2}}(t - t_{ref})\right)}_{\text{decay } ^{71}\text{Ge in situ at LLL}} \\ & + \underbrace{N^{^{71}\mathrm{Ge}}_{ref2} \cdot \left(1 - exp\left(\frac{ln(2)}{T^{^{71}\mathrm{Ge}}_{1/2}}(t - t_{ref})\right)\right)}_{\text{in situ production and decay } ^{71}\text{Ge at KBR}} \end{aligned} \tag{5.7}$$

If the detectors are stored underground for a sufficiently long time, only the in situ activation of ^{71}Ge occurs and the count rate becomes stable. For all other lines only the decay has to be considered:

$$N^{i}(t) = N^{i}_{ref} \cdot exp\left(\frac{ln(2)}{T^{i}_{1/2}}(t - t_{ref})\right) \tag{5.8}$$

For the equations to hold, it is assumed that saturation is never achieved since crystal pulling. During the fit the half-lives are fixed to the values in Table 5.12 as the values are accurately known from literature. The reference time t_{ref} is 24.01.2018, when the detectors were brought to KBR. To convert the count rate at the reference time to the activity per mass of the activated material m_{mat}, the mass and the muon veto dead time correction for reactor ON was included. The branching ratio br of the line as well as the MC detection efficiency ϵ_{MC} also have to be taken into account:

$$A_{ref} = \frac{N^{i}_{ref}}{m_{mat} \cdot c^{ON}_{dt} \cdot br \cdot \epsilon_{MC}} \tag{5.9}$$

As the decay was simulated over the full detector volume and the reduction to the active volume is only taken into account during post-processing, the uncertainty on the active volume of about 1% (see Section 2.2.5) is included as uncertainty on the MC detection efficiency.

Production rates derived from CONUS data

From the activities at reference time evaluated in Table 5.16 and the activation history, the production rates can be derived and compared to literature.

det.	activity [cts/d/kg] at 24.01.2018							
	^{71}Ge	^{71}Ge	^{68}Ge	^{68}Ga	^{65}Zn	^{57}Co	^{57}Co	As
mat.	Ge	Ge	Ge	Ge	Ge	Ge	Cu	Ge
mass	0.975 kg	0.975 kg	0.975 kg	0.975 kg	0.975 kg	0.975 kg	2 kg	0.975
act. loc.	LLL/surface	KBR	surface	surface	surface	surface	surface	surface
1	131.3±14.7	19.3±1.3	40.2±2.4	47.7±3.3	12.2±0.5	2.6±0.4	17.4±3.9	1.1±0.4
2	198.1±56.4	18.0±1.1	25.2±2.2	27.6±2.8	8.0±0.4	nd	nd	nd
3	127.2±16.7	21.5±1.1	20.9±2.1	32.8±2.5	8.1±0.4	nd	nd	nd
4	242.1±15.6	19.9±1.2	21.6±2.2	30.2±2.9	6.7±0.4	nd	nd	nd

Table 5.16: Activity of cosmogenic isotopes in the Ge and Cu of the CONUS detectors on 24.01.2018, when the detectors were deployed at KBR. The activities are determined from a fit to the decay of the line count rates observed during the data collection at KBR.

The alternating activation at surface and decay underground during manufacturing until the reference time was modeled by W. Maneschg. It was searched for a production rate such as to reproduce the activity derived from the data at reference time. The results are shown in Table 5.17. In the literature largely varying production rates from measurements and simulations are found. Therefore, a mean value with standard deviation is given in the table for comparison.

For ^{75}Zn and ^{57}Co activated in Ge an excellent agreement to the mean value found in literature is found. In both cases, it can be assumed that the previous activated isotopes are removed in the crystal pulling process and the observed activation started afterwards, where the activation history is well documented. The ^{68}Ge activation cannot be removed in the crystal pulling process meaning that the state of the activation with the beginning of the documentation is not known. Therefore, two extreme cases were examined: (1) no activation at all and (2) saturation (all available Ge activated) at crystal pulling. The derived production rate differs by a factor of four. For the activities at reference time calculated from the production rate for all four detectors a slightly better agreement for (1) was found, while (2) is closer to the mean value from literature.

The exposure history of the Cu parts is less well known than for the Ge diodes. Under the assumption of no activation before the start of the manufacturing process the derived production rate is about twice as large as excepted from literature. But

due to the large uncertainties the values are still compatible. The observation might indicate that the speculation of zero activation at the start of the fabrication of the detectors is not fully true for the Cu parts.

Contribution to background model

As the CONUS experiments looks for excesses on top of a continuous background, it is important to quantify the time-varying contribution of the decay of the cosmogenic isotopes to the background.

All relevant cosmogenic isotopes are simulated within the Ge diode and the Cu parts. To be conservative for the final estimation, all Cu in the vicinity of the diode is represented by the crystal holder, which has the highest probability for decay radiation within the volume to be seen in the detector. If scaling is required, the total mass of Cu parts of 2 kg is applied. The MC is normalized in the following way:

- visible line background: the activity at reference time is used for scaling and the measurement uncertainties are applied
- no visible line background: the mean production rate and standard deviation from Table 5.12 are used for the normalization

Figure 5.28 and Figure 5.29 contain all the scaled MC contributions and the measured background during the outage of Run1. The two dominant contributions to the low energy background below 10 keV$_{ee}$ come from ^{71}Ge, ^{68}Ge and ^{3}H. For the two first isotopes the integral background is solemnly created by slow pulses, which strongly increase below 1 keV towards the threshold. Tritium decays purely as β decay with an endpoint of 18.6 keV, which makes it the largest cosmogenic-induced contribution to the continuum above the L shell X-ray line at 1.3 keV by ^{71}Ge, ^{68}Ge, ^{68}Ga and ^{65}Zn. At higher energies ^{57}Co and ^{68}Ga are most important. The first one due to the lines visible in the data and the ladder one contributes by a beta decay.

Table 5.18 quantizes the contribution to the integral background for selected time stamps. Due to the different exposure histories the contributions for the four de-

s	material	production rate CONUS data [cts/kg/d]	lit [cts/kg/d]
^{68}Ge	Ge	zero activation at crystal pulling: 136±10	59.1±43.9
^{68}Ge	Ge	saturation at crystal pulling: ∼35	
^{65}Zn	Ge	42±5	50.1±21.9
^{57}Co	Ge	9.0±1.5	7.6±3.9
^{57}Co	Cu	125±27	54.8±19.2

Table 5.17: Production rates of cosmogenic isotopes derived from visible line background in the CONUS experiment including a comparison to measured values from literature ([136] for Cu and [124] - [135] for Ge).

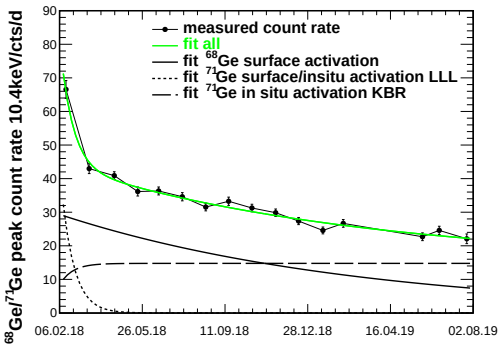

Figure 5.22: Decay of count rate of 10.37 keV line of over time. The single contributions of ^{71}Ge and ^{68}Ge can be disentangled by the fit model.

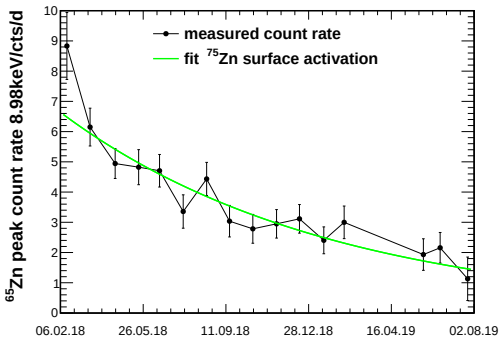

Figure 5.23: Decay of count rate of 8.96 keV line of ^{65}Zn over time with fit.

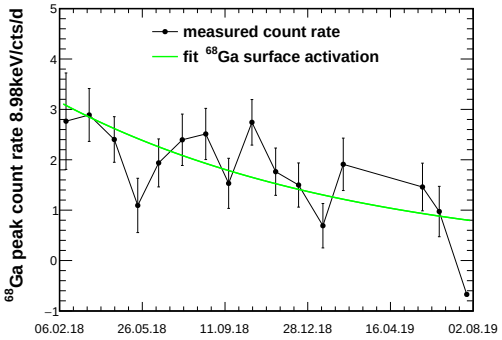

Figure 5.24: Decay of count rate of 9.69 keV line of ^{68}Ga over time with fit.

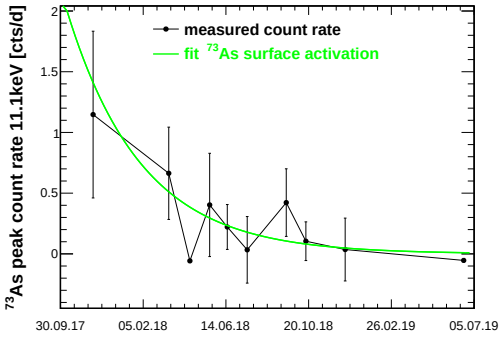

Figure 5.25: Decay of count rate of 11.10 keV line of ^{73}As over time with fit. The line is not visible any more with the start of Run1.

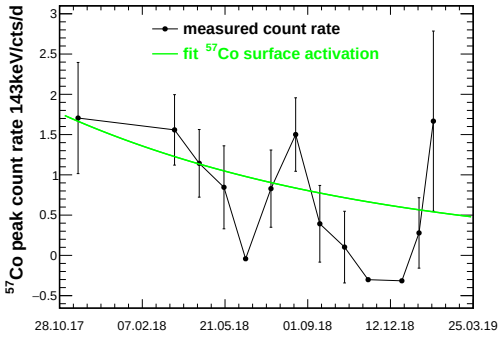

Figure 5.26: Decay of count rate of 143.5 keV line of ^{57}Co over time with fit.

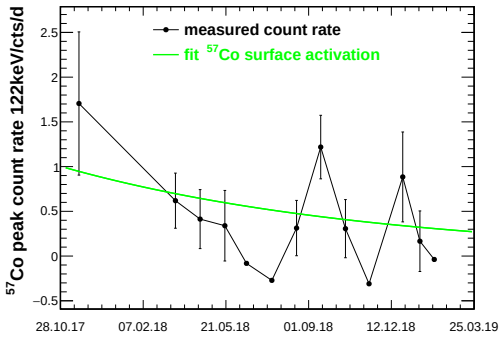

Figure 5.27: Decay of count rate of 122.06 keV line of ^{57}Co over time with fit.

detector	timestamps	[0.3,1]keV$_{ee}$ cts/kg/d	[2,7]keV$_{ee}$ cts/kg/d	[11,440]keV$_{ee}$ cts/kg/d
1	24.01.2018	1.0±0.1	2.5±0.6	15.8±1.5
	15.04.2018	0.5±0.1	1.7±0.6	13.0±1.3
	15.06.2019	0.3±0.1	1.2±0.5	4.8±0.5
2	24.01.2018	1.0±0.2	2.0±0.5	7.6±1.0
	15.04.2018	0.3±0.1	1.1±0.4	6.3±0.9
	15.06.2019	0.2±0.1	0.8±0.4	2.4±0.3
3	24.01.2018	0.6±0.1	1.4±0.3	9.0±1.2
	15.04.2018	0.3±0.1	0.9±0.3	7.4±1.0
	15.06.2019	0.2±0.1	0.6±0.3	2.8±0.4
$\mathcal{O}$(meas. bkg)		∼15	20-30	400-800

Table 5.18: Expected contribution of the decay of the cosmogenic-induced isotopes to different energy ranges including the ROI derived from MC for three selected timestamps (deployment at KBR, outage Run1, outage Run2). The MC was normalized with the measured line count rate if available, else the production rates from literature were used. The order of magnitude of the measured background rates of the Conus detectors is given as reference, showing that the background contribution to the ROI is sub-dominant.

tectors vary with the maximal contribution found for Conus-1. The described composition of the background means for the ROI that the strongest decrease in the count rate is observed shortly after the detector has been brought underground as long as the ^{71}Ge with an half-life of 11.4 d from the surface is still visible. With the start of the physics data taking with the beginning of the outage of Run1 in April 2018, the contribution has almost decayed away. The remaining ^{68}Ge has a much longer half-life of nearly a year and ^{3}H with a half-life of 12.3 yr can be considered stable within data taking periods of several months. For the ROI the energy interval between the outage of Run1 in 2018 and Run2 in 2019 only a maximum difference in the count rate of 0.2 cts/d/kg is expected. This is considered negligible for the CEνNS analysis. Within 2020 the ^{68}Ge will even become fully irrelevant as background contribution and there will only be the stable in situ activation of ^{71}Ge.

For the same reasons, within [2,7] keV$_{ee}$ the variations are also minor with a difference of at most 0.7 cts/d/kg between the outages. This assumption has to rely on the production rate of ^{3}H, which is not well known in literature and leads to the large uncertainties observed.

Above 20 keV the highest absolute decrease occurs as ^{57}Co and the ^{68}Ga (due to the parent isotope ^{68}Ge) have a half-life of about a year. Consequently, between the outages the count rate drops by half. However, the reduction is by far negligible compared to the background from other sources (see Table 5.18).

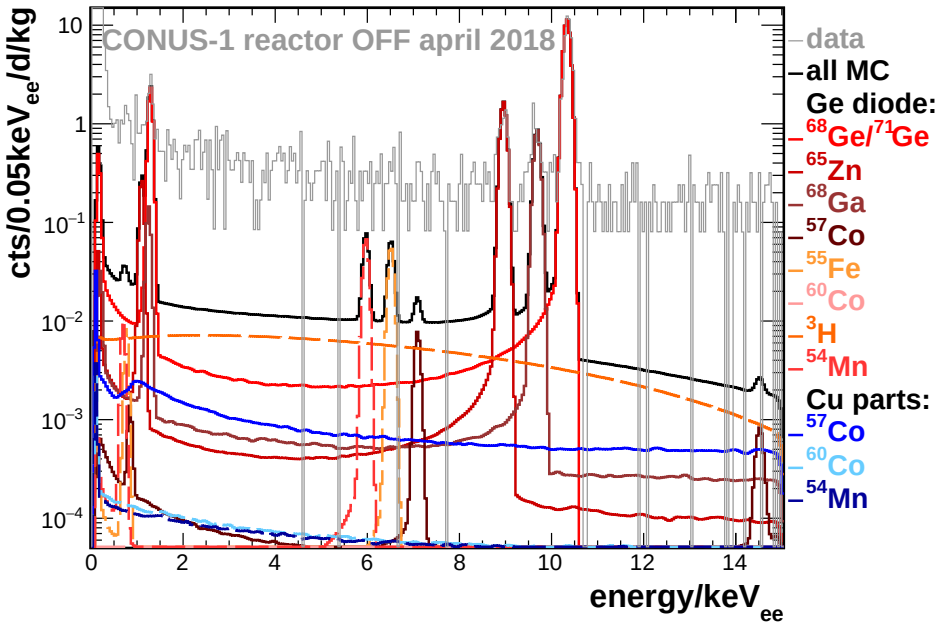

Figure 5.28: Cosmogenic activated contributions in the Ge diode and the Cu parts of the detector from MC in the lowE range. The data of the outage in April 2018 is plotted as comparison. The spectra from decays in Ge are displayed in shades of red and the spectra from decays in Cu in shades of blue. If no line background is visible in the data, the spectra are depicted with dashed lines.

5.5 Radon

5.5.1 Radon as background source

Within buildings and especially underground laboratories Radon with its radioactive isotopes ^{222}Rn and ^{220}Rn needs to be considered as background contribution (see Section 1.5.2). In the LLL, activities around 60 Bq/m^3 were observed, while at KBR inside the containment where there is no exchange with outside air the activity can increase up to the order of 100 Bq/m^3 and more. The Radon is permanently monitored at the CONUS experimental site with a device on top of the shield, also the humidity and temperature are registered. The long term monitoring of the activity at KBR is displayed in Figure 5.30 together with the room temperature. Notably, strong fluctuations during the reactor OFF periods are observed as work is carried out on the ventilation system. Enhancements in the room temperature can foster the outgassing of radon. Figure 5.30 shows similarities between time development of the room temperature and the Radon activity. But there are also discrepancies observed, as the activity is an interplay between factors such as the materials and surfaces, temperature, humidity and air pressure as well as exchange with the air from the connected rooms.

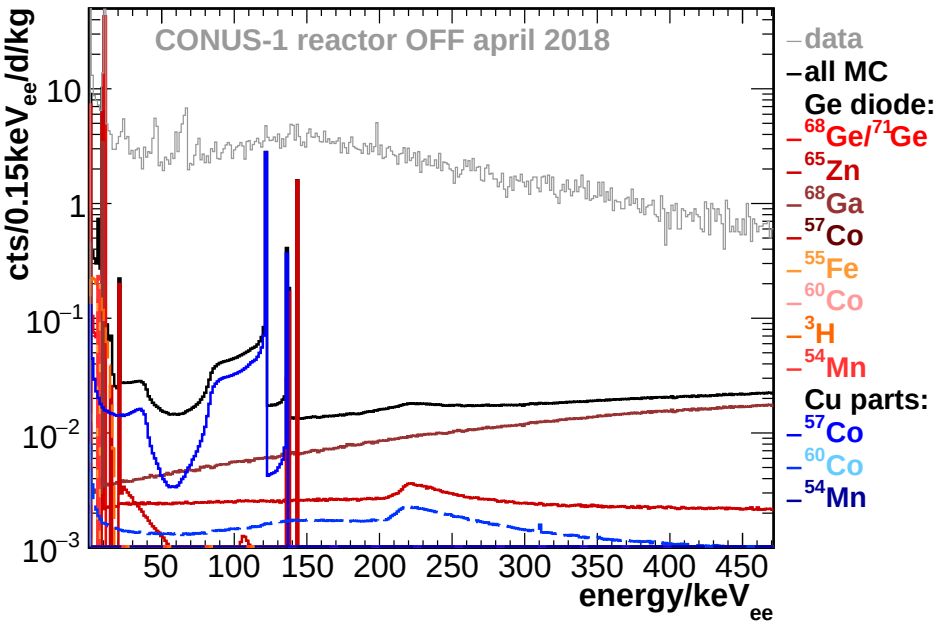

Figure 5.29: Cosmogenic activated contributions in the Ge diode and the Cu parts of the detector from MC in the highE range. The data of the outage in April 2018 is plotted as comparison. The spectra from decays in Ge are displayed in shades of red and the spectra from decays in Cu in shades of blue. If no line background is visible in the data, the spectra are despicted with dashed lines.

With a half-life of 3.8 d ^{222}Rn and its daughters are the dominant contribution. ^{220}Rn has a half-life of 55 s and thus potentially already decays away during the outgassing process or on the way to the detector. The observed natural abundance is 90% of ^{222}Rn and 9% of ^{220}Rn. Thus, the focus lies on ^{222}Rn as potential background contribution. Its α decay as well as the α decays within the decay chain are unproblematic as the particles are completely absorbed in the Cu cryostat and there is no significant contribution by other radiation. However, in the beta decays of short-lived daughter isotopes ^{214}Pb and ^{214}Bi γ-rays and electrons are emitted. Within the energy regime of the CONUS detectors the strongest visible line is at 351.9 keV from the ^{214}Pb. There are also further γ-rays from ^{214}Pb, while the dominant γ-rays from ^{214}Bi have energies above. However, they as well as the numerous β decay emissions contributing to the continuum. The relevant part of the decay chain ends at ^{210}Pb due to its half-life of 22.2 a. As the radon background might change over time, it is important to gauge the impact on the ROI.

5.5.2 Radon mitigation strategies

Normally, the radon background is suppressed by keeping it away from the vicinity of the detector by flushing the volume with boil-off nitrogen. It is usually available

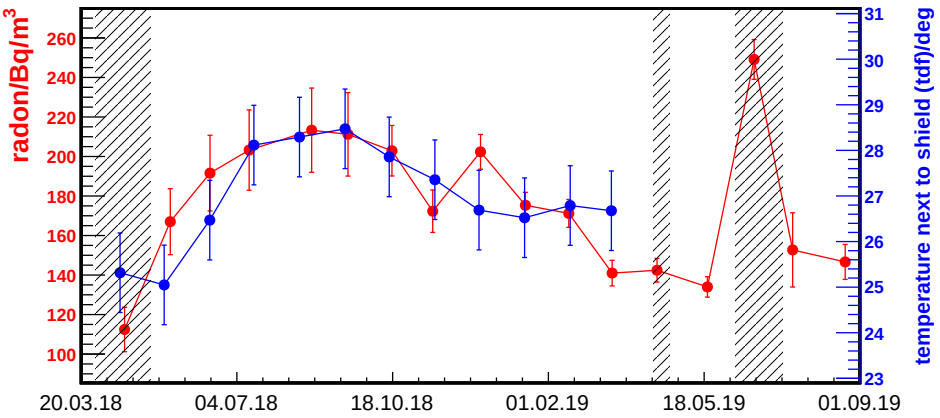

Figure 5.30: Evolution of Radon activity over time compared to the room temperature registered next to the shield with the tdf sensor. Temperature data collection with this sensor at this location stopped with the beginning of Run2. The outages of Run1 and Run2 as well as the mini outage in April 2019 are marked as shaded areas.

from the N_2 cooling of the detector or an alternative source at the laboratory. Due to the cryocooling of the CONUS detectors, no boil-off nitrogen is available, but at LLL there is a pipeline with boil-off nitrogen from the general storage tank. The detector chamber of the CONUS shield was flushed like this for the data taken at LLL. The radon background was successfully suppressed and no line was found at 351.9 keV in the background spectra.

At KBR though this background suppression technique cannot be applied. Due to safety reasons in the closed space, no cryogenic liquids and no gaseous nitrogen are allowed. The shield is enclosed in a steel cage, that was sealed with silicon to inhibit the air exchange with the environment. If this could be fully accomplished, the Radon within the shield would decay away and a Radon free environment would be reached. However, this was not achieved for the CONUS shield. Data collected without additional measures prominently display the 351.9 keV line and an increased continuum. It turned out that the applied silicon is not radon tight enough. This hypothesis was checked with a dedicated test at LLL. A radon detection device enclosed within a Cu box and covered with a Plexi glass window sealed with silicon. The activity was monitored over time, but the decay of radon was not observed. While the activity decreased by two third compared to outside the box, the development of the activity over time stayed correlated to the activity in the air outside.

Therefore, flushing is also required at KBR and was introduced during the commissioning. Instead of gaseous nitrogen, radon free air from breathing air bottles, as used by the fire brigade, is applied. The bottles have to be exchanged regularly every one to two weeks. The air bottles are refilled in house by KBR and the air becomes radon free by waiting approximately three weeks for the Radon in air to decay away. Figure 5.31 shows how the integral count rate of Conus-1 correlates

to the radon activity inside the room before the start of the flushing. With the beginning of the air flushing, the correlations is broken and the count rate decreases by approximately a factor of four.

By examining the integral count rate and the 351.9 keV line from the radon decay chain over time, it could be shown that the flushing works overall as intended. Two new findings over time lead to further improvements of the flushing. During Run1, data in the highE range were collected with Conus-1. Figure 5.32 displays the line count rate and Figure 5.33 the integral count rate, each in monthly binning, both compared to the radon activity in the air surrounding the shield. Comparable plots are shown in Figure 5.34 and Figure 5.35 for Conus-3 during Run2. For Conus-1 Run1, from time to time a small remaining radon-induced line is visible. While for Conus-3 at the beginning of Run2 the line is clearly visible with a much higher count rate. With a night measurement, it was confirmed that the integral background of Conus-1 Run1 was comparable to before during this time period. Short time measurements of the other two detectors revealed comparable line count rates to Conus-1. Within the statistics collected at LLL, no line was seen in the data and thus contaminations of cryostat parts can be excluded. Three assumptions on the source of the remaining radon can be made:

- the ^{228}Th PE source tube above Conus-3, that leads from outside the shield into the detector chamber, while it is closed at the end inside the shield, nevertheless radon diffusion through the PE is possible

- minuscule gaps around the area where the cryostat arm enters the shield and behind the cryocooler (see Figure 1.13), that are slightly larger for Conus-3 by coincidence than for the other detectors

- Radon in the air used for flushing from bottles that were not stored long enough for it to decay away (magnitude comparable for all detectors, thus the contribution cannot explain the excess in Conus-3)

While radon itself is volatile, the decay products stick to the nearest surface, which might explain the higher count rate within Conus-3, if the radon enters the shield close to the detector. To get rid of the background, the flushing was upgraded. The storage time of the bottles was supervised. Moreover, during the outage of Run2 the air flow was increased, which means that the breathing air bottles have to be exchanged more often. Additionally, when not used for a ^{228}Th calibration the source tube was closed to avoid for the surrounding air to enter the shield in this way. The measures proved to be fully successful after the outage of Run2 and ongoing from there on. For the data collected before for a better understanding of the background contribution, MC simulations were carried out as described in the next section.

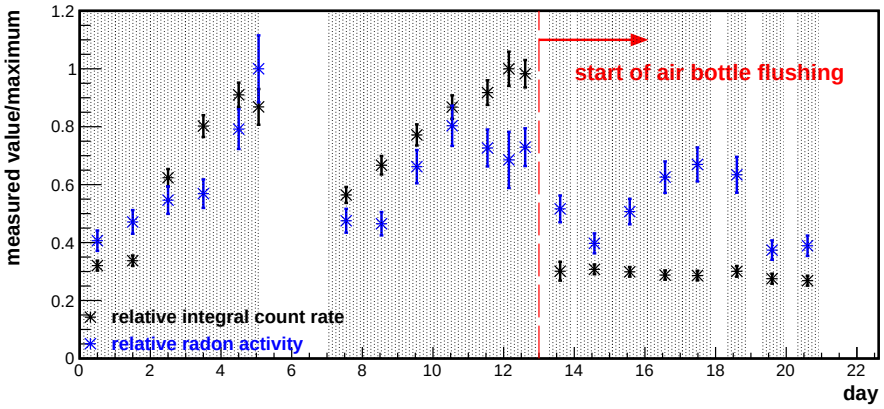

Figure 5.31: Without flushing the integral count rate of Conus-1 correlates with the radon activity in the room. With the start of the flushing the correlation is broken and the Ge count rate is strongly reduced. The shaded areas mark the time periods, when Ge data was collected.

5.5.3 Simulation of the radon background

To investigate the source of the radon and to estimate the contribution to the ROI, MC simulations were carried out.

The relevant part of the decay chain of ^{222}Rn ($T_{1/2}$=3.8 d) consists of the short-lived isotopes ^{214}Pb ($T_{1/2}$=26.8 min) that decays into ^{214}Bi ($T_{1/2}$=19.7 min), as the α radiation emitted by the other isotopes of the decay chain cannot penetrate the cryostat. The air volume of the detector chamber (volume: $\sim$16 dm^3),the surfaces inside the detector chamber and the ^{228}Th calibration source tube (volume: 10^{-6} m^3) were considered as source volumes. Two data sets were prepared, one high in radon (time range before the outage of Run2) and one without in radon (time range after the outage of Run2) (see also Figure 5.34). By comparing the two spectra, the impact of the radon can be clearly seen. The spectra from the MC simulation were now added to the radon free spectrum with the goal to reproduce the spectrum high in radon. For the ^{214}Pb isotope, the MC can be scaled with the observed 351.9 keV line, while there is no visible line background for ^{212}Bi. In secular equilibrium, an equal activity would be expected. However, environmental factors such as temperature, humidity, aerosol in the air and the air flow can all lead to deviations [140]. Thus, the ^{212}Bi component was scaled in such a way as to reproduce the continuum within [100,440]keV$_{ee}$ of the measurement high in radon. Comparing the ^{214}Bi/^{214}Pb ratio for the different source, ^{214}Bi/^{214}Pb=1.5 was found for the air volume of the detector chamber as well as the surface areas of the detector chamber, while ^{214}Bi/^{214}Pb=0.3 for the ^{228}Th calibration source. In all cases, this is a clear deviation from secular equilibrium, but the values are within the range of ratios observed in measurements of air samples in literature before [141]. From the MC an approximate radon activity can be estimated, which is of the order of 10 Bq/m^3 for the detector chamber and 10^6 Bq/m^3 for the ^{228}Th calibration source tube. Regarding the continuum below

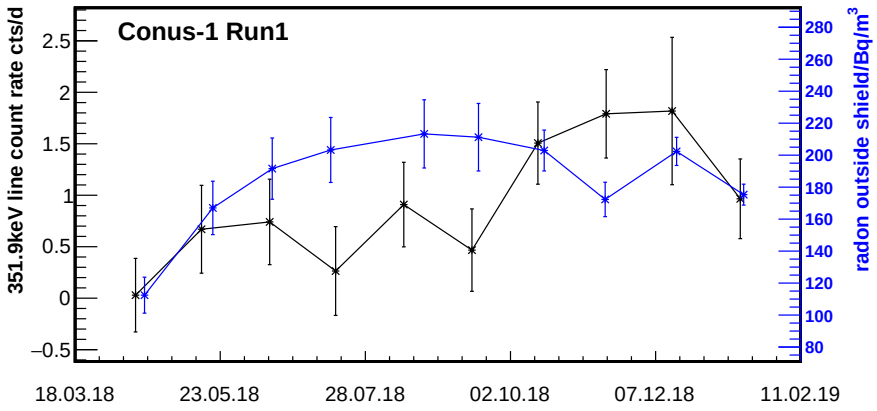

Figure 5.32: Conus-1 Run1: 351.8 keV line count rate over time compared to the radon activity in air. A small remaining radon contribution is observed.

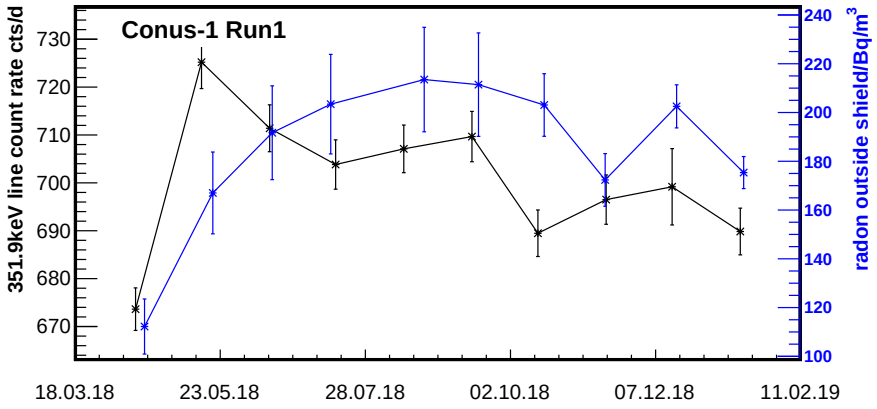

Figure 5.33: Conus-1 Run2: integral count rate in [20,440]keV$_{ee}$ over time compared to radon activity in air. A small remaining radon contribution is observed.

100 keV$_{ee}$, the volume of the detector chamber is slightly favored compared to the ^{228}Th calibration source tube. The agreement is found to be even a little bit better for the surfaces of the detector chamber instead of the full volume. This spectrum is depicted in Figure 5.36. All in all, the extremely high activity required seem to rule out the ^{228}Th calibration source tube as direct origin of the radon. However, radon inside the source tube could diffuse to the outside creating a situation closer to the activity distribution on the surfaces within the detector chamber.

For the estimation of the impact of radon on the ROI in Table 5.19, the MC simulation started from the surfaces of the detector chamber. The line count rate observed within the Conus-3 measurements high in radon was used for scaling, to gauge the maximum impact. For Run1, no highE data were collected for Conus-3. It is assumed that the situation was comparable to the beginning of Run2 (within statistics in consistency with the time development of the integral count rates in Figure 6.5 and Figure 6.6). Thus, for the background model the radon component

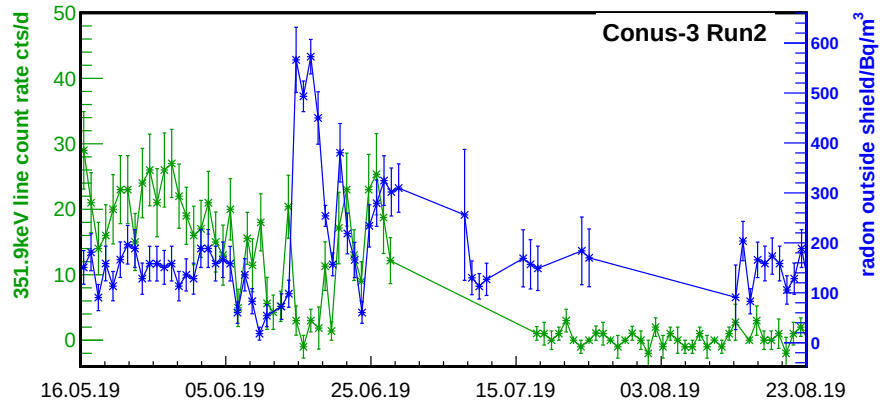

Figure 5.34: Conus-3 Run2: 351.8 keV line count rate over time compared to the radon activity in air. With the end of the outage the upgraded flushing took full effect.

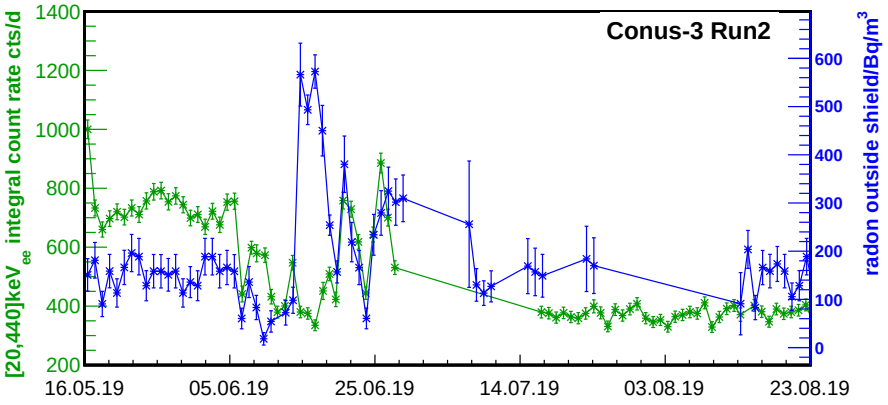

Figure 5.35: Conus-3 Run2: integral count rate in [20,440]keV$_{ee}$ over time compared to radon activity in air. With the end of the outage the upgraded flushing took full effect.

was scaled close to the maximum impact given here. For the outage of Run2, already some of the measures of the upgraded flushing took effect reducing the radon component. For the other detectors, the line count rate and thus the contribution to the continuum are up to one order of magnitude smaller.

5.6 Background from ^{210}Pb decay

Pb is often used as shield material in low background experiments. Often, also the soldering wire applied to the close electronics close to the diode contains Pb. The most important potential contamination to consider is ^{210}Pb with a half-life of 22.3 yr is part of the natural Uranium decay chain (see Figure C.1). Lead ores are often comprised with uranium contaminated minerals. If no separation at the beginning of

integral range	MC cts/kg/d	$\mathcal{O}$(meas. bkg) cts/kg/d
line	20.4	
[0.3, 1]keV$_{ee}$	1.0	∼15
[2,7]keV$_{ee}$	4.4	20-30
[11,440]keV$_{ee}$	372	400-800

Table 5.19: Maximal impact of radon on the count rate within the ROI and above for a 351.9 d line count rate of 20.4 d, which is realistic for Conus-3 until the end of the outage of Run2. The order of magnitude of the measured background rates of the Conus detectors is given as reference.

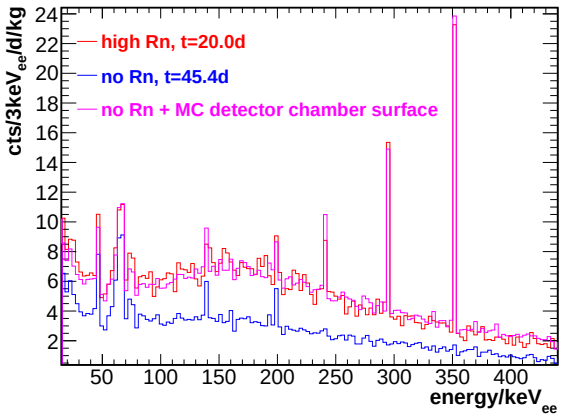

Figure 5.36: The impact of radon on the background spectrum is shown by comparing data containing radon to radon free data. A MC simulation of radon on the surfaces of the detector chamber is added to the radon free data to successfully reproduce the measurement with radon.

the production process occurs, ^{210}Pb will be found in the resulting Pb products [29]. Additional contributions can come from potentially contaminated charcoal used in the reduction of Pb oxide in the furnace during the manufacturing process. Once a contamination occurred, the ^{210}Pb isotopes cannot be removed chemically as they cannot be distinguished from the other Pb isotopes. The only possibility to get rid of the contamination, is for it to wait to decay away. Therefore, old Pb is preferred to construct a shield. Among the radio-purest lead there is the material found on sunken Roman ships [142], where ^{210}Pb could decay away over several thousand years and on the sea floor the ingots are kept away from any new contaminations. However, such Pb as e.g used in the CUORE experiment is extremely sparse and expensive. Other, less rare sources of radio-pure Pb are old church roofs or water pipes.

A second way of a potential ^{210}Pb can come from radon. ^{222}Rn precedes ^{210}Pb in the uranium decay chain and can be found everywhere in the air (see Section 5.5.1 on radon). The radon progenies stick to the surface (especially to statically charged or

cold surfaces) and will decay into ^{210}Pb. The contaminations only becomes sizable if accumulated for long periods of time or if it occurs to surfaces very close to the diode.

An overview on the decay chain of ^{210}Pb is given in [143]. The ^{210}Pb isotope itself decays via β decay with end points of 17.0 keV (84%) and 63.5 keV (16%). Additionally γ-ray lines and Auger electrons are emitted all below 65 keV. The most notably signature is the line at 46.5 keV. The decay results into ^{210}Bi with a half-life of 5.0 d. It decays only by β decay with an endpoint of 1.2 MeV into ^{210}Po. The ^{210}Po isotope is an α emitter. Next to the α particle with an energy of 5.4 MeV, also the recoil (103 keV) of the resulting ^{206}Pb isotope can deposit energy. Moreover, there are minor contributions by X-rays and a γ-ray line.

Outside of the cryostat only the decay of ^{210}Bi is relevant as the decay radiation of the other isotopes will not reach the diode (see efficiency curve in Figure 2.26). The background component for the CONUS shield is described in section 5.6.1. However, close to the diode and on the diode surface the full decay chain has to be considered (see Section 5.6.2).

5.6.1 Lead bricks of the CONUS shield

The CONUS shield contains 25 cm of Pb (see Figure 5.1) in an onion-like shield. Especially the innermost shield layer of the CONUS experiment is made out of Pb. This is beneficial for a lower muon-induced continuum as described in Section 5.2, but it also means that ^{210}Pb as background contribution has to be taken into account. To keep this background as low as possible, first of all Pb bricks that are known or assumed to be low in ^{210}Pb were selected. Among them is old lead that was removed from the "Freiburger Münster" during renovation works. The half-sphere in Figure 5.37 were refurbished into bricks for the CONUS experiment.

Moreover, bricks with low contaminations, previously used in other experiments, were available. Here, the ^{210}Pb could at least decay away over several half-lives. Some of them are LC2 Pb with a certified activity of less than 0.4 Bq·kg^{-1} [29]. These bricks were used for the floor of the detector chamber, which is closest to the diodes. The bricks on top of the detector chamber are less crucial, as there is a 1 cm Cu plate in between, suppressing the ^{210}Bi decay radiation. For the bricks on the sides of the detector chamber, the ^{210}Pb activity was evaluated in several auxiliary measurements during the commissioning phase at LLL:

- Alpha and beta counter measurements at Jagiellonian University, Krakow (by M. Wojcik)
- Gamma spectroscopy measurements with the GIOVE and CORRADO [144] detectors at LLL: to take into account the self-shielding of the radiation in the Pb bricks, a measurement with a brick of known activity was carried out, in the next step the brick was replaced with the sample brick to be tested (taking advantage of the standard size of the Pb bricks), by comparing the count rates of both measurements, an activity could be derived

Figure 5.37: Half-spheres of Freiburger Münster Pb before refurbishment into bricks for the CONUS experiment.

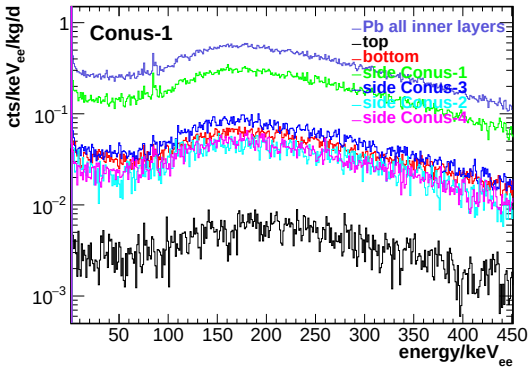

Figure 5.38: MC spectrum of the decay of the ^{210}Pb progeny ^{210}Bi in the inner most shield Pb layer as seen by Conus-1. All contributions are scaled with the respective activity. The largest background contribution comes from the side shield layer closest to the respective detector.

- Commissioning measurements of the CONUS shield: as the shield had been set up several times, various combinations of Pb bricks could be tested, the resulting background spectra gave hints on bricks high in ^{210}Pb

For the Pb bricks fabricated from the "Freiburger Münster" lead used in the final CONUS shield an activity of <1 Bq/kg was determined. Some of the bricks excluded were found to have an up to ten times higher contamination, which might have been introduced during the melting of the half-spheres to create the bricks. The other bricks in the final setup have activities of the order of 2 Bq/kg as well or lower.

All in all, due to the selection process, a weighted mean activity for the site layers of the final shield setup of <1.7 Bq/kg could be achieved. This is small compared to the range of values reported in literature up to 2500 Bq/kg [29]. On the other end of the spectrum, the lowest limit reported 2019 for Roman Pb lies at 715 μBq/kg [142]. Less effort was undertaken for the lead bricks of the outer layers of the shield, as contaminations are shielded by the inner layers. They were arranged according to the information at hand on their with decreasing radio purity from the outside to the inside.

MC simulations were used to determine the contribution of the remaining ^{210}Pb activity to the background spectra. Only the β spectrum of ^{210}Bi and X-rays created in Pb are observed. Figure 5.20 shows the background induced in Conus-1 by the contaminations of the top, bottom and sides of inner most shield layers scaled according to the activity measurements. Table 5.20 contains the respective integral count rates in several energy intervals. The biggest contribution for each detector stems from Pb bricks at the side closest to the detector. Next to the muon-induced contribution the component provides the biggest contribution to the continuum. In

integral range	MC cts/d	$\mathcal{O}$(meas. bkg) cts/kg/d
[0.3, 1]keV$_{ee}$	0.4	∼15
[2,7]keV$_{ee}$	1.6	20-30
[11,440]keV$_{ee}$	140	400-800

Table 5.20: The impact of the ^{210}Pb activity within the innermost shield layer of the CONUS experiment on the highE background and the ROI. Conus-1 is used exemplary, scaled with the measured activities, the normalization is later adapted for the background model. The order of magnitude of the measured background rates of the Conus detectors is given as reference.

the background model, the normalization of the component was adapted to reproduce the measured background spectra. As for each detector the Pb bricks close by are most relevant, the rescaling of the normalization was carried out for each detector individually. The impact on the detectors is regarded as second order effect and was not included into the model.

5.6.2 ^{210}Pb within cryostat

In the background spectrum of all of the four CONUS detectors the 46.5 keV line of ^{210}Pb is visible (see Figure 5.39 for Conus-1). The line must originate from a contamination within the cryostat.

From the material screening measurement, it is known that the soldering wire used for the cold electronics contains ^{210}Pb. However, while with the HPGe gamma spectroscopy measurements, the activity of the lead bricks could be estimated (see Section 5.6.1), for small samples with a complex geometry no activity could be derived. In literature activities of up to 50 kBq/kg were reported for solder [29]. During the manufacturing of the detectors, as little as possible soldering was applied. Another potential candidate could be the contact pin touching the diode at the point contact. Moreover, the background model gave the strong hint on contaminations on the diode surface and the Cu surfaces of the diode holder. Especially for Conus-1 these components are required to be able to describe the background spectrum (see Figure 5.40, the difference between measured spectrum to the muon-induced background and ^{210}Pb contamination of the inner most shield layers corresponds to surface contaminations). The components, mostly the decay on the surface of the diode, add to the 46.5 keV$_{ee}$ line as well. This kind of surface contaminations can potentially occur during manufacturing by Pb contaminations of the work place e.g. due to the soldering wire. The by far biggest contamination is observed for Conus-1, which is in agreement with the detector being the first detector more tests and reassembling were necessary opening up more possibilities of contamination.

For a surface contamination, the dead layer and passivation layer at the borders of the diode become relevant (see Figure 2.1). At the end of the decay chain of ^{210}Pb, ^{210}Po decays to ^{206}Pb by emitting an α particle and energy could also be deposited

detector	46.5 keV line cts/d
1	9.5±0.4
2	6.3±1.1
3	5.7±1.1

Table 5.21: Line count rate in the 46.5 keV for the four CONUS detectors. As structures below the peak were observed (see Figure 5.39), the count rate was evaluated in the range of [39,47] keV_{ee} and background was subtracted left and right thereof.

by a recoil. The α particle has a range of $<20\,\mu$m in Ge and for the recoiling ^{206}Pb nucleus it is <50 nm [145]. Both are fully shielded by the dead layer with a thickness of the order of 0.1 mm. However, the passivation layer is much thinner of the order of 100 nm. This is still enough to avoid energy depositions by the recoiling nucleus, but the α particle might deposit energy in the detector at 5.2 MeV outside of the current data taking range of CONUS.

In the end, for the background model, all ^{210}Pb contaminations were placed on the surfaces of the diode and the diode holder, as this is preferred by the model to reproduce the measured continuum below 10 keV_{ee}. Activities from the range of 10-300 μBq/cm^2 for the diode surface and 0.5-6 mBq/cm^2 for the crystal holder surface were used for scaling (depending on the detector). For Conus-1 a passivation layer of 25 nm was adapted, for the other detectors it was set to 75 nm. Even with this optimization, too many counts are observed in the 46.5 keV line in the model for all detectors. This might origin from the unknown charge collection efficiency in/close by to the passivation layer. It is also unacquainted for how an energy deposition from radiation of the contact pin directly at the point contact, where no passivation layer is present and the electrical field has the steepest gradient, would look like. The peak in Figure 5.39 has a strong tail to the left, that was to this extent not observed in the MC simulation of ^{210}Pb contaminations from any of the volumes close to the diode and could result from incomplete charge collection. While Conus-1 displays a prominent tail, it is much smaller for the other detectors. The second hypothesis on the excess counts in the line in the model is a potential diffusion of the contamination into/through the passivation layer especially if the diode is warmed up.

All in all, the contamination is understood well enough for the current background model. For the future, improvements might be possible by acquiring more information. If the energy range of the data taking can be extended, a detection of the α particle from ^{210}Po might be possible, which could be used to quantize the activity directly. There is also the potential, that the pulse shape of the surface events might differ significantly from events within the active volume such that they could be identified and cut away [146].

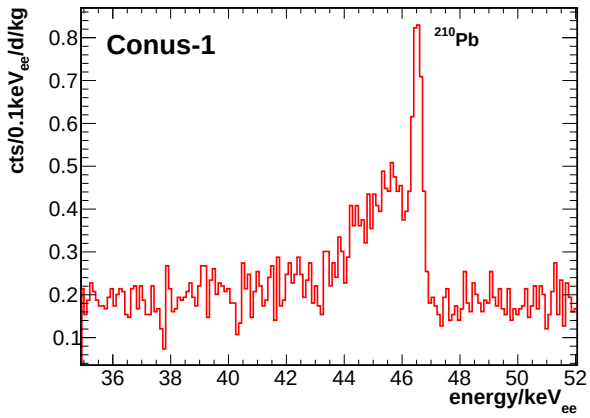

Figure 5.39: 46.5 keV peak in the background spectrum of Conus-1. A tail below the peak is observed that might origin from decays at the diode surface.

5.7 Material screening of cryostat components

All materials within the cryostat were carefully examined on potential radio active contaminations, before they were built into the cryostat. Screening measurements at LLL at MPIK with the GIOVE and CORRADO [144] detector were made. Some of the samples were also examined at LNGS by M. Laubenstein, were due to the much larger overburden a higher sensitivity can be achieved. Due to the results of the measurement campaign, some adaptions were made. The original contact pins were exchanged with ones of higher radio-purity. In Table 5.22, the results are summarized for all samples. Close to the diode the plastic insulation of the HV cable was removed to further suppress any potential contamination. This worked out successfully, as in the final CONUS background spectra, nearly no lines from radioactive contaminations are found (see Figure 5.40). Only for Conus-1 and Conus-2 minor contaminations of the U and Th decay chain seems to be present resulting in a line at 186.2 keV and 238.4 keV. The exact origin of the contaminations could not be identified. For the background model they were placed within the Delrin close to the diode. The contribution to the ROI are predicted to be negligible by the MC with less than 0.1 keV$_{ee}$

5.8 Background model for physics analysis

5.8.1 MC background model

The background model is built up out of the single components described in the previous section. The data for the lowE range corresponds exactly to the data sets used for the CEνNS analysis in Chapter 6. For the highE range, for Conus-1 the data collected during the outage of Run1 was selected. For Conus-2 there is only a measurement during reactor ON time available. For Conus-3, a data set of reactor

sample	amount	unit	^{226}Ra	^{228}Th	^{228}Ra	^{40}K
SMD resistor	500	μBq/#	17±3	<5	<9	<27
FET	100	μBq/#	<0.4	<2	<2	<10
PTFCE	0.19	mBq/kg	<3	<14	<12	<29
Sapphire	0.	mBq/kg	<74	<2	<4	<34
Cuflon	0.46	mBq/kg	13±2	<5	<4	<17
PTFE	0.075	mBq/kg	<8	28±11	<20	<58
HV cable	6	mBq/m	0.7±0.4	<1	1.2±0.7	<3
Signal cable	70	mBq/m	<0.1	<0.1	<0.2	<0.6
soldering wire	104	mBq/kg	<42	<27	<45	<124
Oring	26	μBq/#	570±120	<250	<460	<1500
Delrin	1.3	mBq/kg	4±2	<2	<4	40±12
contact pin	100	μBq/#	<5	<8	<9	<19

Table 5.22: Gamma spectroscopy screening results of various materials used inside the Cu cryostats of the CONUS detectors.

ON data were selected as well, as after the outage of Run2 there is radon free data available, making it possible to better study all other background contributions (see Section 5.5). As Conus-4 is not used in the current CEνNS analysis of Run1 and Run2, the background is not depicted here. It is comparable to Conus-3.

The dominant contribution to the overall continuum comes from the muon-induced component as well as the ^{210}Pb contamination of the inner most Pb layers. The muon-induced contribution without active muon veto is scaled with a factor, the veto efficiency, to represent the measured spectrum with active muon veto. The ^{210}Pb contamination is normalized according to the activity measurements, but also multiplied with a scaling factor due to the sizable uncertainties on the activities. It was found that overall the continuum is well reproduced for a veto efficiency of around 97% and a scaling factor of 0.1 to 1.3 for ^{210}Pb spectrum. The scaling is ambiguous to some extent, as the spectral shapes are similar for both contributions above 50 keV, while differences are observed below due to the recoils of muon-induced neutrons. The scaling was chosen in this way, as by turning the scaling around with more ^{210}Pb and a higher veto efficiency, there would be too little counts at low energies and the Pb X-ray count rates would be too small. Moreover, as for some of the Pb bricks only upper limit of the activity could be determined, there is no tension with the scaling factors smaller than one. The veto efficiency of 97% is consistent with the reduction of the count rate of the muon-induced X-rays (see Section 5.3.1) and higher than evaluated from the BS measurement inside the shield (see Section 5.3.2). It is assumed, that the difference is mostly created by the thermalization of the neutrons inside the BS before detection.

For the neutron-induced meta-stable Ge states (see Section 5.3.4) the measured line count rates are applied as normalization. The count rate within the 23.4 keV cannot be reproduced in this way, . The same is done for the lines from cosmic activation (see Section 5.4.1). If not line background is visible for this component, the production rates from literature are used instead (see Section 5.4.1). The contribu-

tion of the myon-induced neutrons in concrete is derived from the BSS measurement at KBR (see Section 4.4.3).

The ^{210}Pb contamination within the cryostat is scaled in a way to fully reproduce the continuum over all energies. This is especially necessary for Conus-1. Doing so, too many counts are predicted in the [40,48] keV_{ee} interval covering the 46.5 keV_{ee} line. This has been discussed in Section 5.6.2. Other contaminations are within the cryostat are scaled according to the visible line background, but the contribution is negligible compared to the other background components (see Section 5.7).

Radon was added to the background model according to the visible line count rates. If no highE data are available for the time frame, approximations according to the collected data at other times were made.

A comparison between the measured count rates and the model for Run1 is displayed in Table 5.23. Overall, a good agreement was achieved for all detectors. The table also shows the fraction of the different components to the background. The contaminations within the cryostat except ^{210}Pb are not included, as they are negligible in comparison to the other components. According to the model, within the ROI muon-induced background, especially the neutron-induced recoils, and the ^{210}Pb decays within the cryostat together amount to about 80% of the background.

For Run2, minor adaptations were made. The radon contribution is reduced as the upgrade on the flushing started to take effect (see Section 5.5.2). Moreover, adaptations on the veto efficiency by 0.01% were made.

5.8.2 Description of electronics noise threshold

The MC does not include the electronics response of the detectors. Thus, theres is no noise threshold. To be able to nevertheless include it into the model, the threshold was extracted from the reactor OFF data with a fit.

The MC model as described was folded with the detector response. The resulting spectrum, including the muon veto dead time correction, is subtracted from the data. The residuals are fit with the following function in the energy range of 0.25-0.275 keV_{ee} up to 0.45 keV_{ee} (depending on the detector):

$$tr(E) = \frac{p_0}{p_1^2} exp\left(\frac{-E^2}{2p_1}\right) \tag{5.10}$$

The lower threshold of the fit is by several tens of eV_{ee} below the CEνNS analysis threshold as derived in Section 6.4. The analysis threshold is determined by the ratio of the background model rate to the noise rate. Above 0.45 eV_{ee} the noise contribution is negligible in comparison to the MC background. The outcome of the fit is added to the MC background model and the resulting spectrum is used as input for the likelihood analysis (see Section 6.6).

Conus-1	Run1 OFF [0.4,1] keV$_{ee}$	Run1 OFF [2,7] keV$_{ee}$	Run1 OFF [40,48] keV$_{ee}$	Run1 OFF [10,100] keV$_{ee}$	Run1 OFF [100,440] keV$_{ee}$
data Run1	10.8±0.9	34.1±1.6	20.7±0.8	247±3	497±4
bkg model [cts/d]	11.5	34.1	27.0	247	497
prompt μ-induced	33%	32%	19%	27%	44%
metastable Ge states	0.4%	0.3%	0.3%	7%	1%
μ-induced n concrete	6%	4%	0.2%	0.5%	0.2%
cosmogenic	3%	5%	0.6%	18%	2%
^{210}Pb shield	4%	6%	8%	11%	27%
^{210}Pb within cryostat	52%	52%	71%	35%	22%
radon	0.2%	0.3%	0.4%	0.5%	1%
Conus-2	Run1 OFF [0.4,1] keV$_{ee}$	Run1 OFF [2,7] keV$_{ee}$	after Run1 ON [40,48] keV$_{ee}$	after Run1 ON [10,100] keV$_{ee}$	after Run1 ON [100,440] keV$_{ee}$
data Run1	6.1±0.7	22.3±1.3	13.6±0.7	164±2	321±3
bkg model [cts/d]	7.1	22.3	15.1	160	329
prompt μ-induced	53%	47%	28%	39%	66%
metastable Ge states	0.5%	0.3%	0.4%	9%	2%
μ-induced n concrete	10%	6%	0.3%	0.7%	0.3%
cosmogenic	4%	6%	3%	19%	1%
^{210}Pb shield	1%	2%	4%	5%	11%
^{210}Pb within cryostat	27%	29%	61%	20%	8%
radon	4%	7%	3%	4%	9%
Conus-3	Run1 OFF [0.4,1] keV$_{ee}$	Run1 OFF [2,7] keV$_{ee}$	Run2 ON [40,48] keV$_{ee}$	Run2 ON [10,100] keV$_{ee}$	Run2 ON [100,440] keV$_{ee}$
data Run1	12.3±1.1	30.5±1.7	13.7±0.7	161±2	257±3
bkg model [cts/d]	11.1	30.1	20.8	183	246
prompt μ-induced	34%	35%	24%	33%	66%
metastable Ge states	0.4%	0.3%	0.3%	11%	2%
μ-induced n concrete	6%	5%	0.2%	0.6%	0.4%
cosmogenic	2%	3%	0.2%	21%	1%
^{210}Pb shield	0.8%	1%	3%	3%	13%
^{210}Pb within cryostat	51%	43%	72%	30%	15%
radon	6%	13%	0.5%	0.7%	2%

Table 5.23: Integral count rates of CONUS background data of Run1 and Run2 in various energy ranges compared to the background model. For the lowE range, Run1 OFF data is used, for the highE range the available data is employed. The relative contribution of the different background components is given as well. The radon contribution differs due for Conus-3 in the highE and lowE range, due to improvements in the flushing, when the highE data was collected.

5.8.3 Kolmogorov test

With a Kolmogorov-Smirnoff Test [147] (K-S test) as implemented in ROOT the compatibility between the background model and the measured data were checked. The shape and the normalization is compared. The "empirical distribution function" of both histograms is calculated. As described in [148] for N data points Y_i $(i = 1, ..., N)$ (ordered from small to large) it is defined as $n(i)/N$ with $n(i)$ being the number of points less than Y_i. The test statistics is derived from the maximum distance of the empirical distribution functions of both histograms. From the test statistics the probabilities value (p value) is extracted. An equal probability distribution between 0 and 1 is expected for all histograms drawn from the same distribution. This means that a p value much smaller than 1 points towards an incompatibility. The significance level was set to 0.1 and all background model histograms with a lower p value were rejected.

The K-S test was originally developed for unbinned data. For binned data the assumption of an uniformly distributed probability between 0 and 1 does not fully hold (see discussion in Note 3 in ROOT function description [149]). In general, a shift towards slightly higher probabilities is observed. However, as long as the binning is small compared to any physical effects, no significant impact is expected. For the CONUS data this is the case for the $10\,\mathrm{eV}_{ee}$ that was also applied to the likelihood analysis described in Section 6.6, which is about an order of magnitude smaller than the resolution of the physical peaks (see Table 2.3).

In Table 5.24, the p values for the K-S test applied for the background model are depicted. The exact data sets from the data selection for the CEνNS analysis (see Section 6.1) are used. The comparison of the background model to the reactor OFF data were carried out separately in the two energy ranges [0.4,1]keV$_{ee}$ and [2,8]keV$_{ee}$. An energy of $0.4\,\mathrm{keV}_{ee}$ was selected as below the electronics noise significantly contributes to background, which was determined in a fit to the data anyway.

The background model and the data were found to be fully compatible. Only for Conus-1 Run1 a p-value less than 0.1 was found for [0.4,1]keV$_{ee}$ interval, which results from an artifact slightly below $1\,\mathrm{keV}_{ee}$. Thus, the ROI for this detector was restricted to below $0.75\,\mathrm{keV}_{ee}$ for all runs to be on the save side, which improves the p value.

5.9 Summary on CONUS shield and background

The CONUS experiment is set up at shallow depth with an overburden of $\sim$24 m w.e., meaning that the background is dominated by muon-induced components. To reduce it as much as possible, the innermost shield layer is made out of Pb and the shield is equipped with an active muon veto. With the help of MC simulations, the background was examined in detail, consisting out of prompt electro-magnetic signals, neutron recoils at lower energies and meta-stable Ge states from neutron

	p value	
detector/run	reactor OFF [0.4,1]keV$_{ee}$	reactor OFF [2,8]keV$_{ee}$
Conus-1/Run1	0.97 (*)	0.81
Conus-2/Run1	0.29	0.85
Conus-3/Run1	0.93	0.55
Conus-1/Run2	0.86	0.41
Conus-3/Run2	0.33	0.45

Table 5.24: P values from comparison of the background model to the reactor OFF and reactor ON data in different energy ranges. The test confirms that the background model provides a good description of the data as all p values excel the significance level of 0.1. For the p values marked with (*) instead of the [0.4,1]keV$_{ee}$ interval the [0.4,0.75]keV$_{ee}$ was compared due to an artifact in the data.

capture with a life-time longer than the veto window. With a BS measurement inside the shield, it could be shown that Geant4.10. excellently reproduces the muon-induced neutron fluence rate. Comparing the MC to Ge measurements without muon veto, above 100 keV$_{ee}$ a very good agreement is found, while below small adaptations have to be made. In the background model for the spectra with active muon veto, a veto efficiency of ∼97% is estimated. Next to the muon-induced signals, contributions from the decay of ^{210}Pb within the inner most Pb layers and within the cryostat are found. The contributions within the cryostat on the surface of the diode and the surrounding Cu parts create the 46.5 keV line observed in the background spectra. Moreover, radon has to be taken into account, when describing the background spectra. It is removed from around the detector chamber by flushing with radon free air from breathing air bottles. Until the middle of the outage of Run2, the signature of remaining decays of radon daughter isotopes can be seen, especially in the background of Conus-3. The radon could be fully suppressed thereafter with improvements in the flushing. Within the lowE range below 15 keV$_{ee}$ four lines are visible in the measured background. They are K shell and L shell X-ray lines from cosmogenic-induced isotopes. Most of them are created in spallation reactions of high energetic neutrons at the earth's surface and the background is small for the CONUS detectors as they were kept as much as possible under an overburden during manufacturing. The decay of the lines over 15 month were fitted and in this way production rates could be derived, agreeing well with the values found in literature. By simulating all the contributions, it could be shown that the impact of the decay on the continuum in the ROI is negligible. All examined components are combined in the background model used for the CEνNS analysis. It was shown with a Kolmogorov test that the reactor OFF spectra of Conus-1, -2 and -3 are reproduced well.

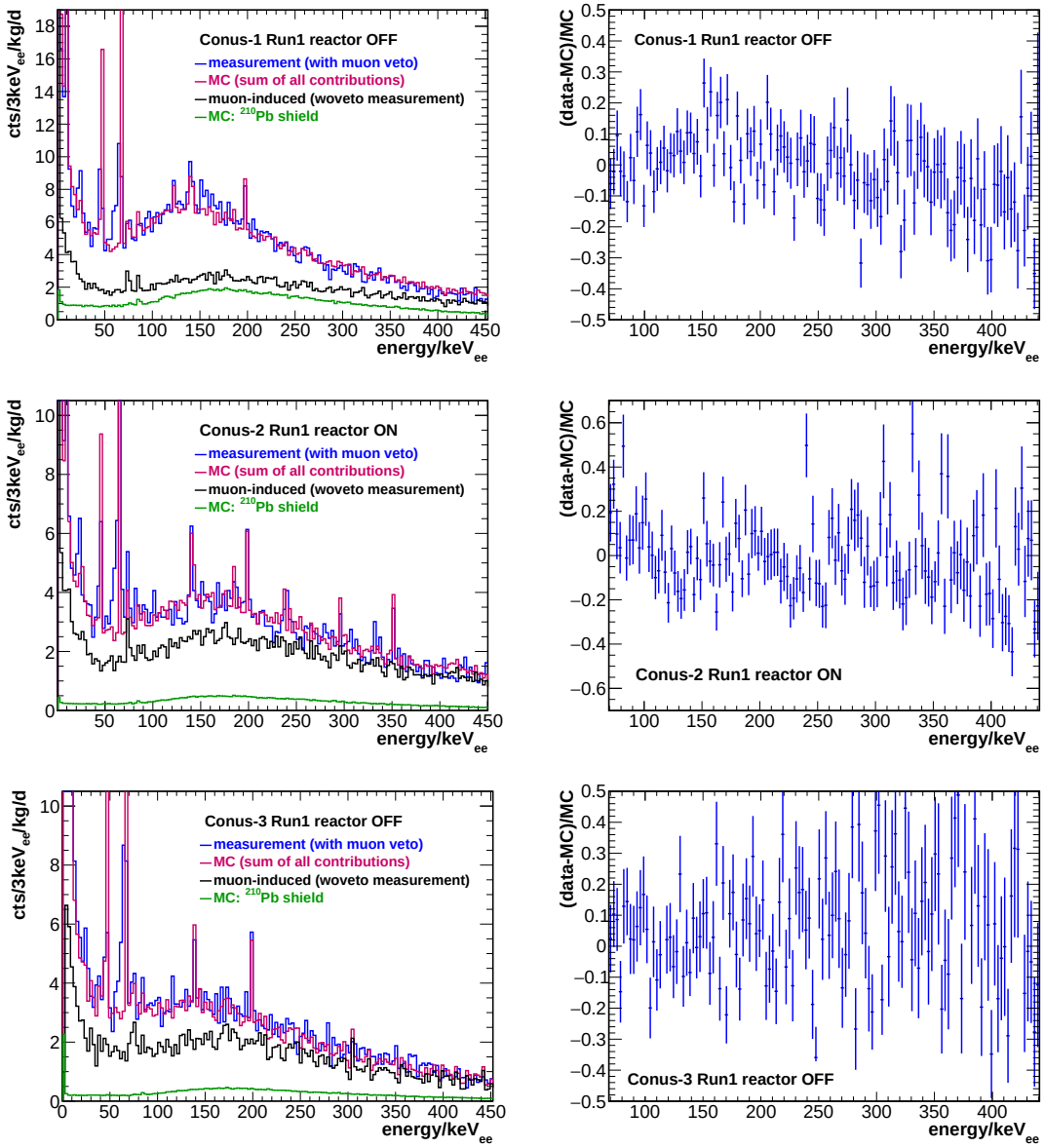

Figure 5.40: (Left) Background model of Conus-1 to Conus-3 for the highE range. The muon-induced background (without veto measurement) and the ^{210}Pb contribution from the innermost shield layer are shown separately. (Right) Residuals of the comparison of the model to the data.

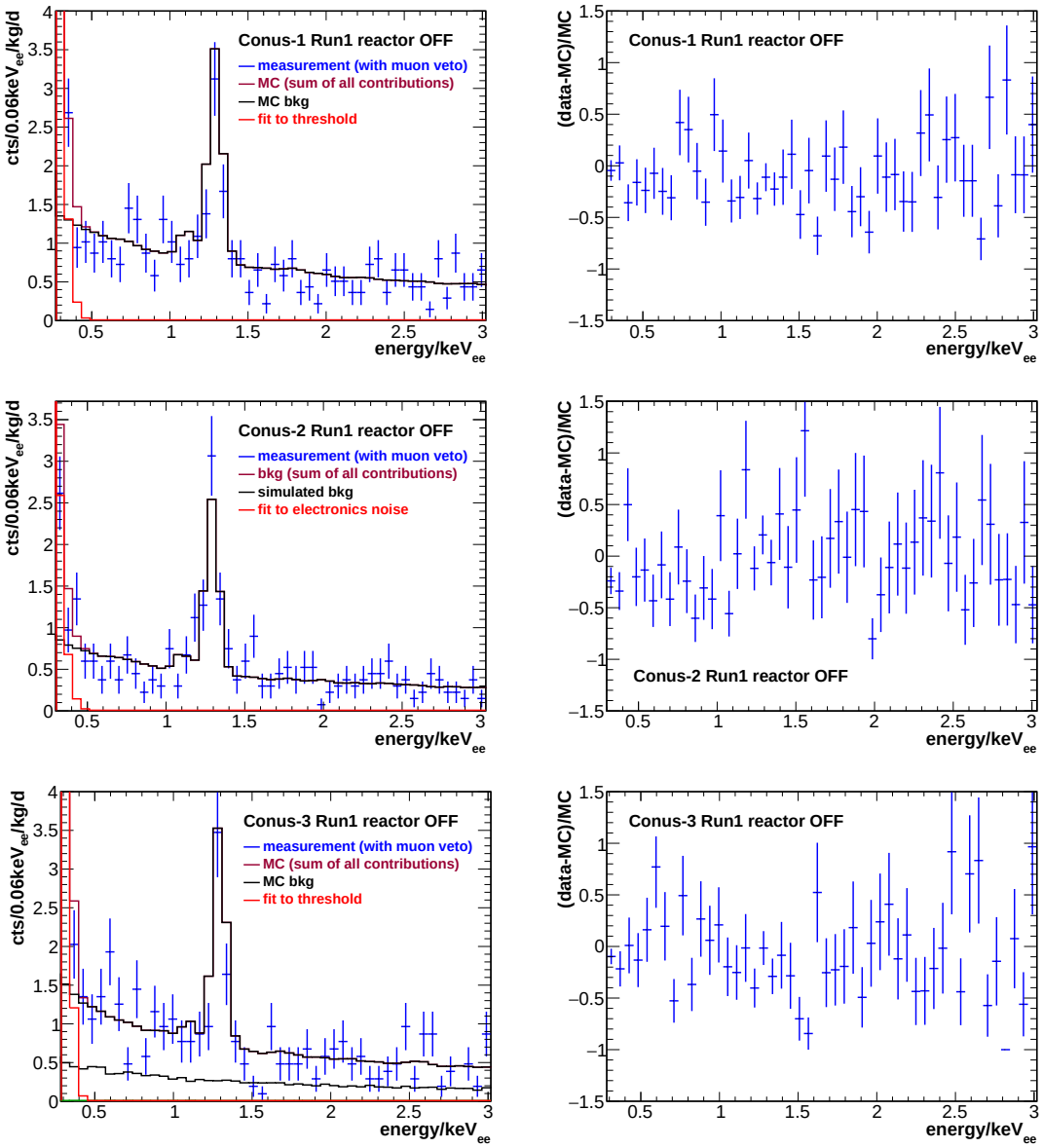

Figure 5.41: (Left) Background model of Conus-1 to Conus-3 for the highE range. The line from the 1.3 keV L shell X-rays is visible. (Right) Residuals of the comparison of the model to the data.

6 CEνNS analysis

In the beginning, the data sets are defined for the CEνNS analysis. A data selection with the goal of a stable and low energy threshold is carried out. The data sets are calibrated and checked for stability. This is followed by the precise definition of the ROI. A likelihood fit is set up and an upper limit for the number of CEνNS counts is derived from the data with a nested likelihood ratio test. The results are discussed in the end.

6.1 Definition of data sets

For the first CEνNS spectral shape analysis, the data taking periods of Run1 in 2018 and Run2 in 2019 are taken into account until the leakage test at KBR (for the time line of the CONUS experiment see Section 1.8). Both runs consist of a regular outage of the nuclear power plant of approximately one month. For Run1, six month of reactor ON time are collected, for Run2 only the weeks before the outage are considered, as the leakage test after the outage significantly changes the characteristics of the detectors.

First of all, the collected event lists are processed and histograms are created. Within the processing routine the TDD cut is applied as described in Section 3.3.2. The impact of the cut on the exposure is negligible compared to the NTC cut. The exposure is defined as the lifetime multiplied with the mass of the detectors.

Second, the noise integral and above noise integral defined in Section 3.2 are examined for stability. Due to the unstable and high room temperature and the subsequent cryocooler-induced noise, large fractions of the collected data are not considered in this analysis. They are removed by the application of the NTC cut (see Section 3.2.3). The objective of the cut is to achieve the most stable and lowest possible energy threshold. This leads to a large reduction by a factor of two or more of the data available for analysis. Table 6.1 summarizes the final exposure. Conus-4 is left out from the analysis of Run1 due to a DAQ artifact at the threshold up to 600 eV_{ee}. For Run2, Conus-2 and Conus-4 are not included as the DAQ settings were changed between the reactor ON time and the outage.

6.2 Energy scale stability and calibration

The stability of the energy scale has been checked regularly during data taking with ^{228}Th calibrations in the highE energy range. The visible lines in the highE and lowE background are also analyzed (highE=up to 450 keV_{ee}, lowE=up to 15 keV_{ee},

detector/run	reactor OFF [kg·d]	reactor ON [kg·d]
Conus-1/Run1	13.8	96.7
Conus-2/Run1	13.4	14.6
Conus-3/Run1	10.4	97.5
Conus-1/Run2	12.1	19.6
Conus-3/Run2	9.2	20.2
all	58.9	248.3

Table 6.1: Exposure of Run1 and Run2 of the CONUS experiment after all data selection cuts.

see also Section 3.1.1). As discussed in Section 2.2.3, the peak position was highly stable. A maximum relative standard deviation of 0.04% was found.

For the lowE range of the CONUS detectors a self-calibration of the data sets is carried out by W. Maneschg. Within this energy range below 15 keV no external γ-rays can reach the diode. The only lines available come from the activation in Ge (see Section 5.4.1). The K shell lines at 8.96 keV (^{65}Zn), 9.69 keV (^{68}Ga) and 10.37 keV (^{71}Ge/^{68}Ge) are fit as single peaks. The L shell peaks are so close to each other that they are fit as a combination of three Gaussians. A linear calibration with the peak positions in channels and the peak energies from literature in Table 5.13 is carried out. The uncertainties of the peak positions from the fit and of the literature values are taken into account. The linearity of the energy scale had been confirmed down to approximately 300 eV_{ee} with pulser measurements. The available statistics of the self-calibration is limited. The isotopes decay with half-lifes of the order of a year (see Section 5.4). Only ^{71}Ge is produced in-situ. Therefore, the reactor OFF and ON data were calibrated together to gather more statistics. This is justified by the highly stable energy scale over time (standard deviation of 4 eV_{ee} for 10.36 keV_{ee} line at maximum within 10 months). The single runs cannot be combined due to adaptations in the DAQ settings leading to a change of the energy range. Moreover, the K/L shell ratios from literature were included into the fit as well to better constrain the L shell peaks. In summary, the uncertainty on the calibrated energy within the ROI amounts to 10-20 eV_{ee}. The only possiblity to improve the statistics is to additionally activate ^{71}Ge with a neutron source. This was done for Run3 of the experiment, but these data are not included in the present analysis.

6.3 Background stability

To confirm the stability of the background, the highE data, only available for one detector at a time, and the lowE data in above the ROI was studied in monthly time binning. The highE data is discussed in connection with the radon background in Section 5.5. While the flushing suppressed the radon background around the diode, remaining radon lines were observed. The corresponding varations in the continuum at low energies are of the same order of magnitude as the statistical fluctuations

in the background. The associated systematic uncertainty is therefore considered negligible for the CEνNS analysis. To reduce the background, the flushing was upgraded as previously described. The improvements took full effect after the outage of Run2, but this time range is not used in the analysis at hand. Figure 6.1 to Figure 6.6 show the lowE background development over time in the energy ranges of [0.5,1] keV_{ee} and [2,7] keV_{ee}. Only statistical uncertainties are given. The time ranges analyzed extent outside the data selection for the CEνNS as the data selection criteria only apply to the noise threshold. No temperature induced instabilities are expected above about 500 eV_{ee}. The measured count rates in the figures are stable within the uncertainties. The decay of the cosmogenic lines activated at the earth's surface is quantized in Section 5.4. For the time range displayed in the figures for both energy intervalls a difference of less than 0.4 cts/d is expected, which is below the statistical uncertainty of the single data points. For the current CEνNS data sets the impact is even smaller, as the runs are restricted to the shorter time ranges marked in the plot and each run is only compared to the corresponding outage. The cryostat of Conus-2 was pumped in between the runs to restore the vacuum and an enhanced count rate has been observed afterwards. The Run2 data of the detector is not taken into account in the current analysis.

6.4 Definition of ROI for CEνNS analysis

The lower bound of the region of interest for the CEνNS analysis, the so-called analysis threshold, has to fulfill three criteria:

1. electronics detection efficiency close to one
2. noise-temperature correlation not visible
3. ratio noise to MC background <4

First of all, the electronics detection efficiency (1) has to be sufficiently large to be able to detect physical signals at all. This gives the lower most bound on the ROI. As described in Section 3.1.3 and Figure 3.1 down to 250 eV_{ee} for Run1 only little and for Run2 no decrease in the efficiency is observed. Thus, other effects limit the analysis threshold. Second, the dependence of the room temperature to the noise (2) has to be taken into account. The impact is restricted with the NTC cut by limiting the data sets to periods of stable noise. However, it is not possible to achieve a fully stable data set in this way. This is only possible after the introduction of the improved control of the environment with the cold house starting after the outage of Run2. To gauge the impact of the remaining room temperature dependence, each reactor ON data set was split into several time periods. For each period, integral count rates for different low energy thresholds in 25 eV_{ee} steps up to 1 keV_{ee} were calculated. The count rates are normalized to the count rate in the first period. Moreover, a mean value of the room temperature for Run1 and for the HOBO temperature data during Run2 for the same time periods were calculated. The

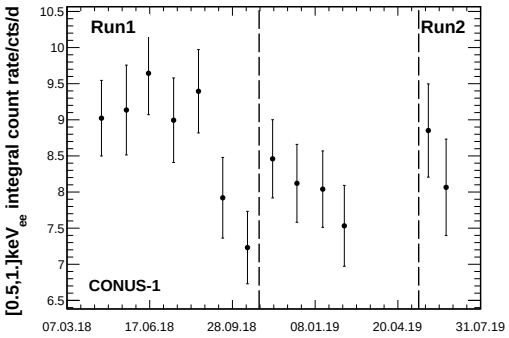

Figure 6.1: Time development of the integral background of Conus-1 within [0.5,1]keV$_{ee}$.

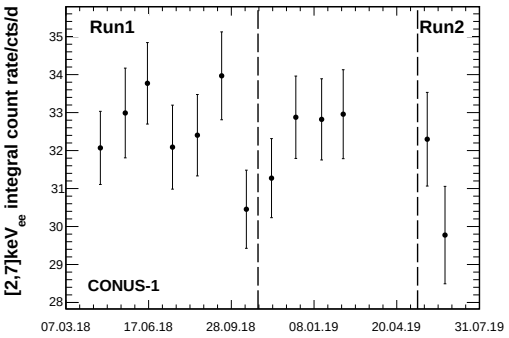

Figure 6.2: Time development of the integral background of Conus-1 within [2,7]keV$_{ee}$.

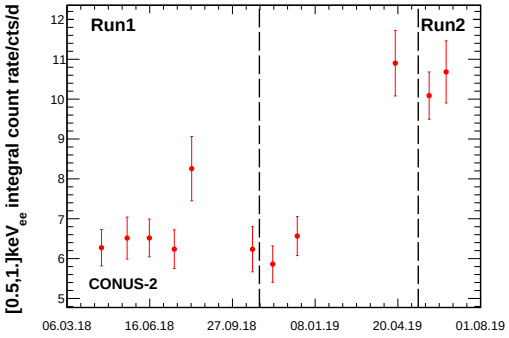

Figure 6.3: Time development of the integral background of Conus-2 within [0.5,1]keV$_{ee}$. The Run2 data is not used in the current analysis.

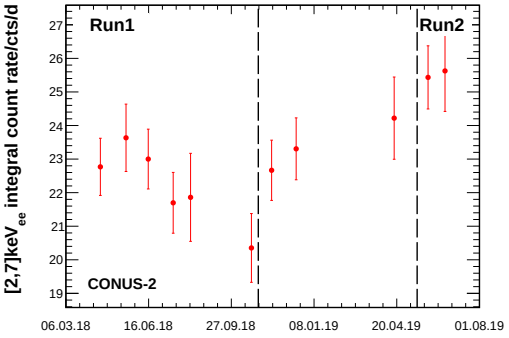

Figure 6.4: Time development of the integral background of Conus-2 within [2,7]keV$_{ee}$. The Run2 data is not used in the current analysis.

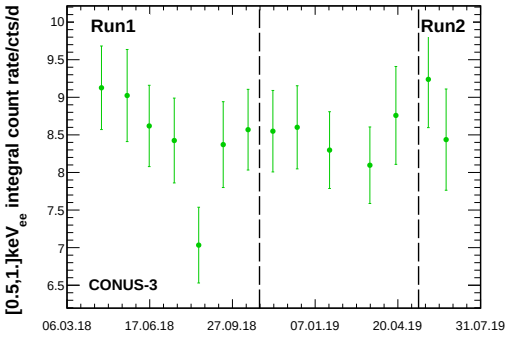

Figure 6.5: Time development of the integral background of Conus-3 within [0.5,1]keV$_{ee}$.

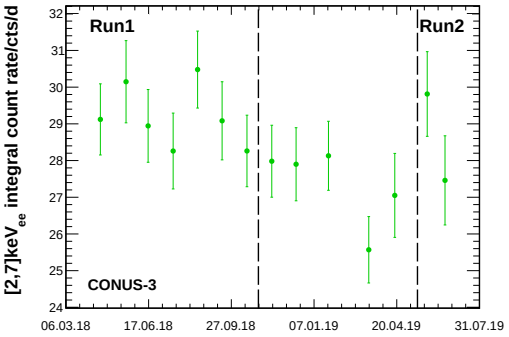

Figure 6.6: Time development of the integral background of Conus-3 within [2,7]keV$_{ee}$.

outcome is compared to the Ge data in Figure 6.7. In this way, the threshold above which the temperature dependence is found not to be visible anymore can be determined, here 275 eV_{ee}, for the other detectors and runs it is between 275 eV_{ee} and 300 eV_{ee}.

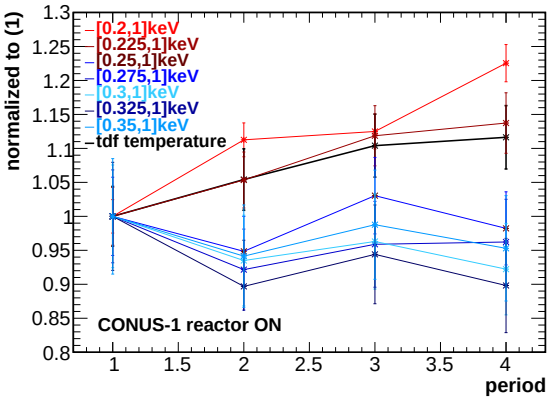

Figure 6.7: Integral noise count rate during reactor ON for Conus-1: the data set was split in four time periods and the count rate is normalized to the first period. For comparison, the room temperature was evaluated for the same periods and normalized in the same way. Up to 275 eV_{ee}, the integral is correlated to the temperature.

The method gives an indication on the remaining temperature dependence, but is limited by statistics and missing temperature data. A precise definition of the threshold is not possible in this way. Therefore, a different approach was pursued. The background model to describe the reactor OFF data is split into the simulated background and the fit to the noise threshold. The ratio between the noise rate and the background rate was calculated (see Figure 6.8 for Conus-1 Run1 and Figure 6.9 for Conus-1 Run2). The bin width of approximately 10 eV_{ee} corresponds to the bin width used in the likelihood fit. To avoid any remaining temperature dependence and other noise instabilities, the criterion for the analysis threshold was set that the noise is allowed to be at maximum four times as large as the background (3), marked as blue line in the figures. The analysis threshold derived in this way is summarized in Table 6.2. Conus-1 within Run1 has the lowest energy threshold according to this criterion and thus the most signal is expected there. About 100 eV_{ee} to 200 eV_{ee} above the analysis threshold the noise contribution drops to one tenth of the background. An implication of this definition of the analysis thresholds is a dependence on the background model.

The upper end of the ROI is in general set to 1 keV_{ee} below the L shell lines of ^{71}Ge, ^{68}Ge, ^{68}Ga and ^{65}Zn. No signal is expected above 0.5 keV_{ee}, even for large quenching factors. Thus, the upper end of the ROI can be used in the likelihood fit to stabilize the background. From the K-S test of the background model (see Section 5.8.3) a non-negligible difference between the data above 0.75 keV_{ee} was found for Conus-1 Run1 and thus this energy range is excluded from the analysis.

detector/run	analysis threshold [eV_{ee}]	ROI upper end [eV_{ee}]
1/1	296	750
2/1	311	1000
3/1	333	1000
1/2	348	750
3/2	343	1000

Table 6.2: ROI for the CEνNS analysis of Run1 and Run2.

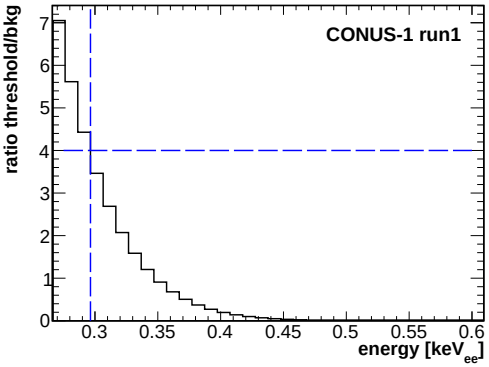

Figure 6.8: Ratio of noise to MC background rate to determine the lower bound of the ROI for Conus-1 Run1.

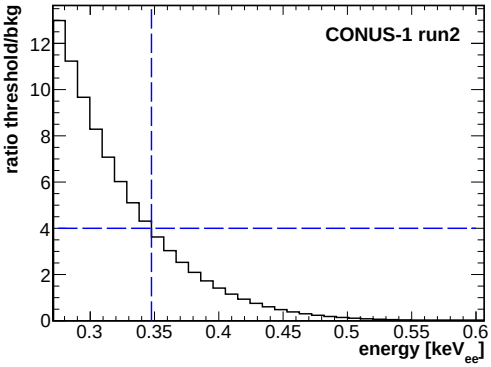

Figure 6.9: Ratio of noise to MC background rate to determine the lower bound of the ROI for Conus-1 Run2.

6.5 Signal expectation

The spectrum of the reactor antineutrinos is taken from Huber (^{235}U, ^{239}Pu and ^{241}P) [150] and from Mueller et al. (^{238}U) [151]. The maximum neutrino energy included is 8.3 MeV. The Daya Bay reactor experiment correction factors for the neutrino event excess seen in the measured spectrum but not found in the theoretical description are included [152]. The fission fractions, which describe the contribution of the different isotopes to the number of fissions, are provided directly by KBR. The fractions evolve with time, when the fuel burns up. While at the beginning of a cycle ^{235}U dominates, the contribution decreases over time. More and more ^{239}Pu is created, which leads to a softer neutrino spectrum. Therefore, an individual spectrum is determined for each detector and run as the data sets cover different time periods in two different reactor ON cycles. For CONUS the neutrinos at higher energies are more important as the recoil energy is larger. This increases the chance to observe a signal above the energy threshold of the detectors.

The corresponding expected CEνNS spectra are calculated by T. Rink (cross section see equation (1.2) in Section 1.1). The thermal power created at KBR is required as input for the calculation. Figure 6.10 shows, how the thermal power varies over time for Run1 and Run2. For the selected data sets during Run1 the average is ∼90%, for Run2 it is ∼95% of the maximum thermal power of 3.9 GW_{th}.

The variation in power of up to 40% comes from variations in demand for power from nuclear power plants. In Germany, if more power is created by renewable technologies such as wind energy, the nuclear power plants have to reduce their input to the power net work. The uncertainty on the thermal power is 2.3% [53]. To determine the signal expectation from theory, the number of fissions needs to be derived from the thermal power and the energy released per fission (see Table 4.8). The calculation is equivalent to the evaluation of the normalization of the MC simulation of the propagation from the fission neutrons from the reactor core to the experimental site in Section 4.2.3. About $3{\cdot}10^{19}$ fissions per s and GW occur and on average $\sim$7.2 neutrinos per fission [20] are emitted in the consecutive β decays. The exact number of neutrinos depends on the fission fractions. Contrary to the neutrons, the neutrino interaction probability is negligible on their way to the experimental site such that only the distance of (17.1 ± 0.1) m and solid angle have to be taken into account. For CONUS the reactor core is considered as point-like antineutrino source. For an extended model of the reactor core only deviations of the order of 1% were found.

Table 6.3 shows the signal expectation for the total exposure of Run1 and Run2 in dependence of a few representative quenching parameters. The analysis threshold evaluated in Section 6.4 is used. The systematic uncertainties include the uncertainty on the thermal power, the fission fractions, the energy released per fission, the distance to the reactor core and the theory parameters. In total, relative uncertainty amounts to 6-10%. The large variation of the expected signal with the quenching factor shows immediately that it is the dominating systematic uncertainty.

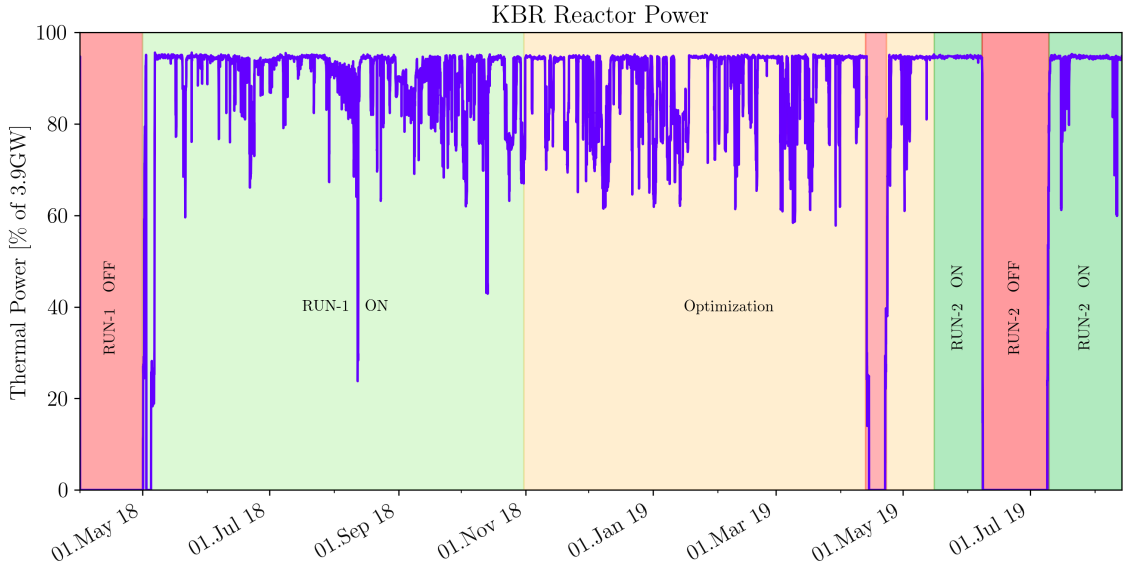

Figure 6.10: Evolution of thermal power over time for Run1 and Run2. Figure prepared by T. Rink.

quenching parameter k	counts
0.1	0.040±0.004
0.15	3.0±0.3
0.2	22±2
0.25	68±4

Table 6.3: Signal expectation combined for Run1 and Run2 provided by T. Rink.
.

6.6 Likelihood function

6.6.1 Binned likelihood function framework

A binned likelihood is set up as the DAQ only provides the energy of the events already binned in channels (see Section 3.1 for description of DAQ). The basic binned likelihood function looks like the following, assuming a Poisson distribution for the content of each bin i. The total number of bins in the ROI is denoted as N:

$$\mathcal{L}(\vec{n};\vec{\theta}) = \prod_{i=1}^{N} \frac{\mu_i^{n_i}}{n_i!} e^{-\mu_i} \tag{6.1}$$

Here, n_i refers to the bin content in the histograms of the measured data and μ_i denotes the bin content of the model with $i = 1, ...N$. To avoid the computation of too large numbers, $-ln(\mathcal{L})$ instead of $-\mathcal{L}$ directly is minimized:

$$-ln(\mathcal{L}(n_i;\mu_i)) = \sum_{i=1}^{N} -n_i ln(\mu_i) + \mu_i + ln(n_i!) \tag{6.2}$$

For the minimization, the constant last term $ln(n_i!)$ can be dropped avoiding the computation of the faculty in this way. The model depends on the m fit parameters denoted by θ_j $(j = 1, ..., m)$. This results in $N - m$ degrees of freedom for the fit. From this point of view a larger number of bins N in the ROI with a smaller bin width is beneficial. The likelihood function is implemented in a TMinuit routine [153] in ROOT, which evaluates the set of parameters $\hat{\theta}_j$ $(j = 1, ..., m)$ minimizing the function:

$$-\frac{\partial ln(\mathcal{L})}{\partial \theta_j} = 0 \tag{6.3}$$

The uncertainty of the parameters is determined by scanning $-ln(\mathcal{L})$ around the minimum (corresponding to the MINOS routine of TMinuit). The $1\,\sigma$ uncertainty is reached for a divergence of ± 1 of $-2ln(\mathcal{L})$. The method can lead to asymmetric uncertainties.

If prior knowledge of the fit parameters is available, this can be included by pull terms added to $-ln(\mathcal{L})$. A pull term assures that the parameters cannot deviate to far from the start value in the fit. The simplest case is an external measurement of a parameter $\theta_{in} \pm \Delta\theta_{in}$ assuming a Gaussian distribution of the uncertainty. Consequently, taking the logarithm of a Gaussian, the pull term added to $-ln(\mathcal{L})$ looks like the following:

$$pull_{Gauss} = -0.5 \left(\frac{\theta_{in} - \theta}{\Delta\theta_{in}} \right)^2 \tag{6.4}$$

For the CEνNS analysis presented here, only Gaussian pull terms are applied.

6.6.2 Binned likelihood function for CONUS

In the CONUS experiment, data including the neutrino signal n_i^{ON} are collected during reactor ON time and the background n_i^{OFF} is measured when the reactor is OFF. The model to describe the reactor ON data is denoted by μ_i^{s+b} and for the reactor OFF time it is called μ_i^b. To take advantage of the knowledge of the background, the reactor OFF and ON data are fitted simultaneously, which means for a single detector:

$$\begin{aligned} ln_{det}(\mathcal{L}(n_i;\mu_i) &= \sum_{i=1}^{N} \left(ln(\mathcal{L}(n_i^{ON};\mu_i^{s+b})) + ln(\mathcal{L}(n_i^{OFF};\mu_i^b)) \right) + pulls_{Gauss} \\ &= \sum_{i=1}^{N} \left(n_i^{ON} ln(\mu_i^{s+b}) - \mu_i^{s+b} + n_i^{OFF} ln(\mu_i^b) - \mu_i^b \right) + pulls_{Gauss} \end{aligned} \tag{6.5}$$

The reactor ON model includes the signal expectation histogram n_s that is scaled with the fit parameter s. The background parameter $b{=}\theta_1$ describes the agreement of the measured data outside the signal range to the background model n_b. There are three additional nuisance parameters, which need to be taken into account for the fit, but are not of direct interest for the analysis. These are the fission flux θ_2, the multiplication parameter θ_3 summarizing uncertainties on the detector response and the active volume, and θ_4 for the energy scale calibration. Thus, for a single detector in total 2 histograms and 5 parameters are required to model the data:

$$\mu_i^{s+b} = \left(s \cdot t_{ON} \cdot \theta_2 \cdot n_i^s + b \cdot n_i^b \cdot \frac{t_{ON}}{t_{OFF}} \right) \cdot c_{dt}^{ON} \cdot \frac{\theta_3}{m_{act}}, \quad \mu_i^{OFF} = b \cdot n_i^b \cdot c_{dt}^{OFF} \cdot \frac{\theta_3}{m_{act}} \tag{6.6}$$

The ratio of the live times of the measurements during the reactor ON and OFF periods t_{ON} and t_{OFF} is used to scale the background model for the reactor ON data. The muon veto dead time correction is represented by $c_{dt}^{ON/OFF}$. The active volume m_{act} is included explicitly for normalization purposes. For better readability, it was foregone to include the implementation of the energy calibration uncertainty

$\Delta E{=}\theta_4$ in the formula above. Next to the parameters incorporated into the likelihood, variations in the shape of the expected CEνNS spectrum due to uncertainties on the reactor antineutrino spectrum and on the quenching factor were studied separately by rerunning the likelihood with different input spectra. In the following, the spectra, all parameters and the inclusion of the systematic uncertainties are described in detail. A summary is given in table 6.4.

description	parameter	unit	det.-dep.	run-dep.	pull term
signal strength	s, scan	cm^2 per fissions	no	yes	no
background	$\theta_1{=}b$	dim. less	yes	yes	no
fission flux	θ_2	fissions per cm^2s	yes	yes	yes ($\sim$3%)
detector, DAQ	θ_3	kg	yes	yes	yes ($\sim$1-5%)
energy scale	$\theta_4{=}\Delta E$	keV	yes	yes	yes (<30% $FWHM_{pulser}$)
shape $\bar{\nu}$ spec.	none	dim. less	yes	yes	no
quenching	none	dim. less	no	no	no

Table 6.4: Overview of input parameters and systematics of the CONUS CEνNS likelihood.

Signal expectation histogram and signal strength

The overall CEνNS signal strength is refereed to by s. It scales the signal expectation to the reactor ON data. The corresponding histogram n_i^s is taken from theory as described in Section 6.5. The integral of n_i^s over the full spectral range is normalized to 1 for each detector. Consequently, the value of s alone has no physical meaning. The integral over the ROI n_{ROI}^s is smaller than 1. When fitting several detectors at once, this integral weights the detectors according to the size of the ROI. The fission flux as normalization is included separately into the fit by the parameter θ_2 to incorporate the known systematic uncertainty on the flux. It refers to the number of fissions per s and GW scaled with the solid angle. The neutrino flux at experimental site can be derived from θ_2 by including the number of neutrinos per fission with the help of the fission fractions.

An individual spectrum is prepared for each detector and run. This is necessary, because of the variation of the neutrino spectrum during the reactor cycle as described in Section 6.5 that leads to changes in the expected shape of the CEνNS spectrum. The impact of the uncertainty of the shape due to the uncertainty on the fission fractions is quantized by rerunning the likelihood with two extreme cases. They were computed by T. Rink by doing a toy Monte Carlo including all the fully correlated uncertainties. The resulting spectra were normalized over all energies and the integral in the ROI was evaluated. The mean of the distribution of the value of this integral correspond to n_i^s and the two spectra with integrals at $3\,\sigma$ difference from the mean represent the extreme cases.

The evolution of the neutrino spectrum over time as well as potential variations in the thermal power also mean that for each detector and run a separate start value

for the fission flux parameter θ_2 is required. It is of the order of 10^{12} fissions per cm^2 and per s. The number is already cropped by the neutrino energy range relevant for the CONUS experiment. It goes from 4 MeV up to the end of the spectrum at 8.3 MeV. The CEνNS-induced recoil of the neutrinos below this energy range is too small to be seen in the detector. The systematics uncertainty of the thermal power [53] as well as on the fission fractions amounts to approximately 3%. This knowledge is included into the likelihood as pull term according to equation (6.4).

Background model histogram and b parameter

The background model is applied as described in Section 5.8.1. Each detector requires an individual spectrum n_i^b. Small adaptations were carried out between Run1 and Run2 due to the improvements in the radon background suppression. Moreover, the DAQ settings were adapted between the runs and changes on the energy threshold were observed. Thus, for each run an individual spectrum is needed with a corresponding fit to the energy threshold. Reactor-correlated neutron background was excluded in Chapter 4. The b parameter scales the model to the reactor OFF and ON data. No pull term is set on the parameter, but the simultaneous fit of the ON and OFF data indirectly constrains the b parameter. The parameter is supposed to be compatible with 1 within the uncertainties.

Detector response and active mass

The detector response summarizes all detector- and DAQ-related factors that have to be taken into account to transfer the signal expectation spectrum and the MC background model into the shape that is read out from the detector. The energy-resolution, electronics trigger efficiency and the muon veto dead time correction are considered.

To include the energy resolution into the models, the spectra are folded with a Gaussian. Its energy-dependent width σ is obtained from the function described in Section 2.2.2. It is assumed that the uncertainty on the folding is negligible compared to the uncertainty on the energy scale calibration. This holds especially as the signal in question is not a peak, but a broad continuum and thus the impact of the smearing with the energy resolution on the shape is small. Therefore, the folding occurs before the fit and no fit parameter is assigned to the energy resolution.

The electronics trigger efficiency ϵ_{trigg} describes the decrease of the detection efficiency in the electronics chain towards very low energies (see Section 3.1.3). It is slightly energy-dependent for Run1, while for Run2 within the ROI no loss of efficiency was detected. It is applied to the input model spectra before the fit. The relative uncertainty $\Delta\epsilon_{trigg}/\epsilon_{trigg}$ is assumed to be energy-independent, being 5% for Run1 and 1% for Run2. Thus, it can be included into the overall multiplication parameter θ_3 with a pull term via $\epsilon_{trigg}(1 - \Delta\epsilon_{trigg}/\epsilon_{trigg})$.

The muon veto dead time correction $c_{dt}^{ON/OFF}$ reduces the live time induced by the muon veto into the analysis (see 3.1.2). It is an energy-independent factor that

effectively reduces the number of detected counts. The value differs for reactor ON and OFF times due to the additional γ-ray background when the reactor is ON that triggers the muon veto. The reactor ON and OFF models are multiplied with the respective correction factor before the fit. The relative uncertainty on the factor of 0.2% is independent of the reactor status. Thus, it can be included into the multiplication factor θ_3 and its pull term similarly as for the electronics trigger efficiency.

The active mass m_{act} is not directly required to convert the input model spectra to the detected spectra. However, the active mass is required for the geometry implementation for the background model. Therefore, the active volume is included into the multiplication parameter θ_3, too. The uncertainty is of the order of 1%. Consequently, in formula (6.6) the input model spectra have to be divided explicitly by m_{act}.

To sum it up, the uncertainty of the multiplication parameter is set up as $\Delta\theta_3 = m_{act} \cdot \sqrt{(\Delta\epsilon_{trigg}/\epsilon_{trigg})^2 + (\Delta c_{dt}/c_{dt})^2 + (\Delta m_{act}/m_{act})^2}$. The different contribution to the uncertainty are added quadratically and in total amount to about 1-5% (depending on the run). It goes into a pull term according to equation (6.4).

Energy scale calibration

The linear calibration parameters a and b used to describe the energy scale (see Section 6.2) are highly correlated. Within the ROI at low energies it was found that the uncertainties translate to a shift ΔE in energy approximately constant over the whole energy range. It is of the order of 10-20 eV_{ee} depending on the statistics available for calibration. The $1\,\sigma$ uncertainty amounts to one to two bins widths, but is small relative to the pulser resolution of about 70 eV_{ee}.

For the likelihood, the shift ΔE is represented by θ_4. The shift is applied to the signal expectation spectrum and the MC spectra of the background model. The MC background model of the energy threshold is not moved as it is determined by a fit directly to the data. In the likelihood function, the fraction of counts added and removed from a bin due to the shift is calculated in dependence of θ_4, assuming a homogeneous distribution of the counts over a single bin. A pull term with a central value of 0 eV (no shift) and the respective uncertainty is used.

Quenching

The quenching factor previously discussed in Section 1.4.5 is by far the largest systematic uncertainty in the CEνNS analysis. The energy-dependent quenching factor in the Lindhard theory is paraphrased by the k factor, which corresponds approximately to the quenching factor for 1 keV_{nr}. Figure 6.11 shows for three exemplary k factors how the signal expectation changes in shape for Conus-1. Especially the number of counts above the analysis threshold strongly decreases with decreasing quenching factor. It was refrained from including the systematic in the fit, as the collected data are not precise enough to set a statement on the value. Instead all

results are displayed in dependence of the k factor. For 14 values of the quenching factor in the range from 0.12 to 0.25 the fit is rerun with a different signal input spectrum corresponding to the respective quenching factor. It was foregone to change the quenching in the neutron components of the background model as the overall background model is in good agreement with the reactor OFF data as shown independently.

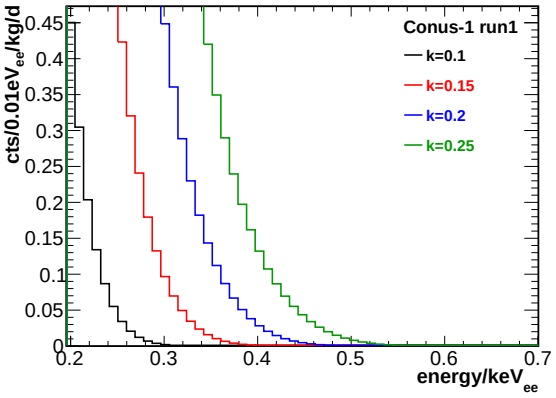

Figure 6.11: Dependence of signal expectation on the quenching factor.

6.6.3 Likelihood ratio test

The constructed likelihood was applied in a so-called "nested Likelihood ratio test" (method described in [154] and in [155]). With the help of this test it can be checked if the data prefers a signal over the null hypothesis. An upper limit can be evaluated at a fixed confidence level, if no signal is found.

The likelihood is scanned for a wide range of values for s. Each time the likelihood value of the best fit $\mathcal{L}_{H_1}$ (alternative hypothesis H_1: a signal is present) is compared to the likelihood value $\mathcal{L}_{H_0}$ for s=0 (null hypothesis H_0: no signal). It is a nested test as the null hypothesis is a subset of H_1. Before the test, the significance level α is fixed to 10% and 1% for the analysis. The significance level is the probability to reject the null hypothesis H_0 even if it is true. The corresponding confidence level is 90% and 99%.

The likelihood ratio is compared to the k_α depending on the fixed significance level α:

$$\frac{\mathcal{L}_{H_1}}{\mathcal{L}_{H_0}} > k_\alpha \tag{6.7}$$

According to the Neyman–Pearson lemma [154] the ratio gives the lowest most probability to reject the alternative hypothesis even if it is true. In practice, the ratio is not calculated directly, but the test statistics q_0 is constructed as follows:

$$q_0 = 2ln(\mathcal{L}_{H_0}) - 2ln(\mathcal{L}_{H_1}) \tag{6.8}$$

If the null hypothesis is prefered, q_0 is positive as the likelihood value is at the maximum for s=0. A two-sided test is carried out to be conservative. It allows for a negative signal, which could be created e.g. by upward fluctuating background due to Radon or tiny shifts in the energy scale in between reactor ON and OFF below the level of the stability check. The probability value (p value) is extracted from a χ^2 distribution:

$$p = \int_{q_0}^{\infty} \chi^2_{dof=1}(q)\mathrm{d}q \tag{6.9}$$

The χ^2 has one degree of freedom as the only additional degree of freedom (dof) in the alternative hypothesis compared to the null hypothesis is the s parameter. The p value expresses the probability to get an outcome of the test at least as extreme as the one observed under the assumption that the null hypothesis is true. Therefore, $1-p$ has to be compared to the confidence level. To find s_{UL} for the 90% confidence level a scan over a wide s parameter range was carried out repeating the fit each time. Derived from formula (6.6), the corresponding number of signal counts n_s during its reactor ON live time for a single detector is given as:

$$n_s = s \cdot t_{ON} \cdot \hat{\theta}_2 \cdot n^s_{ROI} \cdot c^{ON}_{dt} \cdot \frac{\hat{\theta}_3}{m_{act}} \tag{6.10}$$

Combining several detectors and runs, it becomes:

$$n_{s,all} = s \sum_{k=0}^{r} \left(t_{ON,k} \cdot \hat{\theta}_{2,k} \cdot n^s_{ROI,k} \right) \cdot c^{ON}_{dt,k} \cdot \frac{\hat{\theta}_{3,k}}{m_{act,k}} \tag{6.11}$$

The sum goes up to r, which is defined as the number of detectors times the number of runs as the detectors and runs have no common parameters. The hat denotes that the best fit values of the variables from the fit for scan parameter s_{UL} are utilized in the calculation.

In figure 6.12 the resulting $1-p$ values are plotted against n_s exemplary for all detectors for Run1 with the confidence level marked. The upper limit in the number of counts can be read off.

6.7 CEνNS Result

In Figure 6.13 the first upper limit for the detection of CEνNS of reactor antineutrinos is presented. The upper limit for Run1 and Run2 combined is shown for the 90% and the 99% confidence level. The excluded areas are shaded. The black curve corresponds to the Standard Model theory expectation as described in Section 6.5. The uncertainty is marked by the shaded error band. The results were overall confirmed by a cross check likelihood analysis of the data [156]. The upper limit

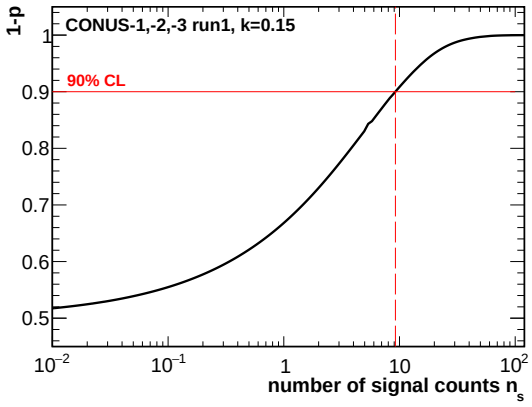

Figure 6.12: Outcome of the nested likelihood ratio test for Run1 for all detectors. The $1-p$ value is evaluated for the number of signal counts n_s. The upper limit is evaluated at 90% confidence level.

has been derived assuming a χ^2 distribution of the test statistics, which should be checked in the near future.

The distance of the upper limit to the expected number of counts strongly depends on the quenching factor, as the number of expected CEνNS counts decreases rapidly for a lower quenching parameter (see Table 6.3). The quenching parameter also has an impact on the upper limit evaluated from the data, as the spectral shape of the CEνNS signal expectation depends on the parameter as well. For smaller values the signal shifts to lower energies (see Figure 6.11). Within this energy range, the noise threshold has already begun to rise and the single bins contain more counts making the statistical uncertainty smaller. A lower limit can be set compared to higher quenching factors as for them the expected signal reaches up to the spectral range where the background dominates and more fluctuations are expected.

The quenching is the dominant systematic uncertainty of the analysis. The available values from literature are covered by an interval from 0.12 to 0.2 (see Section 1.4.5). Under the assumption that the Lindhard model holds the upper limit derived from the CONUS data excludes the quenching parameters above 0.19:

$$\forall\, k \geq 0.19 : n_{s,all}^{90\%UL}(k) \leq n_s^{pred}(k) \tag{6.12}$$

Below, the ratio ρ between the measured upper limit and the Standard Model prediction quickly increases with the quenching factor as depicted in Figure 6.14. For the mean of the interval of the literature values of k=0.16 the ratio amounts to:

$$\rho(k = 0.16) = \frac{n_{s,all}}{n_s^{pred}} \approx 2 \tag{6.13}$$

That means that the current analysis of the CONUS data leads to an upper limit, which is only by a factor of two above the Standard Model expectation. Recent preliminary results of quenching parameter measurements by the COHERENT collaboration [162] hint that the quenching parameter is indeed close to 0.16.

To be able to reliably predict the signal expectation, a precision measurement of the parameter is required. The CONUS collaboration considers as well to conduct such a quenching measurement. The current CEνNS analysis relies on the Lindhard model with adiabatic correction. With the help of such a measurement, not only the k parameter could be evaluated exactly, but it could be tested whether the Lindhard model with the adiabatic correction is indeed a valid description of the quenching effect for small nuclear recoils below 1 keV$_{nr}$.

Next to the quenching, the uncertainty on the energy scale calibration has an impact on the upper limit of the order of 2.0 cts. If it increases or decreases the upper limit, depends on the detector and run. For the data sets at hand within the ROI the uncertainties amount to 10-20 eV$_{ee}$. A smaller uncertainty would stabilize the likelihood fit. The uncertainty of the energy scale is governed by the statistics of the calibration lines. For Run3, it was shown that with the help of a ^{252}Cf source the calibration lines can be activated and the uncertainty can be reduced to below 5 eV$_{ee}$ for all the detectors. Regular ^{252}Cf calibrations at the beginning and end of future runs are planned. The other detector and DAQ related systematics are summarized in the parameter θ_3. The outcome of the likelihood fit is not modified by the parameter.

The impact of the uncertainties of the shape of the reactor antineutrino spectrum is found to be small. It was included into the likelihood by rerunning the fit with the two maximal deviating spectra by three standard deviations (method described in Section 6.6.2). The outcome differs below $\sim$0.5 cts, which is considered negligible. The fit is nearly not sensitive to the fission flux parameter θ_2. It is modified by the fit by less than one tenth of a standard deviation of the starting value. For the prediction in turn the error band on the number of counts is dominated by the uncertainties related to the reactor as antineutrino source. The major contribution comes from the uncertainties on the fission fractions.

Approaches to improve the limit or to achieve the first detection of CEνNS at reactor site are discussed in chapter 8.

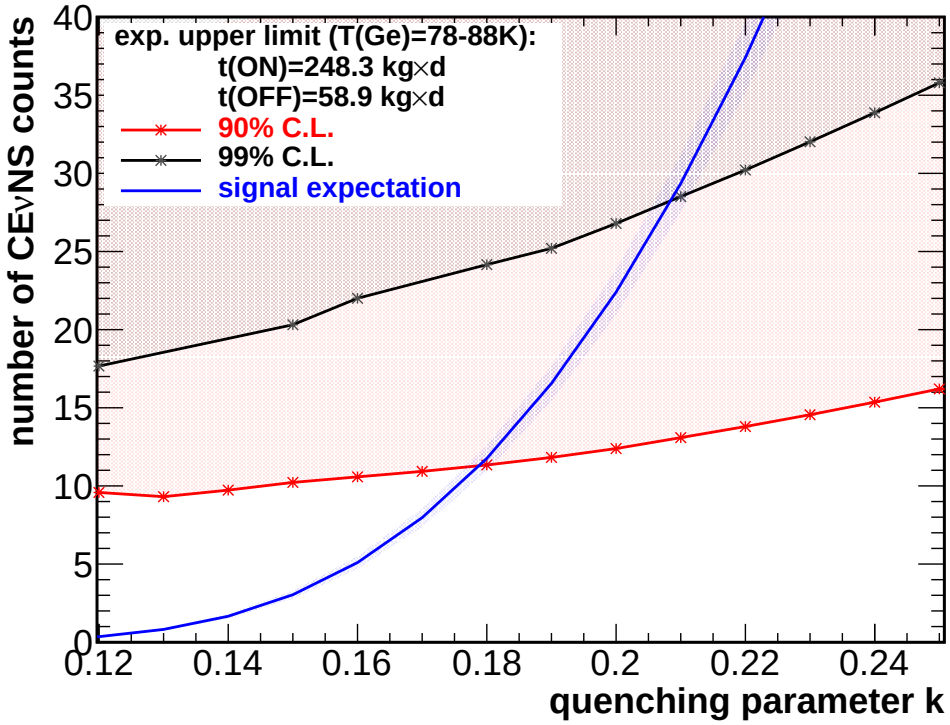

Figure 6.13: Combined upper limit of CEνNS counts as function of the quenching parameter for Run1 and Run2 of the CONUS experiment.

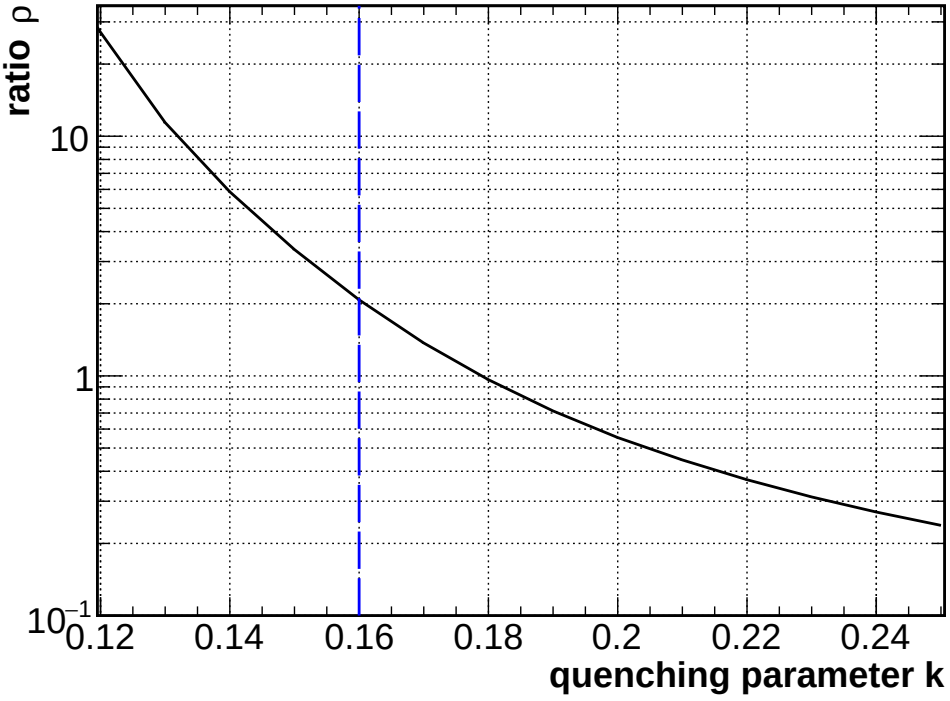

Figure 6.14: Ratio of the number of CEνNS counts from the upper limit of CONUS to the Standard Model prediction. For a realistic quenching parameter of 0.16 the measured upper limit is a factor of two above the expectation.

7 ^{252}Cf source measurements

The ^{252}Cf source measurements at LLL and within the CONUS experiment were carried out for several purposes:

- validation of the propagation of neutrons through a massive shield in the MC
- examination and validation of neutron interactions of Ge in the MC
- activation of ^{71}Ge to improve the statistics of the calibration lines in the lowE range
- examination of the cross section ratio ^{71m}Ge to ^{71}Ge

A ^{252}Cf source is ideal for these purposes, as the average neutron energy of 2.13 MeV [157] is close to the energy of the muon-induced neutrons inside the shield and the concrete (see Figure 4.20).

7.1 Employed ^{252}Cf sources

Neutrons are created in the spontaneous fission of the ^{252}Cf with a branching ratio of (3.086±0.008)% [120] and an average multiplicity of 3,7675±0.0040. The isotope has a half-life of ∼2.6 a [120]. Many fission spectra can be described by a so-called Watt function (see Section 4.1.2 from the neutron-induced fission spectrum of ^{235}U in the reactor core). However, for ^{252}Cf comparing to the measured spectrum deviations are found. Figure 7.1 displays the spectrum. As input for the MC simulations the spectrum from the "ISO Standard 8529 Part 1" [159] is used based on a Maxwellian shape. In the spontaneous fissions reactions, not only neutrons, but also γ-rays up to several MeV are emitted. The spectrum is also shown in Figure 7.1). The average γ multiplicity is 5.87±0.01 [160].

In Table 7.1 gives an overview on the four neutron sources, that were used in measurements with HPGe spectrometers at LLL and KBR. The sources differ in strength and age. The age of the sources is relevant, as in old sources next to ^{252}Cf also ^{250}Cf and ^{242}Cm contribution to the neutron emission. ^{250}Cf is a contamination occurring during the production of the source. The isotope has a five times longer half-live than ^{252}Cf, making the contribution more relevant for old sources. ^{242}Cm is created in the α decay of ^{252}Cf. Thus, the source strength of old sources is bigger than expected from ^{252}Cf alone.

Three different measurement campaigns were carried out up to now:

1. with the GIOVE [30] detector at LLL in 2015: the strong source from MPIK was placed outside the shield and the neutrons arriving inside are registered

source	reference date	neutron strength n/s	date of meas.	detector/lab	source position
strong, by MPIK	15.10.2010	$(0.976\pm0.006)\cdot10^5$	25.11.2015	GIOVE/LLL	outside shield
		$(3.29\pm0.04)\cdot10^4$	17.01.2020	CONUS/KBR	within shield
weak, by PTB	11.04.1988	46.05 ± 1.38	30.07.2017	Conus-4, CONRAD/LLL	within shield
weak, by DC	01.03.2013	4.5	15.01.2020	CONUS/KBR	outside shield
	01.03.2013	4.5	15.01.2020	CONUS/KBR	outside shield

Table 7.1: Overview on all ^{252}Cf sources and measurements with HPGe detectors at LLL and KBR. The intent of the measurements was to study the detector response to fast neutrons and compare to MC. Moreover, ^{71}Ge is activated to improve the statistics of the line count rates for the energy scale calibrations.

2. with Conus-4 and CONRAD inside the CONUS shield at LLL in 2017: a weak and old source lent from PTB was placed within the shield

3. with the CONUS detectors inside the CONUS shield at KBR in 2020: a weak source lent from the Double Chooz (DC) collaboration was placed within the shield, the strong source from MPIK was placed outside the shield

In the following only selected results supporting the previous statements within this thesis will be presented. A complete overview is prepared in an upcoming publication.

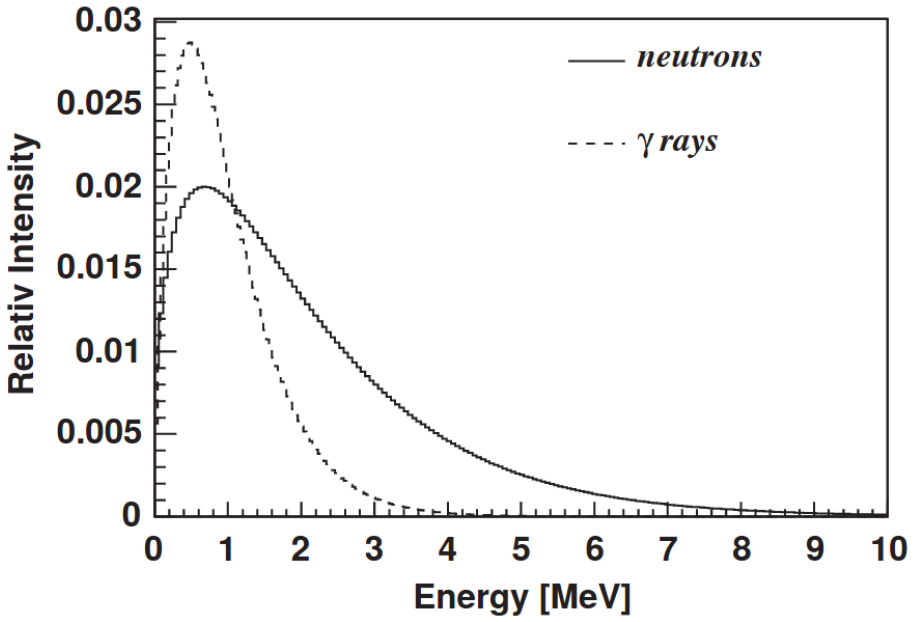

Figure 7.1: Neutron and γ-ray spectra from the spontaneous fission of ^{252}Cf, Figure from [47].

7.2 MC validation of neutron propagation with GIOVE

In connection with the MC simulations of muon-induced neutrons it was of large interest to validate the propagation of neutrons through a massive shield. The measurements were carried out in 2015 with the GIOVE. This is a semi-coaxial detector (m_{act}=(1.8±0.1) kg enclosed in a multi-layered shield comparable to the CONUS shield. Data was collected with a strong ^{252}Cf source over several days. The source was placed at the side of the shield. For ∼10 d it was enclosed in a PE block (see Figure 7.2), while for ∼7 d a measurement was carried without the PE block (see Figure 7.3).

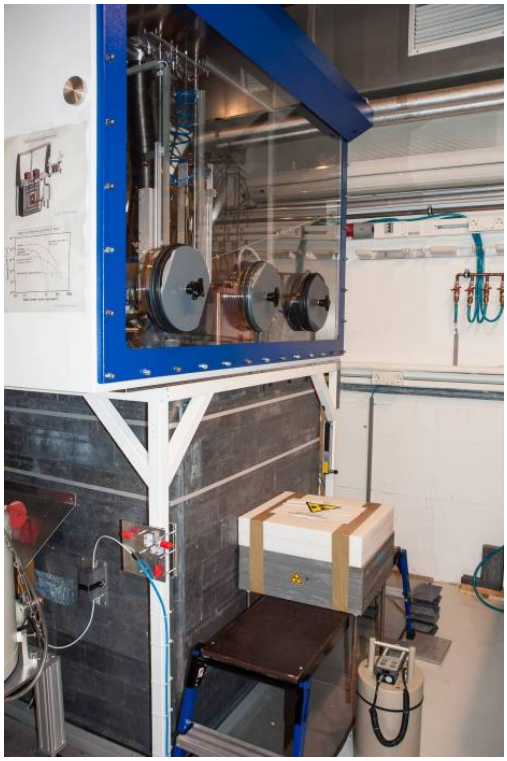

Figure 7.2: ^{252}Cf source measurement with the GIOVE detector. The source is placed inside a PE block (white and gray) at the side of the massive shield.

Figure 7.3: ^{252}Cf source measurement with the GIOVE detector. The source is placed at the side of the massive shield. A neutron monitor for radiation safety measurements is located next to the source.

The measurements were analyzed by W. Maneschg. Among others, the integral count rate within [100,2700]keV$_{ee}$ was evaluated and corrected for the background without source (see Table 7.2). By setting the lower limit at 100 keV$_{ee}$ the impact of the quenching on the spectral shape is negligible (see Figure 7.6a for the effect

integral count rate	integral background [100,2700]keV$_{ee}$ [cts/d/kg]		diff.
	meas.	MC	|data-MC|/data
with PE block	21500±110	17000±1300	(21±6)%
without PE block	77550±150	69300±4800	(11±6)%

Table 7.2: Integral count rate in [100,2700]keV$_{ee}$ of the GIOVE detector during the measurement with a strong ^{252}Cf outside the shield with and without a PE block.

integral count rate	neutron fluence rate [cm^{-2}d^{-1}]		diff.
	data	MC	|data-MC|/data
with PE block	48±6	35±1	(27±9)%
without PE block	124±14	137±2	-(11±13)%

Table 7.3: Neutron fluence rate at the surface of the GIOVE detector during the measurement with a strong ^{252}Cf outside the shield with and without a PE block.

of quenching on the spectral shape). Quenching was examined in more detail in the measurements with the CONUS detectors, that have a lower noise threshold. The count rate of the 139.5 keV line of ^{75m}Ge was determined as well to derive the neutron fluence rate at the diode indirectly as described in Section 5.3.4. Also in this case, the background count rate without source was subtracted.

The measurements were reproduced in a MC simulation of the full setup in Geant4.9.6. The accurate implementation of the MC geometry of the GIOVE detector and the shield are described in [161]. The MC is scaled with the source strength from Table 7.1. The MC prediction is compared to the measured data in Table 7.2 and Table 7.3. An excellent agreement is found for the integral count rate as well as the neutron fluence rate. Figure 7.4 displays a comparison of the spectral shape, which match overall. Only the line strength of some of the lines created in inelastic interactions is too small in the MC. This confirms, that overall the propagation of neutrons through the massive shield is working correctly. Thus, the validity of the results obtained in Chapter 4 with the propagation of reactor-induced neutrons through the shield is strongly supported.

Measurement with and without a PE were made. The PE block considerably moderates the neutrons that are captured within the shield before they can reach the diode such that in the end the count rate registered at the diode is lower by about a factor of 4, while the neutron fluence rate is reduced by a factor of 2.5. In the comparison with the MC, it turns out that a slightly better agreement is achieved for the measurements without PE block. This indicates that the thermalization of the neutrons within the PE block in the MC might not be fully accurate.

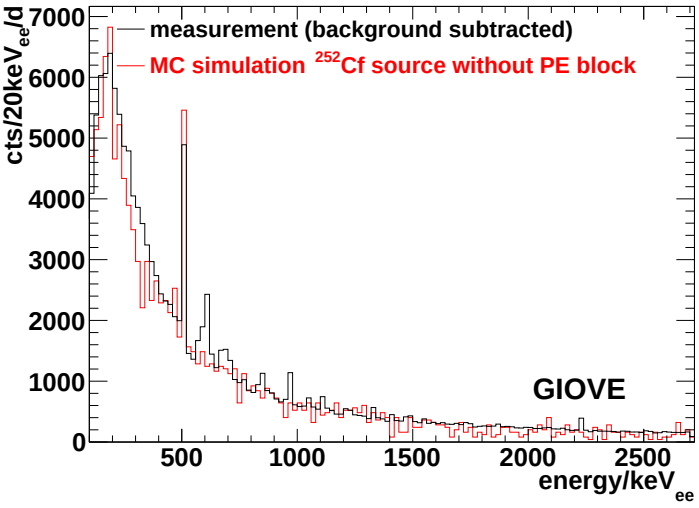

Figure 7.4: Comparison of ^{252}Cf source measurement outside the shield with the GIOVE detector to the MC simulation. Overall, a good agreement was achieved, only some of the line count rates of inelastic neutron interactions on Ge are too small in the MC.

7.3 MC validation of neutron interactions on Ge with CONUS

During the commissioning phase at LLL in 2017, a measurement with a weak ^{252}Cf source half-way inside the shield was carried out for 7 d. At that time, Conus-4 and CONRAD were placed inside the shield. The source was inserted through one of the openings for the cooling fingers of the CONUS detectors not inside the shield. Measurements in three different positions were made: (1) fully inside the detector chamber, (2) after the first two shield layers and (3) after the first three shield layers. For (2) and (3) the space between the detector chamber and the source were filled with Pb. Position (1) is displayed in Figure 7.5.

The weak source (see Table 7.1) was 29 yr old at the time of the measurement. For such an old source, the ^{250}Cf contribution inside the source is relevant. A. Zimbal from PTB did a detailed characterization of the source. A source strength of 46.05±1.38) n/s were evaluated, thereof 50% by ^{252}Cf, 48% by ^{250}Cf and 2% by ^{248}Cm. Moreover, next to the γ-ray emission in spontaneous fission, also sizable contaminations from other Cf isotopes (total 9.29 kBq), ^{60}Co (98 Bq), ^{137}Cs (75 Bq) and ^{90}Sr (75 Bq) were found. They fully dominate the measurement inside the detector chamber. However, already the first two shield layers suppressed most of it and neutron induced lines become visible. The following neutron interactions were observed:

- lines from neutron capture on Ge, especially the metastable Ge states, Cu and Pb

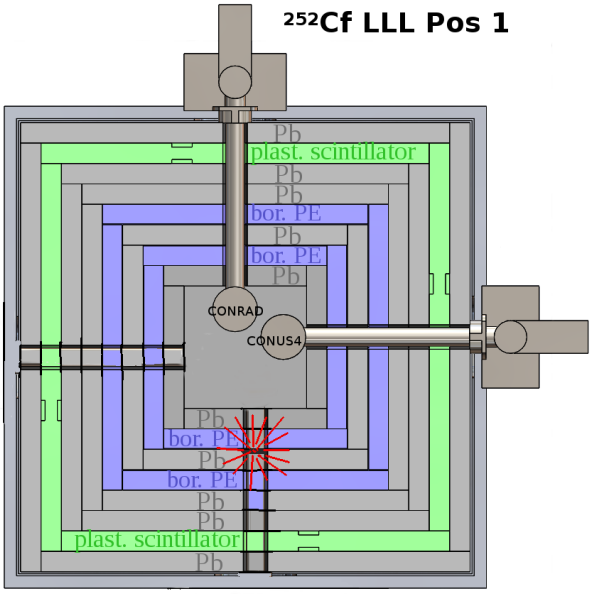

Figure 7.5: View from above on the ^{252}Cf source measurement inside the CONUS shield at LLL with Conus-4 and CONRAD: in position 1, the source in red was placed after two shield layers.

- lines from inelastic neutron scattering on Ge with a tail towards higher energies due to the energy deposition by recoils added to the γ-ray energy
- increase towards lower energies due to Ge recoils

Figure 7.8a and 7.8b display the spectra taken with Conus-4 in the two positions with the shield. They are corrected for the background without source. The only inelastic interaction visible comes from ^{73}Ge(n,n'γ)^{73}Ge at 69 keV, where the tail due to recoiling Ge nuclei is seen. The visible line background corresponds to the metastable Ge states and neutron capture on Cu. Due to the weak source strength there is no significant activation of ^{71}Ge.

The measurements were also reproduced in the MC. To first order, it was assumed that the spontaneous fission spectrum of ^{250}Cf is close to the one of ^{252}Cf, so only the ladder was simulated and normalized with the source strength from Table 7.1. The spontaneous fission γ-rays were also simulated, but the contribution is already negligible in position 1. The same is true for the γ-rays from contaminations except for ^{60}Co has a small impact. The MC spectra are added to Figure 7.8a and 7.8b for a quenching parameter of k=0.2. The continuum is successfully reproduced, especially the increase due to recoils at lower energies. Due to the DAQ settings data for the comparison to the MC is only available down to 6 keV$_{ee}$. A comparison for various integral ranges is given in Table 7.4. An good agreement within 2-30% is found. A better agreement is achieved at low energies, where nearly all energy depositions come from recoiling Ge nuclei, but this range is strongly impacted by quenching (as discussed below). At position 1, 7% of the integral count rate is

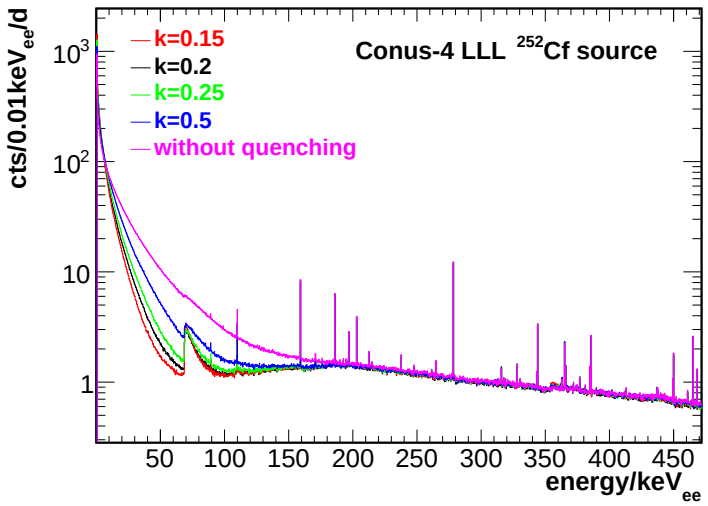

(a) The recoil energy deposition below $\sim$100 keV$_{ee}$ are strongly influenced by the quenching parameter k. There is also an impact on the tail of the line induced by inelastic scattering on Ge nuclei.

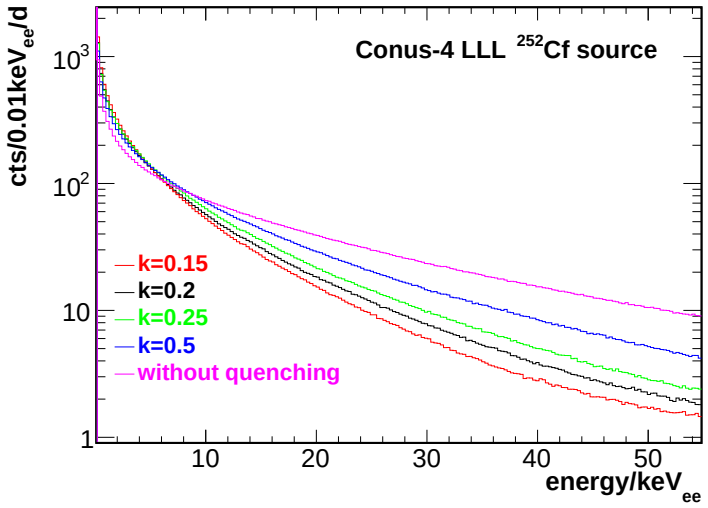

(b) Zoom into the energy range below 60 keV$_{ee}$ of Figure 7.6a. Below 7 keV$_{ee}$ the integral range is enhancement for smaller quenching parameters k.

Figure 7.6: Comparison of different quenching parameters k and no quenching in the MC for the ^{252}Cf source measurement at LLL in position 1 within the CONUS shield registered with Conus-4.

created by spontaneous fission and ^{60}Co γ-rays emitted by the source, at position 2, the contribution is negligible. The metastable states are not created in the MC, while all other lines are visible, but small discrepancies in the count rates are found. The neutron spectra were also registered in the MC. They are shown in Figure 7.7

in comparison to the muon-induced neutron spectrum showing that the spectra are indeed similar and results obtained from the ^{252}Cf can be transfered to the muon-induced neutron spectra.

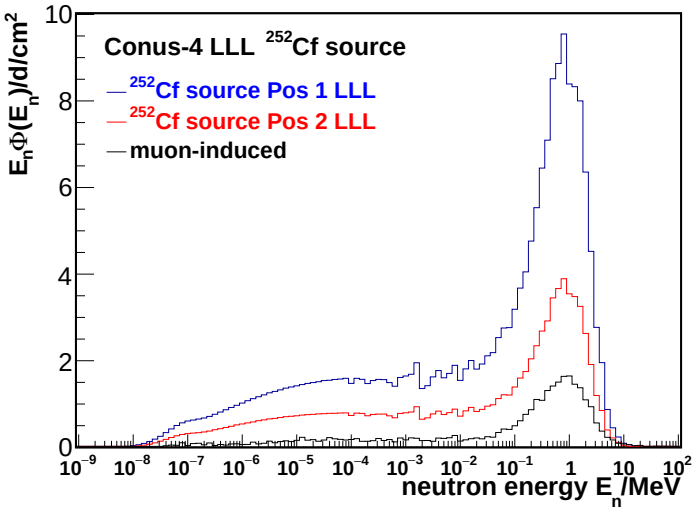

Figure 7.7: Neutron spectra induced by the ^{252}Cf placed within the Conus shield in position 1 and 2. They are compared to the spectrum of muon-induced neutrons. The shape is similar, confirming the results obtained in the validation of the MC with the ^{252}Cf source measurements can be transfered to the MC of muon-induced neutrons.

The measurements are furthermore used to examine the effect of quenching in more detail. Figure 7.6a shows a comparison of MC spectra for various quenching parameters and without quenching. Due to the quenching, energy depositions below 100 keV$_{ee}$ are shifted towards lower energies and at the same time the spectral shape towards lower energies becomes steeper. For a lower quenching parameter the shift becomes stronger. Down to ∼7 keV$_{ee}$ quenching reduces the integral count rate. At lower energies an enhancement is observed (see Figure 7.6b), as from this point on more energy depositions at higher energy are moved into the energy range then energy depositions are shifted to even lower energies. Also the tail to higher energies at the line at 69 keV$_{ee}$ from inelastic neutron scattering is influence by the quenching parameter.

From the MC to data comparison, it can be seen, that the implementation of the quenching in the post-processing of the MC as described in Section 1.7 works as intended to adapt the MC to reality.The quenching parameter is not well known and the dominant systematic uncertainty of the CONUS experiment (see Section 6.7). The comparison here confirms that a quenching parameter of k=0.12-0.25 as used in the CONUS analysis (see Chapter 6) is realistic, but there are too many uncertainties in the MC to do a more precise evaluation. While in the current comparison, an excellent agreement to the data below 100 keV$_{ee}$ is observed with k=0.2, lowering k to 0.15 would result in a similar discrepancy between data and MC than observed

Conus-4	integral background [cts/d/kg]				
position 1	data	MC k=0.2	|data-MC|/data k=0.2	MC k=0.15	|data-MC|/data k=0.15
[6,100] keV_{ee}	3360±30	3280±100	2±3%	2930±90	13±4
[100, 440] keV_{ee}	1740±30	1400±40	20±4%	1420±40	19±4
position 2	data	MC k=0.2	|data-MC|/data k=0.2	MC k=0.15	|data-MC|/data k=0.15
[6, 100] keV_{ee}	1490±30	1420±40	5±4%	1220±40	18±4
[100, 440] keV_{ee}	830±20	620±20	26±6%	600±20	27±6

Table 7.4: Comparison of integral count rates from the ^{252}Cf source measurement at LLL with the source within the CONUS shield to the MC scaled with the source strength. The count rates for Conus-4 are shown and an agreement within 2-30% is found depending on the energy range and the quenching parameter. Within other systematics such as the distance between source and detectors, no preference for one quenching parameter can be derived from the data.

at higher energies above 100 keV_{ee}. Most likely the enhancement at lower energies for a quenching parameter of 0.2 cancels out other systematic uncertainties of the order of 20% (e.g. distance of detector to source or material compositions) leading to the supposingly better match. Dedicated quenching parameter measurements are a necessity to precisely determine the quenching parameter.

Within the results in this section no difference in the performance of Geant4.9.6 to Geant4.10 was observed. All in all, similar to Section 7.2, overall a good performance of the MC in the propagation of neutrons and the interactions on Ge nuclei is observed. More detailed examinations are planned for.

7.4 Cross section ratio of ^{71}Ge to ^{71m}Ge for fast neutrons

The strong neutron source used in the validation of the neutron propagation through the GIOVE shield in the MC (see Section 7.2) was brought to KBR in 2020. The source was placed inside a PE shield for radiation safety reasons and placed next to the CONUS shield with the intent to activate ^{71}Ge in neutron capture to improve the statistics for the energy scale calibration (see Section 6.2). The source was deployed for 13 d 22 h. The activation was successfully achieved and the count rate in the 10.37 keV_{ee} increased by a factor of 3 to 9 depending on the location of the detectors relative to the source compared to the in situ production rate by muon-induced neutrons (see Table 5.16 for the in situ production rate).

The collected data can be used to examine the relationship between the 10.37 keV line count rate of the activated ^{71}Ge isotope and the 198.3 keV line count rate of ^{71m}Ge. As described in Section 5.3.5 for the in situ activation, in some of the neutron capture reactions ^{70}Ge(n,γ)^{71}Ge the metastable Ge state ^{71m}Ge is created,

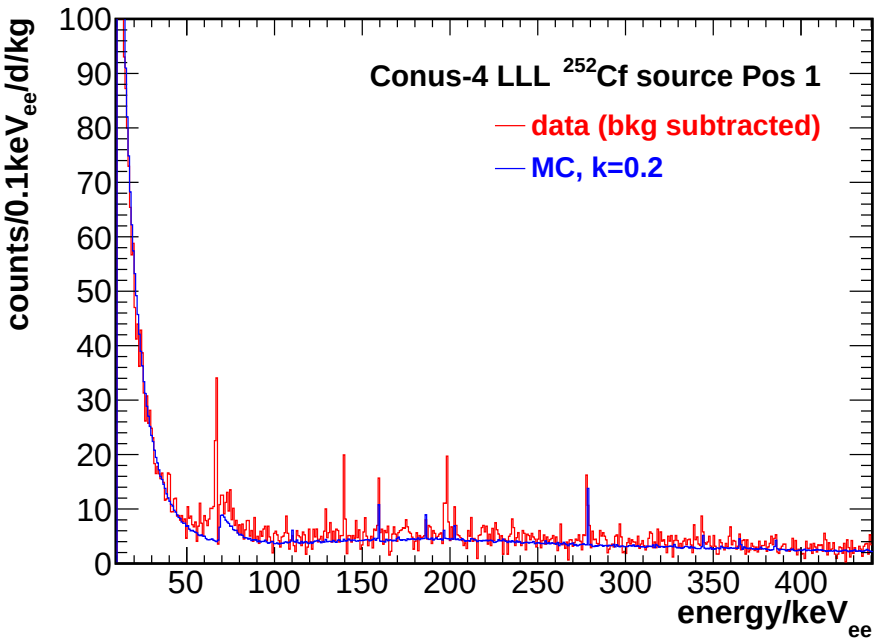

(a) Position 1.

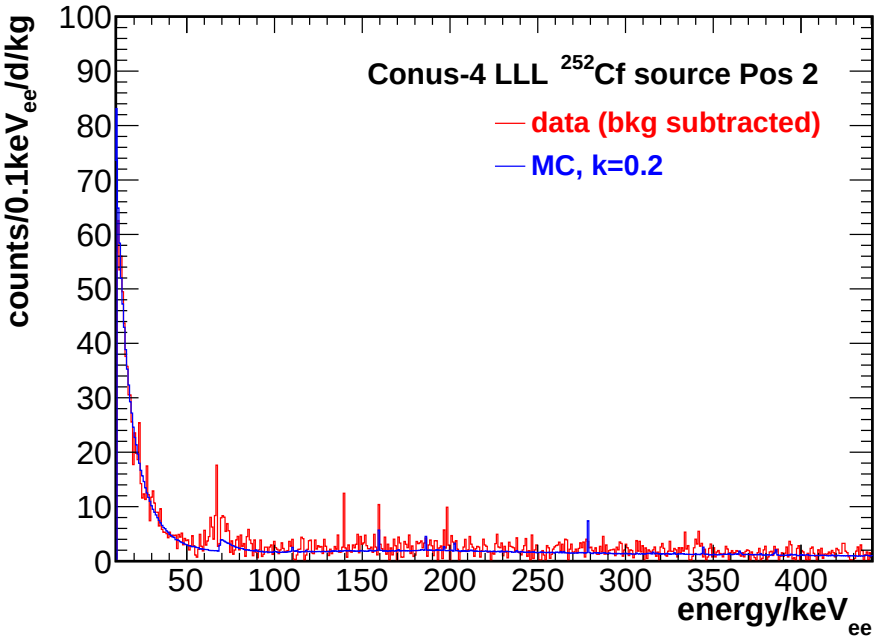

(b) Position 2.

Figure 7.8: Comparison of ^{252}Cf measurements at LLL within the CONUS shield in position 1 and 2.

which decays to ^{71}Ge with the emission of 198.3 keV. By calculating the ratio of the

line count rates, conclusions on the cross section for the creation of ^{71m}Ge can be drawn.

To do this, the production rate of ^{71}Ge during the ^{252}Cf source measurement is derived from the 198.3 keV line count rate, the branching ratio $br_{^{71}\mathrm{Ge}}$ and detection efficiency $\epsilon_{^{71m}\mathrm{Ge}}$ from MC. It depends on the cross section ratio $r^{71} = \sigma_{^{71}\mathrm{Ge}}/\sigma_{^{71m}\mathrm{Ge}}$. To be able to compare to the activated 10.37 keV count rate at the end of the ^{252}Cf source measurement, the decay of ^{71}Ge during the measurement with a half-life of 11.4 d must be taken into account and the branching ratio $br_{^{71}\mathrm{Ge}}$ and detection efficiency $\epsilon_{^{71}\mathrm{Ge}}$ are included:

$$N_{^{71}\mathrm{Ge}}(t_{source}) = \frac{ln(2)}{T_{1/2}^{^{71}\mathrm{Ge}}} r^{71} N_{^{71m}\mathrm{Ge}} \frac{br_{^{71}\mathrm{Ge}} \cdot \epsilon_{^{71}\mathrm{Ge}}}{br_{^{71m}\mathrm{Ge}} \cdot \epsilon_{^{71m}\mathrm{Ge}}} t_{source} \left(1 - exp\left(\frac{ln(2)}{T_{1/2}^{^{71}\mathrm{Ge}}} t_{source}\right)\right) \tag{7.1}$$

In the equation, t_{source} corresponds to the time, the ^{252}Cf source was placed at the CONUS shield. The count rates, already corrected for the in situ activation, and the efficiencies are summarized in Table 7.5. For the collected data, $r^{71}_{meas,^{252}Cf}$= 5.8±1.3 is derived. This can be compared to $r^{71}_{meas,insitu} = 4.1 \pm 0.4$ from the in situ production by muon-induced neutrons (see Section 5.3.5). The ratios are similar within the uncertainties. For thermal neutrons in literature $r^{71,therm}_{lit} = 10.5 \pm 2.2$ is evaluated, while for fast neutrons no cross section for ^{71m}Ge was found in literature by the author of the thesis. The ratio is not expected to be constant over all energies, e.g. for ^{75}Ge and ^{75m}Ge in Table 5.5, where a measured value is available, the ratio differs by a factor of two. The discrepancies of the measured ratio to the value derived from literature strongly indicate, that mostly not thermal neutrons are responsible for the activation of ^{71}Ge, but fast neutrons have a significant contribution. This is in agreement with the MC prediction that most of the neutrons arriving at the diode in the MC have energies around 1 MeV (see Figure 5.10).

From r^{71}_{meas} and the ^{71}Ge cross section of ∼0.04 b at 1 MeV from the JENDL4.0 data base [117] a cross section of ∼0.008 b for the creation of ^{71m}Ge can be estimated for fast neutron energies. The mean value of the cross section ratios from in situ production and the ^{252}Cf source measurement was used. A more detailed analysis of the different neutron spectra is planned to understand, whether a significant difference for the ratios would be expected. Moreover, while most of the neutrons arriving at the diodes have higher energies, there are some thermal neutrons. With the help of the neutron spectrum from MC a correction for the activation by thermal neutrons can be made.

To sum it up, r^{71} can provide valuable information for HPGe measurements:

- if 198.3 keV and 10.37 keV line count rates are known: comparing the ratio of the line count rates to $r^{71,therm}_{lit}$ reveals whether mostly thermal neutrons or mostly fast neutrons are responsible for the activation

Conus-3, 31.01.2020	^{71m}Ge	^{71}Ge
line	198.3 keV	10.37 keV
count rate N in cts/d/kg	15.8±2.5	53.8±5.6
MC efficiency	0.67	0.94
branching ratio	1	0.876
activity A in cts/d/kg	66.5±6.9	23.9±3.8

Table 7.5: Count rate in the 198.3 keV line in Conus-3 during the ^{252}Cf source measurement corrected for the background count rate without source. It is related to the activation of ^{71}Ge. The count rate at the end of the ^{252}Cf source measurement corrected for the in situ production was determined by W. Maneschg. From the ratio of the line count rates, information on the cross section of ^{71m}Ge can be gained. The branching ratios and detection efficiencies from MC are required as well.

- if the 198.3 keV count rate and the neutron energies at the diode are known: for a thermal neutron field at the diode, the expected count rate in the 10.37 keV line can be derived from $r_{lit}^{71,therm}$, for a fast neutron field approximations can be made with r_{meas}^{71} evaluated above

7.5 Summary of ^{252}Cf source measurements

Measurements with ^{252}Cf sources and various HPGe spectrometers were carried out with the goal to examine the propagation of neutrons through massive shields and the interaction of neutrons with Ge nuclei. Overall, a good agreement in the continuum is found, supporting the validity of the neutron Geant4 MC simulations within this thesis. By placing a ^{252}Cf source within the shield, neutron induced recoils at low energies are observed and can be compared to the MC. It is shown, that the implementation of the quenching in the post-processing routine works sufficiently well to describe the spectrum. Moreover, the activation of ^{71}Ge is examined in connection with the 198.3 keV line count rate from the decay of ^{71m}Ge. From the ratio to the activated 10.37 keV line count rate, the ratio of the cross section can be determined. It deviates clearly from the ratio in literature for thermal neutrons, confirming that most muon-induced neutrons at the diode have higher energies as predicted by the MC.

8 Conclusions and outlook

The CONUS experiment is looking for CEνNS of reactor antineutrinos from the commercial nuclear reactor KBR at a distance of 17 m to the reactor core. Three prerequisites need to be fulfilled for the detection: (1) a low enough energy threshold to be able to see the tiny neutrino-induced recoils, (2) a source with a high neutrino flux and (3) a successful background suppression. In the following, it is shown how CONUS meets this challenges and the main findings of the thesis are highlighted.

CONUS employs four low threshold HPGe spectrometer equipped with electrical cryocoolers. The detectors and the DAQ were thoroughly characterized during the commissioning at MPIK and the data taking at KBR. The detectors have an excellent resolution as has been confirmed in measurements with a pulse generator (64-77 $_{ee}$ at FWHM) and radioactive sources ($\sim$330 eV$_{ee}$ at FWHM of 59.54 keV line of ^{241}Am). Also a highly stable energy scale over the course of several months was observed (standard deviation $\sim$4 eV for 10.37 keV line). Due to the high resolution, it is even possible to examine peak shifts within this standard deviation more closely. It could be shown, that on this high level a correlation to the temperature of the surrounding persists due to the energy dependence of the energy required to create an electron hole pair. Moreover, the active volume of the detectors was evaluated. This includes the determination of the dead layer and transition layer. Because of the incomplete charge collection within the transition layer events are not observed at their original full energy in the detector, but at lower energies contributing to the continuum down to the energy threshold. A model for the transition layer is required as input for the MC background model. Also, the electronics noise at the energy threshold was examined in detail. The time difference distribution cut on the time difference between events was introduced. It removes microphonics events and events from DAQ artifacts that can be clearly separated from the physics events by the time difference between the events. No exposure is lost due to this cut. Moreover, a correlation of the noise rate over time to the cryocooler power was found. Frequencies related to the cryocooler could be extracted from the noise peak. The cryocooler power on the other hand is correlated to the room temperature. This is highly relevant for the data taking at KBR, as strong variations in the room temperature over time were observed at KBR. This leads to the respective variations in noise rate. For the analysis of Run1 and Run2 the NTC cut was introduced, which ensures that only data with a noise rate within prefixed boundaries is included. The cut strongly reduces the exposure of the experiment. For the CEνNS analysis, a stable energy threshold of around 300 eV$_{ee}$ was achieved.

The detectors were brought to KBR and deployed in the shield at the beginning of

2018. As the nuclear reactor is located at earth's surface only a shallow overburden is available. An elaborate shield consisting out of 25 cm of Pb to shield against natural radioactivity, layers of borated PE to moderate and capture neutrons and an active muon veto made out of plastic scintillator plates is required. At a distance of 17 m to the reactor core, a high antineutrino flux is guaranteed, but also a potential reactor-correlated background has to be examined. Especially neutrons that are created in the fission reactions in the reactor core can be a problematic background as they induce nuclear recoils as well. Thus, before the setup of the experiment the neutron background at the experimental site was measured with the Bonner Sphere spectrometer NEMUS in cooperation with the PTB. The propagation of the reactor neutrons from the reactor core to the experimental site was carried out in an ab initio MC simulation including the full geometry of the reactor core to the experimental site to support the analysis. The measured reactor-correlated neutron fluence rate is about a factor of two smaller than on the earth's surface. More than 80% of the neutrons are thermalized and the maximum neutron energy is about 1 MeV. Deviations of ∼20% in the thermal fluence rate within a few meters were found, showing how important it is to characterize the background at the exact location of the experiment. In a second MC simulation the neutron spectrum was propagated through the CONUS shield and the expected count rate in the Ge spectrometers within the ROI was found to be negligible with ∼0.01 cts/d/kg in [0.3,0.6]keV$_{ee}$. Data collected with a ^{252}Cf source were used to validate the MC regarding the propagation of neutrons through the shield and the neutron interactions on Ge.

Next to neutrons there is also a thermal power correlated γ ray background. It was observed with the unshielded γ ray spectrometer CONRAD. The line background above the natural radioactivity (above 2.7 MeV$_{ee}$) is observed. The dominant lines are created by the decay of ^{16}N in the cooling water cycle of the power plant. The ^{16}N contribution is created by neutron activation of water in the reactor core. It is long-lived and decays in the cooling circuit closer to the experimental site. A highly accurate correlation of the line count rates to the thermal power was observed, also during the ramp down and ramp up of the nuclear power plant at the beginning and the end of an outage. Moreover, high energetic γ rays from neutron-capture on iron from the steel enforced concrete and on copper of the cryostat are observed. Together with MC simulations, the measurement was used to approximately confirm the findings of the Bonner Sphere measurements. As further MC simulations showed, this γ ray background is shielded by the Pb within the shield.

The non-reactor correlated background without applying the active muon veto is dominated by muon-induced electro-magnetic cascades and neutrons in the Pb. By comparing this background measured at LLL with a known overburden of 15 m w.e. to the background determined at KBR a depth of about 24 m w.e. was extrapolated. The prompt muon-induced background was reproduced in a MC simulation. It was shown that the fluence rate of muon-induced neutrons in the CONUS shield is reproduced excellently in the used simulation code. Nevertheless, small deviations in the continuum at low energy were found that required adaptations to reproduce the data for the background model. Within the model, an active muon veto efficiency

of ∼97% was estimated. Additional components to the background model are ^{210}Pb from the innermost Pb layer of the shield and within the cryostat. There is also a small contribution from muon-induced neutrons in the concrete of the building. Additional, lines from the decay of radon were observed. Radon is removed from the air around the detectors by flushing with radon free air from breathing air bottles. However, until the end of the outage of Run2 remaining decays were observed. With the help of a MC the contribution to the ROI was estimated. Fluctuations were found to be negligible within the statistic uncertainties. An increased air flow and the closing of the ^{228}Th calibration source tube should guarantee a low background for the future.

The second potentially varying background contribution is the decay of cosmogenic activated isotopes in Ge and Cu at earth's surface. From the decay of visible lines in the background (^{68}Ge/^{71}Ge, ^{68}Ga, ^{65}Zn and ^{57}Co), the activity of the isotopes were determined at the time when the detectors were brought underground. With the known exposure histories production rates could be evaluated that are in good agreement with the literature. As the detectors and materials were kept underground as much as possible during detector construction, the overall activation is small. With MC simulations of the activated isotopes with and without line background, it could be shown that the decaying background in the ROI with a difference of the decay rate of less than 0.4 cts/d after 14 month can be neglected for the CEνNS analysis. Taking all described background contributions into account, a background model for the reactor OFF data collected during the outages of Run1 and Run2 is developed. Below 400-500 eV$_{ee}$ the increasing electronics noise threshold is described by an analytical functions. A Kolmogorow-Smirnow-Test confirmed that the model is suited to be used in the likelihood analysis of the data.

From the CONUS Run1 and Run2 data the first upper limit for CEνNS of reactor antineutrinos in the fully coherent regime below 10 MeV is derived. An analysis energy threshold of around 300 eV$_{ee}$ depending on the detector was used. The result is based on an exposure of 248 kg·d reactor ON data and 59 kg·d reactor OFF data after all cuts. It has been derived assuming a χ^2 distribution of the test statistics, which should be checked in the near future. The upper limit is determined in dependence of the quenching parameter, which is the main systematic uncertainty of the analysis. The literature values are covered by an interval of 0.12 to 0.2, which corresponds to a difference in the signal expectation of more than a factor of 40. Many of the literature values in Ge were determined for the 77-87 K regime and they rely mostly on the Lindhard theory with/without adiabatic correction. The quenching does not only modify the normalization of the CEνNS neutrino spectrum, but also the shape. The CONUS upper limit excludes quenching factors above 0.19 with a 90% C.L. for the Lindhard model with adiabatic correction. For the mean value of the range of literature values of 0.16 the obtained upper limit is only about a factor of two away from the Standard Model signal expectation (see Figure 8.1). To reduce the uncertainty on the signal prediction, primarily a precise measurement of the quenching factor would be required. The CONUS collaboration is considering

such a measurement in the near future. The quenching factor can be evaluated by neutron scattering measurements on Ge.

Three approaches can be pursued to improve the limit towards the detection of CEνNS at reactor site: a lower and more stable energy threshold, a lower and more stable background and more statistics, especially during reactor OFF time.

The biggest improvement can be expected from a lower energy threshold. The signal expectation in Figure 6.11 shows independent of the quenching parameter a near exponential increase towards lower energies. Assuming a quenching parameter of 0.16, lowering the energy threshold from 330 eV_{ee} to 300 eV_{ee} increases the signal expectation by approximately a factor of three, for an energy threshold of 250 eV_{ee} it is even more than a factor of 16. For larger quenching parameters the effect is weaker, while for smaller quenching parameters it is even bigger. For smaller quenching parameters due to the shift of the signal towards lower energies a lower threshold is in any case a necessity to be able to observe a signal at all. Next to a low threshold also a stable threshold is desired to be able to collect statistics over long time periods. As has been shown in section 3.3.4, the noise close at the energy threshold is strongly influenced by the cryocooler and the cryocooler performance dependence on the room temperature. With the outage of Run2, the cold-house was introduced to keep the temperature around the detectors stable and low. This was further improved within the following reactor ON time with the adjustment of the AC. Unfortunately, due to the leakage test at KBR, it was not possible to take full advantage of the upgrade as the noise and background properties of the detectors were changed. For future runs however, a more stable and potentially lower threshold is expected. The strict cuts on the exposure should be unnecessary. Moreover, while the TDD cut removes parts of the microphonics noise only due to the time difference of the events, it might be possible to further suppress the noise by observing the pulse shape of the events with an upgraded DAQ. For the far future, active noise canceling as descried in [163] could be beneficial.

While a lower noise threshold drastically increases the expected number of CEνNS, a lower and more stable background would enable the detection of a smaller number of signal counts. It would also be beneficial for other analyses such as searches for a neutrino magnetic moment.

Moreover, the muon veto trigger rate is increased by the ^{16}N γ ray lines correlated to the thermal power of the reactor. This correlation could be avoided with an additional Pb shield towards the side of the reactor. In this way, a more stable dead time can be achieved and it might also be possible to better tune the muon veto and increase the efficiency of the suppression of the muon-induced background. From the veto trigger rate the number of ^{16}N γ rays that hit the shield can be estimated. This count rate gives hints that the original assumption of the angular distribution of the γ rays does not hold and potentially a slightly higher count rate within the shield can be expected. Such kind of background enhances the continuum and is flat towards low energies (except for slow pulses). Thus, only the b parameter of the fit would be modified and there is no danger to mistake it for a signal. Nevertheless,

further studies are necessary and additional Pb could improve the situation.

Regarding the background suppression, for CONUS improvements can be made in two places. First of all, slow pulses from energy depositions within the transition layer increase the continuum below 6 keV_{ee} (see Figure 2.25). The pulse shape of these events differs from the pulse shape of events registered within the active volume of the detector. By registering the pulse shape, a large fraction of these events could be removed (e.g described in [164]). It might also be possible to distinguish ^{210}Pb surface events by their pulse shape and cut them. Without the slow pulse contribution the background model could also be further improved as all uncertainties on the location of interactions within the Ge and the charge collection efficiency drop out. Removing the slow pulses can also improve the background model, as all uncertainties related to the modeling of the transition layer could be reduced.

Second, up to now, the CONUS experiment does not make use of anti-coincidences between the detectors. According to the background model even with the applied muon veto there is still a sizable contribution of muon-induced background. As this background is created within the shield, simultaneous hits in several detectors at once can be expected. In principle, those events could be removed, if the data collection of the four detectors is synchronized. However, the exponentially increasing noise count rate at the energy threshold could lead to many accidental coincidences.

For future CONUS like experiments it might be possible to achieve improvements by replacing Pb with tungsten (W). Tungsten has a higher density of 19.25 $\mathrm{g/cm^3}$ [165] than Pb with 11.34 $\mathrm{g/cm^3}$ [166]. The γ ray attenuation coefficient at 2-3 MeV is only lower by about 5% [110]. This means that the 25 cm Pb of the CONUS shield could be replaced by $\sim$15 cm W. In this way, the shield could be built more compact, allowing for a shorter cooling finger, which helps due to the easier cold transfer to achieve a higher energy resolution. Moreover, the more compact shield provides less targets for the muons to produce neutrons. Preliminary MC simulations showed a reduction in the neutron fluence rate at the diode by about 30%. However, W as shield material needs to fulfill the requirements on the radio purity. A good step forward in this direction was already achieved by screening samples from various manufacturers as well as the powders used as input for the manufacturing process. Further improvements are planned.

Lastly, collecting more statistics especially during reactor OFF times helps to be able to extract a CEνNS from the data. There is only one regular outage of about four weeks each year, but at the end of 2021, when the KBR nuclear power plant will shut down, the statistics on the background data will quickly increase. Next to a detection of CEνNS the CONUS data collected in the CONUS experiment can also be used to look for a neutrino magnetic moment and beyond the Standard Model neutrino interactions. Also for these analyses, on the long run, the additional extended reactor OFF data will provide valuable input.

The current generation of HPGe spectrometers such as the CONUS ones providesnoise thresholds at the verge of being able to detect CEνNS interactions within the fully coherent regime. However, in the future with lower noise thresholds large statistics could be collected and CEνNS could be used as tool for reactor monitoring.

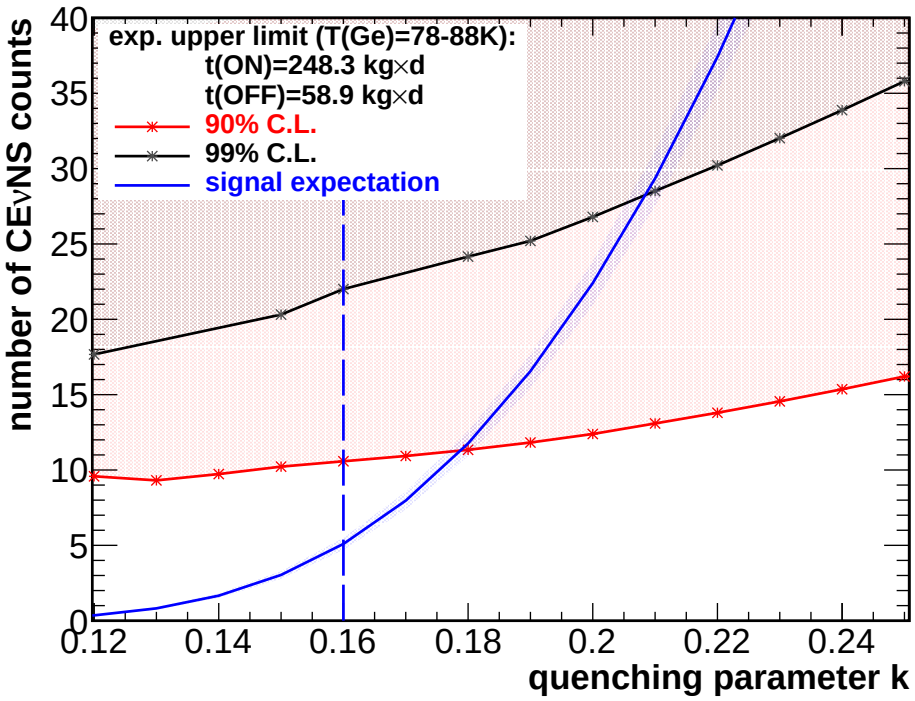

Figure 8.1: Combined upper limit of CEνNS counts as function of the quenching parameter for Run1 and Run2 of the CONUS experiment. The quenching parameter of 0.16, which corresponds to the mean in literature, is marked.

Part I

Appendix

A Appendix A - Measurement uncertainties of monitoring devices

measured variable	uncertainty
Radon Scout monitor	
radon	stat. display (24h@300 $\frac{\text{Bq}}{\text{m}^3}$: 15%)
temperature	syst. <0.4 °C (0.3 °C typ.)
humidity	syst. <4.5% (3% typ.)
air pressure	syst. <2.2 mbar
Canary radon monitor	
radon 1 day	syst. + stat. ±20%
radon longterm	syst. + stat. ±10%
Tdf temperature sensor	
temperature	syst. ±0.8%
humidity	syst. ±5%
HOBO temperature sensor	
temperature	syst. ±0.1% of value
Canberra Cryocooler	
cold head	±0.5 °C
cold tip	±0.5 °C
11A temperature logger	
temperature	syst. ±0.5 °C

Table A.1: List of devices to monitor the environment within the CONUS experiment with the respective uncertainties.

B Appendix B - Calculation of the energy per electron hole pair

The derivation of the energy deposited in the diode is related to the number of freed electron hole pairs N and the energy per electron hole pair ϵ:

$$E_{peak} = N_{ref} \cdot \epsilon_{ref} = N_{meas} \cdot \epsilon_{meas} \tag{B.1}$$

From this, it follows for energy per electron hole pair ϵ_{meas} derived from the measurement:

$$E_{peak} = \frac{N_{ref}}{N_{meas}} \cdot \epsilon_{ref} = \frac{E_{ref}}{E_{meas}} \cdot \epsilon_{ref} \tag{B.2}$$

In the last step, it was used that the energy is proportional to the number of free charge carriers.

C Appendix C - Natural decay chains

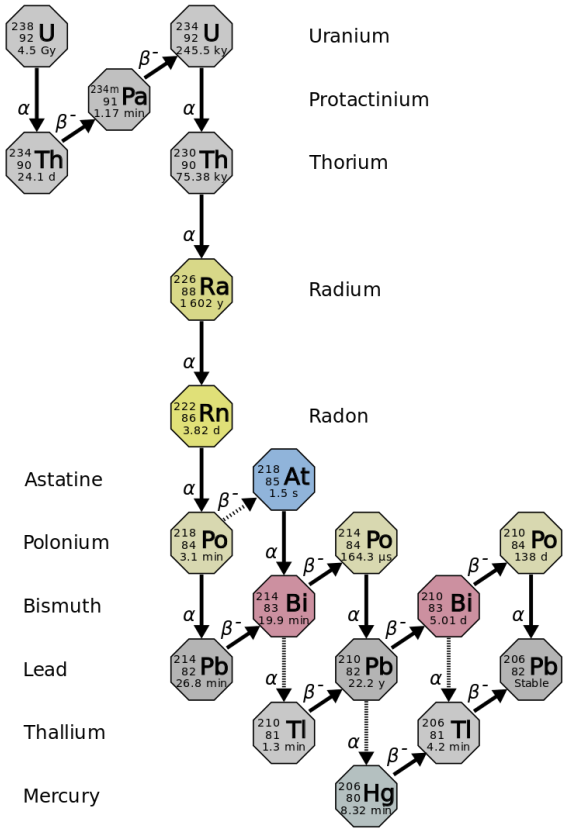

Figure C.1: Uran decay chain. [32]

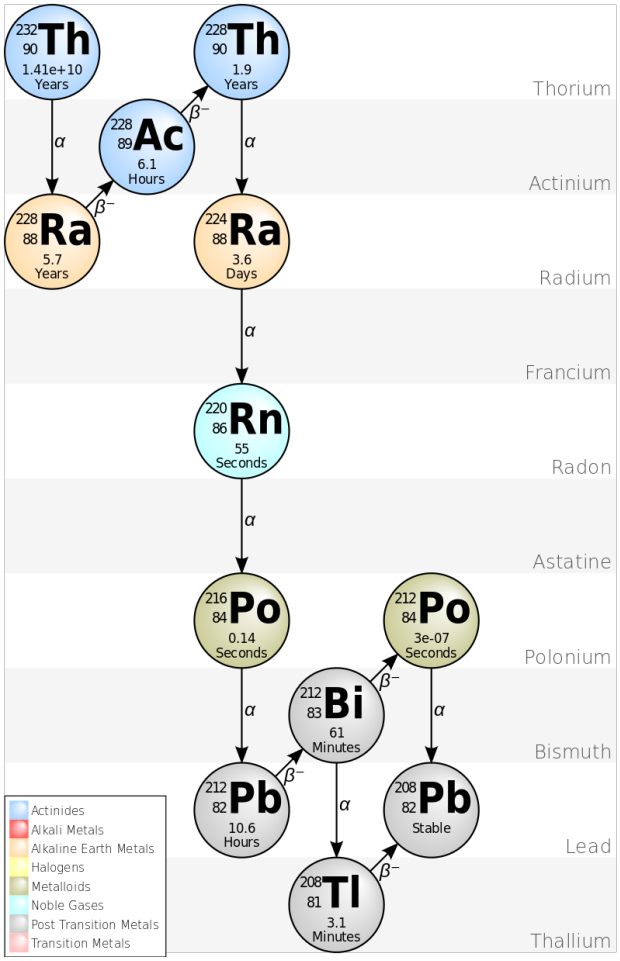

Figure C.2: Thorium decay chain. [33]

D Lists

D.1 List of Figures

D.2 List of Tables

E List of publications by Janina Hakenmüller

CONUS collaboration:

- **J. Hakenmüller** et al. (CONUS collaboration), Neutron-induced background in the CONUS experiment, Eur. Phys. J. C (2019) 79:699, https://doi.org/10.1140/epjc/s10052-019-7160-2
- **J. Hakenmüller** on the behalf of the CONUS collaboration, Proceeding TAUP conference 2017, A novel experiment for coherent elastic neutrino nucleus scattering: CONUS, J. Phys. Conf. Ser. 1342 (2020) 1, 012094, doi:10.1088/1742-6596/1342/1/012094
- **J. Hakenmüller**, W. Maneschg and G. Heusser, Proceeding TAUP conference 2015, Simulation and verification of the cosmogenic background at the shallow depth GIOVE detector, J. Phys. Conf. Ser. 718 (2016) 4, 042028
- W. Maneschg on behalf of CONUS collaboration, The Status of CONUS, Talk at XXVIII International Conference on Neutrino Physics and Astrophysics, 4-9 June 2018, Heidelberg, Germany, DOI: 10.5281/zenodo.1286927
- C. Buck on behalf of CONUS collaboration, Proceeding Moriond conference 2019 EW Interactions and Unified Theories, Latest results of the CONUS reactor neutrino experiment

GERDA collaboraton:

- M. Agostini et al. (GERDA Collaboration), Limit on the radiative neutrinoless double electron capture of ^{36}Ar from GERDA Phase I, The European Physical Journal C volume 7
- M. Agostini et al. (GERDA Collaboration), Limits on uranium and thorium bulk content in Gerda Phase I detectors, Astroparticle Physics 91 (2017) 15-21.
- M. Agostini et al. (GERDA Collaboration), Background-free search for neutrinoless double β decay of 76Ge with GERDA, Nature 544 (2017) 47
- A.J. Zsigmond on behalf of the GERDA Collaboration, GERDA Phase II: search for neutrinoless double beta decay, PoS (EPS-HEP2017) 150

- M. Agostini et al. (GERDA Collaboration), Improved Limit on Neutrinoless Double-beta Decay of 76Ge from GERDA Phase II, Phys. Rev. Lett. 120 (2018) 132503
- M. Agostini et al. (GERDA Collaboration), Upgrade for Phase II of the GERDA experiment, Eur. Phys. J. C 78 (2018) 388
- M. Agostini et al. (GERDA Collaboration), Characterization of 30 ^{76}Ge enriched Broad Energy Ge detectors for GERDA Phase II, Eur. Phys. J. C. 79 11 (2019) 978
- M. Agostini et al. (GERDA Collaboration), Probing Majorana neutrinos with double-beta decay, Science 365, 1445 (2019)
- M. Agostini et al. (GERDA Collaboration), Modeling of GERDA Phase II data, Journal of High Energy Physics volume 2020 139
- M. Agostini et al. (GERDA Collaboration), First Search for Bosonic Superweakly Interacting Massive Particles with Masses up to $1\,\mathrm{MeV/c^2}$ with GERDA, Phys. Rev. Lett. 125, 011801 2020

Else:

- A. Bischoff et al., The Stubenberg meteorite - An LL6 chondrite fragmenal breccia recovered soon after precise prediction of the strewn field, Meteoritics & Planetary Science 1-12 (2017)
- A. Bischoff et al., The Renchen L5-6 chondrite breccia - The first confirmed meteorite fall from Baden-Württemberg (Germany), Geochemistry, Volume 79, Issue 4, December 2019, 125525

F Bibliography

[1] Fukuda, Y. et al., Evidence for oscillation of atmospheric neutrinos, Physical Review Letters, Volume 81, Issue 8, 1998, Pages 1562-1567.

[2] W. N. Cottingham and D. A. Greenwood, An introduction to the Standard Model of Particle Physics, Second Edition, Cambridge university press, UK

[3] F. Reines and C. L. Cowan, Jr., Detection of the Free Neutrino, Phys. Rev. 92, 830 – Published 1 November 1953

[4] D. Akimov et al., Observation of coherent elastic neutrino-nucleus scattering, Science 15 Sep 2017:Vol. 357, Issue 6356, pp. 1123-1126 DOI: 10.1126/science.aao0990

[5] D.Z.Freedman, Phys. Rev. D9 (1974) 1389

[6] BJ Scholz et al., Measurement of the low-energy quenching factor in germanium using an ^{88}Y/Be photoneutron source, Phys.Rev.D 94 (2016) 12, 122003, DOI: 10.1103/PhysRevD.94.122003

[7] J. Lindhard, V. Nielsen, M. Scharff, and P.V. Thom-sen,Mat. Fys. Medd.33(1963) no. 10

[8] Janka HT. (2017) Neutrino Emission from Supernovae. In: Alsabti A., Murdin P. (eds) Handbook of Supernovae. Springer, Cham. https://doi.org/10.1007/978-3-319-21846-5_4

[9] James R. Wilson, Coherent Neutrino Scattering and Stellar Collapse, Phys. Rev. Lett. 32, 849 – Published 15 April 1974

[10] J. Billard, E. Figueroa-Feliciano, and L. Strigari, Implication of neutrino backgrounds on the reach of next generation dark matter direct detection experiments, Phys. Rev. D 89, 023524 – Published 27 January 2014

[11] Bhaskar Dutta and Louis E. Strigari, Annual Review of Nuclear and Particle Science, Vol. 69:137-161 (Volume publication date 19 October 2019)

[12] K. Patton et al., Phys. Rev. C 86 (2012) 0246

[13] J.Erler, A.Freitas, PDG, ch.10, 2016

[14] Lindner, M., Rodejohann, W., & Xu, X. (2017). Coherent neutrino-nucleus scattering and new neutrino interactions. Journal of high energy physics:JHEP, 2017(3): 097. doi:10.1007/JHEP03(2017)097.

[15] L Ludhova and Borexino Collaboration 2020 J. Phys.: Conf. Ser.1342 012033

[16] A.G. Beda et al., Gemma experiment: The results of neutrino magnetic moment search, Phys.Part.Nucl.Lett. 10 (2013) 139-143

[17] H. B. Li et al. (TEXONO Collaboration), Limit on the Electron Neutrino Magnetic Moment from the Kuo-Sheng Reactor Neutrino Experiment, Phys. Rev. Lett. 90, 131802 – Published 1 April 2003

[18] M. Askins et al, The Physics and Nuclear Nonproliferation Goals of WATCHMAN: A WAter CHerenkov Monitor for ANtineutrinos, arXiv:1502.01132 [physics.ins-det], 2015

[19] C. Bellenghi et al., Coherent elastic nuclear scattering of ^{51}Cr neutrinos, Eur.Phys.J.C 79 (2019) 9, 727, doi:10.1140/epjc/s10052-019-7240-3

[20] A.G. Beda et al, The first result of the neutrino magnetic moment measurement in the gemma experiment, Physics of Atomic Nuclei 2007

[21] H T Wong et al. J. Phys. Conf. Ser. 39, 266 (2006)

[22] V. Belov et al., The νGeN experiment at the Kalinin Nuclear Power Plant, JINST 10 (2015) 12, P12011

[23] Rothe, J., Angloher, G., Ardellier-Desages, F. et al. NUCLEUS: Exploring Coherent Neutrino-Nucleus Scattering with Cryogenic Detectors. J Low Temp Phys 199, 433–440 (2020). https://doi.org/10.1007/s10909-019-02283-7

[24] Practical Gamma-ray Spectrometry - 2nd Edition Gordon R. Gilmore, 2008 John Wiley & Sons, Ltd. ISBN: 978-0-470-86196-7

[25] Soo Hyun Byun, lecture notes, Med Phys 4RA3, ARB3, 6R03, McMaster University, Hamilton, Ontario, Canada, Version 2016-17, https://www.science.mcmaster.ca/radgrad/programs/courses.html?id=224

[26] Croft, S. & Bond, D. A determination of the Fano factor for germanium at 77.4 K from measurements of the energy resolution of a 113 cm3 HPGe gamma-ray spectrometer taken over the energy range from 14 to 6129 keV. Int. J. Radiat. Appl. Instrumentation. Part A. Appl. Radiat. Isot. 42, 1009–1014 (Jan. 1991)

[27] Marco Salathe, Study on modified point contact germanium detectors for low background applications, Heidelberg University, 2015

[28] Z. Ahmed et. al. (CDMS), Results from a Low-Energy Analysis of the CDMS II Germanium Data, Phys. Rev. Lett.106, 131302 (2011)

[29] G. Heusser, Low-radioactivity background techniques,Annu. Rev. Nucl. Part. Sci. 1995. 45:543-90

[30] M Weber et al, GIOVE: a new detector setup for high sensitivity germanium spectroscopy at shallow depth, Eur. Phys. J. C (2015) 75:531 DOI 10.1140/epjc/s10052-015-3704-2

[31] M Agostini et al, Limits on uranium and thorium bulk content in Gerda Phase I detectors, Astroparticle Physics Volume 91, May 2017, Pages 15-21

[32] By User:Tosaka - File:Decay chain(4n+2, Uranium series).PNG, CC BY 3.0, https://commons.wikimedia.org/w/index.php?curid=33293646

[33] By http://commons.wikimedia.org/wiki/User:BatesIsBack - http://commons.wikimedia.org/wiki/File:Decay_Chain_of_Thorium.svg, CC BY-SA 3.0, https://commons.wikimedia.org/w/index.php?curid=16983885

[34] 220,22Rn Radon-Exposition in Innenraeumen, Schwankner et al.

[35] Tibor J. Dunai, Cosmogenic Nuclides - Principles, Concepts and Applications in the earth Surface Sciences, Cambridge University Press, Cambridge, 2010.

[36] P. P. Povinec et al, New Isotope technologies in environmental physics, acta physica slovaca vol. 58 No. 1, 1-154, February 2008.

[37] L.N. Bogdanova et al., Cosmic muon flux at shallow depths underground, Phys.Atom.Nucl. Vol. 69, No. 8 (2006) 1293-1298, arXiv:nucl-ex/0601019.

[38] K. Nakamura et al.(PDG), JP G 37, 075021 (2010).

[39] J. Hakenmüller, master thesis, university of Heidelberg, 2015

[40] Best et al., Low energy neutron background in deep underground laboratories, Volume 812, 11 March 2016, Pages 1-6

[41] Chapter: 4 Atomic and nuclear physics, Subsection 4.7.3, Tables of Physical & Chemical Constants (16th edition 1995). 2.1.4 Hygrometry. Kaye & Laby Online. Version 1.0 (2005) www.kayelaby.npl.co.uk

[42] P. M. Rinard, Neutron Interactions with Matter, Los Alamos 1997, Technical Report, http://www.fas.org/sgp/othergov/doe/lanl/lib-www/la-pubs/00326407.pdf

[43] E. Armengaud (EDELWEISS Collaboration), Measurement of the cosmogenic activation of germanium detectors in EDELWEISS-III, Astropart.Phys. 91 (2017) 51-64, DOI:10.1016/j.astropartphys.2017.03.006

[44] J.H. Kelley et al., Nuclear Phys. A 564, 1–183 (1993)

[45] M.J. Berger et al, Stopping-Power & Range Tables for Electrons, Protons, and Helium Ions, NIST Standard Reference Database 124

[46] M Baginova et al., Investigation of neutron interactions with Ge detectors, Nuclear Inst. and Methods in Physics Research, A 897 (2018) 22–31

[47] Ljungvall J. and Nyberg J., A study of fast neutron interactions in high-purity germanium detectors, Nucl. Instrum. Methods Phys. Res. A, 546 (2005), pp. 553-573

[48] M. Boswell et al., IEEE Trans. Nucl. Sci. 58, 1212–1220 (2011)

[49] S. Agostinelli et al., Nucl. Instrum. Meth. A 506, 250–303 (2003)

[50] J. Allison et al., IEEE Trans. Nucl. Sci. 53, 270–278 (2006)

[51] P.A. Zyla et al. (Particle Data Group), Prog. Theor. Exp. Phys. 2020, 083C01 (2020) (43. Monte Carlo Particle Numbering Scheme)

[52] T. Schierhuber, Ultra-Low Background Germanium Spectroscopy: commissioning an experimental shielding for a future neutrino experiment, master thesis, Heidelberg University (2017)

[53] J. Hakenmüller et al., Neutron-induced background in the CONUS experiment, Eur. Phys. J. C (2019) 79:699 https://doi.org/10.1140/epjc/s10052-019-7160-2

[54] Mirion Technologies (Canberra Lingolsheim), 1 Chemin de la Roseraie, 67380 Lingolsheim, France

[55] D. Willems, R. Arts and J. Douwen, State-of-the art cryocooler solutions for HPGe detectors, technical paper, Mirion technologies

[56] de Waele A.T.A.M., Basic Operation of Cryocoolers and related thermal machines, J Low Temp Phys (2011) 164:179–236 DOI 10.1007/s10909-011-0373-x

[57] DIN 25482-5:1993-06. Nachweisgrenze und Erkennungsgrenze bei Kernstrahlungsmessungen; Zählende hochauflösende gammaspektrometrische Messungen ohne Berücksichtigung des Probenbehandlungseinflusses, Ausgabedatum 1993-06

[58] Wei, W.Z. et al. JINST 12 (2017) no.04, P04022 arXiv:1602.08005 [physics.ins-det]

[59] R.H. Pehl, F.S. Goulding, D.A. Landis, M. Lenzlinger. Nucl. Instr. and Meth., 59 (1968), p. 45

[60] Agostini, M., Bakalyarov, A.M., Andreotti, E. et al. Characterization of 30 76Ge enriched Broad Energy Ge detectors for GERDA Phase II. Eur. Phys. J. C 79, 978 (2019). https://doi.org/10.1140/epjc/s10052-019-7353-8

[61] C. Buck et al, A novel experiment for coherent elastic neutrino nucleus scattering: CONUS, J.Phys.Conf.Ser. 1342 (2020)

[62] D. J. Thomas and A.V. Alevra, Nucl. Instrum. Meth. A **476**, 12 (2002)

[63] A. V. Alevra and D.J. Thomas, Radiat. Prot. Dosim. **107**, 37 (2003)

[64] B. Wiegel and A.V. Alevra, Nucl. Instrum. Meth. A **476**, 36 (2002)

[65] Centronic Ltd, 267 King Henry's Dr, New Addington, Croydon CR9 0BG, Great Britain

[66] B. Wiegel et al., Nucl. Instrum. Meth. A **476**, 52 (2002)

[67] Mirion Technologies (Canberra Olen), Lammerdries-Oost 25, 2250 Olen, Belgium

[68] A. Zimbal et al., AIP Conf. Proc. **1549**, 70 (2013)

[69] M. Reginatto et al., AIP Conf. Proc. **1553**, 77 (2013)

[70] M. Reginatto, Radiat. Prot. Dosim. **180**, 403 (2018)

[71] D. Budjáš et al., Appl. Radiat. Isot. **67**(5), 706-710 (2009)

[72] I. Endrizzi et al., in *Proceedings of the Workshop on Core Monitoring for Commercial Reactors: Improvements in Systems and Methods Workshop Proceedings Stockholm, Sweden, 1999* (OECD proceedings, Paris, 2000) p. 223

[73] Analysebericht, Kompetenzzentrum Analytik BASF, Carl-Bosch-Strasse 38, 67056 Ludwigshafen am Rhein, Germany

[74] G. Heusser, in *Proceedings of the 14th Europhysics Conference on Nuclear Physics, Rare Nuclear Processes, Bratislava, Czecho-Slovakia, 1992*, ed. by P. Povinec (World Scientific Publishing Co. Pte. Ltd., Singapore, 1992) p. 247

[75] A. Eštoková and L. Palaščáková, Int. J. Environ. Res. Public Health **10**, 7165-7179 (2013)

[76] M.K. Singh et al., Indian J Phys **91**(10), 1277-1291 (2017)

[77] E. Schlünder et al., *VDI-Wärmeatlas. Berechnungsblätter für den Wärmeübergang*, 7nd end. (VDI-Verlag GmbH, Düsseldorf, 1994)

[78] V. I. Kopeikin et al., Physics of Atomic Nuclei **67** No. 10, 1892–1899 (2004)

[79] A. Ziegeler and H. Allelein, *Reaktortechnik Physikalisch-technische Grundlagen*, 2nd edn. (Springer, Berlin, Heidelberg, 2013)

[80] O. W. Hermann and C. W. Alexander, Review of Spent-Fuel Photon and Neutron Source Spectra. ORNL/CSD/TM-205 (Oak Ridge National Lab., TN, USA), report available from NTIS, PCA02/MF A01 as DE86006764 (1986)

[81] E. Poon and F. Verhaegen, Med. Phys. **32**, 1696-1711 (2005)

[82] S. Hurtado et al., Nucl. Instrum. Methods Phys. Res. A **518**, 764-774 (2004)

[83] K. Amako et al., IEEE Trans. Nucl. Scie. **52**, 910-917 (2005)

[84] National Nuclear Data Center: Thermal Neutron Capture γ's (CapGam), last updated September 20, 2013, https://www.nndc.bnl.gov/capgam/index.html

[85] International Atomic Energy Agency, *Database of prompt gamma rays from slow neutron capture for elemental analysis* (IAEA, Vienna, 2007), https://www-nds.iaea.org/pgaa/egaf.html

[86] D. S. Sivia and J. Skilling, *Data Analysis: A Bayesian Tutorial*, 2nd edn. (Oxford University Press, Oxford, 2006)

[87] F. Fernández et al., Radiat. Prot. Dosim. **110**, 517-521 (2004)

[88] V. Lacoste et al., Radiat. Prot. Dosim. **125**, 304-308 (2007)

[89] M. Reginatto, Radiat. Prot. Dosim. **121**, 64 (2006)

[90] D. J. Lunn et al., Stat. Comput. **10**, 325 (2000)

[91] N. Tricot and U. Jendrich, Neutron fluence at the reactor pressure vessel wall - A comparison of french and german procedures and strategies in PWRs (EUROSAFE Forum 2002: convergence of nuclear safety practices in Europe Papers, Germany, 2003), http://www.eurosafe-forum.org

[92] Aapo Tanskanen, Assessment of the neutron and gamma sources of the spent BWR fuel, Interim report on Task FIN JNT A 1071 of the Finish support progamme to IAEA Safeguards, October 2000

[93] JE Fast et al, Spent Nuclear Fuel Measurements, PNNL-23561, 2014

[94] B. Ma et al., Phys. Rev. C **88**, 014605 (2013)

[95] F. P. An et al. (Daya Bay Collaboration), Chin. Phys. C **41**(1), 013002 (2017)

[96] Z. Djurcic et al., J. Phys. G **36**, 045002 (2009)

[97] N. Soppera et al., Nucl. Data Sheets **120**, 294–296 (2014)

[98] J. H. Kelley et al., Nuclear Physics A **564**, 1–183 (1993)

[99] NIST Standard Reference Database 8 (XGAM), M.J. Berger et al., NIST, PML, Radiation Physics Division, DOI: https://dx.doi.org/10.18434/T48G6X

[100] Hakenmüller J, Maneschg W and Heusser G 2016J. Phys.: Conf. Ser.718042028

[101] S. C. Blyth, Measurement of Cosmic-ray Muon-induced Spallation Neutrons in the AberdeenTunnel Underground Laboratory, Nuclear and Particle Physics Proceedings, Vol 273–275, 2016

[102] private communication W. Maneschg

[103] H Gastrich et al, The Dortmund Low Background Facility — Low-background gamma ray spectrometry with an artificial overburden, Appl.Radiat.Isot. 112 (2016) 165-176

[104] N. Jovančević et al., Neutron induced background gamma activity in low-level Ge-spectroscopy systems, Nuclear Instruments and Methods in Physics Research A 612 (2010) 303–308

[105] P Vojtyla, Experimental and simulated cosmic muon induced background of a Ge spectrometer equipped with a top side anticoincidence proportional chamber, NIM in Physics Research B 86 (1994) 380-386

[106] S. Niese, Messung geringer Radioaktivitäten in Untertagelaboratorien mit Hilfe mehrdimensionaler Spektrometrie, VKTA - 87 Januar 2008

[107] L Vanhoefer, Limitations of Rare Event HPGe Experiments due to Muon-Induced Neutron Background, phd thesis, Technical University of Munich, 2018

[108] C Wiesinger et al., Virtual depth by active background suppression: revisiting the cosmic muon induced background of Gerda Phase II, Eur. Phys. J. C 78, 597 (2018). https://doi.org/10.1140/epjc/s10052-018-6079-3

[109] X-RAY DATA Booklet, Center for X-ray Optics and Advanced Light Source, Lawrence Berkeley National Laboratory Table 1-2

[110] J. H. Hubbell and S. M. Seltzer, X-Ray Mass Attenuation Coefficients, NIST Standard Reference Database 126

[111] https://en.wikipedia.org/wiki/Isotopes_of_germanium, last accessed on 16.08.2020

[112] G. Meierhofer et al., Phys. Rev. C **81**, 027603, (2010)

[113] G. Meierhofer et al., Thermal neutron capture cross-section of 76Ge, Eur. Phys. J. A 40, 61–64 (2009)

[114] M. Bhike et al., Phys. Lett. B **741**, 150–154 (2015)

[115] Firestone, R.B., Choi, H.D., Lindstrom, R.M. et al. Database of prompt gamma rays from slow neutron capture for elemental analysis, Lawrence Berkeley National Laboratory, 2014 https://escholarship.org/uc/item/1wj43711

[116] Table of Radionuclides (Comments on evalution), Volumes 1-4, 2008,BUREAU INTERNATIONAL DES POIDS ET MESURES, Pavillon de Breteuil, F-92310 S VRES.

[117] Nuclear Data Center, Japan Atomic Energy Agency (JAEA), available at https://wwwndc.jaea.go.jp/jendl/j40/j40f32.html

[118] A. Bearden and A.F. Burr, Rev. Mod. Phys. 39, 125 (1967)

[119] J.C. Fuggle and N. Martensson, J. Electron Spectrosc. 21, 275-81 (1980)

[120] `www.nucleide.org`; E. Schönfeld, Appl. Radiat. Isot. Vol. 49, No. 9-11, pp. 1353-1357 (1998)

[121] Perkins, S.T., Cullen, D.E., Chen, M.H., Hubbell, J.H., Rathkopf, J., & Scofield, J. (1994). EADL: Evaluated Atomic Data Library of the Lawrence Livermore National Laboratory, USA Summary documentation (IAEA-NDS–156). Lemmel, H.D. (Ed.). International Atomic Energy Agency (IAEA)

[122] M. Pepin, Low-Mass Dark Matter Search Results and Radiogenic Backgrounds for the Cryogenic Dark Matter Search, phd thesis, University of Minnesota, 2016

[123] A. Sonay et al (TEXONO collaboration), Neutron background measurements with a hybrid neutron detector at the Kuo-Sheng Reactor Neutrino Laboratory, Phys. Rev. C 98, 024602 2018

[124] F.T. Avignone III , et al. , Nucl. Phys. B 28A (1992) 280

[125] H.S. Miley , et al., Nucl. Phys. B 28A (1992) 212

[126] J.F. Ziegler , IBM J. Res. Develop. 42 (1998) 117

[127] H.V. Klapdor-Kleingrothaus , et al. , Nucl. Instrum. Meth. A 481 (2002) 149

[128] M.S. Gordon , et al. , IEEE Trans. Nucl. Sci. 51 (2004) 3427

[129] I. Barabanov , et al. , Nucl. Instrum. Meth. B251 (2006) 115–120

[130] J.J. Back , Y.A. Ramachers , Nucl. Instrum. Meth. A 586 (2008) 286

[131] D.M. Mei, Z.B. Yin, S.R. Elliott, Astropart. Phys. 31 (2009) 417–420

[132] W.-Z. Wei et al. / Astroparticle Physics 96 (2017) 24–31

[133] E. Armengaud et al. (Edelweiss III Coll.), Astropart. Phys. 91 (2017) 51–64

[134] J. Amare et al, J. Astropart. Phys. 97 (2018) 96-105

[135] R.Agnese et al. (CDMS coll), Astroparticle Physics 104 (2019) 1-12, exp and calc

[136] S. Cebrián et al, Cosmogenic activation of materials, International Journal of Modern Physics A, 2017.·

[137] E Aguayo et al, PNNL-21302, Optimization of the Transport Shield for Neutrinoless Double-beta Decay Enriched Germanium, 2012.

[138] https://twiki.cern.ch/twiki/bin/view/Geant4/LoweOverview

[139] R.N. Hall, J. Phys. Chem. 57 (1953) 836

[140] L. M. Panero, A simple approach to measure the radon equilibrium factor F from air filter gross beta counting, Radiation Protection Dosimetry (2014), pp. 1–4

[141] Radon series disequilibrium in southern California coastal air

[142] L. Pattavina et al., Radiopurity of an archaeological Roman lead cryogenic detector, Eur. Phys. J. A (2019) 55: 127 DOI 10.1140/epja/i2019-12809-0

[143] P. Redl, Accurate Simulations of 206 Pb Recoils in SuperCDMS, J Low Temp Phys (2014) 176:937–942 DOI 10.1007/s10909-014-1102-z

[144] D. Budjáš et al., Highly Sensitive Gamma-Spectrometers of GERDA for Material Screening: Part II, Proc 14th Intern. School, Particles and Cosmology, Baksan, Apr. 16–18, 2007, ed. by S.V. Demidov, V.A. Matveev, V.A. Rubakov, (INR RAS, Moscow 2008), pp. 233–238

[145] E. Armengaud et al, EDELWEISS Collaboration, Performance of the EDELWEISS-III experiment for direct dark matter searches, JINST 12 (2017) 08, P08010

[146] A. Hegai, Study on pulse shapes of germanium detectors with a point like contact geometry for the GERDA and MAJORANA experiments, phd thesis, Tübingen university, 2018

[147] Chakravarti, Laha, and Roy, Handbook of Methods of Applied Statistics, Volume I, John Wiley and Sons, pp. 392-394, 1967

[148] NIST/SEMATECH e-Handbook of Statistical Methods, https://www.itl.nist.gov/div898/handbook/eda/section3/eda35g.htm, 10.08.2020

[149] ROOT implementation of Kolmogorov-Smirnov test (TH1::KolmogorovTest()), https://root.cern.ch/doc/master/classTH1.html, 10.08.2020

[150] P. Huber, Determination of antineutrino spectra from nuclear reactors, Phys. Rev. C 84, 024617 – Published 29 August 2011; Erratum Phys. Rev. C 85, 029901 (2012)

[151] Th. A. Mueller et al, Improved predictions of reactor antineutrino spectra, Phys. Rev. C 83, 054615 2011

[152] F. P. An et al. (Daya Bay Collaboration), Evolution of the Reactor Antineutrino Flux and Spectrum at Daya Bay, Phys. Rev. Lett. 118, 251801 2017

[153] F. James, Minuit Function Minimization and Error Analysis, Reference manual, Version 94.1 CERN Program Library Long Writeup D506

[154] Statistical Data Analysis, Glen Cowan, 1998 Oxford University Press, Great Clarendon Street, Oxford OX26DP

[155] Luca Lista, Pratical Statistics for Particle Physics, arXiv:1609.04150v2 [physics.data-an] 25 Jul 2017

[156] private communication T. Rink and T. Hugle

[157] W. Mannhart, Information on the Cf-252 fission-neutron spectrum deduced-from integral experiments, PTB

[158] David Thomas, The 252Cf neutron spectrum in ISO Standard 8529, ESARDA BULLETIN, No. 51, December 2014

[159] International Organization for Standardization, Reference neutron radiations-Part 1: Characteristics and methods of production, International Standard, 8529-1, (ISO, Geneva, Switzerland) 2001

[160] D. Regnier et al, Monte Carlo Simulation of Prompt Fission Gamma Emission, Physics Procedia 31 (2012) 59-65

[161] J. Hakenmüller, Charakterisierung des Gammaspektrometers GIOVE, bachelor thesis, 2012

[162] L. Li, B. Cabrera-Palmer, and P.S. Barbeau, Quenching Factor Measurements for Germanium Detectors at TUNL, poster neutrino conference 2020 Chigaco

[163] A.D'Addabbo et al., An active noise cancellation technique for the CUORE Pulse Tube cryocoolers, Cryogenics Volume 93, July 2018, Pages 56-65

[164] L.T. Yang et al, Bulk and surface event identification in p-type germanium detectors, Nuclear Instruments and Methods in Physics Research Section A: Accelerators, Spectrometers, Detectors and Associated Equipment Volume 886, 1 April 2018, Pages 13-23

[165] https://en.wikipedia.org/wiki/Tungsten

[166] https://en.wikipedia.org/wiki/Lead

G Danksagung

Zunächst möchte ich mich bei Herrn Prof. Dr. Dr. h.c. Manfred Lindner für die Möglichkeit bedanken unter den hervorragenden Rahmenbedingungen in der Astroteilchenphysik Abteilung des MPIK zu promovieren. Ich bin dankbar für die Chance, an so einem interessanten Experiment von Anfang an Mitarbeiten zu dürfen. Ich freu mich auch über die Konferenzen und Sommerschulen, die ich besuchen konnte. Ich möchte mich auch für die Unterstützung durch das IMPRS-PTFS Graduiertenprogramm bedanken.

Ich danke Frau Prof. Loredana Gastaldo für ihre freundliche Unterstützung als Zweitgutachterin, sowie für die Möglichkeit CONUS beim VISTAS Detector Workshop präsentieren zu können.

Zudem gilt mein Dank Dr. Werner Maneschg für die Unterstützung, Ratschläge und zahllosen Diskussionen in den letzten Jahren. Danken möchte ich auch Dr. Gerd Heusser, von dem ich unglaublich viel gelernt habe. Danke an Herbert Strecker für die Lösung zahlreicher praktischer Probleme, an Dr. Aurélie Bonhomme für Aufmunterungen im richtigen Moment und wissenschaftliche Diskussionen, an Thomas Rink, Dr. Christian Buck, Tobias Schierhuber und Thomas Hugle für ihre Ideen und Unterstützung. Insgesamt danke ich der CONUS Kollaboration, ihr habt meine Promotionszeit zu etwas Besonderem gemacht.

Vielen Dank an die Mitarbeiter des Kernkraftwerks Brokdorf für ihre unbezahlbare Unterstützung und große Begeisterung für das Experiment. Ich danke insbesondere Herrn Dr. Fülber and Herr Dr. Wink für ihre detaillierten Erklärungen und das Bereitstellen von Daten. Vieles in dieser Arbeit ist so erst möglich geworden.

An dieser Stelle will ich auch den Mitarbeitern der PTB danken. Die Zusammenarbeit hat toll geklappt und ich habe viel von euch gelernt, insbesondere von Dr. Miroslav Zboril and Dr. Marcel Reginatto.

Dankbar bin ich auch für die Unterstützung zahlreicher Mitarbeiter am MPIK. Herr Dr. Köck sei insbesondere gedankt. Ohne die ganzen Cluster Jobs and das Bereitstellen des Speicherplatzes wäeren viele Seiten leer geblieben.

Vielen Dank an die Korrekturleser dieser Arbeit, viele aus der CONUS Kollobration, ohne euch wäre diese Arbeit sicher viel mühsamer zu lesen.

Bei meinen Freuden möchte ich für all die Unternehmungen, Spieleabende und Gespräche der letzten Jahre bedanken. Insbesondere sei hier Marianna Drabek erwähnt, die immer ein offenes Ohr für mich hatte.

Ein großes Dankeschön zum Schluss an meine Eltern Carmen und Johannes und meine Schwester Jasmin für ihre unbezahlbare Unterstützung! Ihr habt immer an

mich geglaubt, mir Mut gemacht und euch meine Sorgen angehöhrt. Ein besonderer Dank gilt auch meiner Oma Halina, die die beste Oma war, die ich mir wünschen konnte.